

## **REMARKS**

Claims 13, 14, 17-20, and 54-60 were allowed in the application. Applicant hereby submits this request for continued examination (RCE) and requests consideration of the enclosed Information Disclosure Statement (IDS).

### **Information Disclosure Statement**

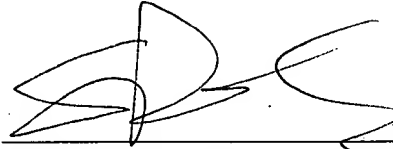
The enclosed IDS contains cites references that were not previously considered by the Examiner. The Notice of Allowance of October 29, 2003, indicated that the Examiner did not consider some references due to an absence of publication dates.

Applicant has provided with the instant IDS all known dates of publication, dates of Internet publication, and dates of retrieval where possible in accordance with MPEP 707.05(e).

The Examiner objected to the IDS mailed on September 25, 2003 as lacking the required fee set forth in 37 C.F.R. 1.17(p). Applicant notes that the Fee Transmittal authorized an IDS fee and any additional fees incurred during the pendency of the application.

## CONCLUSION

Applicant graciously acknowledges the allowance of claims 13, 14, 17-20, and 54-60.



**STEPHEN S. ROCHE, REG. NO. 52,176**

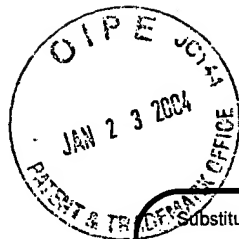
Duft Setter Ollila & Bornsen LLC

Telephone: (303) 938-9999 ext. 15

Facsimile: (303) 938-9995

**CORRESPONDENCE ADDRESS:**

**CUSTOMER NO. 036122**



PTO/SB/08b(05-03)

Approved for use through 04/30/2003. OMB 0651-0031

U.S. Patent and Trademark Office; U.S. DEPARTMENT OF COMMERCE

Under the Paperwork Reduction Act of 1995, no persons are required to respond to a collection of information unless it contains a valid OMB control number

Substitute for form 1449A/PTO

**INFORMATION DISCLOSURE  
STATEMENT BY APPLICANT**

(use as many sheets as necessary)

Sheet 1 of 2

**Complete if Known**

Application Number	09/920,235
Confirmation Number	5852
Filing Date	8/1/01
First Named Inventor	Mark W. Smith
Group Art Unit	2878
Examiner Name	Constantine Hannaher
Attorney Docket Number	36032/094

**OTHER PRIOR ART -- NON PATENT LITERATURE DOCUMENTS**

Examiner Initials *	Cite No. <sup>1</sup>	Include name of the author (in CAPITAL LETTERS), title of the article (when appropriate), title of the item (book, magazine, journal, serial, symposium, catalog, etc.), date, page(s), volume-issue number(s), publisher, city and/or country where published.	T <sup>2</sup>
	1	MATR MOPITT Airborne Test Radiometer, retrieved from <a href="http://www.eos.ucar.edu/matr/Welcome.html">http://www.eos.ucar.edu/matr/Welcome.html</a> [internet], date of publication unknown, [retrieved on 5/30/01].	
	2	MOPITT, retrieved from: <a href="http://www.atmosp.physics.utoronto.ca/MOPITT/home.html">http://www.atmosp.physics.utoronto.ca/MOPITT/home.html</a> [internet], date of publication 30 October 1993, date retrieved 5/30/01.	
	3	"Gas Correlation Spectroscopy" OPTO-KNOWLEDGE: The Source for Special Imaging - Press, retrieved from: <a href="http://www.techexpo.com/WWW/opto-knowledge/gas-corr.html">http://www.techexpo.com/WWW/opto-knowledge/gas-corr.html</a> , Internet, date of publication, unknown; date retrieved 10/3/00.	
	4	SANDSTEN, JONAS, EDNER, HANS, SVANBERG, SUNE, and WEIBRING, PETER, "Gas imaging using gas-correlation spectroscopy" retrieved from: <a href="http://www-atom.fysik.lth.se/AFDOCS/Progrep978/c3.htm">http://www-atom.fysik.lth.se/AFDOCS/Progrep978/c3.htm</a> , Internet, date of publication unknown; date retrieved 10/3/00.	
	5	SMITH, MARK W., "Technical Report for: MOPITT Airborne Test Radiometer (MATR), retrieved from: <a href="http://www.eos.ucar.edu/Matr.Welcome.html">http://www.eos.ucar.edu/Matr.Welcome.html</a> , Internet, Date of Publication 15 March 2000, date retrieved unknown.	
	6	"Measurements of Pollution in The Troposphere MOPITT," retrieved from: <a href="http://www.atmosp.physics.utoronto.ca/MOPITT/home.html">http://www.atmosp.physics.utoronto.ca/MOPITT/home.html</a> , Internet, date of publication unknown, date retrieved 9/20/2000.	
	7	MOPITT Project, retrieved from: <a href="http://eos.acd.ucar.edu/mopitt">http://eos.acd.ucar.edu/mopitt</a> , Internet, date of publication 11/18/99, date retrieved unknown.	
	8	Measurements of Pollution in the Troposphere, MOPITT Overview, retrieved from: <a href="http://www.atmosp.physics.utoronto.ca/MOPITT/overview.html">http://www.atmosp.physics.utoronto.ca/MOPITT/overview.html</a> Internet, Date of Publication August 2, 1995; date retrieved 9/20/00.	
	9	Measurement of Pollution in The Troposphere (MOPITT), Measurement of Pollution in The Troposphere (MOPITT) Program; retrieved from <a href="http://www.acd.ucar.edu/asr99/MOPITT.html">http://www.acd.ucar.edu/asr99/MOPITT.html</a> , Internet, Date of Publication unknown, date retrieved 9/20/00.	
	10	CLERBAUX, CATH, HADJI-LAZARO, JULIETTE, "Assimilation of carbon monoxide measured from satellite in a three-dimensional chemistry-transport model," retrieved from: Journal of Geophysical Research, year of publication 2000, date retrieved unknown.	
	11	BAER-RIEDHART, JENNY, "ERAST: Scientific Applications and Technology Commercialization," Mezzanine Plenary Session, pgs. 43-66, Dryden Flight Research Center, Date of Publication unknown, Date retrieved unknown.	

Examiner Signature	Date Considered
-----------------------	--------------------

\*EXAMINER: Initial if reference considered, whether or not citation is in conformance with MPEP 609. Draw line through citation if not in conformance and not considered. Include copy of this form with next communication to applicant.

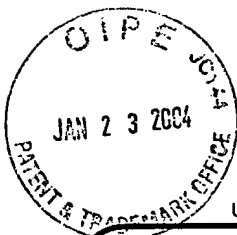
1 Applicant's unique citation designation number (optional). 2 Applicant is to place a check mark here if English language Translation is attached. This collection of information is required by 37 CFR 1.98. The information is required to obtain or retain a benefit by the public which is to file (and by the USPTO to process) an application. Confidentiality is governed by 35 U.S.C. 122 and 37 CFR 1.14. This collection is estimated to take 120 minutes to complete, including gathering, preparing, and submitting the completed application form to the USPTO. Time will vary depending upon the individual case. Any comments on the amount of time you require to complete this form and/or suggestions for reducing this burden, should be sent to the Chief Information Officer, U.S. Patent and Trademark Office, U.S. Department of Commerce, P.O. Box 1450, Alexandria, VA 22313-1450. DO NOT SEND FEES OR COMPLETED FORMS TO THIS ADDRESS. SEND TO: Commissioner for Patents, P.O. Box 1450, Alexandria, VA 22313-1450.

If you need assistance in completing the form, call 1-800-PTO-9199 and select option 2.

01/29/2004 HAHMED1 00000081 09920235

02 FC:1806

180.00 DP



PTO/SB/08b(05-03)

Approved for use through 04/30/2003. OMB 0651-0031  
U.S. Patent and Trademark Office; U.S. DEPARTMENT OF COMMERCE

Under the Paperwork Reduction Act of 1995, no persons are required to respond to a collection of information unless it contains a valid OMB control number

Substitute for form 1449A/PTO

**INFORMATION DISCLOSURE  
STATEMENT BY APPLICANT**

(use as many sheets as necessary)

Sheet 2 of 2

**Complete if Known**

Application Number	09/920,235
Confirmation Number	5852
Filing Date	8/1/01
First Named Inventor	Mark W. Smith
Group Art Unit	2878
Examiner Name	Constantine Hannaher
Attorney Docket Number	36032/094

**OTHER PRIOR ART -- NON PATENT LITERATURE DOCUMENTS**

Examiner Initials *	Cite No. <sup>1</sup>	Include name of the author (in CAPITAL LETTERS), title of the article (when appropriate), title of the item (book, magazine, journal, serial, symposium, catalog, etc.), date, page(s), volume-issue number(s), publisher, city and/or country where published.	T <sup>2</sup>
	12	KHATTATOV, BORIS, LYJAK, LAWRENCE, and GILLE, JOHN, "On Application of Photochemical Models to the Design of Measurement Strategies," Atmospheric Chemistry Division, National Center for Atmospheric Research; Date of Publication March 2000; pgs. 1-4.	
	13	RODGERS, CLIVE D., "Inverse Methods for Atmospheric Sounding Theory and Practice," Series on Atmospheric, Oceanic and Planetary Physics—Vol. 2, World Scientific, Date of Publication 2000.	
	14	SMITH, MARK, W., "Remote sensing of atmospheric carbon monoxide with the MOPITT Airborne Test Radiometer (MATR), pgs. 1-11 Date of Publication, unknown	
	15	WYATT, C. L., "Radiometric System Design, Chapter 8 The Radiometric Performance Equation," MacMillan Publishing, pgs. 109-113, Date of Publication 1987, New York	
	16	Atmospheric Absorption, Field Measurements of Atmospheric Transmittance, Fig. 5-31, Date of Publication unknown.	
	17	PAN, LIWEN, et al., "Analysis and Characterization of the Retrieval Algorithm for Measuring Tropospheric CO using the MOPITT instrument," SPIE Vol. 2830, pgs. 159-168, Date of Publication 1996.	
	18	TOLTON, BOYD T., et al., "Calibration of a length modulated radiometer," SPIE Vol. 2830, pgs. 253-263, Date of Publication 1996.	

Examiner  
SignatureDate  
Considered

\*EXAMINER: Initial if reference considered, whether or not citation is in conformance with MPEP 609. Draw line through citation if not in conformance and not considered. Include copy of this form with next communication to applicant.

1 Applicant's unique citation designation number (optional). 2 Applicant is to place a check mark here if English language Translation is attached. This collection of information is required by 37 CFR 1.98. The information is required to obtain or retain a benefit by the public which is to file (and by the USPTO to process) an application. Confidentiality is governed by 35 U.S.C. 122 and 37 CFR 1.14. This collection is estimated to take 120 minutes to complete, including gathering, preparing, and submitting the completed application form to the USPTO. Time will vary depending upon the individual case. Any comments on the amount of time you require to complete this form and/or suggestions for reducing this burden, should be sent to the Chief Information Officer, U.S. Patent and Trademark Office, U.S. Department of Commerce, P.O. Box 1450, Alexandria, VA 22313-1450. DO NOT SEND FEES OR COMPLETED FORMS TO THIS ADDRESS. SEND TO: Commissioner for Patents, P.O. Box 1450, Alexandria, VA 22313-1450.

If you need assistance in completing the form, call 1-800-PTO-9199 and select option 2.





### Project Leader:

- Mark Smith
- NCAR, PO Box 3000, Boulder, CO 80307-3000
- Phone: 303-497-1856
- E-mail: [mwsmith@ucar.edu](mailto:mwsmith@ucar.edu)

### Staff Members:

- Mark Smith, Steve Shertz, Nuri Delen

### Scientific Objectives:

- Provide data to test and improve MOPITT retrieval algorithms.
- Provide data to help validate MOPITT retrieval results.

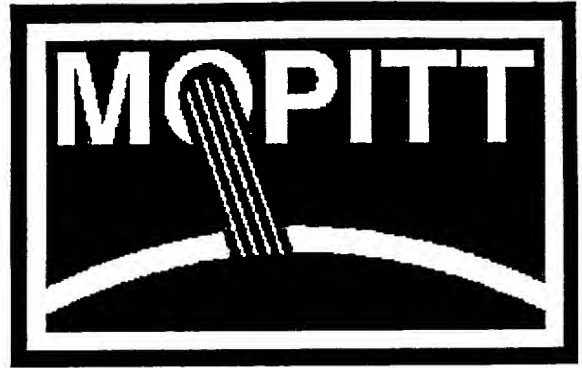
- Participate in regional scale studies of carbon monoxide distribution and transport.

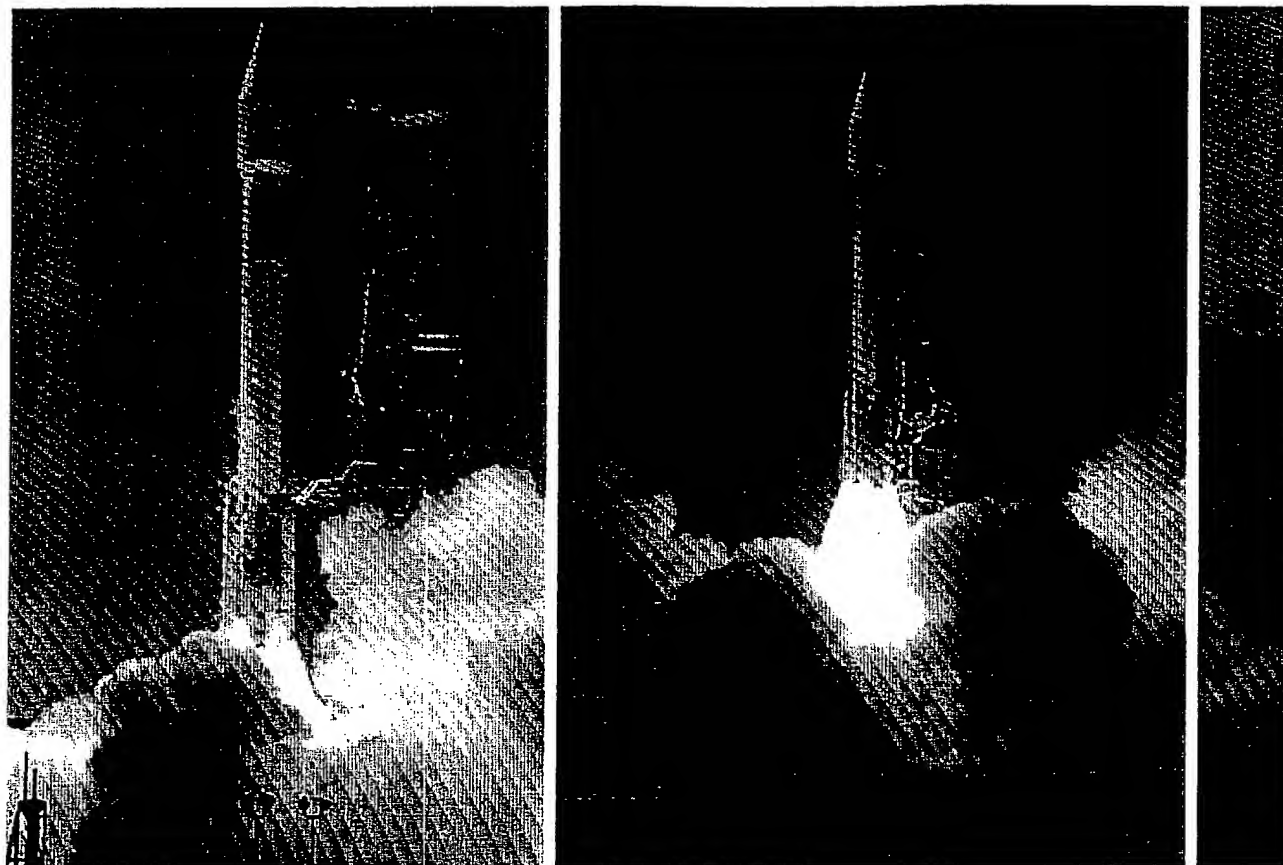
## **Additional Information:**

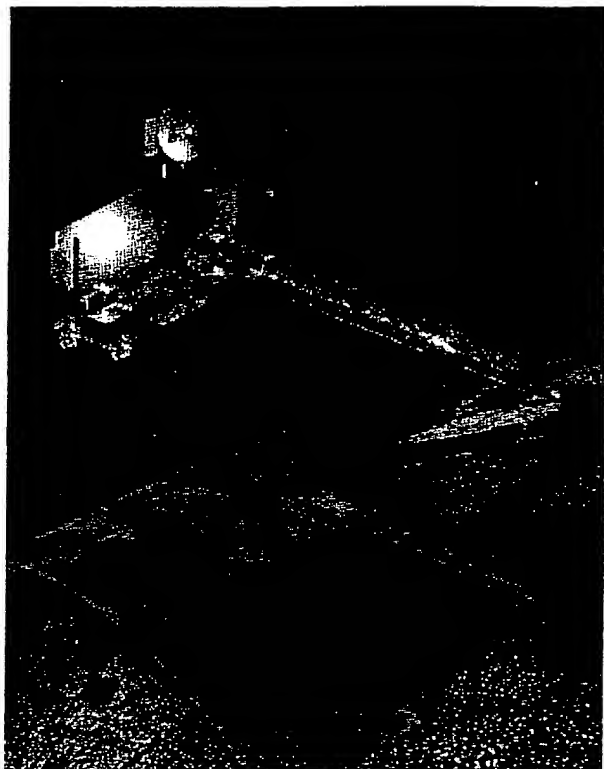
- [NCAR MOPITT Home Page](#)
- [University of Toronto MOPITT Home Page](#)
- [MOPITT Data Validation Home Page](#)
- [NASA EOS Home Page](#)
- [Air Pollution and Tropospheric Chemistry Research Information](#)
- [MATR Technical Report of 15 March 2000](#)

# Measurements Of Pollution In The Troposphere

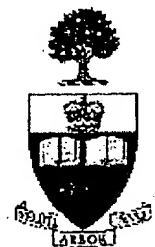
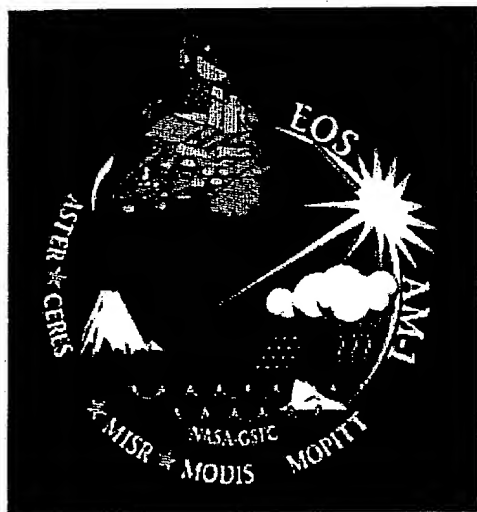
---











# MOPITT Mission Description Document Index

## 1 Introduction

- 1.1 Science
- 1.2 Measurement Concepts
- 1.3 Verification
- 1.4 Calibration and Validation
- 1.5 Data Processing
- 1.6 Instrumentation

## 2 Science

- 2.1 Objectives of Project
- 2.2 Science Background
  - 2.2.1 Introduction
  - 2.2.2 OH
  - 2.2.3 Sources of CO
  - 2.2.4 CO Sinks
  - 2.2.5 CO Distribution
  - 2.2.6 Transport of CO
  - 2.2.7 Modelling
    - 2.2.7.1 General
    - 2.2.7.2 3-D Photochemical Modelling
    - 2.2.7.3 Dynamical Modelling
  - 2.2.8 3-D Modelling Effort
  - 2.2.9 Integrating Measurements into Models
  - 2.2.10 Significance of Studies of Carbon Monoxide
  - 2.2.11 Atmospheric Methane
  - 2.2.12 Methane Sources
  - 2.2.13 Methane loss and mixing ratios
  - 2.2.14 Satellite Observations of Methane
  - 2.2.15 Summary of CH<sub>4</sub> Measurement Potential

## 3 Instrument Concept

- 3.1 Principles of Operation
  - 3.1.1 The Pressure Modulator Radiometer
  - 3.1.2 The Length Modulated Radiometer
  - 3.1.3 PMR vs. LMR
  - 3.1.4 Pressure Control and Stabilisation
- 3.2 Requirements and Performance Calculations
  - 3.2.1 Science Requirements
  - 3.2.2 Instrument Performance Evaluation
- 3.3 Carbon Monoxide (CO) Instrumentation
  - 3.3.1 Correlation Spectroscopy of Carbon Monoxide
  - 3.3.2 Carbon Monoxide in the Atmosphere
  - 3.3.3 Carbon Monoxide Signal Functions
  - 3.3.4 CO Profile Measurements - Performance Requirements
  - 3.3.5 Total Column Measurements
  - 3.3.6 CO Column Measurements - Performance Requirements
- 3.4 Methane (CH<sub>4</sub>) Instrumentation
  - 3.4.1 Correlation Spectroscopy of Methane
  - 3.4.2 Methane in the Atmosphere
  - 3.4.3 CH<sub>4</sub> Measurements - Performance Requirements
- 3.5 Instrument Field-of-View Considerations
- 3.6 Input Signal Range
- 3.7 Correlation Cell Pressures
  - 3.7.1 Correlation Cell Pressure Stability
  - 3.7.2 Correlation Cell Pressure Knowledge
- 3.8 Instrument Performance Summary

## 4 Verification

- 4.1 Purpose
- 4.2 Instrument Performance Verification
- 4.3 Science Performance Verification



**5 Calibration and Validation**

5.1	Calibration
5.1.1	Thermal (Emission) Channels
5.1.2	Solar (Reflection) Channels
5.1.3	Other Calibration Considerations
5.2	Validation
5.2.1	Level 0 Data (Raw Instrument Output)
5.2.2	Level 1 Data (Calibrated Radiances)
5.2.3	Level 2 Data (Retrieved profiles and column amount)

**6 Data Analysis**

6.1	Overall Plan
6.2	Data Products
6.2.1	Level 0
6.2.2	Level 1
6.2.3	Level 2
6.2.4	Level 3
6.2.5	Special Products
6.3	Ancillary Data Required
6.3.1	Global Temperature Data
6.3.2	Global Water Vapour Data
6.3.3	Global Cloud Data
6.3.4	Wind and Geopotential Height Data
6.4	Algorithm Development
6.4.1	Level 0-1
6.4.2	Level 1-2
6.4.3	Level 2-3
6.5	Data Processing Requirement and Volume

**7 MOPITT Instrument Science Requirements**

7.1	Introduction
7.1.1	General
7.1.2	Spacecraft Resource Allocations
7.1.3	Lifetime Requirement
7.1.4	Channel Configuration
7.2	Subsystem Configuration
7.2.1	Optical Subsystem
7.2.1.1	Instrument Field-of-View
7.2.1.2	Field of View Alignment
7.2.1.3	Scanning Mirrors
7.2.1.4	Pressure Modulator Cells
7.2.1.5	Length Modulator Cells
7.2.1.6	Choppers
7.2.1.7	Beamsplitters
7.2.1.8	Detector Elements
7.2.1.9	Focussing Requirements
7.2.1.10	Stray Light
7.2.1.11	Polarisation
7.2.2	Signal Channels
7.2.2.1	Length Modulator Cell Output
7.2.2.2	Pressure Modulator Cell Output
7.2.3	Science Data Output
7.2.4	Internal Calibration
7.2.4.1	Targets for Longwave Channels
7.2.4.2	Targets for Shortwave Channels
7.2.4.3	Temperature Monitoring
7.2.4.4	Pressure
7.2.4.5	Positions and Rates
7.2.4.6	Space View
7.2.5	Stirling Cycle Coolers (SCCs)
7.2.6	Instrument Computer
7.2.7	Instrument Port Covers
7.2.8	Heaters and Thermostats
7.2.8.1	Molecular sieve

	7.2.8.2	Survival Heaters
	7.2.8.3	Other Heating/Thermostating Requi:
7.3	<u>Instrument Performance Requirements</u>	
	7.3.1	Introduction
	7.3.2	Filter Profiles
	7.3.3	Signal Channel Performance
7.4	<u>Operating Modes</u>	
	7.4.1	Off
	7.4.2	Survival
	7.4.3	Launch
	7.4.4	Safe
	7.4.5	Science
	7.4.5.1	Normal Scan
	7.4.5.2	Short Calibration
	7.4.5.3	Long Calibration
	7.4.5.4	Commandable Scan
	7.4.6	Other Modes
7.5	<u>Data Output</u>	
	7.5.1	Data Streams
	7.5.2	Radiometric Data
	7.5.3	Housekeeping
	7.5.3.1	Temperatures
	7.5.3.2	Rates and Positions
	7.5.3.3	Voltages
	7.5.3.4	Currents
7.6	<u>Commands</u>	
	7.6.1	Packetised Commands
	7.6.1.1	Memory loads
	7.6.1.2	Parameter loads
	7.6.1.3	Operational Commands
	7.6.2	Discrete Commands and Telemetry
7.7	<u>Ground Support Equipment (GSE)</u>	
	7.7.1	Electrical - Bench Checkout Unit (BCU)
	7.7.1.1	Power supply
	7.7.1.2	Command Capability
	7.7.1.3	Data Capability
	7.7.1.4	Data Storage
	7.7.1.5	Interface
	7.7.1.6	Ancillary Equipment
	7.7.2	Mechanical
	7.7.3	Thermal
7.8	<u>Software Requirements</u>	
	7.8.1	Instrument Software
	7.8.2	Ground Support (pre-launch) Software

**A An Introduction to Correlation Spectroscopy**

A.1	<u>An Introduction to Correlation Spectroscopy</u>	
	A.1.1	Introduction
	A.1.2	Correlation Spectroscopy Techniques
	A.1.3	MOPITT CR Design
	A.1.4	Application of Double-Chopping CR to Nadir Soundin
A.2	<u>Historical Reference List for Correlation Radiometers</u>	

**B CO and CH4 Chemistry**

B.1	<u>Detailed Equations of OH Chemistry</u>
B.2	<u>Detailed Chemistry of Methane</u>

**C Pressure Modulator Cells**

C.1	<u>Summary</u>
C.2	<u>History</u>
C.3	<u>Operational Theory</u>
C.4	<u>Optical Realisation</u>
C.5	<u>Mechanical Realisation</u>
C.6	<u>Electronic Drive Subsystem</u>
C.7	<u>Resonant Frequency</u>

C.8	<u>Molecular Sieve Operation</u>
C.9	<u>Customisation and Accommodation Data</u>
C.10	<u>Performance Verification of GFE</u>
C.11	<u>Physical Data</u>

**D Length Modulator Cells**

D.1	<u>Summary</u>
D.2	<u>History</u>
D.3	<u>Operational Theory</u>
D.4	<u>Optical Realisation</u>
D.5	<u>Mechanical Realisation</u>
D.6	<u>Electronic Drive Subsystem</u>
D.7	<u>Molecular Sieve Operation</u>
D.8	<u>Double-Pass Optical System</u>
D.9	<u>Customisation and Accommodation Data</u>
D.10	<u>Physical Data</u>

**E Stirling Cycle Coolers****F Instrument Calibration**

F.1	<u>In-flight Calibration</u>
F.2	<u>Pre-Launch Calibration and Characterisation</u>
F.2.1	<u>Radiometric Targets</u>
F.2.2	<u>Gaseous Targets</u>
F.2.3	<u>Space Simulation</u>
F.2.4	<u>Spectral Sources</u>
F.2.5	<u>Correlation Cell Amounts</u>
F.2.6	<u>Field-of-View</u>
F.2.6.1	General
F.2.6.2	Pixels
F.2.6.3	Scanning
F.2.6.4	Pixel Co-location
F.2.6.5	Polarisation

**G Instrument Calibration Facility (ICF)**

G.1	<u>Simulated Coldplate</u>
G.2	<u>Radiometric Targets</u>
G.3	<u>Gaseous Targets</u>
G.4	<u>Space Simulation</u>
G.5	<u>Spectral Sources</u>
G.6	<u>Correlation Cell Amounts</u>
G.7	<u>Field-of-View</u>
G.7.1	General
G.7.2	Pixels
G.7.3	Scanning
G.7.4	Pixel Co-location
G.8	<u>Polarisation</u>

**H Reliability Issues and Mission Success**

H.1	<u>Introduction</u>
H.2	<u>Possible Failure Modes</u>
H.2.1	Fatal
H.2.2	Severe
H.2.3	Minor
H.3	<u>Science Recovery for Various Failures</u>
H.3.1	Fatal
H.3.2	Severe
H.3.2.1	Single cooler failure
H.3.2.2	Correlation Cell Failure
H.3.2.3	Chopper Failure
H.3.2.4	Scan mirror Failure
H.3.2.5	Blackbody Failure
H.3.2.6	Detector Array Failure
H.3.3	Minor
H.3.3.1	Single pixel detector failure

H.3.3.2

Increased Radiometric Noise

H.4 Conclusions

I References

---

*MOPITT Mission Description Document - 30 October 1993*

# Introduction to the EOSDIS Information Management System

## *Table of Content*

- Overview
  - DAACs: The Data Source
  - EOSDIS Version 0 Information Management System (V0 IMS)
  - How to Install the V0 IMS Clinet
- 

## Overview

The Earth Observing System (EOS) is an integral part of the NASA Mission to Planet Earth (MTPE), a long-term global change research program designed to improve the understanding of the Earth's atmosphere-ocean-land processes, in particular the causes and processes of global climate change and the consequences of human activities.

The EOS Data and Information System (EOSDIS) will provide a structure for data management and user services for derived products from EOS satellite instruments slated for launch over the next two decades and other NASA Earth science data. Within the EOSDIS framework, the Distributed Active Archive Centers (DAACs) are responsible for providing data and information services to support the global change research community.

Although much of the development has been in anticipation of the future launch of the EOS instruments (MOPITT being one of the five instruments scheduled to be launched in 1998 on board of the EOS AM-1 satellite), each of the DAACs now has accumulated significant data holdings, mainly from previous satellite expeditions.

Historically it has been difficult for scientists conducting interdisciplinary research to locate useful data, because it was necessary to contact many different data centers regarding data holdings and availability. The Version 0 Information Management System (V0 IMS) is a prototype system designed to overcome such difficulty by allowing a user to search for and order data from any DAAC, or a combination of DAACs, in a single on-line session. Based on Client-server computing technology, the V0 IMS will accomplish one of the goals of EOSDIS: To make global change research data more visible and accessible for interdisciplinary research.

The V0 IMS is now available free of charge to the scientific community. This article serves as a brief introduction to the V0 IMS for users who would like to know more about the functionality of the V0 IMS and how to install the V0 IMS on their own computer. For more detailed descriptions, readers are referred to the following documentations:

*(1) EOSDIS Information Management System, Users Manual, by Hughes STX Corporation, November 1994.*

*(2) V0 IMS Installation Guide (client and support files). by NASA Goddard Space Flight Center, June 15, 1995.*

---

## DAACs: The Data Source

There are currently nine Distributed Active Archive Centers (DAACs) responsible for data archival, product development, distribution and user support. The DAACs are distinguished from one another by data subject area. Linked by V0 IMS, DAACs will appear to users as a single system. User can search for and order data from any or all of them, and can contact the User Services staff at any DAAC to obtain assistance in using the IMS or to find out more about a particular data product.

In addition to the capabilities provided by V0 IMS, some DAACs will have individual on-line systems, allowing them to provide unique services for users of a particular type of data. These "DAAC-unique" systems will look and function much like the V0 IMS, but will emphasize products or services specific to that DAAC.

There are a number of different agencies and data centers cooperating within the MTPE framework to make data more accessible. One example of this cooperation within EOSDIS is the Satellite Active Archive (SAA) developed by the National Oceanic and Atmospheric Administration (NOAA). The SAA is searchable using V0 IMS in the same way as are the DAACs. In addition, USGS data at EDC and CDIAC data at ORNL are visible through the V0 IMS. Listed below are the DAACs and the SAA with their subject area.

<u>DAAC Name</u>	<u>Scientific Discipline</u>
ASF DAAC Alaska SAR Facility	Polar Regions and SAR Data
EDC DAAC EROS Data Center	Land Processes
GSFC DAAC NASA Goddard Space Flight Center	Upper Atmosphere Global Biosphere Atmospheric Dynamics Geophysics
JPL DAAC NASA Jet Propulsion Laboratory	Physical Oceanography
LaRC DAAC NASA Langley Research Center	Radiation Budget Tropospheric Chemistry Clouds and Aerosols
MSFC DAAC NASA Marshall Space Flight Center	Hydrologic Cycle
NSIDC DAAC National Snow and Ice Data Center	Snow and Ice Cryosphere and Climate
ORNL DAAC Oak Ridge	Biogeochemical Dynamics

National Laboratory

SEDAC  
Socioeconomic Data  
and Applications Center

NOAA SAA  
Satellite Active Archive

Human Impact on  
Global Change

Satellite Remote Sensing

---

## EOSDIS Version 0 Information Management System (V0 IMS)

The goals of the EOSDIS Version 0 IMS are to facilitate Earth science research through improved access to existing data, and to serve as a prototyping testbed for the EOSDIS Core System (ECS). The ECS is being built to accommodate the tremendous amounts of data expected from the EOS instruments to be launched beginning in 1998.

The V0 IMS provides a consistent view of data sets held at EOSDIS data centers, allowing users without specific prior knowledge of the data to search science data holdings, retrieve high level descriptions of data sets and detailed descriptions of the data inventory, view browse images, and place orders for data. In short, the V0 IMS is designed to provide users with a "one-stop shopping" tool for archived data.

### V0 IMS Functionality

The V0 IMS system provides the following services through its easy to use interface:

#### *Directory Information for DAAC Data Sets*

The Directory provides brief concise high-level information about data sets from any point in the system.

#### *Guide Subsystem*

The Guide provides detailed descriptions about data sets, platforms, sensors, projects, data centers, and includes algorithm descriptions and calibration information.

#### *Inventory*

The Inventory Search function provides descriptions of specific observations or collections of observations of data (granules) that are available for request from a data center.

#### *Coverage Maps*

The Coverage Map is a two-dimensional graphical representation of the geographic coverage of selected inventory granules. It displays the Earth in an orthographic projection.

#### *Browse*

The Browse function allows a user to locate and retrieve reduced resolution images as an aid to data selection. The user may either view the image in the IMS interface or have it staged for FTP pickup.

#### *Order Data*

This function allows users to view information pertaining to orderable data products, and then construct a request which is forwarded to the relevant archive for order processing.

### ***Access to Global Change Master Directory***

The Global Change Master Directory (GCMD) is a multidisciplinary data base of information about Earth and space science data. It contains high level descriptions of data set holdings of various agencies and institutions.

## **User Interface**

The V0 IMS system is accessible over the Internet. Currently, there are three types of user interface available: a character-based interface, an X-Windows based graphical interface and a World Wide Web (WWW) Browser. All three interfaces support data search and order, directory searches, guide information, and image browse. Descriptions of each interface are given below separately.

### ***Character User Interface***

The Character User Interface (ChUI) is intended for users who do not have access to an X-terminal, have a small monitor screen, or are accessing the system via low-bandwidth communications (e.g. via modem). Although it is designed to run on a VT100-standard terminal, it also operates on VT2xx- and VT3xx-class terminals, as well as other terminals that support VT100 terminal emulation. ChUI is an old type of interface, and is now being phased out and replaced by the WWW user interface.

### ***Graphical User Interface***

The Graphical User Interface (GUI) is a graphical environment which operates under the X-window system, allowing the user to display multiple windows simultaneously, and supports a mouse for easy user interaction. It combines the most sophisticated capabilities among the three existing interfaces offered so far by the V0 IMS. It also allows search areas to be specified from a global map, and provides an interactive data browse facility and coverage map of data products.

In order to run the GUI, the hardware display device must be able to run the X Windows System and communicate over the Internet. The software targets a 1024 x 768 resolution screen. The minimum number of supported color planes is eight, and monochrome monitors are not supported. A standard X terminal can be used, as well as any personal computer with a compatible X server or emulator.

The following X-Window emulators have been used successfully for the GUI client:

1. Macintosh: MacX from Apple Computer (both MacOS and AU/X versions)
2. DOS/Windows: X-Vision and PC-XView packages with limited success. The Hummingbird X-Window emulator proven popular for the GUI client. Xwin and Xdemo also used.
3. OS/2: Run successfully using the IBM-supplied TCP/IP protocol stack and IBM X-Window server.

### ***WWW User Interface***

The WWW User Interface is the latest development in the V0 IMS system, which is still in the rapidly evolving stage. It provides many of the capabilities of the GUI, but allows users who do not have access to X-Window, or who do not need the full capability of the GUI IMS, to search for V0 data regardless of platform using a WWW browser. The WWW interface is available at the following URL:

<http://eos.nasa.gov/ims/welcome>



---

## How to Install the V0 IMS GUI Client

The installation of the V0 IMS Client takes two steps: installing the Binary Port and the Source Port. A step-by-step instruction on the installation can be found in the document V0 IMS Installation Guide (client and support files) June 15, 1995, which is available through the World Wide Web as

[http://harp.gsfc.nasa.gov:1729/eosdis\\_documents/Installation.html](http://harp.gsfc.nasa.gov:1729/eosdis_documents/Installation.html)

Here we only provide some additional useful information and tips to help users understand the installation process, which turned out to be a non-trivial exercise. Some tips only apply to the installation of a GUI interface.

The binary port is a core part of the V0 IMS, which includes binary executable files for either GUI or ChUI interface (under a subdirectory bin) and client support files (under a subdirectory lib). The source port will add two more subdirectories ims and public to form a complete V0 IMS Client. The subdirectory ims contains all the source code related to the V0 client. And public contains several third party packages used by the V0 IMS Client.

### Hardware Requirements

For a binary port, the user must have a machine similar to one of the "blessed" development machines, supported currently by the V0 IMS system. At the time of this writing, only SGI Irix 4, SGI Irix 5 or SunOS 4.1.3 UNIX Operating Systems are the supported platforms. The user also needs to have about 7 MB available for the binary and the script. The support files require about 5 MB. Therefore, a total of 12 MB of free disk space is needed for the binary port.

The source port is considerably more complex. Space needed for the third-party libraries is about 40 MB. And Client source code including .c and .o files requires roughly 17 MB. By adding 12 MB for binary and support files, a minimum of the disk space for a V0 IMS Client port is about 70 MB.

As far as RAM is concerned, at least 32 MB of RAM or preferably more is required. The client uses a lot of memory, particularly when large result sets are returned.

### Software Requirements

In order to compile source codes for the third-party libraries, several tools are required:

- An ANSI C compiler and library suite. If a native compiler is not available, gcc should be used.
- The make utility (GNU make preferred).
- A debugger. If dbx is not available, use the GNU debugger, gdb.
- Libraries and include files for Motif 1.1.
- Uncompress and tar tools.

### Download the Binary and Source Files

There are two ways of download the binary and source files: anonymous FTP from a remote site or transfer files through the World Wide Web (WWW).

### (1) Anonymous FTP:

Users can type the following command to log on to a designated site:  
[ftp killians.gsfc.nasa.gov](ftp://killians.gsfc.nasa.gov)

Enter "anonymous" as a user name and your own e-mail address as a password. When you successfully log on to killians, get down to a directory /dist/dist, under which there are four separate subdirectories: binaries, lib, public and ims. They correspond to the four directories we introduced for the binary port and source port. Under each of these subdirectories, the user can fetch the corresponding files, which are all compressed tar files.

It should be noted that under binaries the user needs to choose a platform corresponding to the computer machine they will install the V0 IMS Client. As mentioned before, the currently supported machines are SGI Irix 4, SGI Irix 5 and SunOS 4.1.3. There are individual subdirectories under binaries for each of these machines.

### (2) Transfer through WWW:

To download files through the WWW, go to the EOSDIS home page by using the following URL:

[http://harp.gsfc.nasa.gov:1729/eosdis\\_documents/eosdis\\_home.html](http://harp.gsfc.nasa.gov:1729/eosdis_documents/eosdis_home.html)

Then, click a hyperlinked item called "Download the V0 IMS Graphical User Interface (GUI) Client" to get into a new page. You could choose Version 4.5 or Version 5.0.3 software for your particular computer system. Download is done on-line and some browser could uncompress the tar files as the files are downloaded.

### Compile Third-Party Libraries

The binary file for the V0 IMS Client is precompiled and executable. Once placed in place, it is ready to run. The most difficult part in the installation is compiling all of the third-party libraries from their individual source codes. The following public domain codes need to be downloaded using FTP:

- GDBM 1.5
- HDF 3.3r1
- Mosaic 2.0
- ODL 1.2
- freeWAIS 0.2
- loadimage
- mdutils

V0 IMS Installation Guide (client and support files) gives a step-by-step guide to compiling these individual libraries. This document is available through the World Wide Web as

[http://harp.gsfc.nasa.gov:1729/eosdis\\_documents/Installation.html](http://harp.gsfc.nasa.gov:1729/eosdis_documents/Installation.html)

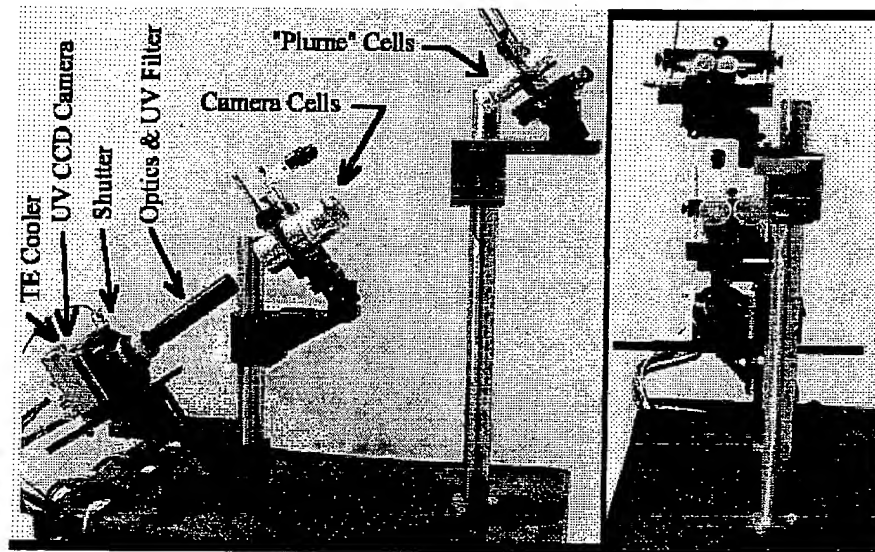
The user may encounter different problems during compilation depending on the computer platform of their choice. Most of the problems arise due to missing include files and/or lack of proper options in the makefile.

### Miscellaneous

It was our experience that the colour setting was an important factor for running the V0 IMS properly through the Hummingbird X-Window emulator under the Windows 3.1 environment. A choice of 256 colours setting works fine with the V0 IMS, while 65,536 colours setting will result in errors in I/O address.

## Gas Correlation Spectroscopy

An imaging gas correlation camera operation was demonstrated under STTR Phase-I project funded by NASA.



Concept Demonstration Experiment Setup

The camera is intended to produce realtime 2-D optical density maps of target gas in a plume. In gas correlation spectroscopy, a cell containing the target gas is placed in front of the sensor. The scene is viewed twice, through the target gas cell and through an empty cell. The gas in the cell serves as a "matched filter" to the target gas in the plume. The "modulated" transmission of the system is very high at the spectral bands of the target gas while it practically blocks transmission at all other wavelengths. The system has a very high Etendue (throughput) and is simultaneously responsive to several spectral lines or bands -- increasing the overall sensitivity.

In the present application, a UV sensitive CCD camera is used to detect  $\text{SO}_2$  presence in plumes.  $\text{SO}_2$  exhibits a strong signature in the UVA range (~300 to 320 nm), as well as in the LWIR. It can be detected in emission or absorption against the sky scattered solar UV radiation.

In these experiments, a thinned, back-illuminated Hamamatsu CCD is used for a camera. The plume is simulated by a second set of cells that hold the target gas in the field of view of the camera (see setup image above).

The application will allow ground calibration of spaceborne UV instrument (e.g., TOMS); study of volcanic plumes; emission monitoring from industrial facilities, etc. A battery operated portable version of the system will be built for these applications.

Gas correlation spectroscopy can also be utilized in other portions of the spectrum, and IR instruments are also being explored for the detection of other compounds.

The performance of the UV system has been simulated using the Modtran model in which sensitivities, SNR values and other performance parameters were established.

Return to OKSI's homepage

Go to TechExpo Homepage.

## Gas imaging using gas-correlation spectroscopy

---



---

*Jonas Sandsten, Hans Edner, Sune Svanberg and Petter Weibring*

A new method for remote visualisation of gas flows, based on infrared absorption and gas-correlation techniques, has been further developed. Two images of flowing gases are formed simultaneously on an IR-sensitive detector with a split-mirror Cassegrainian telescope. A suitable bandpass filter is used to isolate a small region containing absorption features of the gas to be studied. One of the images is further filtered by a short cell filled with a high concentration of the gas. After image processing the two images can be used to eliminate differences in background illumination as well as the interference by other gases and particles. The end result is a grey-scale or false colour-coded image showing the distribution of a specific gas in the area studied. We have recently demonstrated gas correlation spectroscopy of flowing gases in real time with natural thermal background radiation as the only radiative source. The applications we have been working on are remote methane ( $\text{CH}_4$ ) visualisation of leakages from pipelines, other hydrocarbon emissions such as ethene ( $\text{C}_2\text{H}_4$ ), visualisation of hazardous gases, for example ammonia ( $\text{NH}_3$ ) after a transportation accident, and working environment studies using nitrous oxide ( $\text{N}_2\text{O}$ ) flowing turbulently in air.

The experiments on methane, ethene and ammonia were performed with simulated gas leakages from a gas tanker at the gas exercise site at Malmö Fire Department. The tanker itself was radiating the thermal background used in this passive gas-correlation technique. A new infrared camera with a set of optimised filters was used in combination with fast capture of images, and the whole set-up was placed 20 metres from the truck.

We have also explored the possibilities of using a quantum-well infrared-photodetector-based camera which has narrow responsivity and very high quantum efficiency, both advantageous features in passive gas correlation spectroscopy, at the R&D department of the infrared camera manufacturer, Agema.



---

*Atomic Physics, LTH. [Lena.Roos@fysik.lth.se](mailto:Lena.Roos@fysik.lth.se), 990603*

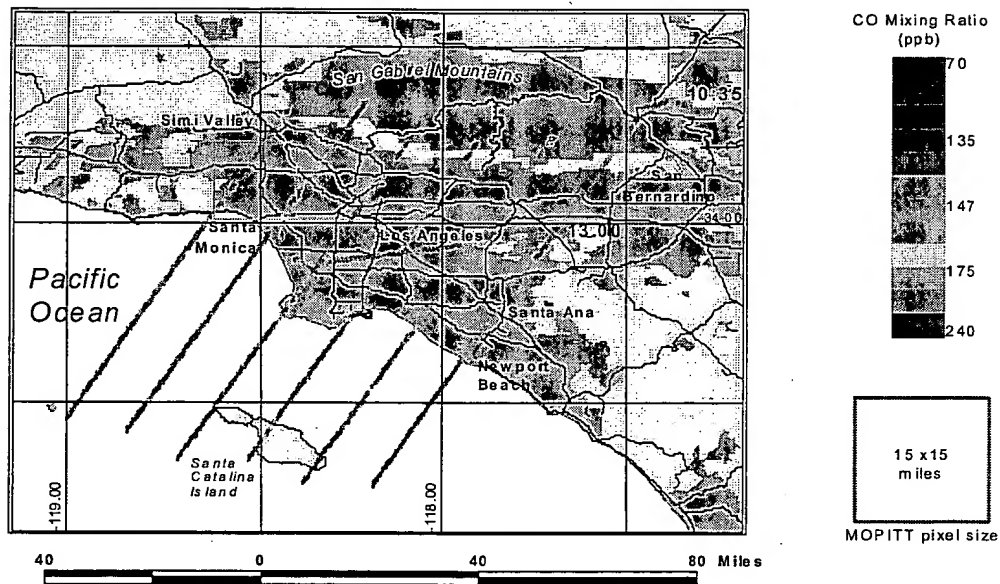
---

# TECHNICAL REPORT FOR: MOPITT AIRBORNE TEST RADIOMETER (MATR)

Prepared by: Dr. Mark W. Smith

Date: 15 March, 2000

## CO Mixing Ratio Over Los Angeles January 22, 1999



February 29, 2000

<b>1. INTRODUCTION.....</b>	<b>4</b>
1.1 BACKGROUND OF THE MATR PROJECT .....	4
1.2 MATR CONTRIBUTIONS TO MOPITT.....	4
<i>Retrievals using real LMC and PMC data .....</i>	<i>4</i>
<i>CO retrievals for MOPITT data validation.....</i>	<i>5</i>
<i>Test and refine cloud detection thresholds and cloud clearing algorithms .....</i>	<i>5</i>
<i>Detailed study of PMC behavior.....</i>	<i>6</i>
<i>Correction of LMC imbalance through radiometric calibration .....</i>	<i>6</i>
<i>Design of in-flight radiometric calibration assembly transferred to MOPITT-A.....</i>	<i>6</i>
<i>Investigate difficult scenes.....</i>	<i>7</i>
<i>Regional scale studies with sub-pixel resolution and real time retrievals.....</i>	<i>7</i>
1.3 MATR, MOPITT, AND MOPITT-A .....	7
<i>MATR compared to MOPITT and MOPITT-A .....</i>	<i>7</i>
<i>How data from each MATR channel are used .....</i>	<i>8</i>
<i>Validation with MATR vs. MOPITT-A.....</i>	<i>8</i>
<b>2. RESULTS OF FIELD DEPLOYMENTS .....</b>	<b>10</b>
2.1 ENGINEERING TEST FLIGHTS IN 1998.....	10
2.2 CO RETRIEVAL RESULTS FOR CARR, COLORADO FOR 4 FEB. 1999.....	10
<i>MATR data and CO retrievals for 4 Feb. 1999.....</i>	<i>10</i>
2.3 RETRIEVAL RESULTS FOR LA AND PACIFIC OCEAN FOR 22 JAN 1999.....	11
<i>The flight path.....</i>	<i>11</i>
<i>Retrieval procedure .....</i>	<i>11</i>
<i>2-D data map.....</i>	<i>12</i>
2.4 CLOUD DETECTION RESULTS.....	12
<i>Overview .....</i>	<i>12</i>
<i>Results using MATR data.....</i>	<i>12</i>
<i>How additional MATR flight data will be used.....</i>	<i>13</i>
<b>3. RESULTS OF LABORATORY TESTS .....</b>	<b>13</b>
3.1 EXTERNAL GAS CELL RESULTS FOR 4.6 UM LMC CHANNEL.....	13
3.2 PMC TEST RESULTS.....	14
<b>4. SUMMARY.....</b>	<b>14</b>
<b>APPENDIX I: REMOTE SENSING THEORY.....</b>	<b>16</b>
IA REMOTE SENSING OF TROPOSPHERIC TRACE GASES.....	16
IB FORWARD MODEL CALCULATIONS.....	16
<i>Basic equations.....</i>	<i>16</i>
<i>Relationship between MOPITT and MATR forward models .....</i>	<i>18</i>
IC RETRIEVAL METHODOLOGIES.....	18
<i>Fundamental retrieval procedure: constrain and equate.....</i>	<i>18</i>
<i>MOPITT retrievals.....</i>	<i>18</i>
<i>MATR retrievals.....</i>	<i>19</i>
<b>APPENDIX II: PHYSICAL DESCRIPTION OF MATR.....</b>	<b>19</b>
II.A THE BASIC INSTRUMENT .....	19
<i>Optical table.....</i>	<i>19</i>
<i>In-flight radiometric calibration assembly.....</i>	<i>20</i>
<i>Thermal control.....</i>	<i>20</i>
<i>Data acquisition, storage, processing, and display.....</i>	<i>20</i>
II.B FLIGHT CONFIGURATION .....	21
<i>Auxiliary in-flight instrumentation.....</i>	<i>21</i>
<i>Size, Weight and Power.....</i>	<i>21</i>
<i>Citation aircraft .....</i>	<i>21</i>



<b>APPENDIX III: MATR CALIBRATION .....</b>	<b>21</b>
III.A THE INSTRUMENT "MODEL" .....	21
III.B CALIBRATION RESULTS.....	22
<i>Calibration of engineering channels .....</i>	<i>22</i>
<i>Blackbody calibrations.....</i>	<i>22</i>
<i>Linearity of detector channels.....</i>	<i>23</i>
<i>Spectral response "sans gas" .....</i>	<i>23</i>
<i>Need to determine LMC path lengths .....</i>	<i>23</i>
<b>REFERENCES .....</b>	<b>24</b>

#### LIST OF TABLES

- Table I: MATR compared to MOPITT and MOPITT-A
- Table II: Validation capabilities of MATR and MOPITT-A

#### LIST OF FIGURES

- Figure 1: In situ profile, MATR profile and MATR averaging kernel for Carr, Colorado
- Figure 2: In situ weighted average and MATR column averages for Carr, Colorado
- Figure 3: Plot of CO retrieved over Los Angeles and Pacific on 22 Jan 1999
- Figure 4: Confirmation of MOPITT cloud detection thresholds with MATR data
- Figure 5: Gas amount "retrievals" for laboratory gas cell
- Figure 6: Measured and calculated PMC pressure and temperature cycles.
  
- Figure A1: Diagram of atmospheric remote sensing
- Figure A2: Atmospheric transmittance and radiance near 2.3  $\mu\text{m}$
- Figure A3: Atmospheric transmittance and radiance near 4.6  $\mu\text{m}$
- Figure A4: Sketch of MATR optical table
- Figure A5: Cessna Citation II aircraft
- Figure A6: Average signal spectral response function for 4.6  $\mu\text{m}$  LMC channel
- Figure A7: Difference signal spectral response function for 4.6  $\mu\text{m}$  LMC channel

## 1. Introduction

### 1.1 Background of the MATR project

The MOPITT program has always had an aircraft instrument associated with it. The initial proposal in 1988 included a plan for the Canadian Space Agency (CSA) to develop an aircraft instrument. The airborne instrument was to function as a test-bed for the development of the satellite instrument, and was also to provide data that could be used to test and tune retrieval algorithms, since no one had looked at the troposphere through "eyes" like the LMC's and PMC's. The use of the airborne instrument for post-launch validation was also discussed.

This plan was subsequently modified when it became clear that limitations in time, personnel, and funds would not allow CSA to apply adequate resources to both MOPITT and the airborne instrument.

Oxford University then offered to lead the activity, in conjunction with an aircraft facility in England. Plans were made, but two successive proposals to UK funding agencies were declined. At that point Oxford withdrew from this effort.

By this time the development of the flight model was far enough along that lessons learned from the aircraft model would not be in time to influence the flight instrument. However, more detailed consideration of the validation of MOPITT data led to additional emphasis being placed on the use of an airborne instrument.

At that juncture there was still a need for an instrument to allow us to get additional insight into the MOPITT measurement process, and to test the algorithms for applicability and robustness, and to unearth problems before MOPITT was launched. NCAR then proposed to build MATR (MOPITT Airborne Test Radiometer) as an instrument that would use the same physical principles as MOPITT, but would be much simpler and less expensive to build. It would not have an optical train as complex as MOPITT, which at that time was causing concern, and would not have automated or computer controlled operation, but would fly in a pressurized cabin accompanied by an operator. Although the choice of a pressurized cabin aircraft was made primarily for the sake of convenience, it has subsequently proven to offer some advantages in terms of the flexibility of the flight profiles.

The possibility that CSA would develop an aircraft instrument was never really eliminated, but rather lay dormant for several years while work focussed on MOPITT itself. The CSA plans have been revived fairly recently, and the MOPITT engineering qualification model is being modified for use aboard an ER-2, and will be called MOPITT-A.

### 1.2 MATR contributions to MOPITT

#### Retrievals using real LMC and PMC data

**Work to date:** One role for MATR is to demonstrate that accurate retrievals of tropospheric CO and CH<sub>4</sub> can be made using actual data from a real LMC and a real PMC. CO retrievals that were made using in-flight data from MATR differed by only 10% from in situ measurement results for the one case in which data were acquired at the same place at the same time, as presented in section 2.2. Measurements made with a laboratory gas cell suggest that similar agreement can be expected for a much wider range of surface temperatures and gas column amounts, as discussed in section 3.1.

**Future work:** Now that MOPITT is on orbit and becoming operational, future retrievals using MATR data will no longer play the simple role of demonstrating the capabilities. The retrieved

CO values will be used as part of MOPITT data validation, to investigate difficult scenes in detail, and as part of regional scale scientific studies.

### CO retrievals for MOPITT data validation

**Work to date:** As MOPITT data validation has not yet quite begun, work to date has consisted of preparing for MOPITT validations. A key step has been a demonstration of 10% accuracy for retrieved CO relative to NOAA in situ measurements. This is described in section 2.2. These results have been buttressed by laboratory tests using a gas cell, as described in section 3.1.

**Future work:** MATR will provide on-going support to the MOPITT program by producing retrieved CO amounts for the purpose of validating MOPITT retrieved CO amounts. The unique capabilities of MATR compared to other sources of validation data are a product of several factors. MATR produces high precision measurements (as good as 2 ppb in column averaged CO mixing ratio) with sub-pixel spatial resolution (as small as 1.2 x 2.5 km oblongs for MATR compared to 22 x 22 km squares for MOPITT). The MATR deployment platform, a Cessna Citation aircraft, has a range of about 1600 km when fully loaded, and can climb comfortably to 12 km altitude. The Citation has good maneuverability, and can map out prescribed flight lines with ease (see the cover and section 2.3 for an example of mapping over the Los Angeles basin). In addition, an inlet interface has been made for the Citation so that on future flights in situ canister samples can be collected using a canister sampling system developed by the NOAA CMDL. One very promising capability of MATR is the ability to build up vertical profiles out of successive column measurements by having the Citation aircraft climb in stages.

Because of the flight range of the Citation, MATR can easily investigate CO gradients that may extend over a large number of MOPITT pixels. Alternatively, by making use of its good spatial resolution, MATR can collect a large number of measurements over only a few MOPITT pixels to judge the degree of, and investigate the effect of, sub-pixel variability in CO distributions. The data collection portion of a MATR flight typically lasts for 1 to 2 hours, which corresponds to a total flight path of 600 to 1200 km. With 2.5 km horizontal resolution, this equates to 240 to 480 separate CO retrievals per MATR flight. These capabilities are quite distinct from those of ground-based spectroscopic instruments, which make only fixed point measurements, and from in situ canister sampling, which produces at most 1 or 2 profiles per day at a given validation site even during a period of intensive validation.

A full comparison of MATR validation capabilities versus MOPITT-A validation capabilities will be made in section 1.3.

### Test and refine cloud detection thresholds and cloud clearing algorithms

**Work to date:** MOPITT will use a combination of techniques to identify, and eventually correct for, the presence of clouds in the instrument's field of view. One of the identification techniques makes use of radiometric threshold tests that are applied to the average signal radiances from the 2.3  $\mu\text{m}$  and 4.6  $\mu\text{m}$  LMC channels. These threshold tests were applied to MATR radiometric data that was acquired during flights over a land scene, and MATR video data was used to verify that clouds were correctly identified. This work is described in section 2.4 and in a paper (Warner, et al., 2000).

**Future work:** MATR data from future flights will be used to refine the cloud detection thresholds. Because the MATR FOV is relatively small, about 1.2 x 2.5 km, it should be possible to select cloud free segments of data from within partially cloudy MOPITT pixels, each of which is 22 x 22 km square. We will test how well the MOPITT cloud clearing algorithms work by comparing MOPITT CO retrievals for partially cloudy scenes with MATR CO retrievals for cloud free subsets of data.

### Detailed study of PMC behavior

**Work to date:** The instrument spectral response functions for each MOPITT and MATR channel are treated as the product of two terms. The first term is the measured end-to-end transmittance (normalized to a peak value of 1.0) of all the instrument optics except for the gas in the modulator cells. The second term is the transmittance of the gas in the modulator cells, calculated for each state (i.e., pressure, temperature, and length) of each cell. This calculation is especially problematic for the PMC's (pressure modulator cells) because the temperature of the gas in the cells cannot be measured directly. Pressure is estimated indirectly in MOPITT, and is measured directly in MATR. Nominal pressure values and a constant temperature (i.e., isothermal gas cycle) have been used to calculate the instrument spectral response functions for MOPITT to date. The isothermal assumption was based on work done previously with PMC's. However, all of this work involved stratospheric sounders, with low gas pressures in the PMC's. MOPITT uses much higher pressure PMC's for its tropospheric sounding, and the true temperature cycle under these conditions has been a long standing subject of concern.

We hosted a graduate student from Oxford, Kate Paulin, during the summer of 1999 to work on this problem. We helped Kate make measurements while she was here, and since returning to Oxford she has analyzed the results under the direction of her adviser, Clive Rodgers. The measurements made using the MATR PMC's (see section 3.2) indicate that in fact the temperature cycle is closer to adiabatic, with a significant phase shift between the pressure and temperature cycles. Sensitivity studies predict a 20% to 40% change in the PMC difference signal radiances depending on whether the PMC's are isothermal or adiabatic. The MATR measurement results are being used to improve the calculation of the spectral response functions for the MOPITT PMC channels.

**Future work:** While we have made progress with the PMC's, their behavior is not yet fully understood. We will again host Kate during the summer of 1999 to continue work on this problem.

### Correction of LMC imbalance through radiometric calibration

**Work to date:** Another long standing subject of concern for the MOPITT project has been the so-called LMC (length modulator cell) imbalance. In an LMC, the path length of the correlation gas in the cell is changed by moving a  $\text{CaF}_2$  rotor through the cell. In the ideal situation, the only change in transmittance for the two states is due to the change in absorption path length. However, because the cell optics are also changing, some spurious modulation (called imbalance) also exists, even with the careful design chosen for the MOPITT LMC's (Tolton and Drummond, 1997). With MATR we seem to have eliminated this problem by using a slightly different radiometric calibration scheme than has been chosen for MOPITT.

**Future work:** The MATR radiometric calibration scheme could be applied to the MOPITT data, although this would require re-work of the Level 0 to Level 1 (digital counts to radiances) processing software. We will double check the improved performance for MATR before deciding whether to apply this calibration scheme to MOPITT.

### Design of in-flight radiometric calibration assembly transferred to MOPITT-A

**Work to date:** The in-flight radiometric calibration assembly that was designed and built at NCAR for MATR is, we believe, a notable innovation (Smith and Shertz, 1996). For the sake of convenience, we wished to operate MATR from inside a pressurized cabin jet aircraft. If the instrument is to be maintained at cabin pressure it must look through a pressure sealing window, and the optical effects of the window could cause problems with the radiometric calibration of the instrument. We solved this problem by placing the radiometric calibration targets outside the window, but in a structure which protects the calibration targets and allows them to operate at

stable temperatures. The window becomes just one more element in the optical system and its optical effects are included in the radiometric calibration.

**Future work:** Our basic design for an in-flight radiometric calibration assembly has been adopted for MOPITT-A (Bailak, et al., 1999). As this design seems to work well for MATR, we have no plans for future design changes.

### Investigate difficult scenes

**Work to date:** As MOPITT data collection is only beginning, work to date has consisted of preparation. Our results over Los Angeles (see section 2.3) demonstrate the ability to achieve sub-pixel resolution with MATR.

**Future work:** We anticipate that the MOPITT retrieval algorithms will initially encounter scenes for which they fail to produce good results. Very cold scenes, which will correspond to very low radiance levels, could prove difficult to work with. Regions of active burning are of great interest as sources of CO, but heating by fires could cause extreme, and unusual, atmospheric temperature gradients which might make retrievals difficult in the immediate vicinity of the fire. Mountainous regions could also prove difficult at first because of the large fluctuations in surface level and surface temperature that will be present inside of a single MOPITT 22 x 22 km pixel. MATR should be a good tool to investigate these difficult scenes in detail because of its combination of sub-pixel resolution, good horizontal range, good aircraft maneuverability, and the ability to schedule flight times according to events. Detailed MATR data acquired over these difficult types of scenes will be used to refine the MOPITT retrieval algorithms so that they can handle scenes which might be poorly understood at first.

### Regional scale studies with sub-pixel resolution and real time retrievals

**Work to date:** Again, as MOPITT data collection is only beginning, work to date has consisted of preparation. Our flights over Los Angeles (see section 2.3) were made in part as practice for the MIRAGE (Mega-city Impacts on Regional And Global Environments) program and as a demonstration of our capabilities. We have stayed in close contact with Darrel Baumgardner, who is leading the efforts on MIRAGE, and we have consistently made requests to NASA for airborne support to participate in MIRAGE.

**Future work:** MATR will add scientific value to the MOPITT data for specific regional studies by providing CO retrievals in real time with sub-pixel resolution. The proposed MIRAGE program is a good example. One or more intensive field campaigns in the Mexico City region have been proposed as part of MIRAGE. MATR would provide detailed information about CO spatial distributions within the Mexico City basin, and possibly extending to the region around Mexico City. The MATR data flights would be timed to coincide with flights made by the NCAR/NSF C-130 aircraft. In fact, if MATR real time retrievals work well, the CO measured by MATR could be used as a real time tracer to guide the flights of the C-130. MOPITT of course will provide data that extends from the regional to the global scale, and with repeat coverage about twice a week year after year for 5 to 6 years. However, the MOPITT data will not show any features for scales smaller than 22 x 22 km and will not be timed around specific events.

## 1.3 MATR, MOPITT, and MOPITT-A

### MATR compared to MOPITT and MOPITT-A

A top level comparison of MATR, MOPITT and MOPITT-A is presented in Table I. MATR in its standard configuration uses a single pressure modulated cell (PMC) filled with CO coupled to a 4.6  $\mu\text{m}$  detector, and a single length modulated cell (LMC) filled with CO coupled to 4.6  $\mu\text{m}$  and 2.3  $\mu\text{m}$  detectors. The pressures in both the PMC and LMC can be varied for lab testing and

between flights, if desired. Alternatively, the LMC can be filled with  $\text{CH}_4$ , and coupled to a 2.2  $\mu\text{m}$  detector. The band centers and band widths for MATR were specified to be exactly the same as listed in MOPITT design documents. The differences that are shown in Table I are due to manufacturing variability. The MATR field of view that is listed includes the smearing effect due to aircraft motion during a standard signal averaging period.

MOPITT-A is in fact the engineering qualification model of MOPITT, with adaptations for use aboard an ER-2. MOPITT-A is therefore essentially "half a MOPITT", with only a few values in Table I that require explanation. Although MOPITT-A is listed as using MOPITT channels 1 to 4, the pressures in the LMC's and PMC can be changed for laboratory testing or between flights. Therefore MOPITT-A could just as well be configured to mimic MOPITT channels 5 to 8, or some mixture of channels. However, it will always have one PMC filled with CO coupled to a 4.6  $\mu\text{m}$  detector, one LMC filled with CO coupled to 4.6  $\mu\text{m}$  and 2.3  $\mu\text{m}$  detectors, and one LMC filled with  $\text{CH}_4$  coupled to a 2.2  $\mu\text{m}$  detector. MOPITT-A and MOPITT will have the same  $1.8^\circ \times 1.8^\circ$  field of view. The field of view that is listed for MOPITT-A is the ground instantaneous field of view for a flight altitude of about 20 km. In practice some signal averaging may well be required for the MOPITT-A data, and this will smear out the FOV along the aircraft flight line, but no actual values are yet available.

#### How data from each MATR channel are used

Not all MATR channels have proven equally useful. All retrieval results to date have been obtained using in-flight data only from the 4.6  $\mu\text{m}$  LMC channel, which in fact corresponds roughly to the MAPS CO gas correlation channel. The in-flight data from the 2.3  $\mu\text{m}$  LMC channel has been plagued by poor signal-to-noise ratio for the difference signal, which contains almost all of the information about CO total column absorption in the atmosphere. This is unavoidably related to the fact that the CO 2.3  $\mu\text{m}$  band is an overtone band, and line intensities are about 120 times weaker than for the fundamental band at 4.6  $\mu\text{m}$ . However, the average signal for the 2.3  $\mu\text{m}$  LMC channel has a good signal-to-noise ratio. This signal carries information about the surface albedo at 2.3  $\mu\text{m}$ , and it has been combined successfully with the 4.6  $\mu\text{m}$  average signal, which carries information about surface temperature, for cloud detection. The 4.6  $\mu\text{m}$  PMC channel is similar to the 4.6  $\mu\text{m}$  LMC channel, except that its weighting functions and averaging kernels peak at higher altitudes (lower pressures) than for the LMC channel. Roughly speaking, the 4.6  $\mu\text{m}$  LMC channel provides CO information weighted in the mid-troposphere, while the 4.6  $\mu\text{m}$  PMC channel should provide CO information weighted in the upper-troposphere. However, as will be discussed later, it has been difficult to determine the correct spectral response function for the PMC's. While we have made strides in laboratory characterizations of the underlying correlation gas pressure and temperature cycles, this has not yet been translated into successful retrievals using data acquired in-flight.

#### Validation with MATR vs. MOPITT-A

Because MOPITT-A has not yet produced any flight data, either engineering or science data, it is impossible to make a quantitative comparison of MATR and MOPITT-A. However, Table II summarizes some general statements that can be made.

Before discussing the unique capabilities that are available with MATR but not MOPITT-A, we will first mention the roles that only MOPITT-A can fill. Because MOPITT-A is the engineering qualification model of MOPITT and will operate from an ER-2, the possibility exists to use MOPITT-A to validate the MOPITT level 1 data, or top-of-atmosphere radiances. An ER-2 of course does not really fly at the top of the atmosphere, but much less extrapolation is required to estimate satellite radiances when the data is acquired from 20 km than from 12 km. In addition, the MOPITT-A spectral response functions will be as close to the MOPITT functions as

is possible. While both MATR and MOPITT-A will be useful for validating the MOPITT level 2 data, or retrieved CO and CH<sub>4</sub> amounts, MOPITT-A will collect CO and CH<sub>4</sub> data simultaneously on each flight, while MATR will not. Aside from these deficiencies, MATR has several potential advantages compared to MOPITT-A, and we will discuss these next.

The standard operating mode for both MATR and MOPITT-A is to have the aircraft climb to a fixed altitude and cruise during data collection. In this standard mode of operation, both instruments will be limited to a maximum of 3 pieces of CO profile information, and this is assuming that all 3 CO channels (2.3  $\mu\text{m}$  CO LMC, 4.6  $\mu\text{m}$  CO LMC, and 4.6  $\mu\text{m}$  CO PMC) work well. The ability of the Citation to fly at different altitudes provides MATR with the unique capability to produce CO profiles by climbing in steps. In this scenario the vertical resolution is not limited by the number of working channels, but rather by the ability to resolve the radiance change between each step.

A related issue is the ability of the Citation to fly between or beneath clouds to validate the ability of the cloud-clearing algorithm to predict cloud free radiances in cloudy or partly cloudy scenes. In partly cloudy scenes, both MATR and MOPITT-A will probably acquire some data that is cloud free, since both instruments have relatively small ground instantaneous fields of view. However, the Citation will have greater maneuverability than the ER-2 to purposely fly between clouds. The Citation could also fly under clouds, if the cloud base is not extremely close to the ground.

The ability to perform real time CO retrievals and guide flights accordingly is another unique possibility with MATR operating from the Citation. While we have not yet demonstrated this capability, we believe that it is possible, using a regression retrieval scheme for maximum speed. MATR has the real time display capabilities to show these results "on the fly". An instrument operator normally accompanies MATR, and can communicate with the Citation pilots. This means that the Citation could be guided in flight based on CO features that appear. Because CO is a fairly good tracer for polluted air, the Citation could even act as a scout or guide for a more heavily instrumented research aircraft.

In addition, the Citation can accommodate an in situ canister sampling system along with MATR. We have made arrangements to use one of the packages that NOAA CMDL has developed for their world wide monitoring network. Flask, or canister, samples will be collected during the ascent and/or descent of the Citation, and the samples will be returned to NOAA for analysis. Thus a correlative CO profile can be collected on each MATR flight using a completely independent, and very well established, measurement technique. While similar in situ sampling capability should be possible with an ER-2, the logistics will probably be simpler for the Citation.

The last three lines of Table II show the accuracy, precision, and horizontal resolution of the CO measurements. While the goal is to produce CO profiles, the values shown for MATR pertain to the CO uniform mixing ratio that was retrieved using the 4.6  $\mu\text{m}$  LMC channel. The accuracy of the MATR retrievals is calculated from the average of three retrievals that were made over Carr, Colorado on a day (4 Feb 1999) when in situ results were collected simultaneously by NOAA CMDL. While this is admittedly a very limited set of measurements, we stress that the MATR entries for both accuracy and precision are based on actual flight results, while no such values are yet available for MOPITT-A.

There is a tradeoff between precision and horizontal resolution. While the MATR ground instantaneous field of view (ground IFOV) is about 1.2 km from 12 km flight altitude, the ground track is smeared out by signal averaging requirements. The FOV that is listed for MATR is consistent with the amount of aircraft motion that occurs at the Citation's typical cruise speed (660 km/hr) during a standard 14 second data averaging period. With this amount of signal averaging, MATR retrieved CO mixing ratios with a root-mean-square deviation of only about 2 ppb over the ocean near LA. The average value was about 134 ppb, so the precision was about 1.5%. While this precision is far better than the MOPITT target of 10%, radiance fluctuations increase when the aircraft flies over less uniform surfaces, and radiance precision requirements

will increase if we build profiles by flying at stepped altitudes. These factors will translate into poorer precision and/or poorer horizontal resolution for CO retrievals over complicated scenes and for stepped-level CO profiles.

Finally, we believe that it will be far easier to schedule the Citation for small, focussed single instrument validation flights using MATR than it will be to schedule ER-2 time for MOPITT-A. This will give us added flexibility for all of the key flight activities listed above: MOPITT data validation, refinement of the MOPITT cloud detection thresholds, investigation of difficult scenes in detail, and regional scale scientific studies.

## **2. Results of field deployments**

### **2.1 Engineering test flights in 1998**

A breadboard instrument with a single detector channel and a single LMC filled with CH<sub>4</sub> was flown in June and Sept 1996 (Smith and Shertz, 1996), but the first engineering test flights with the 3-channel MATR instrument were made in February and March 1998. Two engineering-type problems were discovered during the 1998 flights. First, the thermal control of the optical table was not nearly as good in the Citation aircraft as in a laboratory setting. Second, the LMC was discovered to have an appreciable leak. Both problems were corrected before the next set of flights in 1999.

CO retrievals were performed using the data from the 1998 test flights. Data was collected on one day for clear conditions over Los Angeles and the nearby Pacific Ocean. Data was also collected on three different days over the DOE ARM/CART site in north central Oklahoma, for both clear and cloudy conditions. The retrieval results that were obtained for the 4.6  $\mu\text{m}$  LMC channel can be summarized as showing reasonable precision (about 13 ppb over the ocean) but unrealistically high values (about 250 ppb of CO over the ocean). Retrievals for data collected near the ARM/CART site returned values of 200 to 300 ppb. In situ results for the ARM/CART site, although collected on different days, indicated 100 to 200 ppb of CO, depending on altitude. The 2.3  $\mu\text{m}$  LMC D-signal, as mentioned earlier, showed very poor signal-to-noise ratio and was not useful for CO retrievals. On the other hand, the 2.3  $\mu\text{m}$  LMC A-signal, which indicates surface albedo at 2.3  $\mu\text{m}$ , showed quite adequate SNR for the purpose of cloud detection. As explained in section 2.4, some of this data was used to test and refine the cloud identification thresholds that have been set for MOPITT.

The next set of flights was made in January and February 1999 and included one flight over the Los Angeles basin and four flights over Carr, Colorado. The results from Carr will be presented first.

### **2.2 CO retrieval results for Carr, Colorado for 4 Feb. 1999**

#### **MATR data and CO retrievals for 4 Feb. 1999**

A flight was made with MATR over the NOAA/CMDL monitoring site at Carr, Colorado each day from 1 Feb. 1999 to 4 Feb. 1999 in an effort to validate our MATR retrieval results against in situ sampling results. However, simultaneous data collection by MATR and the NOAA in situ canister sampling system was obtained only on 4 Feb. 1999. MATR made three overpasses of the Carr site on that date, and a retrieval was made for each overpass using data from the 4.6  $\mu\text{m}$  LMC channel and the iterative retrieval scheme described in Appendix I. The MATR retrieval yields a surface temperature and a scaling parameter for a "profile" that consists of a uniform mixing ratio. The NOAA in situ profile is plotted in Fig. 1 along with the average of the three MATR "profiles".



A quantitative comparison between the in situ results and the MATR retrieval results requires the introduction of an averaging kernel for the MATR retrievals. This averaging kernel is also plotted in Fig. 1. An averaging kernel can be described as the derivative of the retrieved value(s) with respect to a perturbation in the assumed true values. In our case the retrieved value is the uniform mixing ratio. The assumed true values are the CO mixing ratios at each level in the forward model that is used to calculate radiance. The MATR averaging kernel is a broad and smoothly varying function that peaks near 7.5 km altitude. The general shape of the averaging kernel can be understood as the product of two functions: temperature contrast and number density. The temperature contrast between the ground and atmosphere increases with altitude, and increased temperature contrast corresponds to increased net absorption and increased sensitivity to changes in CO mixing ratio. On the other hand, total number density decreases with altitude, and since we are working with mixing ratios, a given change in mixing ratio corresponds to smaller changes in total absorber amount as altitude increases. The averaging kernel increases as a function of altitude since temperature contrast with the surface is increasing, but eventually decreases again as the effect of reduced number density becomes dominant.

A quantitative comparison between the three MATR retrievals and the NOAA in situ results is presented in Fig. 2. To make the comparison, the NOAA profile has been converted to a weighted average value using the MATR averaging kernel. The weighted average of the NOAA in situ profile is 117 ppb. The uniform CO mixing ratios retrieved from the MATR overpasses range from 126 to 133 ppb, or from 8% to 14% higher than the NOAA value. The average of the three MATR retrievals is 129 ppb, or 10% higher than the NOAA values. The accuracy goal for the MOPITT measurements is 10%. Although these results are only a "spot check" of the accuracy of the MATR retrievals, measurements made with a laboratory gas cell (see section 3.1) show relatively constant accuracy for CO amounts that are equivalent to atmospheric mixing ratios ranging from 100 to 450 ppb. Accuracy is slightly degraded below 100 ppb.

### **2.3 Retrieval results for LA and Pacific Ocean for 22 Jan 1999**

#### **The flight path**

On 22 Jan 1999 a flight was made over the Los Angeles basin and nearby Pacific Ocean. The major portion of the flight consisted of 6 transects (shown in Fig. 3) that run from the San Gabriel Mountains, across the Los Angeles Basin, and a short ways over the Pacific. The first of these transects is the one passing through Santa Ana, and the sixth is the one passing near Simi Valley. Data collection for the first transect started at 10:35 AM, and data collection for the sixth transect stopped at 12:43 PM. This is a total of about 130 minutes, or 22 minutes per transect. Radiometric calibrations were performed at the beginning and end of each transect, while the Citation was turning and lining up for the subsequent transect. The concluding portion of the flight line returns back over downtown Los Angeles, with data collection ending at 1:00 PM.

#### **Retrieval procedure**

Retrievals for this flight data started with the iterative scheme mentioned before. Because this scheme requires about an hour of computer time (real time, not CPU time) per retrieval, it was not practical to use it to make direct retrievals for all 800 plus data points collected during the flight (this number of points is for the standard 14 second period for signal averaging). Therefore, 12 separate retrievals, 6 over LA and 6 over the ocean, were first made using the iterative retrieval scheme to find surface temperatures and average CO mixing ratios using the 4.6  $\mu\text{m}$  LMC average and difference signal radiances. Next a regression matrix was calculated to relate retrieved surface temperature and CO mixing ratio to the A-signal and D-signal radiances. Finally, the regression coefficients were used to predict surface temperature and CO mixing ratio for all remaining data points.

## 2-D data map

The results of the retrievals are presented in Fig. 3. Fig. 3 shows a stark contrast between the low CO values measured over the Pacific Ocean and San Gabriel Mountains, and high CO values measured over LA. It also shows that CO is quite inhomogeneously distributed over the urban areas. Some correlation with major expressways and degree of urban development can be seen. Near Newport Beach, which is quite built up, the CO values jump quickly when going from ocean to land. However, west of Santa Monica, over the Santa Monica Mountains National Recreation Area, the CO values remain low when crossing from ocean to land. The CO values then jump dramatically near Simi Valley. The CO values spike quite noticeably when the flight line passes over Highway 101 and Interstate 5 in Simi Valley. A box the size of a MOPITT 22x22 km (15x15 mile) pixel is drawn near Simi Valley. MATR clearly has sub-pixel resolution compared to MOPITT. The ability to produce detailed maps of CO distribution over major urban areas could be of real importance in regional scale pollution studies. MOPITT will show how the CO from these concentrated sources disperses over regional and global scales and MATR could provide more detailed information over selected areas. And as mentioned before, real time retrievals from MATR could be used to guide a more heavily instrumented aircraft.

## 2.4 Cloud detection results

### Overview

MATR data has been used to validate and refine the MOPITT cloud detection thresholds. One element of the MOPITT cloud detection method compares observed radiances for an actual scene to radiances that were calculated for clear conditions for the same scene. Disagreement in excess of certain thresholds is attributed to the presence of clouds in the actual scene. Most of the thresholds were determined from simulated data. MATR has been the only instrument to make MOPITT like measurements, which include both the channel average and difference signals and the contribution from the filtering CO cells.

MATR collected some data for clear conditions as well as over a large cloud bank over northern Oklahoma on 2 March 1998. Video imagery from the flight was used to positively identify clear and cloudy data segments.

The MATR data from the clear portions of the flight track was used to first test the forward model calculations for clear sky radiances. It was determined that the model results were sensitive to the surface temperatures. Since the surface temperature was not available for the observational period, the MATR clear radiances were used to determine the quantity. Second, one of the MOPITT cloud detection thresholds could not be clearly set by the simulated data, and a range of values (1.5-3.0) was normally used. By examining the MATR cloudy data set, it was clear that a value of 1.5 was necessary. Third, the MATR cloudy data was used to test all the MOPITT cloud detection thresholds. This test confirms that the MOPITT cloud detection thresholds are appropriately set.

### Results using MATR data

Figure 4 shows the cloud detection results, where the abscissas in all three panels represent the time of the observation in UTC, and the ordinates represent the quantities used for cloud detection. The vertical solid lines indicate the times when transitions between clear and cloudy occurred as indicated by the videotapes. The dotted horizontal lines are the thresholds for each test. In (a), the ordinate represents the ratio of the observed radiances over the calculated for 2.3  $\mu\text{m}$  A-signals. A threshold of 1.5 is used. The open circles depict those pixels detected as clear, and the solid circles are detected as cloudy by any one of the thresholds. Some pixels observed between 17.5 and 17.98 UTC were detected as cloudy by the thermal thresholds, but not by the solar channels. These pixels may have been under broken cloud conditions (as verified by the

videotapes), where the shadows affected the average radiances. Shadows on the ground appear to be darker and colder than the average surface, and thus, when averaged with cloud radiances, they show stronger signal in the thermal channels, and weaker in the solar channels. In (b), the thermal ratio test is shown and a threshold of 0.93 is used. Panel (c) shows the thermal difference test where a threshold of 0.005 is used. Most of the pixels detected by the solar channel threshold were also detected by the thermal ones. It is necessary to stress that in MOPITT cloud algorithm a test based on information from one channel is not sufficient, and all thresholds are necessary for cloud detection.

### How additional MATR flight data will be used

Additional MATR flight data will help improve the MOPITT cloud detection and clearing algorithm in the following ways. A large part of the MOPITT cloud algorithm is based on the CH<sub>4</sub> total column measurements. When a uniformly mixed CH<sub>4</sub> concentration in the troposphere is assumed, the total column amount represents a column amount above cloud or surface. Thus, an equivalent cloud top pressure can be estimated, and the presence of a cloud is determined. This technique does not require an accurate model calculation or correct meteorological data inputs. However, it requires sufficient validations, using for example MATR CH<sub>4</sub> measurements under clear/cloudy conditions. The MOPITT threshold method is based on comparing the clear column radiances and the observed radiances. To validate the thresholds without involving other complications from the model calculation and the input uncertainties, measurements of the clear and cloudy radiances under the same meteorological conditions are required. As mentioned before, MATR will be able to collect this data because of its small field of view and because of the ability of the Citation to fly over and between (or even under) clouds.

## 3. Results of laboratory tests

This section discusses only the results of high level tests that are specific to the operation of the LMC and PMC. General instrument calibration is discussed in Appendix III.

### 3.1 External gas cell results for 4.6 $\mu$ m LMC channel

The most comprehensive end-to-end test of MATR that has been performed in a laboratory setting is to make measurements viewing an external gas absorption cell that is illuminated by a blackbody source. This provides a very simplified way to mimic the earth-atmosphere system, in which the blackbody substitutes for the emission from the earth's surface, and the gas cell substitutes for the atmosphere.

Results of one set of external gas cell measurements made with the 4.6  $\mu$ m LMC channel are shown in Fig. 5. The ratio of "retrieved" gas amount to true gas amount is plotted as a function of total amount of CO in the cell. Data collected viewing a cold blackbody (about 2 °C) are plotted in blue. Data collected viewing a hot blackbody (about 40 °C) are plotted in red. The external gas cell was insulated and its temperature was monitored, but not actively controlled. The temperature of the gas was therefore close to the temperature of the room, about 26 °C. The pressure in the external cell was varied from 0 to 80 kPa in steps of approximately 10 kPa. The gas in the cell was a mixture of 2.8% CO in air. Given the cell length, temperature, and mixing ratio, a pressure of about 18 kPa corresponds to one total column of atmospheric CO at a uniform atmospheric mixing ratio of 100 ppb.

The "retrieved" gas amounts were determined by simply inverting the results of forward calculations of the expected radiometric signals, rather than by using the full iterative retrieval scheme that is used for flight data. The "retrieved" gas amounts show fairly constant errors of always less than 8% for equivalent atmospheric mixing ratios greater than 100 ppb. There is some degradation in accuracy for smaller amounts of CO. The results are similar for the hot blackbody (about 40 °C) and the cold blackbody (about 2 °C). These results should be regarding

as merely suggesting the magnitude of error that will be present in retrievals, as the laboratory measurements were obtained for a very simplified situation. Additional sources of error will no doubt be present in real atmospheric measurements. However, the gas cell retrieval results are very encouraging in so far as they show fairly small errors for a large range in CO amounts and for two very different source temperatures. These results suggest that the 10% level of accuracy demonstrated for the Carr, Colorado retrievals (section 2.2) should be valid for a large range of conditions.

### **3.2 PMC test results**

A student at Oxford, Kate Paulin, has done all of the analysis of the PMC data. The complete results are the subject of a separate report and only a small subset of the results will be highlighted here. As outlined in Appendix III, the instrument spectral response functions are treated as the product of two terms. The first term is the measured end-to-end transmittance of all the instrument optics except for the gas in the modulator cells. The second term is the transmittance of the gas in the modulator cells, calculated for each state (i.e., pressure, temperature, and length) of each cell. Pressure is estimated indirectly in the MOPITT PMC's, and is measured directly in the MATR PMC. This leaves the temperature cycle as the most important unknown parameter.

Test data was collected over a range of pressures during the summer of 1999. The temperature cycle of the CO in the PMC was then "retrieved" by making a careful analysis of the thermal emission from cell. A computer model that had been developed at Oxford earlier by Peter Venters was then used to predict the pressure and temperature cycles, using quantities such as cell volume and piston displacement as the driving inputs. A comparison between the measurements and the model calculations is shown in Fig. 6, with measurements shown as solid lines and calculations shown as dashed lines. The model predicts the pressure cycle reasonably well, capturing the amplitude and the shape well. The fit between model and measurement is better at lower pressures. The modelled temperature cycle has the correct magnitude but the amplitude swing is smaller than measured and the shape is not quite correct. An investigation is being made into which parameters in the model need to be revised to produce better predictions of the actual pressure and temperature cycles, especially at the highest cell pressures.

The model is being applied to the MOPITT PMC's to provide improved estimates of the true pressure and temperature cycles, and hence improved spectral response functions. As mentioned before, only nominal pressure values and a constant temperature (i.e., isothermal gas cycle) have been used to calculate the instrument spectral response functions for MOPITT to date. The laboratory measurements made using the MATR PMC's indicate that in fact the temperature cycle is closer to adiabatic, with a significant phase shift between the pressure and temperature cycles.

## **4. Summary**

The MOPITT Airborne Test Radiometer (MATR) was built to test retrievals using MOPITT-like data acquired using an LMC and PMC and to contribute to MOPITT data validation. We have performed retrievals using MATR data with good results, we plan to participate in MOPITT data validation, and we have made various additional contributions to the MOPITT program. Our accomplishments and plans are summarized below.

We have made retrievals with good accuracy (about 10% higher than in situ values) and with good precision (about 2 ppb rms over the ocean) using data from the 4.6  $\mu\text{m}$  LMC channel. We have demonstrated sub-pixel resolution compared to MOPITT, and have produced a CO distribution map that shows complicated, but quite plausible, features over Los Angeles and the Pacific.

These flight results have been buttressed by laboratory measurements made using an external gas cell and a blackbody source at hot (40 °C) and cold (2 °C) temperatures. The lab results suggest that we can expect an almost constant level of accuracy (i.e., about 10%) from the 4.6 μm LMC channel for source temperatures ranging from 40 °C to 2 °C, and for atmospheric CO amounts ranging from a uniform mixing ratio of 100 ppb to 450 ppb, with slight degradation of accuracy at lower values.

Data from the 2.3 μm LMC channel has unfortunately been plagued by poor signal-to-noise ratio for the purpose of CO retrievals, but this data has been useful for testing the MOPITT cloud detection algorithms. This data will continue to be used to refine the cloud detection algorithms.

We are still unraveling the behavior of the 4.6 μm PMC channel. However, laboratory measurements using MATR and subsequent modeling analysis have been carried out by collaborators to the MATR project. It now appears that the MATR and MOPITT PMC's operate with a temperature and pressure cycle that is close to adiabatic, rather than isothermal as was previously assumed. This work represents the most detailed examination that has been made of the MOPITT-type PMC's, and it is having a direct impact on the calculation of the MOPITT spectral response functions for the PMC channels.

We have implemented a radiometric calibration procedure that has apparently eliminated the LMC "imbalance" problem. This calibration procedure may be transferred to MOPITT, pending additional confirmation of the MATR results.

Our scheme for an in-flight radiometric calibration assembly is being used, with modification, by MOPITT-A.

MATR will contribute to MOPITT data validation. Our first planned data validation activity is the MOPITT Validation Experiment (MOVE) campaign that will be centered over the DOE Southern Great Plains ARM/CART site in Oklahoma and is scheduled for May 8 to May 28. The Canadian airborne instrument (MOPITT-A) may or may not be ready for this campaign, but is still an unproven performer. MATR will be used primarily to characterize possible CO gradients in the extended vicinity of the ARM/CART site.

We are making plans to participate in the MIRAGE (Mega-city Impacts on Regional And Global Environments) program, with flights anticipated in summer 2001. The MATR data, with sub-pixel resolution, will be complementary to MOPITT data for the region.

Even after MOPITT-A becomes fully operational, MATR will have several unique capabilities. These include the ability of the Citation aircraft to maneuver around or under clouds, the possibility of performing stepped retrievals with MATR to improve vertical resolution, and the possibility of performing real time retrievals to guide the flight of the Citation or another aircraft.

Finally, we believe that it will be far easier to schedule the Citation for small, focussed single instrument validation flights using MATR than it will be to schedule ER-2 time for MOPITT-A. This will give us added flexibility for all of the key flight activities listed previously: MOPITT data validation, refinement of the MOPITT cloud detection thresholds, investigation of difficult scenes in detail, and regional scale scientific studies.

## Appendix I: Remote sensing theory

### I.a Remote sensing of tropospheric trace gases

The general process used for remote sensing of tropospheric trace gases, either from a spaceborne or an airborne platform, is depicted schematically in Fig. A1. Two distinct physical processes can occur. In one case, radiation is emitted by the sun, propagates down through the earth's atmosphere, and is scattered at the earth's surface. Some of the radiation that has been scattered, or reflected, at the earth's surface is detected by a down-looking remote sensing instrument. Radiation will be absorbed along both the downward and upward paths by trace gases in the atmosphere, at wavelengths that are characteristic of particular molecular species. In the second case, radiation is emitted at the earth's surface and is partially absorbed and re-emitted as it propagate upwards through the atmosphere, again at wavelengths that are characteristic of particular molecular species. In both cases, the remote sensing instrument measures electromagnetic radiation, and trace gas concentrations in the atmosphere are estimated, or retrieved, based on the amount of radiation detected at particular wavelengths.

For wavelengths shorter than 4  $\mu\text{m}$ , solar radiation becomes dominant, while for wavelengths longer than 4  $\mu\text{m}$ , radiation emitted by the earth becomes dominant. Measurements using solar radiation yield total column absorption throughout the atmosphere. This is because the effective radiating temperature of the sun is so high (about 5800 K) compared to the temperature of the atmosphere (about 255 K) that re-emission of radiation is negligible. However, the temperature difference between the earth (290 K on average) and the atmosphere (255 K on average) is not nearly so great, and at wavelengths longer than 4  $\mu\text{m}$  re-emission by the atmosphere becomes an important contribution to the radiation field. Measurements using these longer wavelengths yield not a total column, but rather a weighted average of trace gas concentration in the atmosphere. The averaging kernel for the MATR 4.6  $\mu\text{m}$  channels will be discussed in section 5.

Fig. A2 shows calculated vertical column transmittances through the atmosphere for radiatively active gases near 2.2 to 2.3  $\mu\text{m}$ , and top-of-the-atmosphere radiance for solar radiation that has passed down and back up through the atmosphere. Fig. A3 shows calculated vertical column transmittances through the atmosphere for radiatively active gases near 4.6  $\mu\text{m}$ , and top-of-the-atmosphere radiance for upwelling thermal radiation that was emitted by the earth's surface. These figures show the relative importance of various absorbers, and give some idea of just how complicated a function atmospheric radiance is when viewed at high spectral resolution.

### I.b Forward Model Calculations

#### Basic equations

The basic equations that describe radiative transfer in the atmosphere can be cast into several different forms. I will start with a straightforward version:

$$(1) I_{\nu}(\nu, z_{obs}) = I_{\nu}(\nu, z_s) \tau(\nu, z_s, z_{obs}) + \int_{z_s}^{z_{obs}} B(\nu, T(z)) \left[ \sum_i k_i(\nu, z) \rho_i(z) \right] \tau(\nu, z, z_{obs}) dz$$

where

$I_{\nu}(\nu, z_{obs})$  = spectral radiance at wavenumber  $\nu$  at observer altitude  $z_{obs}$ , in units  $W/(m^2 \cdot sr^{-1} \cdot cm^{-1})$

$I_{\nu}(\nu, z_s)$  = spectral radiance leaving the surface, including both reflected and emitted radiation

$\tau(\nu, z_s, z_{obs})$  = transmittance at  $\nu$  between  $z_s$  and  $z_{obs}$ , which is a dimensionless quantity

$B(\nu, T(z))$  = Planck function for the temperature  $T$  at altitude  $z$ , with units of  $W/(m^2 \cdot sr \cdot cm^{-1})$   
 $k_i(\nu, z)$  = monochromatic absorption coefficient of  $i^{th}$  absorber, with units of  $1/(molecules \cdot cm^{-2})$   
 $\rho_i(z)$  = number density of  $i^{th}$  absorber at altitude  $z$ , with units of  $molecules \cdot cm^{-3}$   
 $\tau(\nu, z, z_{obs})$  = transmittance at wavenumber  $\nu$  from altitude  $z$  to the observer at  $z_{obs}$

The radiance that is detected by the  $n^{th}$  instrument channel is the product of atmospheric spectral radiance and instrument spectral response for that channel, integrated over wavenumber:

$$(2) \quad I_{n,obs} = \int_{\nu=-\infty}^{\nu=+\infty} I_{\nu}(\nu, z_{obs}) F_n(\nu) d\nu$$

where

$I_{n,obs}$  = band-integrated radiance observed by  $n^{th}$  channel, with units of  $W/(m^2 \cdot sr \cdot l)$

$I_{\nu}(\nu, z_{obs})$  = spectral radiance at wavenumber  $\nu$  at the observer altitude  $z_{obs}$

$F_n(\nu)$  = instrument spectral response function of  $n^{th}$  channel at wavenumber  $\nu$

By using the following explicit expression for transmittance along a path:

$$(3) \quad \tau(\nu, z_1, z_2) = \frac{I_{\nu}^{z_2}(\nu)}{I_{\nu}^{z_1}(\nu)} = \exp\left(-\int_{z_1}^{z_2} \sum_i k_i(\nu, z) \rho_i(z) dz\right)$$

One can rearrange Eq.(1) into the following form:

$$(4) \quad I_{\nu}(\nu, z_{obs}) = I_{\nu}(\nu, z_s) - \int_{z_s}^{z_{obs}} \left[ I_{\nu}(\nu, z_s) - B(\nu, T(z)) \right] \left[ \sum_i k_i(\nu, z) \rho_i(z) \right] \tau(\nu, z, z_{obs}) dz$$

So far the surface radiance term,  $I_{\nu}(\nu, z_s)$ , can include reflected radiation that originated at the sun, reflected radiation that was emitted downward by the atmosphere, and radiation that was emitted upward by the surface. For the MOPITT and MATR 4.6  $\mu m$  channels, the dominant term will be radiation emitted upward by the surface, and Eq. (4) can be approximated as:

$$(5) \quad I_{\nu}(\nu, z_{obs}) = \epsilon_s B(\nu, T(z_s)) - \int_{z_s}^{z_{obs}} \left[ \epsilon_s B(\nu, T(z_s)) - B(\nu, T(z)) \right] \left[ \sum_i k_i(\nu, z) \rho_i(z) \right] \tau(\nu, z, z_{obs}) dz$$

where

$T(z_s)$  = surface temperature

$\epsilon_s$  = surface emissivity (dimensionless and  $0 \leq \epsilon_s \leq 1$ )

The advantage of Eq. (5) is that it clearly shows the importance to the 4.6  $\mu m$  channels of the temperature difference, or temperature contrast, between the surface and the atmosphere. For the special case in which  $\epsilon_s = 1$  (perfect emitter) and  $T(z) = T(z_s)$  for all  $z$ , the spectral radiance that reaches the observer is simply equal to the spectral radiance that is emitted by the surface.

Physically, one can say that in this special case all of the radiation that is absorbed by the atmosphere is re-emitted with equal intensity, and there is no net change in radiance. However, in the far more typical case  $T(z)$  is equal to or less than  $T(s)$  at the bottom of the atmosphere and  $T(z)$  decreases further with altitude. Thus in typical situations the atmosphere re-emits less radiation than it absorbs, resulting in net absorption. (A temperature inversion, with  $T(z)$  increasing with altitude, is also possible over a limited altitude range but is somewhat atypical).

### Relationship between MOPITT and MATR forward models

Various computer models can be used to calculate values of  $I_V(v, z_{obs})$  and  $I_{n,obs}$ . The most general and detailed models for calculating  $I_V(v, z_{obs})$  are line-by-line models, which calculate  $k_i(v, z)$  explicitly for all atmospheric absorbers for a large number of discrete layers in the atmosphere. However, these models are relatively slow to execute and some type of fast, simplified model is usually employed for the purpose of making atmospheric retrievals. The general purpose line-by-line model that is used at NCAR, GENLN2, has been described in a publication (Edwards, 1992). The fast models, MOPFAS and MOPABS, that have been derived using GENLN2 have been described in another publication (Edwards, et al., 1999). MOPITT operational retrievals will use the MOPFAS model for maximum speed. The MOPABS code, which is more flexible, is used for MATR retrievals as well as for analyzing laboratory measurements and for performing sensitivity studies for both MOPITT and MATR.

### 1.c Retrieval methodologies

#### Fundamental retrieval procedure: constrain and equate

The remote sensing process measures electromagnetic radiation, and trace gas column amounts or profiles are estimated, or retrieved, based on the amount of electromagnetic radiation that is measured at various wavelengths. In particular, a forward model is used to calculate the radiance that one expects to observe for a particular absorber profile,  $\rho_i(z)$ , based on Eq. 1, and the absorber profile is adjusted until the calculated radiance is equal to the measured radiance, to within some prescribed limit or error band. The resulting profile is the retrieved profile.

The spectral radiances that are calculated according to Eq. 1 in general depend on a very large number of parameters. These parameters include  $\rho_i(z)$  for each radiatively active gas species and  $T(z)$  at each level  $z$  (integration over  $z$  is usually replaced by summation over a few dozen discrete levels), as well as  $\epsilon_s$ , and  $I_V(v)$  emitted by the sun. The solution to Eq. 1 is almost always underdetermined by the measured radiances. Auxiliary data such as surface emissivity,  $\epsilon_s$ , radiation emitted by the sun,  $I_V(v)$ , atmospheric temperature profile,  $T(z)$ , and profiles,  $\rho_i(z)$ , for background absorbers, are usually introduced as climatological or independently measured values. Some additional constraint, such as smoothness or adherence to a priori values, is usually imposed on the profile of the retrieved species. In the end the only values that are retrieved directly are profile values for the gas of interest at a limited number of discrete levels, or perhaps just a single scaling parameter for an assumed profile shape. Surface temperature and reflectance are sometimes also retrieved directly, and can prove very useful for applications such as cloud detection. Also note that if  $\rho_i(z)$  is known, as for  $\text{CO}_2$ , a temperature profile,  $T(z)$ , can be retrieved rather than gas mixing ratios.

#### MOPITT retrievals

A variety of techniques can be used to constrain Eq. 1 and to find, or retrieve, a profile,  $\rho_i(z)$ , for the gas of interest such that calculated radiances agree with measured radiances. MOPITT ultimately will use a maximum likelihood method to retrieve  $\text{CO}$  profiles (Pan, et al., 1998). This



is a relatively sophisticated method that is often described as the optimum method (terminology from the field of statistical analysis) for combining instrument measurements and a priori information. While combining all information at once is "optimal", it can also obscure problems in particular instrument channels. Therefore, the MOPITT team also plans to make some early retrievals using a simple regression scheme.

### MATR retrievals

MATR retrievals to date have made use only of the 4.6  $\mu\text{m}$  LMC channel data. We felt that using a maximum likelihood retrieval to produce CO profiles would mostly reflect a priori inputs, and would obscure the one piece of CO information available from the 4.6  $\mu\text{m}$  LMC D-signal. Therefore a simple iterative retrieval scheme was developed for MATR. Surface temperature is initialized to the temperature of the lowest level of the atmosphere as reported by meteorological data sources. CO is simply initialized to a uniform "profile" of 100 ppb mixing ratio. Surface temperature and average CO mixing ratio are then adjusted iteratively until suitable agreement is reached between calculated and measured radiances for both the 4.6  $\mu\text{m}$  LMC A-signal and D-signal. The final value of the CO mixing ratio is completely unconstrained and reflects only information from the MATR instrument (i.e., no a priori values are weighted in), but the profile shape is constrained to a somewhat unrealistic uniform mixing ratio at all altitudes. This method could easily be modified to use a profile shape that is consistent with a priori data for a particular site, but a scaling factor would still be determined from the MATR data.

We plan to develop a regression scheme for MATR retrievals. This will allow a more direct evaluation of the MOPITT regression retrieval. A regression retrieval can also be very fast, and could produce real time retrievals of CO while MATR is in flight. This could be useful for adjusting the Citation flight path to study interesting CO features. It could also allow the MATR CO measurements to be used as a real time tracer to guide the flight path of a more heavily instrumented aircraft.

Finally, it would be useful to use a single retrieval scheme to combine the data from all three MATR channels, once the data from all channels is adequately understood for each channel individually. Either a regression scheme (very simple) or a maximum likelihood scheme (statistically "optimal") could be used for retrievals that combine data from different channels.

## Appendix II: Physical description of MATR

Only a very brief physical description of the MATR instrument will be presented in this section. A more complete description has been published (Smith, et al., 1999).

### II.a The basic instrument

#### Optical table

Fig. A4 is a simple sketch of the MATR optical table and in-flight radiometric calibration assembly. A rotating input mirror selects one of four sources of input radiation: scene, cold blackbody, hot blackbody, or tungsten lamp. The last three sources are used for in-flight radiometric calibration. MATR collects scene data with a nominally nadir view, except when the aircraft is pitched up or down or is banking. The instrument full angle field of view (FOV) is approximately  $5.7^\circ$ , or 0.1 radians, producing a ground instantaneous FOV of about 1.2 km from the standard 12 km flight altitude.

The basic paths that infrared radiation take inside the instrument are shown as heavy red lines. MATR has three optical channels, one corresponding to each photo-voltaic InSb detector. The filter that predominately sets the spectral pass band of each detector channel is located externally to the detectors, in a well-collimated optical beam, and at a carefully controlled temperature near

32 °C. A second band pass filter is located in each detector Dewar, where it is cooled to liquid nitrogen temperature for the purpose of blocking thermal background radiation. This background blocking filter is about three times as wide as the external filters, so that its pass band will not be unduly shifted by the highly convergent beam that is being focussed on each detector element.

The operation of both an LMC and PMC have been described at length elsewhere (Tolton and Drummond, 1997; Houghton, et al., 1984; Taylor, 1983). Briefly, in a PMC (pressure modulated cell) the pressure of the correlation gas in an optical absorbing cell is varied by means of pistons that change the volume of a gas reservoir. The MATR PMC is nearly identical in its optical performance to a MOPITT flight PMC, as both were built to the same design at Oxford University. However, the MOPITT PMC's are coupled to a molecular sieve gas reservoir while the MATR PMC simply uses a valve to contain the gas.

In an LMC (length modulated cell), the absorption path length inside the correlation cell is varied by means of a transparent optical rotor, or gas-displacing element, that rotates through the optical beam. The MATR LMC uses  $\text{CaF}_2$  windows, while the MOPITT(-A) LMC's use coated Ge windows. Furthermore, the MOPITT(-A) LMC's use "double pass" optics so that the optical path length is double the physical path length.

The gas correlation cells introduce small modulations onto the detected power at frequencies of about 50 Hz (PMC) and 25 Hz (LMC). This modulation occurs only at wavelengths at which the gas in the correlation cells are optically active. A second chopper, operating at about 400 Hz, produces a strong modulation that is used to discriminate against broadband thermal background radiation.

### In-flight radiometric calibration assembly

In-flight radiometric calibration is accomplished with the use of three calibration sources. A pair of blackbodies, one heated to about 40 °C and one cooled to about 2 °C, is used to derive radiometric gain and offset coefficients for the 4.6 micrometer channels. A thin sheet of Spectralon diffusing material that is illuminated by a quartz tungsten halogen (QTH) lamp with a color temperature near 3000 K is used as a source for the 2.3 micrometer channel. The blackbody temperatures as well as the supply voltage and current for the QTH lamp are monitored and recorded in normal operation. The in-flight blackbodies are calibrated in the laboratory against a reference blackbody that has been calibrated directly by NIST. The in-flight QTH source is calibrated against a set of QTH lamps that have calibration traceable to NIST reference standards.

### Thermal control

Stable instrument temperatures are a pre-requisite for a radiometer that measures thermally generated infrared radiation (TIR), which pertains to the MOPITT 4.6  $\mu\text{m}$  channels. The MATR optical table is completely enclosed in a foam insulated box. The interior of the box is stabilized at about 32 °C by a combination of convective and conductive heating. A heat pump removes the power that is generated from the chopper motor, which is the only appreciable heat source on the optical table. Temperatures are monitored and recorded for 16 points throughout the instrument, in addition to the blackbodies. In-flight, temperatures measured throughout the optical table have been stable to within about  $\frac{1}{2}$  °C, or better, per hour. Radiometric calibrations are performed about every 20 to 30 minutes in flight.

### Data acquisition, storage, processing, and display

Instrument control and data acquisition are performed by an industrial grade rack mounted PC computer. A backup copy of data is written in real time onto a 1 Gbyte removable media Jaz disk, which can hold about 8 hours worth of data. All user interaction is handled through graphical user interface (GUI) display panels. The system features numerous real time displays that allow all of the instrument outputs to be viewed either as low level (i.e., unprocessed) values

or as numerically processed values. This has been useful to monitor the instrument for correct operation in-flight, as well as to diagnose problems when they occur. Retrieved values for CO produced "on-the-fly" would be a very useful addition to the real time displays, and we are currently considering how to add this feature using a simple regression scheme to produce the retrievals.

## **II.b Flight configuration**

### **Auxiliary in-flight instrumentation**

Post-flight data analysis requires auxiliary information in addition to the detector outputs and instrument temperatures. A global positioning system (GPS) provides latitude, longitude and geometrical altitude. Ambient pressure at flight altitude, as determined by an aircraft altimeter, is also recorded. A position and orientation system (POS) provides aircraft attitude data. When interpreting the radiometric data, it is useful to know if the scene was clear or cloudy, water or land, vegetated or bare, simple or complex, etc. This information is provided by a nadir-viewing video camera that has a full-angle FOV of  $14.4^\circ$ , which is about 3.5 times greater than MATR's FOV. An in situ flask sampling system will be added as a new capability for the next set of MATR flights. This system has been built by the NOAA CMDL in Boulder, and is one of the series of systems used in the NOAA CMDL global monitoring network. Flask samples will be collected during the MATR flights, and will then be shipped back to the NOAA labs for analysis. This will allow us to collect our own in situ validation profiles extending all the way up to the Citation flight altitude of 12 km.

### **Size, Weight and Power**

The overall size of the MATR optical table is 41 cm wide by 67 cm long by 39 cm high, including thermal and electrical controls, but not including the in-flight radiometric calibration assembly. Additional electronics and the video recorder occupy about 24" in height in a standard 19" wide electronics rack. The POS system uses another 7" of rack height. The power supply electronics use as input 28 V DC and 110 V AC electrical power that is supplied by the aircraft. Total power consumption is somewhat less than 1400 W (50 A) at 28 V DC and less than 330 W (3 A) at 110 V AC. Power for the detectors' pre-amplifiers is provided by a pair of nominally 12 V re-chargeable lead acid storage batteries, for minimum electrical noise. An un-interruptible power supply (UPS) with 110 V AC output ensures power integrity to the computer.

### **Citation aircraft**

MATR has been flown in a Cessna Citation II aircraft (shown in Fig. A5) that is owned by the Department of Energy and operated out of the Remote Sensing Laboratory in Las Vegas, Nevada. The service ceiling for the aircraft is 13 km, but in practice a cruise altitude of 12 km has been used for MATR deployments. The standard cruise speed at 12 km altitude is specified as about 660 km/hr. The flight range (until 30 minute reserve) is about 2,400 km when the aircraft is empty, but is only about 1,600 km when the aircraft is fully loaded.

## **Appendix III: MATR calibration**

### **III.a The Instrument "Model"**

The MATR instrument "model" is really only a high spectral resolution representation of the instrument spectral response function, which is denoted in Eq. 2 as  $F_n(\nu)$ . For forward model calculations this function is tabulated at 200 points per  $\text{cm}^{-1}$  for the  $2200 \text{ cm}^{-1}$  ( $4.6 \text{ }\mu\text{m}$  CO)

channels, and at 400 points per  $\text{cm}^{-1}$  for the  $4300\text{ cm}^{-1}$  ( $2.3\text{ }\mu\text{m CO}$ ) and  $4400\text{ cm}^{-1}$  ( $2.2\text{ }\mu\text{m CH}_4$ ) channels. A correct determination of this function is probably the most critical element of the MATR calibration. The average signal spectral response function for the  $4.6\text{ }\mu\text{m CO}$  channel is shown in Fig. A6, and the difference signal spectral response function is shown in Fig. A7.

The instrument spectral response function is treated as the product of two terms: 1) the normalized transmittance of all optics except for the gas in the correlation cells, and 2) the transmittance of the gas in the correlation cells. The transmittance of all the optics sans gas is dominated by the bandpass filters and is a relatively smoothly varying function of wavelength. This function has been measured directly for MATR using a monochromator for a source. The measurements were made at 1 to 2  $\text{cm}^{-1}$  intervals and were then interpolated to the very high resolution grid cited above. Our radiometric calibration convention specifies that this response function be normalized to a peak value of 1.0. The transmittance of the gas in the correlation cells is calculated for each state of each correlation cell (short and long paths in the LMC and high and low pressures in the PMC), and average and difference states are then derived. The transmittance calculations combine line parameters from the HITRAN data base with measured, or estimated, values of correlation cell length, temperature, and pressure for each gas state. We calculate these values because it is very difficult to make the direct measurements with high accuracy at the high spectral resolution that is required. On the other hand the line parameters in the HITRAN data base have been determined using the best experimental techniques possible for these particular measurements. The same separation of effects is employed to determine the MOPITT spectral response functions.

### **III.b Calibration results**

#### **Calibration of engineering channels**

The engineering data channels in MATR collect information about parameters such as power supply voltages, temperatures at various points throughout the instrument, and pressures in the correlation cells. The most critical parameters as far as data analysis is concerned are the temperatures of the calibration blackbodies, and the temperatures and pressures recorded for the LMC and PMC. Error analysis shows that the temperatures are determined with a precision of a 0.02 to 0.05  $^{\circ}\text{C}$ , depending on the channel, while the absolute accuracy is about 0.2  $^{\circ}\text{C}$ . The pressure in the LMC is determined with a precision of about 0.02% and an accuracy of about 0.3% at the standard 80 kPa fill pressure. The pressure in the PMC is determined with a precision of about 0.5% and an accuracy of about 1% at the standard 7.0 kPa mean pressure.

#### **Blackbody calibrations**

The blackbodies that are used for in-flight radiometric calibrations have been calibrated against a transfer blackbody that was calibrated by NIST against a water bath blackbody standard. The NIST results were reported in the form of equivalent radiometric temperatures, assuming an emissivity of 1.0 for the transfer source. (Note that this means that any departures of the emissivity from 1.0 would show up as equivalent radiometric temperatures that are slightly lower than the temperature as indicated by a thermometer). Comparison of the in-flight sources to the transfer source shows that the radiometric temperature of the cold blackbody is within 0.1  $^{\circ}\text{C}$  of its indicated temperature, and the radiometric temperature of the hot blackbody is within 0.25  $^{\circ}\text{C}$  of its indicated temperature. Small correction factors are used in the data processing so that the indicated temperatures are converted to appropriate radiometric temperatures for use in radiance calculations.

### Linearity of detector channels

To make sure that a two point radiometric calibration, using a hot and a cold blackbody, is sufficient to convert the data from digital counts to radiances, the linearity of the detector channels has to be verified. Linearity of the 4.6  $\mu\text{m}$  channels was tested in the laboratory by using the transfer blackbody set to 12 different temperatures. The temperature of the blackbody source was converted from a spectral radiance to a band-integrated radiance by integrating the Planck function over the spectral response function of the instrument. To keep the spectral response function simple, the gas was evacuated from the modulator for these tests. A linear fit of digital counts as a function of radiance was then made for each 4.6  $\mu\text{m}$  channel. The residuals of the fits averaged about 0.15% of full scale, were never greater than 0.5% of full scale, and formed no discernable pattern. This indicates very linear behavior for the end-to-end radiometric response of the 4.6  $\mu\text{m}$  detectors, signal processing electronics, and data acquisition electronics. Because of the relatively small signal levels, the same blackbody source could not be used to test the linearity of the 2.2  $\mu\text{m}$  and 2.3  $\mu\text{m}$  channels. A different test was made using precision apertures that were placed at the exit port of an integrating sphere that was illuminated by a high temperature quartz tungsten halogen lamp. These tests indicated a possible quadratic non-linearity of approximately 1% of the full scale response. However, the non-linearity could be present in either the test setup or the detection system, and further tests are required.

### Spectral response "sans gas"

As discussed in section 4.1, the spectral response of each channel is determined as the product of two terms: 1) the normalized transmittance of all optics except for the gas in the correlation cells, and 2) the transmittance of the gas in the correlation cells. The end-to-end transmittance of the optics sans gas was measured by using a 1/3 meter monochromator that was illuminated by a high temperature (2200 K) tungsten lamp with a ZnSe window. The spectral scale for the monochromator was calibrated directly against the CO absorption lines over the working ranges. The measured end-to-end spectral response for the 4.6  $\mu\text{m}$  channels was shifted about 15 nm to longer wavelengths than shown by the manufacturer's results, which are for a single bandpass filter chosen randomly from the production lot. The LMC and PMC channels show slightly different responses, possibly due to the effects of the dichroic beamsplitter that splits the radiation for the two channels.

### Need to determine LMC path lengths

The transmittance calculations for the LMC states depend on the gas temperature, pressure, and absorption path lengths. Error analysis indicates that the temperature and pressure are being measured with sufficient accuracy, but to date we have used only nominal values for the LMC path lengths. We are still evaluating the best technique for determining the actual optical path absorption path lengths in the LMC. The same uncertainty exists for MOPITT.

## References

- G. V. Bailak, G. R. Davis, J. R. Drummond, L. Jounot, G. Mand, A. Philips, B. T. Tolton, "MOPITT airborne validation instrument: MOPITT-A" *Proc. of SPIE*, **3756**, 468-474 (1999).
- D. P. Edwards, "GENLN2: A general line-by-line atmospheric transmittance and radiance model: Version 3.0 description and users guide," *Rep. NCAR/TN-367+STR*, Natl. Cent. For Atmos. Res., Boulder, CO (1992).
- D. P. Edwards, C. M. Halvorson, and J. C. Gille, "Radiative transfer modeling for the EOS Terra satellite Measurement of Pollution in the Troposphere (MOPITT) instrument," *J. Geophys. Res.*, **104**, 16,755-16,775 (1999).
- J. T. Houghton, F. W. Taylor, C. D. Rodgers, *Remote Sounding of Atmospheres*, 93-107, Cambridge University Press, Cambridge (1984).
- L. Pan, J. C. Gille, D. P. Edwards, and P. L. Bailey, "Retrieval of tropospheric carbon monoxide for the MOPITT experiment," *J. Geophys. Res.*, **103**, 32,277-32,290 (1998).
- M. W. Smith and S. R. Shertz, "Current plans and status of MOPITT Algorithm Test Radiometer (MATR)," *Proc. of SPIE*, **2820**, 78-86 (1996).
- M. W. Smith, S. R. Shertz, N. Delen, "Remote sensing of atmospheric carbon monoxide with the MOPITT Airborne Test Radiometer (MATR)," *Proc. of SPIE*, **3756**, 475-485 (1999).
- F. W. Taylor, "Pressure Modulator Radiometry", in *Spectrometric Techniques, Vol. III*, G. A. Vanasse, Ed., 137-196, Academic Press, New York (1983).
- B. T. Tolton and J. R. Drummond, "Characterization of the length-modulated radiometer," *Appl. Opt.* **36**, 5409-5420 (1997).



	<b>Table II: Validation with MATR vs. MOPITT-A</b>		
		<b>MATR</b>	<b>MOPITT(-A)</b>
Level 1 (radiance) validation		No	Yes
Level 2 (CO and CH4) validation		Yes	Yes
Simultaneous CO and CH4 retrievals		No	Yes
Ability to perform stepped retrievals		Possible	No
Ability to maneuver around or under clouds		Yes	Very limited
Real time retrievals to guide flights		Possible	No
In situ sampling capability		Yes	Possible
Accuracy of CO average mixing ratio		About 10%	Unknown
Precision of CO average mixing ratio		2 ppb over ocean	Unknown
Horizontal resolution for stated precision		1.2 x 2.5 km	Unknown



Figure 1: MATR retrieved CO vs. NOAA in-situ values over Carr, Colorado.

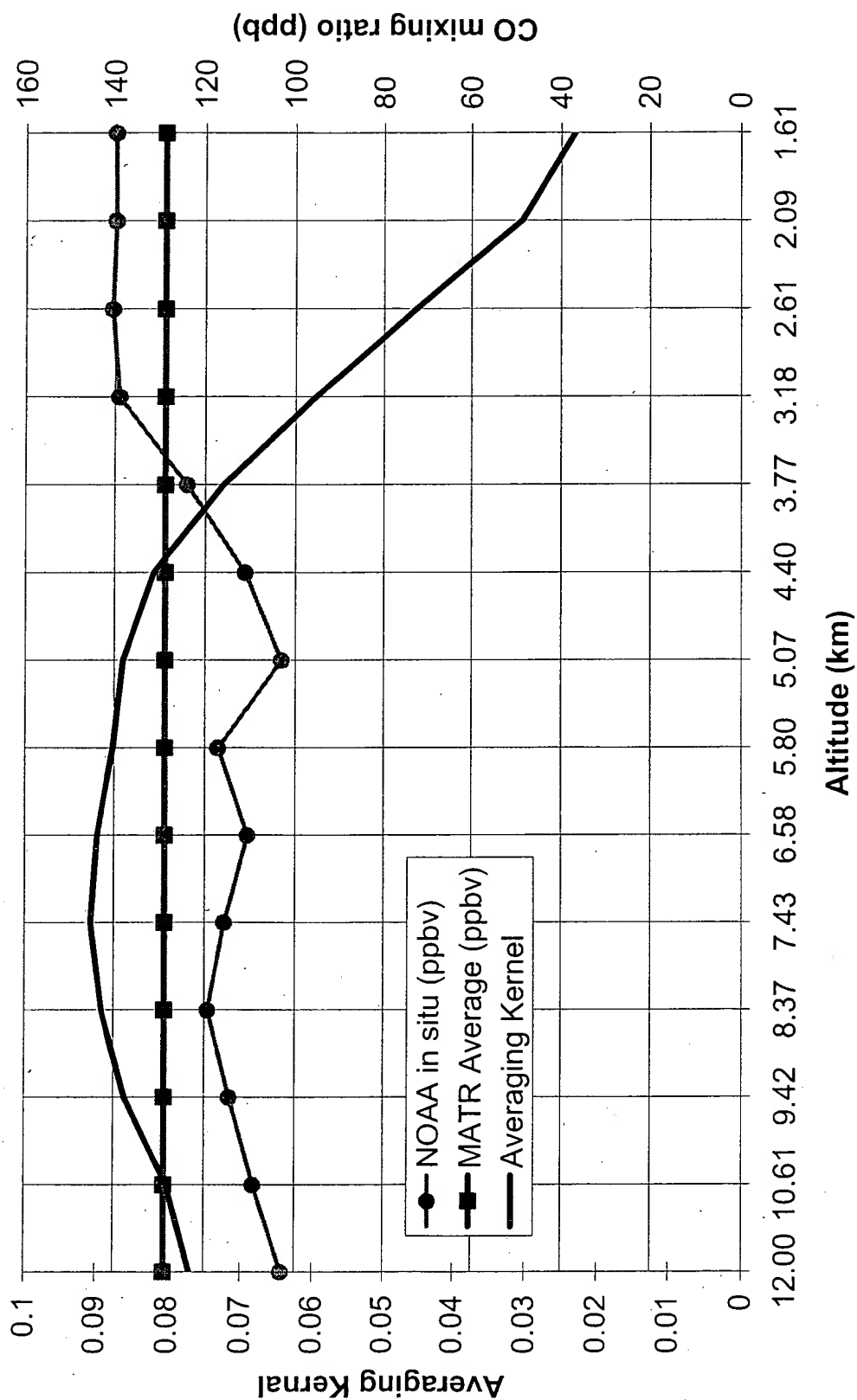
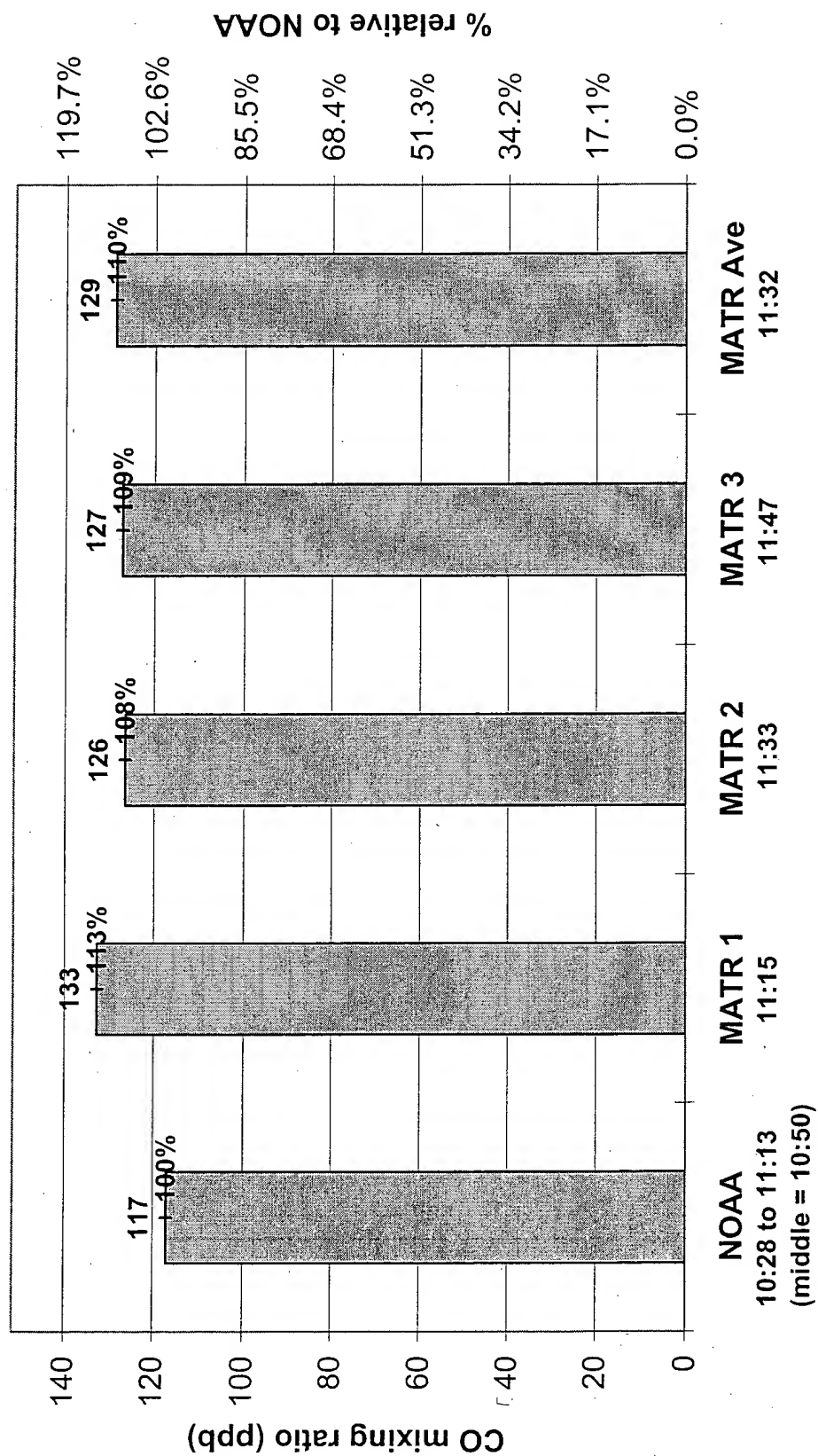
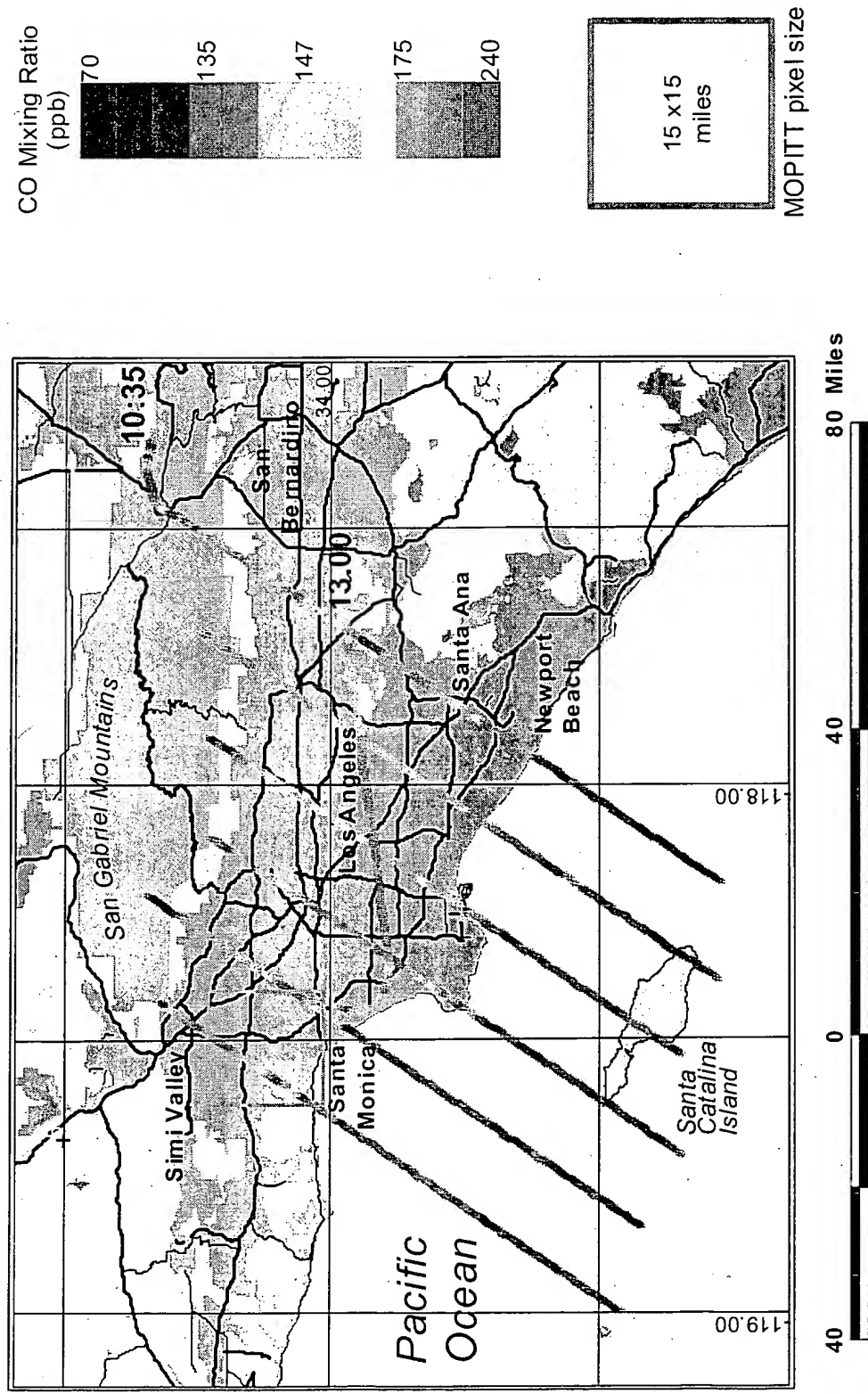


Figure 2: CO retrieved from 3 MATR overpasses of Carr, Colorado compared to NOAA/CMDL in situ results also acquired on 4 Feb 1999.



**Fig 3: CO Mixing Ratio Over Los Angeles on 22 Jan. 1999**



February 29, 2000

Figure 4: Checking cloud detection thresholds

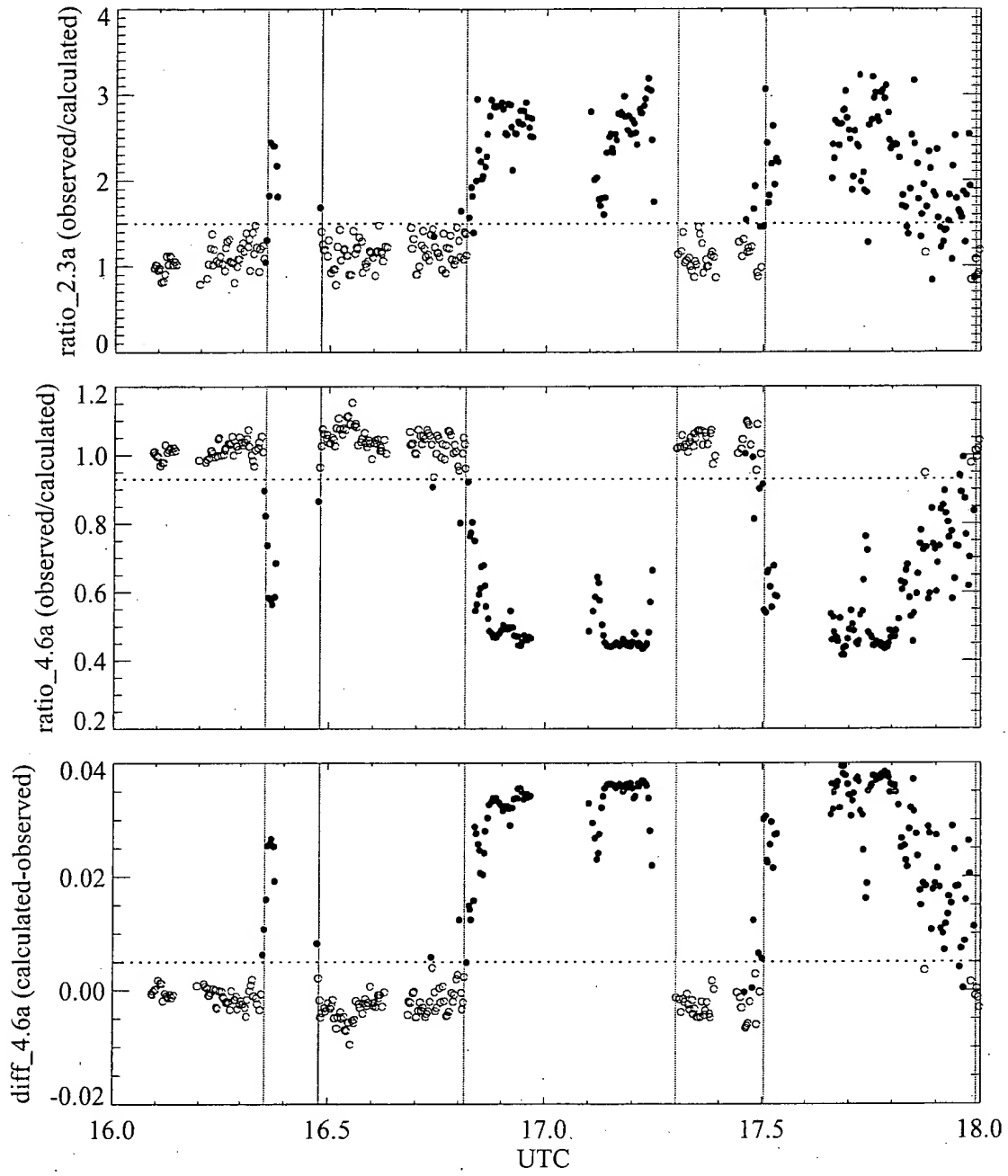
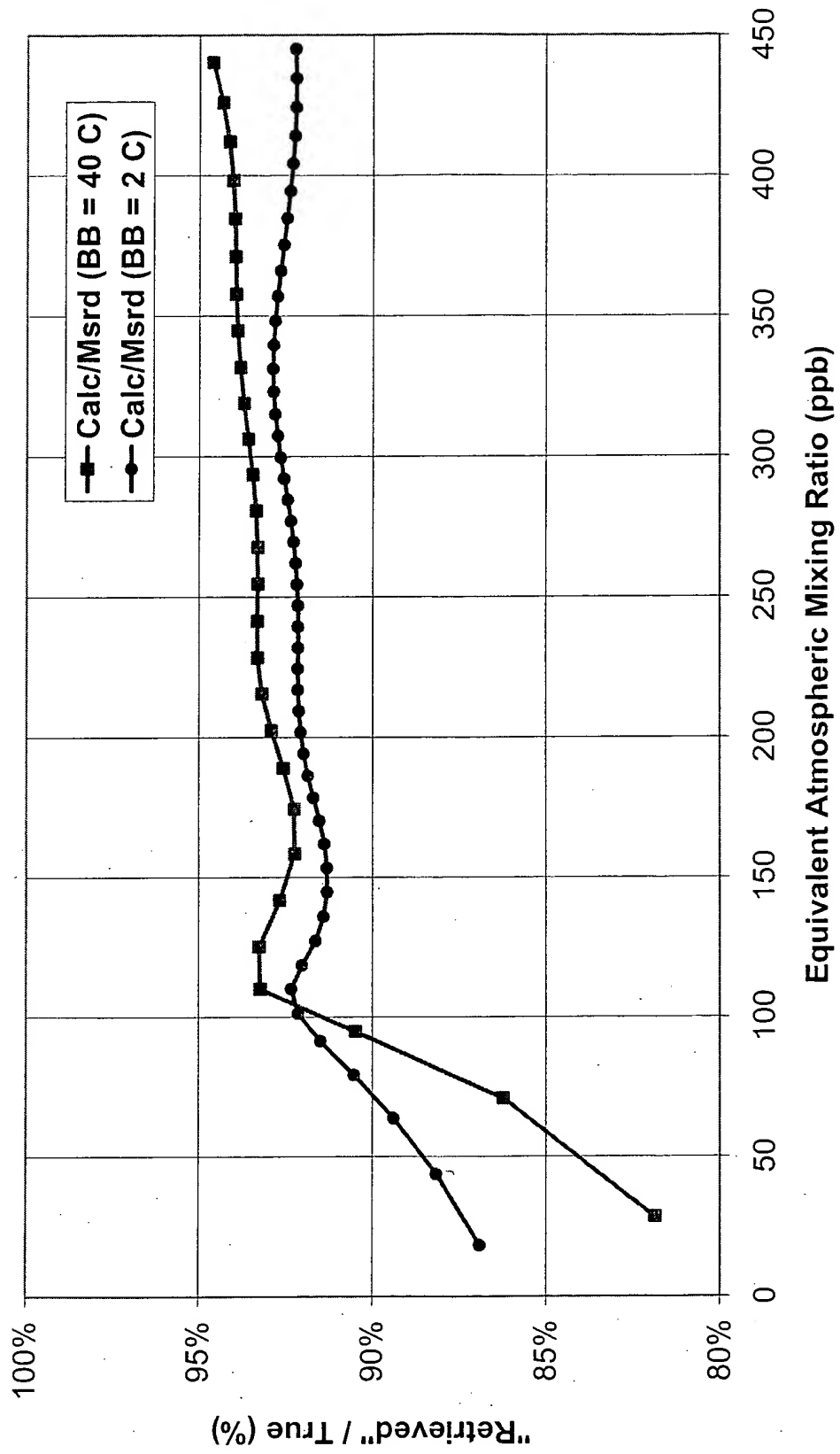
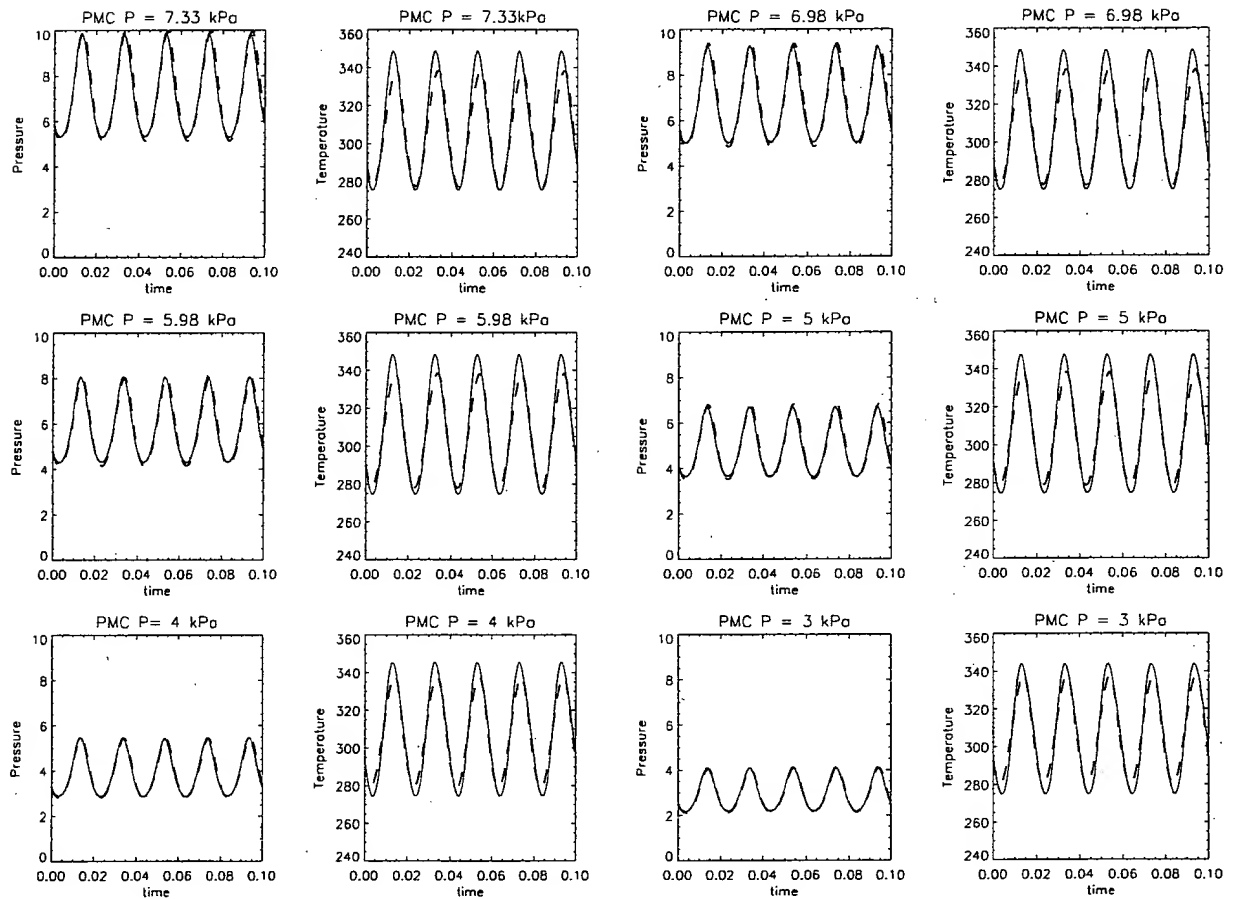


Figure 5: "Retrieved" / True CO amounts for MATR  
 4.6  $\mu$ m LMC using nominal 10.0 / 2.0 mm path lengths.



**Figure 6: PMC pressure and temperature cycles**



**Figure A1: Remote sensing of atmospheric CO and CH<sub>4</sub>  
by means of infrared radiometry**

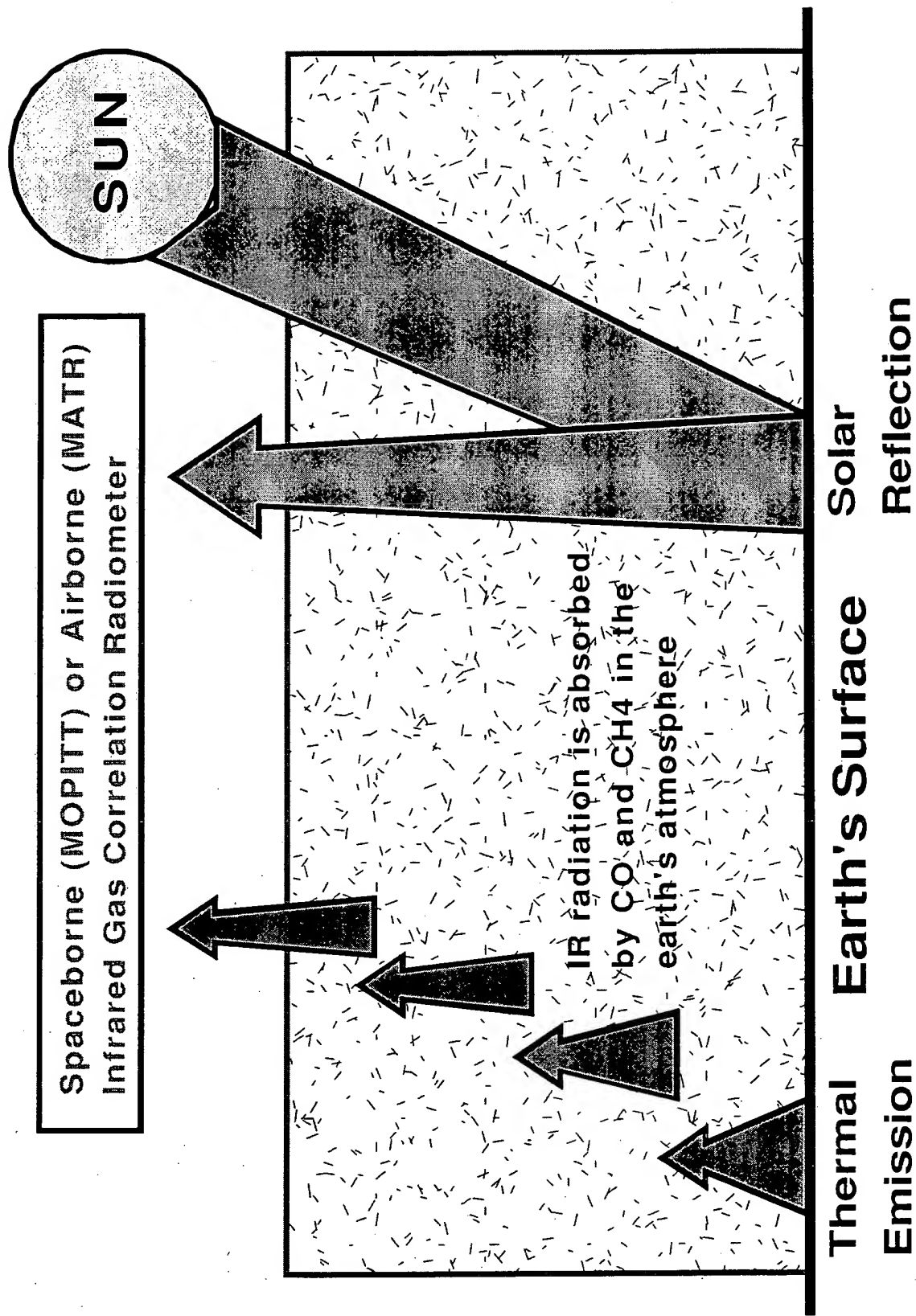


Figure A2: Atmospheric transmittance and radiance near 2.3 $\mu\text{m}$

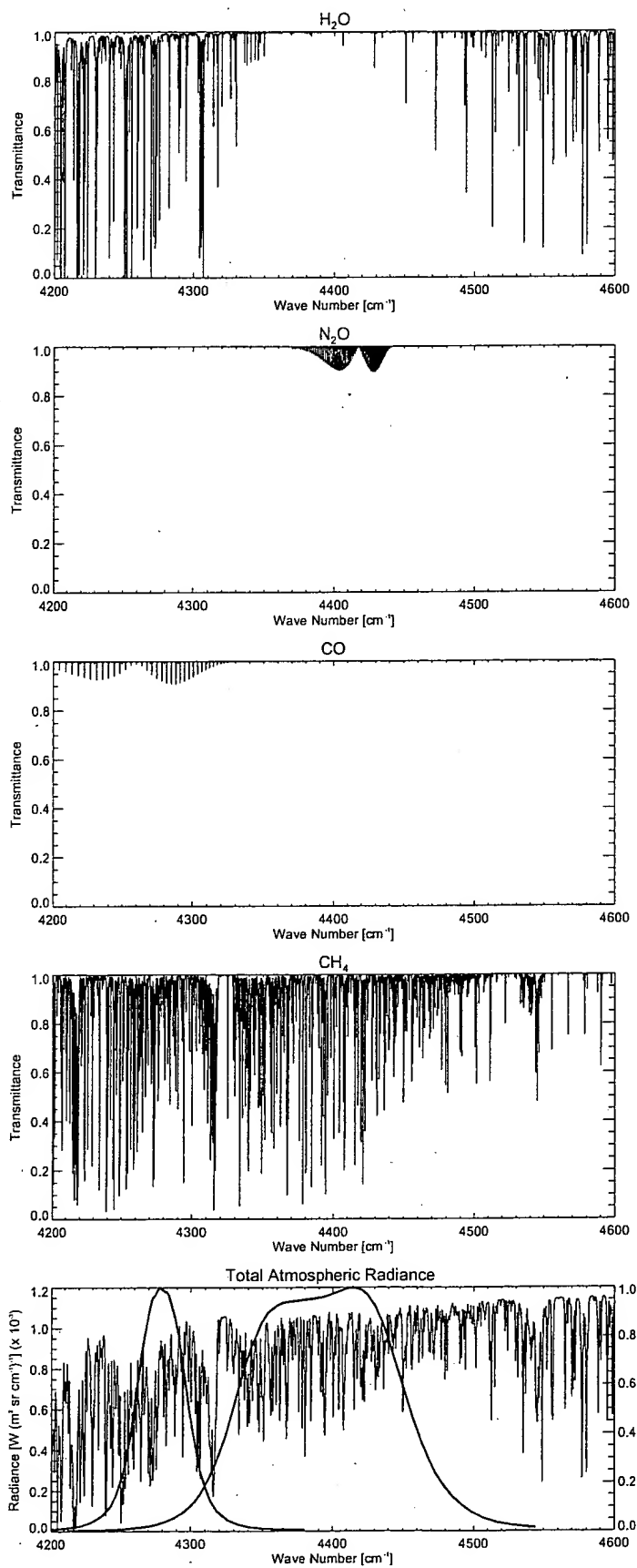




Figure A3: Atmospheric transmittance and radiance near 4.6 $\mu\text{m}$

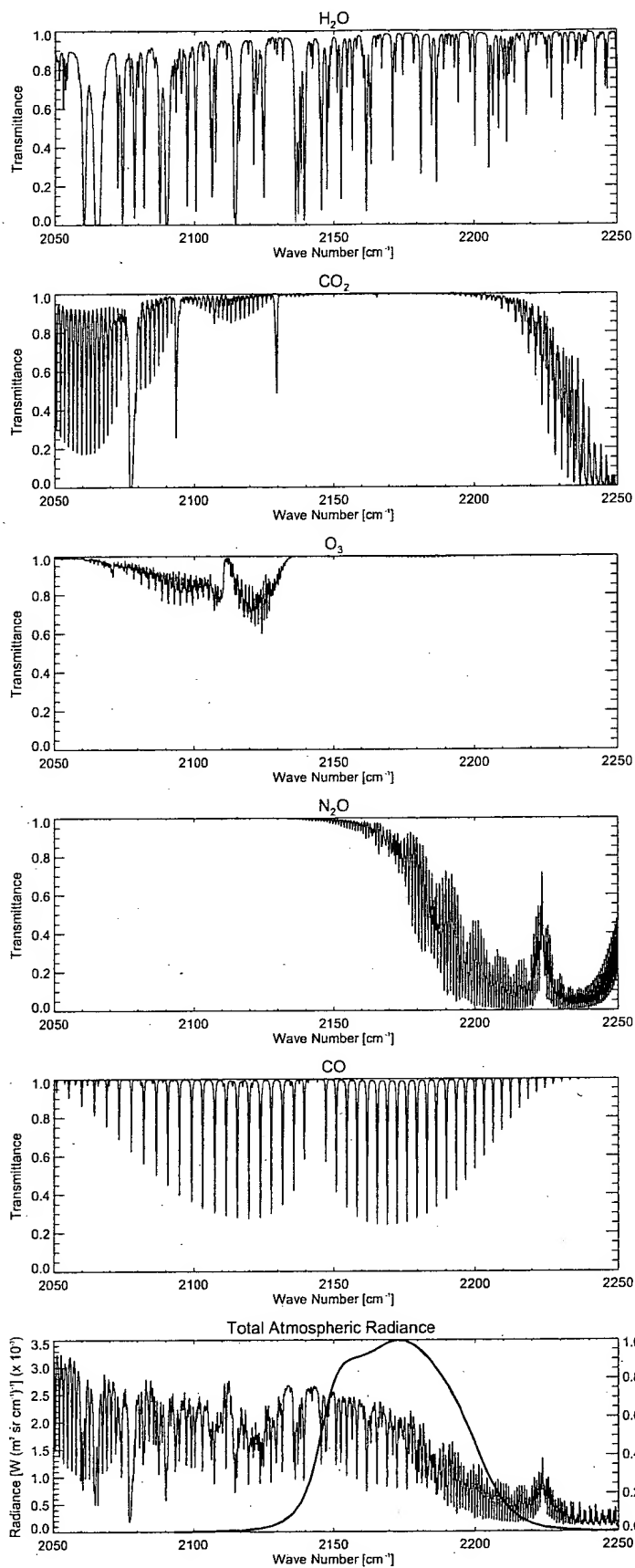


Figure A4: Top view of MATR optical table

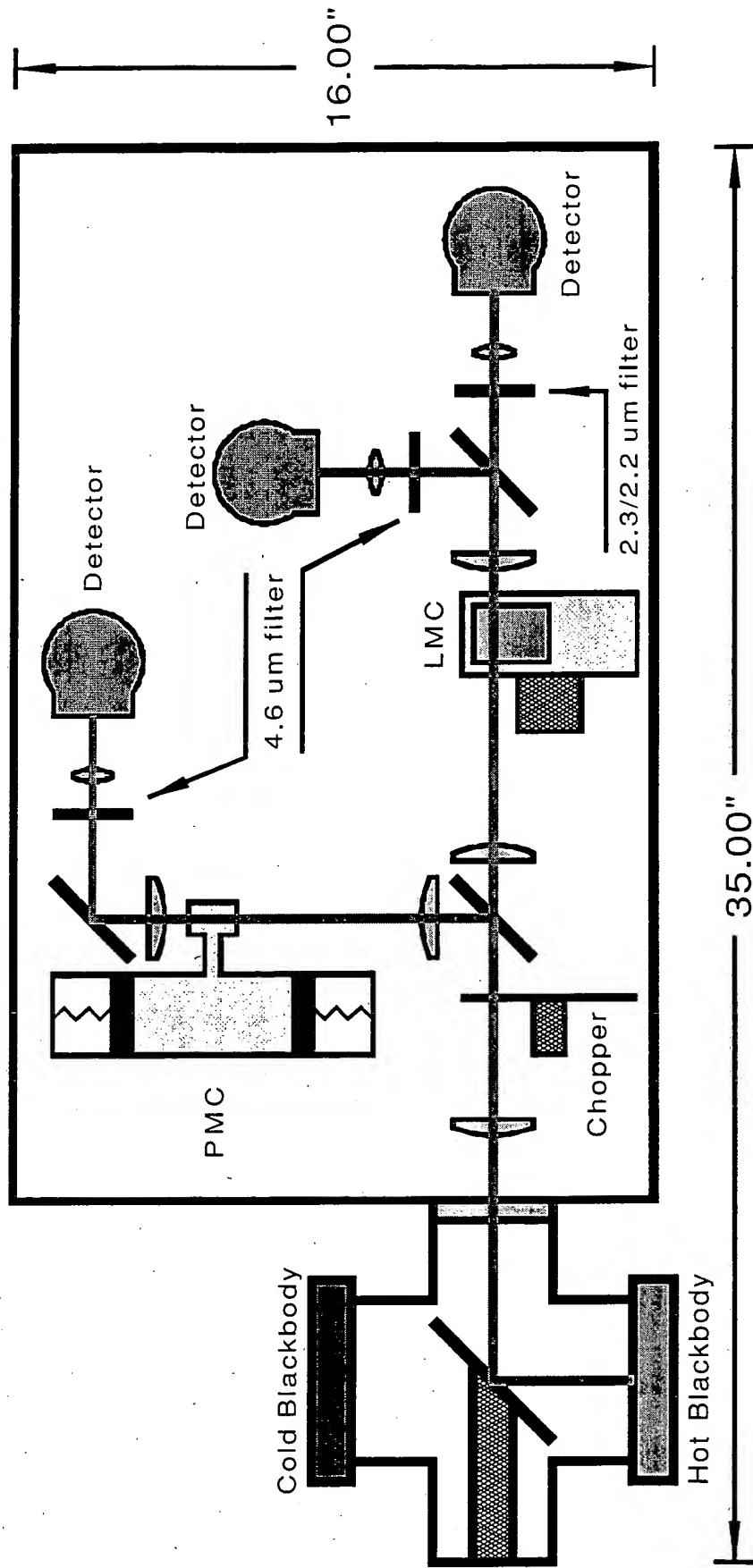


Figure A5: DOE Cessna Citation II aircraft

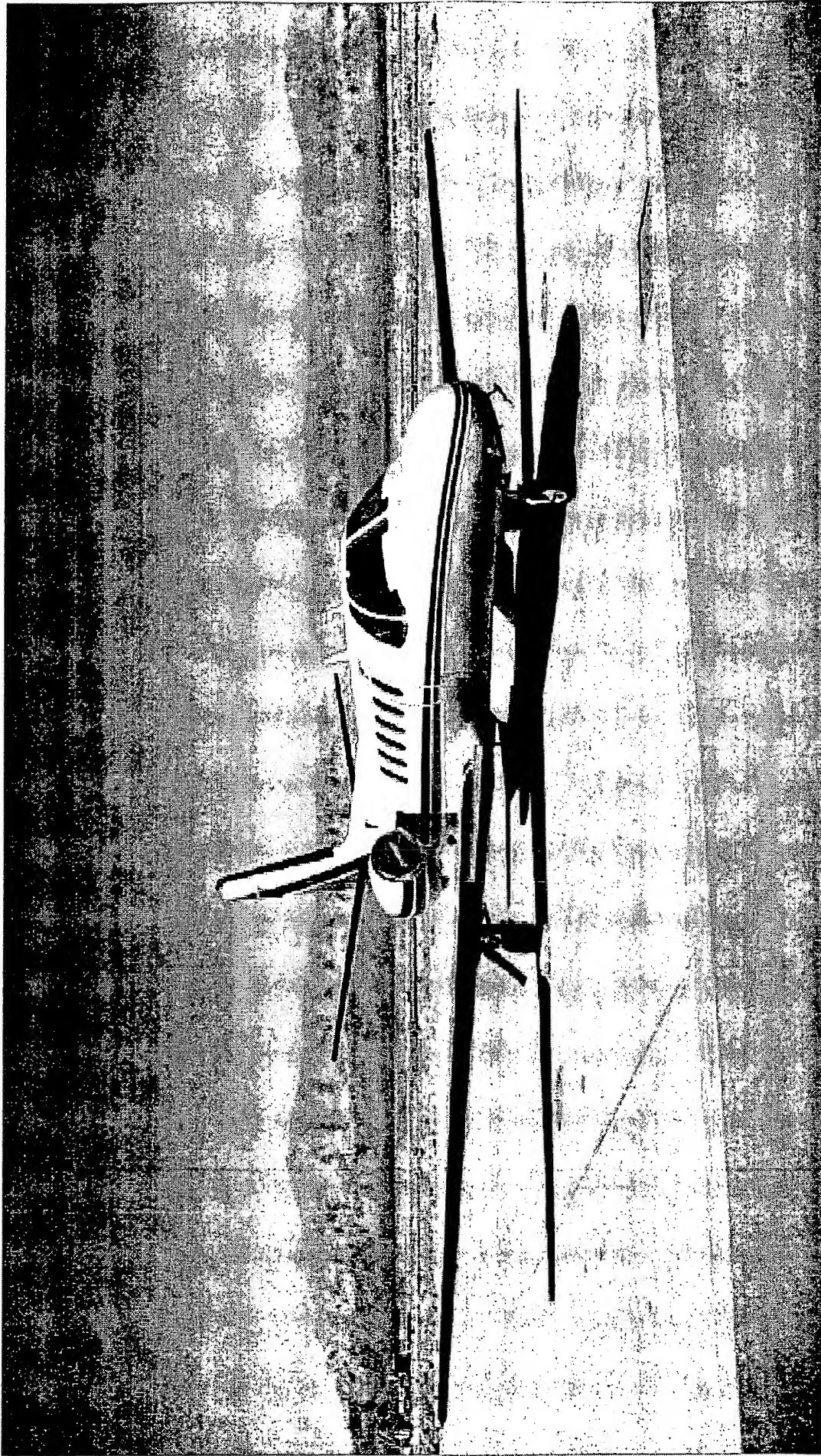


Figure A6: COL\_LMC\_AV\_80.36

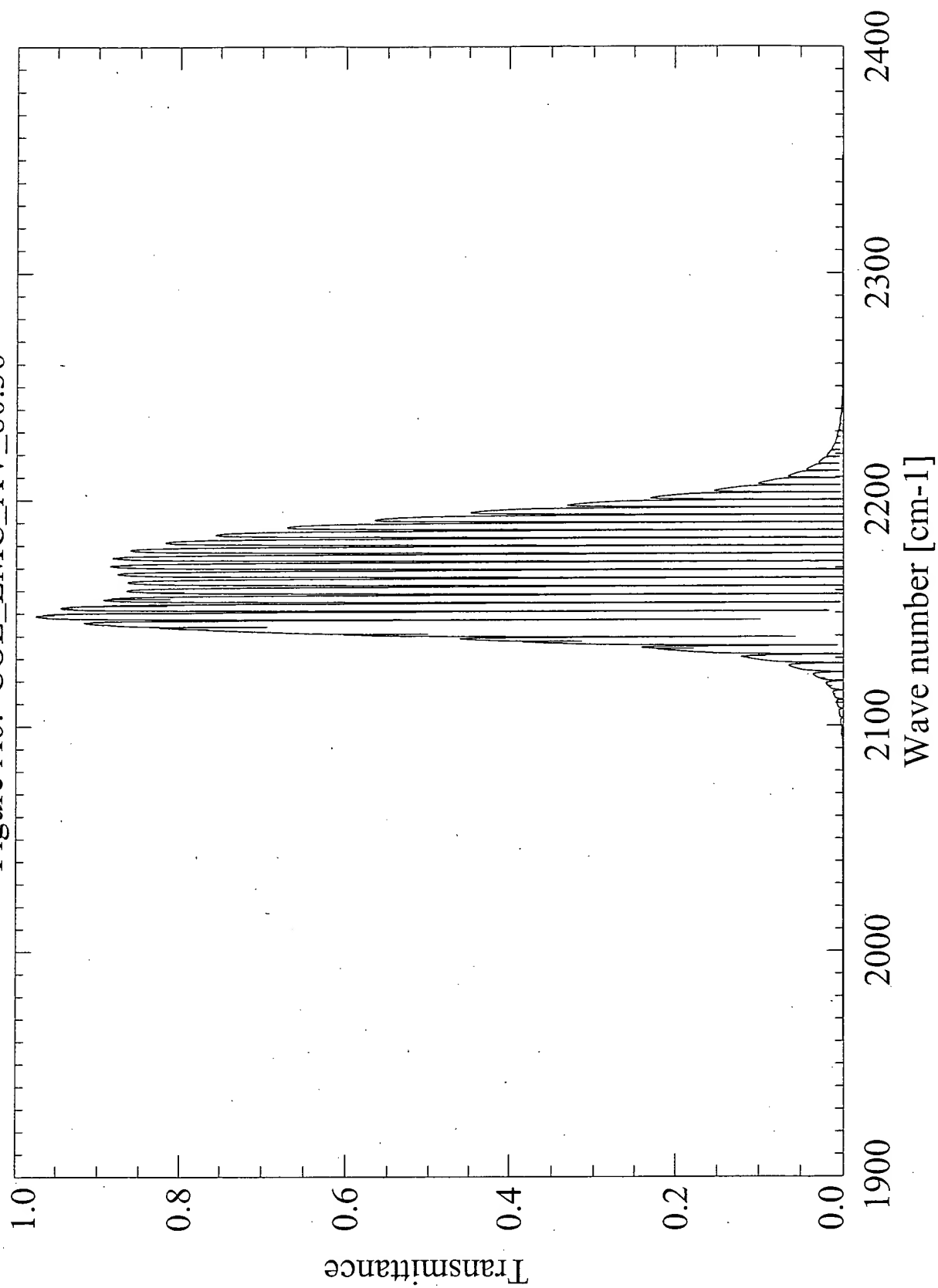
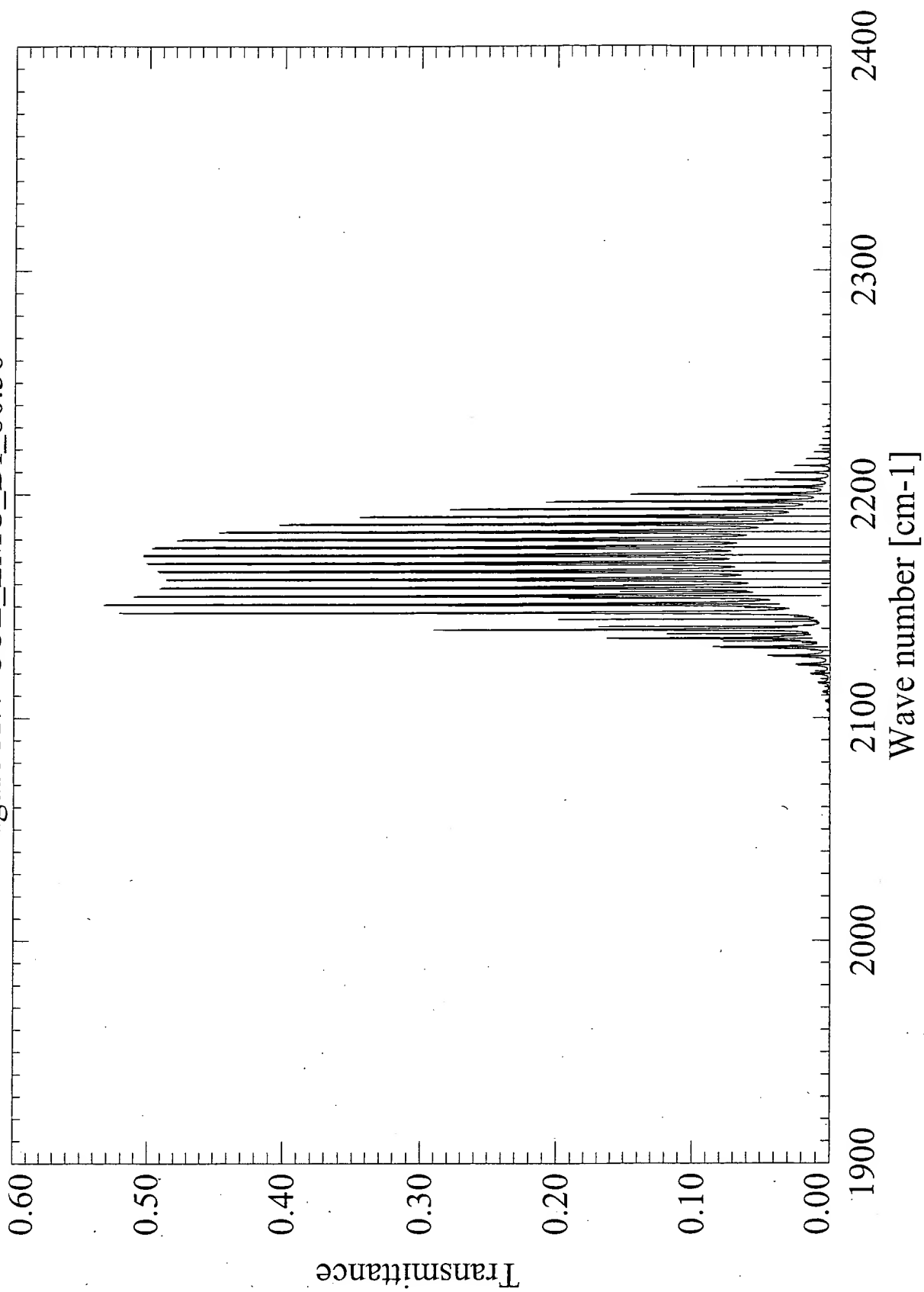


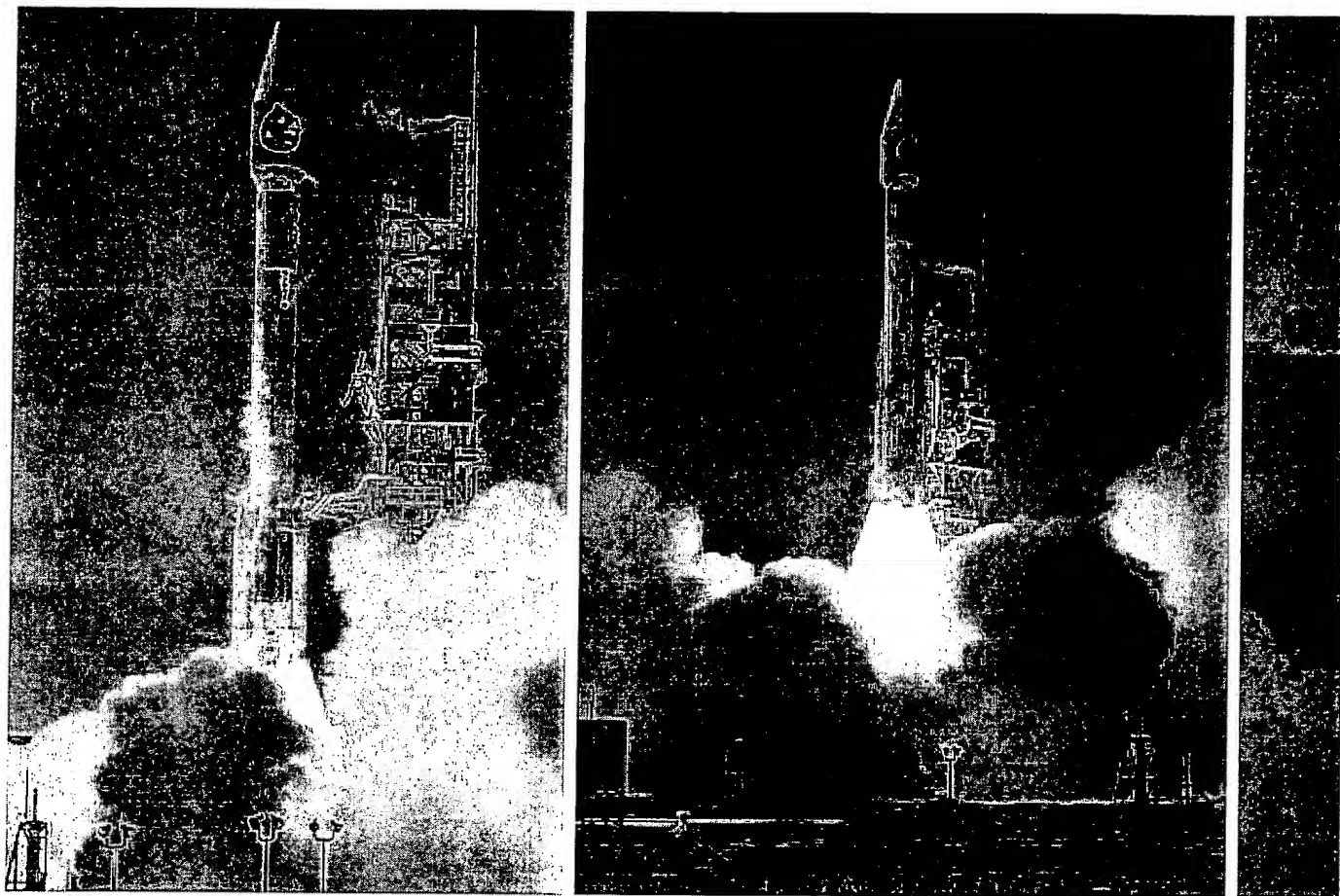
Figure A7: COL\_LMC\_DI\_80.36

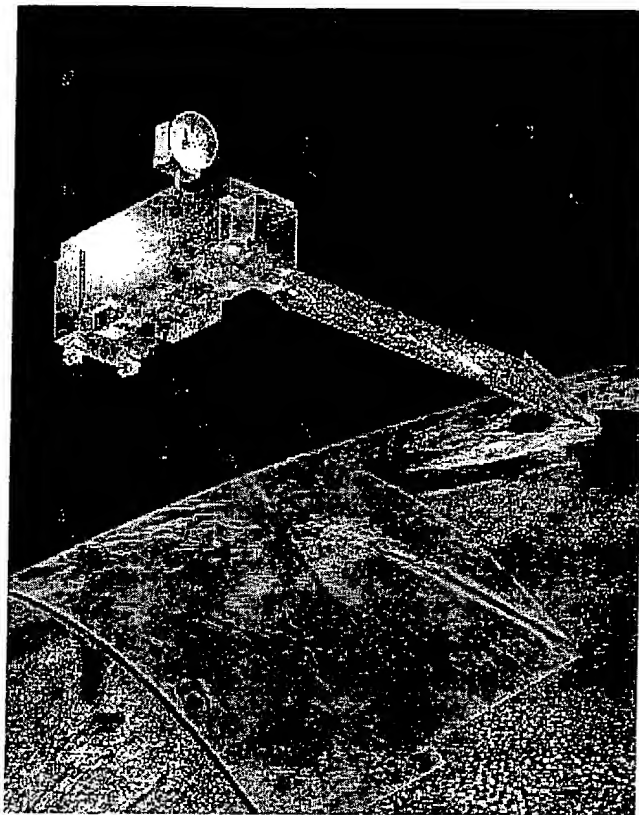


# Measurements Of Pollution In The Troposphere

---







# Instrument Description Document (SC October 1993)

~~NEW~~

~~NEW~~

1. Introduction

2. Instrument Description

3. Instrument Performance

4. Instrument Calibration

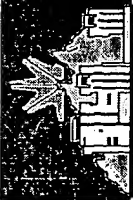
5. Instrument Data Products

6. Instrument Maintenance

7. Instrument History

8. Instrument Future Plans





<http://eos.acd.ucar.edu/mopitt>



## MOPITT Project

- **Mission:** The Measurements of Pollution in the Troposphere (MOPITT) is an eight-channel gas correlation radiometer selected for the EOS Terra spacecraft. The goal of the experiment is to support studies of the oxidizing capacity of the lower atmosphere on large scales by measuring the global distributions of carbon monoxide (CO) and methane (CH<sub>4</sub>) and, thus, will represent a significant advancement in the application of space-based remote sensing to global pollution and tropospheric chemistry research.

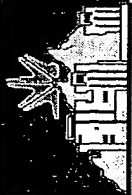
- **International Collaboration:** MOPITT is a collaboration between U. S. and Canada. Canada team provides the instrument. U. S. team is responsible for data processing.

- **NCAR MOPITT Team:**

Jinxue Wang - MOPITT Project Leader, Co-I  
Guy Brasseur - ACD Director, MOPITT Co-I  
Steve Carson - software engineer  
Charles Cavanaugh - software engineer  
Cheryl Craig - software engineer  
Merritt Deeter - scientist  
David Edwards - scientist  
Gene Francis - scientist  
Boris Khattatov - scientist

John Gille - U. S. MOPITT P.I.  
Daniel Ziskin - Data Manager  
Jean-Francois Lamarque - scientist  
Leslie Mayer - software engineer  
Steve Shertz - scientist  
Mark Smith - scientist  
Daniel Packman - software engineer  
Juying Warner - scientist  
David Grant - graduate student

11/18/99

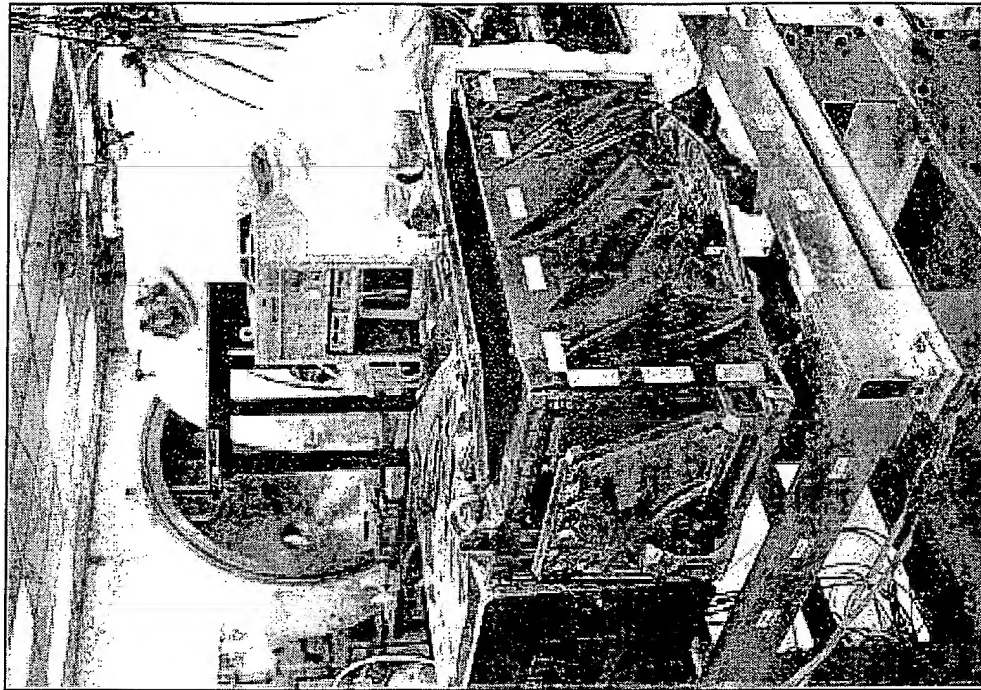


<http://eos.acd.ucar.edu/mopitt>



## MOPITT Data Products

- MOPITT measures the absorption and emission of thermal and solar radiation by atmospheric carbon monoxide (CO) and methane ( $\text{CH}_4$ ) molecules.
- These measurements can be used to derive global distribution of troposphere CO profiles and  $\text{CH}_4$  total column through the retrieval process using complex algorithms.
- Standard MOPITT CO and  $\text{CH}_4$  Products
  - > CO mixing ratios at 7 tropospheric pressure levels with a nominal horizontal resolution of  $22\text{km} \times 22\text{km}$ : surface, 850 mb, 700 mb, 500 mb, 350 mb, 250 mb, 150 mb.
  - >  $\text{CH}_4$  total column.



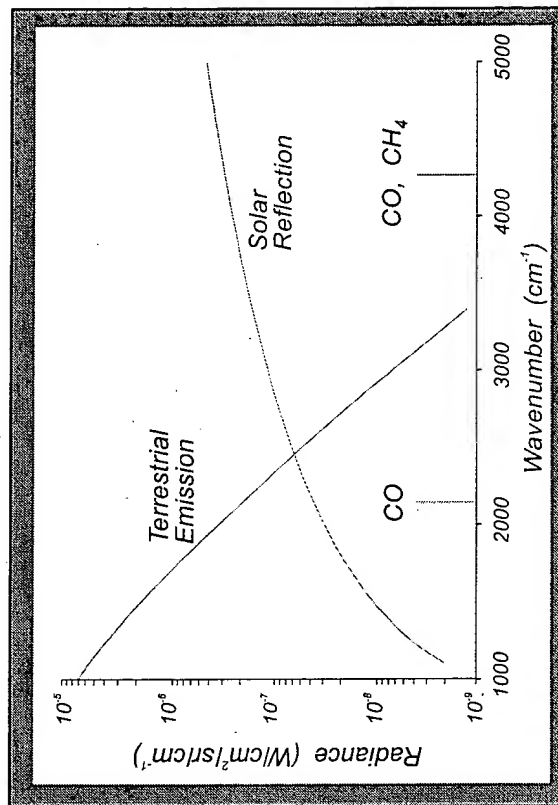
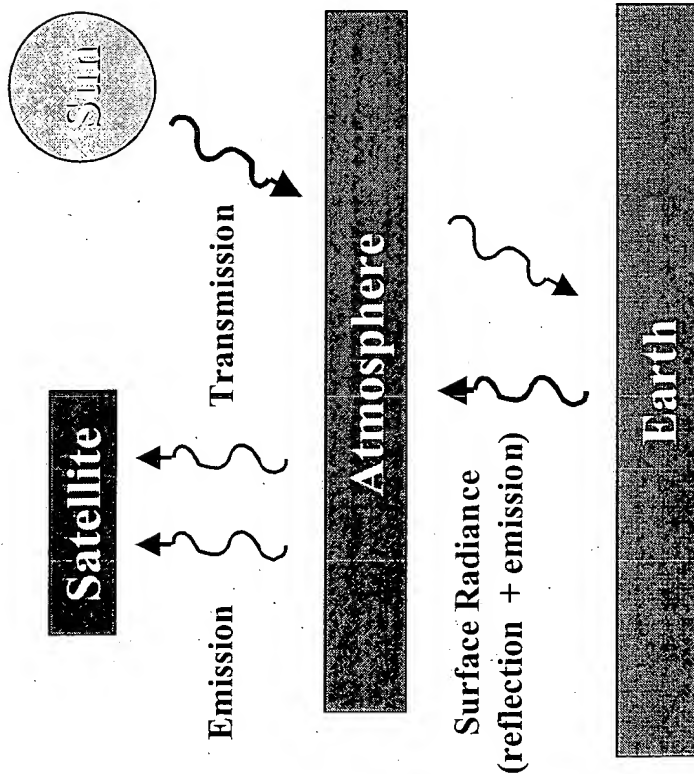
MOPITT at University of Toronto testing facility.



<http://eos.acd.ucar.edu/mopitt>



## MOPITT Technique and Spectral Bands



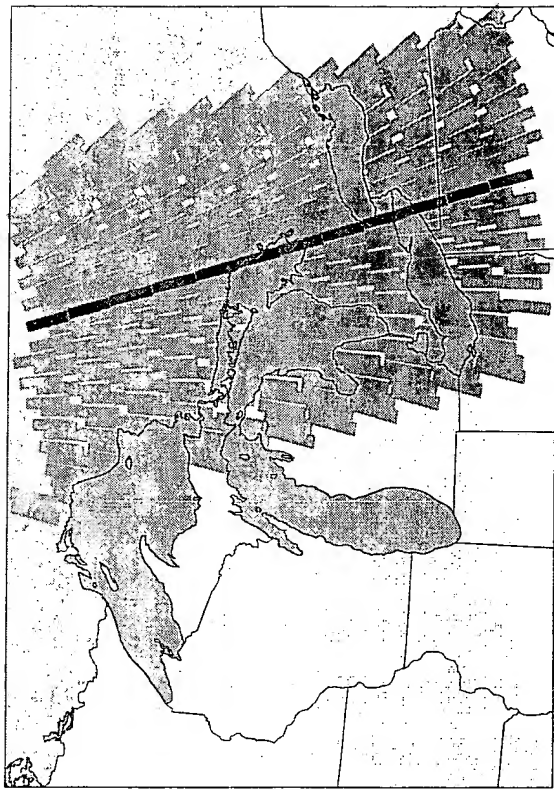
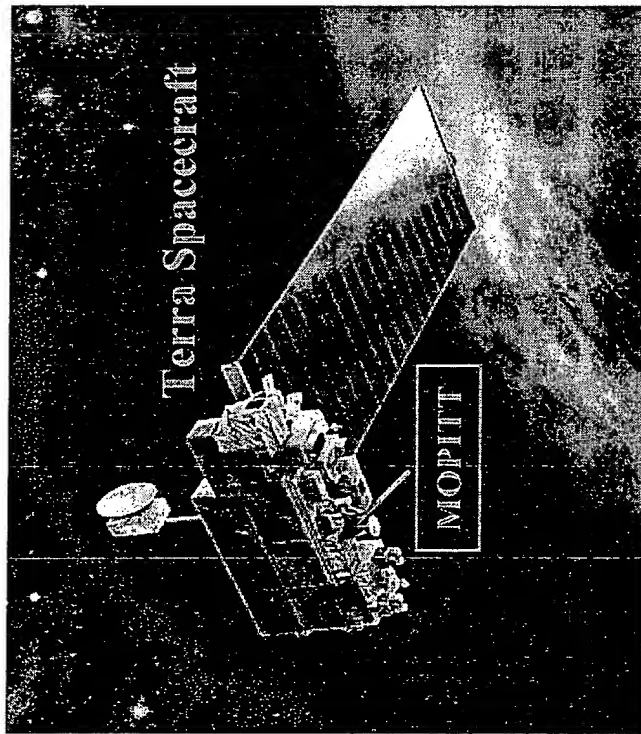
- MOPITT operates by sensing infra-red radiation from either:
  - > The thermal emission/absorption at 4.7  $\mu m$  for CO profiles.
  - > Reflected sunlight at about 2.2-2.4  $\mu m$  for CO and CH<sub>4</sub> column measurements in daylight. The use of solar channels enhances the instrument sensitivity to the atmosphere boundary layer.
- The radiation is modified by absorption/emission processes in the atmosphere and these changes are detected in the MOPITT instrument using Correlation Radiometry (CR) techniques



<http://eos.acd.ucar.edu/mopitt>



## EOS Terra Spacecraft and MOPITT Coverage



Close-up look of MOPITT footprints at U. S. and Canada border in the great lakes region.

- EOS Terra is the first of a series of satellites dedicated to observing the Earth and the atmosphere. It has a nominal orbit altitude of 705 km, an inclination of  $98.2^\circ$ , and an equator crossing time of 10:30 AM.
- MOPITT scans across Terra ground track with 29 pixels in each scan line. The maximum scan angle is  $26.1^\circ$  off -axis, which leads to a swath width of 640 km.



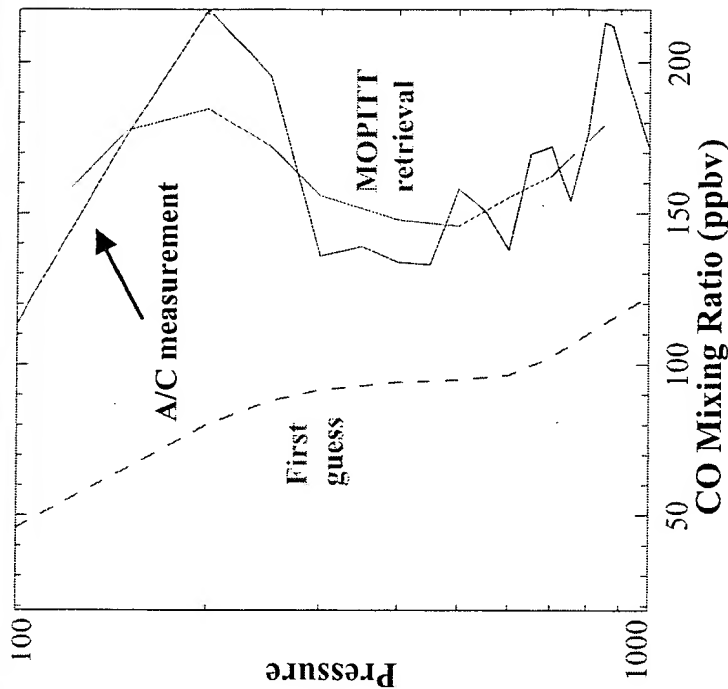
<http://eos.acd.ucar.edu/mopitt>



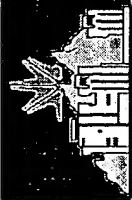
## MOPITT Troposphere CO Retrieval: A Simulation



Biomass burning in South America during NASA GTE TRACE-A experiment (courtesy of Ken Pickering and Anne Thompson).



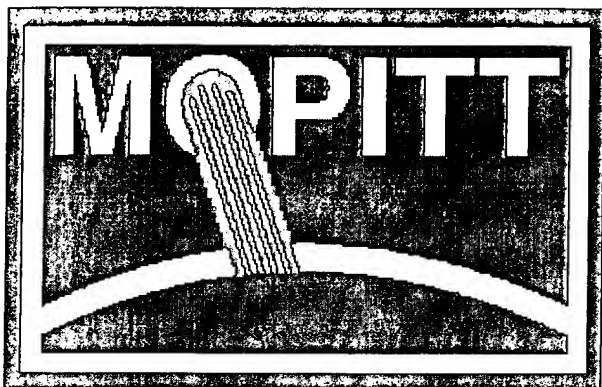
- MOPITT retrieval simulation using aircraft *in situ* CO profiles taken during NASA GT TRACE-A experiment in South America and Africa. About 10-40% of CO emitted by biomass fires in a typical burning season over Brazil would be vented out to the free troposphere by deep convect ion.
- In the figure on the right. The blue line with sharp CO gradient is a typical airborne *in situ* CO profile during TRACE-A. The sharp CO gradients are the results of biomass burning CO emission and strong convection in this region. The dash green line is the retrieval first guess. The red line is the retrieved CO profile using simulated MOPITT measurement.



## References and Additional Information on MOPITT

- Drummond, J. R., 1992: Measurements of Pollution in the Troposphere (MOPITT). *The use of EOS for Studies of Atmospheric Physics*, J. Gille and G. Visconti, Eds., North Holland, 77-101.
- Drummond, J. R., and G. S. Mand, 1996: The measurement of pollution in the Troposphere (MOPITT) instrument: overall performances and calibration requirements," *J. Atmos. Oceanic. Technol.*, **13**, 314-320.
- Pan, L., J. C. Gille, D. P. Edwards, P. L. Bailey, C. D. Rodgers, 1998: Retrieval of tropospheric carbon monoxide for the MOPITT experiment. *J. Geophys. Res.*, **103**, 32,277- 32,290.
- Wang, J., J. C. Gille, P. L. Bailey, J. R. Drummond, and L. Pan, 1999: Instrument sensitivity and error analysis for the remote sensing of tropospheric carbon monoxide by MOPITT. *J. Atmos. Oceanic. Technol.*, **16**, 465-474.
- Wang, J., J. C. Gille, P. L. Bailey, L. Pan, D. Edwards, and J. R. Drummond, 1999: Retrieval of tropospheric carbon monoxide profile from high resolution interferometer observations: a new digital gas correlation (DGC) method and applications. *J. Atmos. Sci.*, **56**, 219-232.
- NASA EOS project homepage: <http://eosps0.gsfc.nasa.gov/>
- University of Toronto MOPITT homepage: <http://www.atmosp.physics.utoronto.ca/MOPITT/>





## Measurements Of Pollution In The Troposphere

The MOPITT instrument is scheduled for launch on the AM-1 platform of NASA's Earth Observing System (EOS). The AM-1 satellite will be placed in a 705km, sun-synchronous orbit with a 10:30am equator crossing time. MOPITT will measure carbon monoxide and

methane in the troposphere over the entire globe for a period of five years.

Despite the fact that we all live in the troposphere, monitoring of the tropospheric composition from space has lagged considerably behind our monitoring of the upper regions of the earth's atmosphere mainly because of the technical difficulty of such measurements. The presence of the earth's surface provides considerable interference to most measurement methodologies and the presence of clouds further impedes the mission. Overcoming these problems requires a very precise instrument with a very high performance.

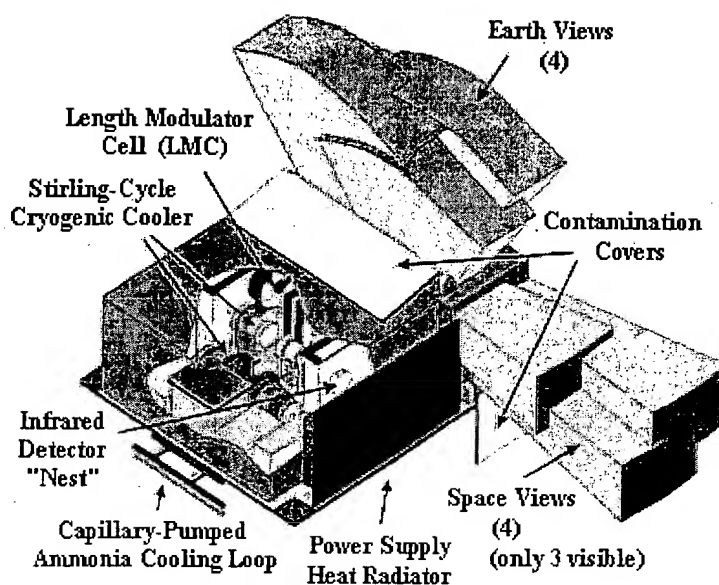
We want to monitor carbon monoxide and methane because they will help us understand how the troposphere reacts to various stimuli. These can range from natural phenomena such as the growth of forests, through agricultural sources such as rice paddies, to catastrophic events such as biomass burning. Most of these sources can, and indeed are, being modified by human activity on the planet.

Carbon monoxide is particularly interesting because of its potential for showing us how chemicals are transported in the troposphere as well as giving us information about chemical reactions in the troposphere.

Measurements have already shown us the production of carbon monoxide in biomass burning and its transport by atmospheric circulation systems. This needs to be understood on a global scale and incorporated into models of tropospheric transport.

Methane is a greenhouse gas and the major issue here is its source strength. There are a large number of potential sources, such as northern wetlands, ruminant animals, and natural gas leakage. However the actual strength of the individual sources is very poorly known. Since methane's greenhouse effect is far stronger than that of the better known carbon dioxide, changes in methane, although small in themselves, can potentially have a significant effect on the overall climate system.

Measurements of these gases are made by intercepting the infra-red radiation coming from the planet and then isolating the required signals. MOPITT is a nadir sounding instrument since this gives the maximal chance of avoiding cloud features, but this implies that it can "see" the surface of the planet and the desired signals must be seen against the background of the surface radiation. The field-of-view of MOPITT is 22 x 22km and it views four fields simultaneously by the use of a 4 x 1 array of detector elements. The field of view is also continuously scanned through a swath about 600km wide as the instrument moves along the orbit increasing both the spatial coverage of the instrument and the chance of finding gaps in the cloud coverage.

**MOPITT Instrument**

The MOPITT instrument makes use of the principle of correlation spectroscopy whereby a cell of the gas to be measured is used as an optical filter in the infra-red to measure the signal from the same gas in the atmosphere. The amount of gas in the instrument cell is modulated by varying either the pressure or the length. In addition to the correlation technique MOPITT makes use of mechanically cooled detectors and filters (at 100K) to enhance the overall performance. The use of this cooling technique, which relies on Stirling Cycle coolers supplied by British Aerospace, is relatively new in satellite instrumentation having been used on only two civilian satellite instruments before. The use of mechanical cooling rather than stored cryogen or radiative cooling permits a relatively large amount of cooling - sufficient for both the detectors and the filter systems - whilst still permitting a five year instrument life.

The MOPITT science team is international, having members from Canada, the United States and the United Kingdom. The instrument itself is being constructed by a consortium of Canadian companies: COMDEV Atlantic of Moncton, BOMEM from Quebec City, Hughes-Leitz from Midland and SED from Saskatoon. The instrument is funded by the Space Science Division of the Canadian Space Agency. The instrument will be tested in the University of Toronto.

MOPITT completed its Preliminary Design Review in December 1993 and the Critical Design Review is scheduled for April 1995. Instrument delivery will be late in 1996 and the launch of the AM-1 platform will be in mid- 1998. Discussions are under way regarding a second copy of the instrument to be launched in the 2003 time frame to permit the dataset of carbon monoxide and methane to be extended to ten years to look for long term effects.

#### MOPITT science team

---

**MOPITT is funded by the  
Canadian Space Agency.**

---

**MOPITT Prime Contractor  
COM DEV Atlantic of Moncton, NB**



---

**For further information about MOPITT, contact:**

*Prof. James R. Drummond  
Department of Physics  
University of Toronto  
60 St. George Street,  
Toronto, Ontario,  
CANADA M5S 1A7  
([jim@atmosp.physics.utoronto.ca](mailto:jim@atmosp.physics.utoronto.ca))*

---

*Last updated August 2, 1995*

## Measurement of Pollution in The Troposphere (MOPITT)

The Measurement Of Pollution In The Troposphere (MOPITT) is a joint Canadian-US development of an experiment to measure and interpret the global distributions of tropospheric carbon monoxide and methane, and thus to support studies of the oxidizing capacity of the lower atmosphere on large scales. This will represent a significant advancement in the application of space-based remote sensing to global tropospheric chemistry research. James Drummond (University of Toronto) is the Principal Investigator for the Canadian-built instrument; the Science Team includes ACD members John Gille (US PI), Guy Brasseur and Jinxue Wang. ACD Science Team member Paul Bailey retired from NCAR at the end of 1998. Additional team members include Gary Davis (University of Saskatchewan), Gurpreet Mand (University of Toronto), John McConnel (York University), Guy Peskett (Oxford University), Henry Reichle (North Carolina State University), and Nigel Roulet (McGill University). More information about the MOPITT project can be found at <http://www.atmosp.physics.utoronto.ca/MOPITT/home.html> and <http://www.eos.ucar.edu/mopitt/>.

The MOPITT launch on NASA's Earth Observing System (EOS) Terra platform is scheduled for December 1999 after a extended delay due to flight software and launch vehicle problems.

### MOPITT Retrieval Algorithm Development and Validation

Gille organized a special session on MOPITT at the SPIE conference in Denver in July, under the topic of Optical Spectroscopic Techniques and Instrumentation for Atmospheric and Space Research III. He has put special emphasis on understanding the calibration data, especially the measurements of external gas cells that simulate the atmospheric observing situation.

Merritt Deeter and Wang completed the re-design and coding of the MOPITT Level 1-2 algorithms to retrieve tropospheric CO profiles and CH<sub>4</sub> column from MOPITT radiance observations. New features include explicit inclusion of forward model error, explicit inclusion of ancillary data error, new *a priori* data, and new diagnostic tools. Extensive algorithm tests and retrieval simulations have been conducted. The algorithm features and simulation results were presented at the SPIE conference in Denver, and published in the proceedings, Optical Spectroscopic Techniques and Instrumentation for Atmospheric and Space Research III.

Wang collaborated with Cathy Clerbaux (Service'd Aeronomie du CNRS, France) in a CO retrieval intercomparison. Four CO retrieval algorithms were compared. The results were published in the *Proceedings of the 8th International Workshop on Atmospheric Science from Space using Fourier Transform Spectrometry (ASSFTS)*, Toulouse, France, 16-18 November 1998. Wang also continued the development and application of the Digital Gas Correlation (DGC) method for the retrieval of tropospheric trace species from high resolution interferometer measurements. A paper summarizing the validation study of the MOPITT retrieval algorithm from IMG observations during WINCE was accepted for publication in the *Journal of Atmospheric and Oceanic Technologies*.

MOPITT team member, Steve Carson, has completed the development of a fast regression based CO and CH<sub>4</sub> retrieval algorithm. Deeter, Wang and Gille contributed to the development of the regression algorithm. The main purpose of the regression algorithm is to provide first-look CO and CH<sub>4</sub> products and generate first guesses for the subsequent maximum likelihood based retrieval algorithm.

David Edwards and Gene Francis developed an improved version of the MOPABS forward model,

incorporating improved accuracy at large zenith angles, a frequency-dependent solar spectral envelope, and channel calculations for the MODIS Airborne Simulator (MAS). A new infrared radiative transfer technique extending the correlated-k method was developed. It allows a general spectral filter to be incorporated into the calculation of band averaged transmittances, with a wide range of applications: the inclusion of an instrument response filter; accounting for the spectral variation of the thermal emission across a channel passband; and allowing for a source function spectrum such as absorption lines in the solar irradiance. A computer model incorporating these developments (and the MOPABS improvements mentioned above) has been written and applied to the calculation of MOPITT channel radiances. These works were reported in a paper published in the proceedings of *Optical Spectroscopic Techniques and Instrumentation for Atmospheric and Space Research III* and another paper submitted for publication in the *Journal of Geophysical Research*.

Juying Warner continued the development and test of MOPITT cloud detection and clearing algorithms. She validated the MOPITT cloud detection thresholds with aircraft measurements from MAS and MATR programs. Warner also studied CO retrieval errors introduced by MOPITT cloud detection and clearing algorithms. These works were reported in two conference papers published in the proceedings of *Optical Spectroscopic Techniques and Instrumentation for Atmospheric and Space Research III* and another paper to be submitted.

## **MOPITT Data Validation Plan and Activities**

The analysis of data from the first MOPITT intercomparison campaign called the Pre-launch MOPITT Validation Exercise (Pre-MOVE) conducted from March 2 to March 6, 1998 at the Department of Energy (DOE) Atmospheric Radiation Measurement (ARM) CART site in Oklahoma was completed by the MOPITT validation team. The results were summarized in an article entitled "The Pre-launch MOPITT Validation Exercise (Pre-MOVE)" published in *The Earth Observer*, Vol. 11, No. 1, January/February 1999.

MOPITT instrument and correlative team members have actively participated in the planning of the SAFARI-2000 mission in South Africa for AM-1 validation in 1999 and 2000. Wang participated in two SAFARI-2000 planning workshops, one at NCAR in May 1999, and the other at the University of Botswana in July 1999. Wang worked with the NASA EOS Validation Scientist, David Starr, in the evaluation of MOPITT validation investigations.

## **MOPITT Airborne Test Radiometer (MATR)**

Mark Smith, Steve Shertz and Nuri Delen made a variety of improvements to the MATR instrument, most importantly in the areas of thermal control and data acquisition software. They conducted a set of flights with the MATR instrument in January and February 1999. These flights demonstrated the improved thermal performance. An overpass with exact time and space coincidence with NOAA CMDL in situ CO profile measurements was achieved at the Carr, Colorado site. Various retrievals of CO weighted column amounts using the 1999 flight data were performed, but the results indicated the need for better instrument characterization. They built equipment for various laboratory tests and calibrations of the MATR instrument, and conducted a variety of lab tests and calibrations with MATR. The MATR project also hosted Katherine Paulin (graduate student, Oxford University) from June to mid-August, 1999. She made a variety of laboratory test measurements with the MATR pressure modulator cell (PMC). She also worked on analyzing the PMC pressure and temperature cycles, and on retrieving CO amounts from the PMC flight data. A poster describing MATR was presented at the Fall AGU conference in San Francisco in December 1998 and another poster describing MATR at the Fourth International Airborne Remote Sensing

Conference in Ottawa in June 1999. Some of their work was also reported in a paper published in the proceedings of *Optical Spectroscopic Techniques and Instrumentation for Atmospheric and Space Research III*.

## Modeling and Data Assimilation

Guy Brasseur, Boris Khattatov and Jean-Francis Lamarque, continued the development of 3-D tropospheric chemical and transport models for tropospheric chemistry studies and future MOPITT data interpretation. They have implemented a data assimilation algorithm using simulated MOPITT CO measurements and performed a number of successful experiments with these simulated measurements.

Lamarque and Khattatov modified the data assimilation algorithm for use with MAPS total column CO measurements and successfully assimilated the Measurement of Air Pollution from Space (MAPS) CO observations. The results were reported in a paper to be published in the *Journal of Geophysical Research* (in press). Khattatov developed and implemented a sequential assimilation scheme for assimilation of simulated MOPITT data in the 3-D CTM MOZART 2. Khattatov also collaborated with Clerbaux, who applied the technique for analysis and gridding of IMG CO observations. Their works were reported in several publications in the *Geophysical Research Letters* and the *Journal of Geophysical Research*.

# Assimilation of carbon monoxide measured from satellite in a three-dimensional chemistry-transport model

Cathy Clerbaux, Juliette Hadji-Lazaro, Didier Hauglustaine and Gérard Mégie  
Service d'Aéronomie, Institut Pierre-Simon Laplace, Paris, France

Boris Khattatov and Jean-François Lamarque  
National Center for Atmospheric Research, Boulder, CO

Short title: ASSIMILATION OF CO FROM SATELLITE

**Abstract.** Carbon monoxide measurements are obtained from the analysis of the spectra provided by the Interferometric Monitor for Greenhouse Gases (IMG) instrument, which flew on-board the Japanese ADEOS satellite. The averaging kernel function of the instrument, which provides the sensitivity of retrieved CO to the vertical atmospheric layers, is calculated. A sequential assimilation approach is used to incorporate this CO dataset, along with a detailed associated error budget, into a global three-dimensional chemistry-transport model (MOZART version 2). We show how data assimilation allows to highlight the differences between modeled and observed CO global distribution. Surface CO mixing ratios computed after assimilation of total columns provided by the IMG instrument are compared with the NOAA/CMDL in-situ measurements and a good agreement is found between the two datasets.

## 1. Introduction

Large uncertainties remain on the estimated strengths of tropospheric sources and sinks and global budget of ozone ( $O_3$ ), carbon monoxide (CO) and methane ( $CH_4$ ) [Brasseur *et al.*, 1999]. These three compounds are strongly coupled through chemical reactions involving the hydroxyl radical (OH), and their global distributions are correlated with anthropogenic emissions. A change in the concentration of one of these species modifies the oxidizing capacity of the troposphere and therefore affects the lifetimes and abundances of many other trace gases [Gupta *et al.*, 1998].

Satellite measurements performed by tropospheric remote sensors in the nadir geometry will provide unprecedented information on the key chemically and radiatively active species. Within ten years, several instruments have been or will be launched on polar-orbiting platforms, recording atmospheric spectra from which concentrations of trace gases that provide a significant absorption contribution may be retrieved. In the past, the Measurement of Air Pollution from Space (MAPS) experiment, which flew on-board the space shuttle, provided global coverage of CO for four specific periods [Connors *et al.*, 1999]. The Interferometric Monitor for Greenhouse Gases (IMG) which operated in 1996-1997 on the Japanese ADEOS platform was a forerunner of the next generation missions, recording high-resolution spectra from which infrared-absorbing molecules (e. g.  $H_2O$ ,  $O_3$ , CO,  $CH_4$ ,  $N_2O$ ) may be retrieved [Kobayashi *et al.*, 1999a]. The Measurements Of Pollution In The Troposphere (MOPITT) instrument [Drummond and Mand, 1996] was launched in December 1999 on-board the EOS-TERRA platform

and provides global distribution of CO and CH<sub>4</sub>. In the future, the SCanning IMaging Absorption spectrometer for atmospheric CartograpHY (SCIAMACHY) [Bovensmann *et al.*, 1999] on-board ENVISAT, the Infrared Atmospheric Sounding Interferometer (IASI) [Cayla and Javelle, 1995] on the METOP platform, and the Tropospheric Emission Spectrometer (TES) [Beer and Glavich, 1989] on EOS-AURA will also provide measurements for the main trace gases.

These remote sensors are built using different technologies (gas correlation, radiometer, Fourier transform spectrometer) and provide measurements with different spatial and temporal samplings. Data assimilation is a powerful tool for analysis of observations provided by instruments that differ in nature, resolution and accuracy, and distributed irregularly in time and space. This technique also allows to efficiently compare remotely sensed data with in-situ data. As large amounts of new data become available from satellite missions, several chemical assimilation schemes are currently developed to analyze the available data or prepare the future missions. Recent papers describe how tropospheric data assimilation can improve our knowledge on the distribution of ozone [Jeuken *et al.*, 1999; Elbern and Schmidt, 1999] and carbon monoxide [Lamarque *et al.*, 1999].

This paper presents an integrated approach to study the global distribution of CO, combining measurements provided by a remote sensor with model results using data assimilation techniques. The first part of the paper is focused on the description of the IMG instrument and the retrieval of CO data for June 1997, and the averaging kernel function associated with the inversion is calculated (section 2). Section 3 provides a



short description of the chemistry-transport model used. Details of assimilation theory and the obtained results are provided in section 4.

## 2. IMG Data

### 2.1. The IMG instrument

The IMG instrument was launched on-board the ADEOS satellite on August 17, 1996, and provided 10 months of data until the destruction of the platform solar paddle [Kobayashi *et al.*, 1999b]. IMG is a nadir looking Fourier transform spectrometer which recorded the thermal emission of Earth between 600 and 3030  $\text{cm}^{-1}$ , with a spectral resolution of  $\sim 0.1 \text{ cm}^{-1}$ . Due to the polar orbit of the satellite, the instrument provides a global coverage of the Earth, making  $14\frac{1}{4}$  orbits per day with series of six successive measurements each 86 km along the track, followed by the observation of deep space and of an internal blackbody for calibration purposes. The footprint on the ground is 8 km x 8 km, in three spectral bands corresponding to three different detectors.

### 2.2. CO measurements

From the spectra recorded by the instrument, the atmospheric constituents which present absorption bands within the thermal infrared spectral range may be retrieved. In the 2000-2500  $\text{cm}^{-1}$  spectral interval (IMG band 2), the strong CO 1-0 vibrational transition occurs, allowing the retrieval of atmospheric concentration for this molecule. The global distribution of CO total column amounts was obtained from the Level 1C data (version 5.6, provided by IMGDIS/ERSDAC), using a neural network inversion

approach developed at Service d'Aéronomie in the framework of IASI [Clerbaux *et al.*, 1995; Clerbaux *et al.*, 1998a]. A detailed description of the neural network inversion algorithm (version 1.0) and its performance are provided in Hadji-Lazaro *et al.* [1999], and intercomparison with other CO retrieval algorithms currently developed for MOPITT and IASI were undertaken [Clerbaux *et al.*, 1998b; Clerbaux *et al.*, 1999].

As reported in Clerbaux *et al.* [1999], one of the problems relative to the CO inversion from IMG spectra is the lack of complementary information on the cloud coverage. To obtain accurate and reliable CO data for the present study, a specific cloud filter that works in IMG band 2 (2000-2500  $\text{cm}^{-1}$ ) was developed to remove the pixels contaminated by the presence of clouds [Hadji-Lazaro *et al.*, 2000]. This cloud filter was built using coincident measurements of cloud cover fractions provided by the POLarization and Directionality of the Earth's Reflectance (POLDER) instrument [Parol *et al.*, 1999] that also flew on the ADEOS platform. Figure 1 presents the cloud-filtered CO global distribution as retrieved using the neural network algorithm for the June 16-19 period. This period was selected for the assimilation study because a good spatial coverage is obtained in four days and alignment problems which occurred at the beginning of the IMG mission were fixed at that time [Kobayashi *et al.*, 1999b]. The picture shows that, as expected, there is a strong gradient of CO concentration between the northern and the southern hemisphere. High total column values (more than  $2 \cdot 10^{18}$  molecules/ $\text{cm}^2$ ) are found where high levels of industrial activity (North America, Europe and Asia) and biomass burning (Africa, Asia) occur.

### 2.3. Data accuracy

In a sequential data assimilation approach, each data (measured or modeled) is weighted according to the confidence we have for this value. A detailed error budget on the measured CO column amounts, which accounts for the quality of the signal and the performance of the retrieval algorithm, was calculated for each data point.

**2.3.1. Retrieval error.** A detailed assessment of the error associated with the CO retrieval is provided in *Hadji-Lazaro et al.* [1999]. As a summary, retrievals are generally more reliable above the sea than over the land, mainly due to the difficulty to treat emissivity correctly. High CO concentration at the surface (e.g. biomass burning) may be underestimated due to the low sensitivity of nadir-looking infrared tropospheric sensor to the boundary layer (see discussion in the next section). Furthermore, version 1.0 of the neural network algorithm did not treat the topography correctly, which induced higher retrieval errors above mountains. According to these various contributions, uncertainties associated with the retrieved CO values were estimated to range between 5 and 25%.

**2.3.2. Instrumental error.** The IMG Level 1 data (spectra) are quality-flagged, on three separated criteria: quality of the interferogram, quality of the alignment and phase difference [*Kobayashi et al.*, 1999b]. A preliminary selection was performed by IMGDIS/ERSDAC to remove all bad-quality flagged data, but among the remaining data some were of better quality than others. Uncertainties associated with the quality of the signal were set to values ranging from 0 (3 good flags) to 30% (three

medium-quality flags).

The contribution of these two sources of uncertainties were added (root sum squared), and Figure 2 provides the distribution of the relative accuracy associated with each measured data. Values range from 5 to 40 %, and the average on the whole dataset was calculated to be 10%.

## 2.4. Averaging kernel

In order to characterize the sensitivity of the measurement to the different atmospheric layers, we used the method of perturbation of the CO profile described by *Pougatchev* [1995] to calculate the averaging kernel associated with the retrieved IMG CO data. Using this function, data measured by different instruments or obtained by atmospheric models may be compared. The averaging kernel is used in the assimilation routine to constrain the model CO vertical profiles with the IMG total column amounts.

The averaging kernel function depends on the instrument (its sensitivity to the atmospheric layers) and on the inversion algorithm (spectral range used and ability to provide the available information). To calculate the averaging kernel associated with the CO retrieval, an IMG spectra is simulated using the high resolution radiative transfer code LBLRTM [*Clough and Iacono*, 1995, *Clerbaux et al.*, 1998a] with a surface temperature of 288.2K, an emissivity of 0.98, and the Air Force Geophysics Laboratory (AFGL) U.S. Standard Atmosphere 1976. The 47 vertical layers of the initial CO profile are perturbed sequentially by an increment of concentration  $d = +7.8 \cdot 10^{17}$  molecules/cm<sup>2</sup> ( $\frac{1}{3}$  of the total content), and the CO total column is retrieved for the initial unperturbed

spectrum ( $Q_a$ ) and the 47 perturbed spectra ( $Q_{ret}^k$ ).

The 47 elements  $A^k$  of the averaging kernel vector  $\mathbf{A}$  are obtained from the following equation [Reichle *et al.*, 1999]:

$$A^k = (Q_{ret}^k - Q_a)/d \quad (1)$$

This function, plotted in Figure 3, peaks at 5 km and reflects the low sensitivity of a nadir-looking instrument to the boundary layer as discussed in Clerbaux *et al.* [1998a]. When compared to the MAPS averaging kernel provided in Reichle *et al.* [1999], it can be seen that the maximum contribution peaks lower in the troposphere (maximum contribution was found around 8 km for MAPS). We checked that this averaging kernel, when normalized, does not depend on the increment of concentration and on the CO a priori profile used for the simulation. The averaging kernel vector  $\mathbf{A}$  was then interpolated on the vertical levels of the atmospheric model (described hereafter). A convolution of this vector with the model CO concentration values for each layer allows to compute an integrated amount that directly compares with the measured IMG columns to be assimilated.

### 3. Chemistry-transport Model

MOZART is a three-dimensional chemical-transport model of the global troposphere described and evaluated in Brasseur *et al.* [1998] and Hauglustaine *et al.* [1998] respectively. It provides the global distribution of 50 chemical constituents between the Earth's surface and the pressure level of 3 mbar (approximately 35 km

altitude). The concentration of each species is predicted by individually solving a mass conservation equation taking into account advective, convective, and diffusive transport as well as surface and in-situ emissions, photochemical conversions, and wet and dry surface deposition. MOZART is run at a horizontal resolution of 2.8 degrees in latitude and longitude (T42) and includes 25 levels in the vertical. Dynamical and chemical processes are calculated each 20-minute time step.

The model can be driven either by meteorological fields provided by meteorological centers or by simulations performed by General Circulation Models (GCM). For this study we used MOZART version 2, driven by the National Center for Environmental Prediction (NCEP) reanalysis. A similar version of the model was used by *Lamarque et al.* [1999].

## 4. Data Assimilation

### 4.1. Assimilation Scheme

The basic concepts of data assimilation have been developed for numerical weather prediction [*Courtier et al.*, 1993, *Talagrand*, 1997] and recently applied to the analyze of data for atmospheric constituents [*Fisher et al.*, 1995, *Khattatov et al.*, 1999].

In this study, a 3D sequential assimilation approach (see *Lamarque et al.* [1999] and *Khattatov et al.* [2000] for a detailed description of the assimilation scheme), is used to combine the IMG measurements (CO total columns) with the CO profiles calculated by the MOZART (version 2) model on the global scale. The optimal interpolation

procedure is used to calculate the best estimation of the CO concentration, that minimize the differences between measured and calculated CO distributions, weighted by the associated errors.

The assimilated field  $x^a$  is given by

$$x^a = x^b + K[y - Hx^b]$$

where  $y$  is the observation field,  $x^b$  is the a priori model field,  $H$  is the observation matrix, which represents interpolation from model results to observation places and contains the averaging kernel.  $[y - Hx^b]$  is the innovation vector (difference between observation value and the value predicted by the model at the same time and place), and the gain matrix  $K$  is defined as:

$$K = BH^t(HBH^t + O)^{-1}$$

where  $O$  and  $B$  represent the observational and model associated error covariance matrix respectively.  $K$  is the matrix which, taking into account the respective accuracies of the model and the observations, produces the best estimate, in the sense of the minimum variance, of the  $x$  vector.

#### 4.2. Assimilation results

The sequential assimilation scheme was implemented in the chemical-transport model MOZART (version 2) and run on a VPP300 Fujitsu computer. The cloud-filtered CO total columns and associated errors (see Figures 1 and 2) obtained from the analysis of IMG spectra for the June 16-19 period were used to constrain the model. The

error covariance matrix  $O$  was obtained from the error budget described in section 2.3 according to the reliability of each measurement (diagonal matrix as observation errors are assumed to be independent). The error associated with the model ( $B$ ) was set to 10% (diagonal) to give the same weight, on average, to the model and to the measurements. As the model provides CO profiles at the model resolution, the linear operator  $H$  interpolates the model grid points to the observations locations. Each profile is convolved with the averaging kernel vector calculated in section 2.4 and transformed in an IMG-like measured value, and the assimilated field is calculated according to equations provided in section 4.1.

Two separated runs of the MOZART (version 2) chemical-transport model were undertaken for the June 16-19 period: one reference run to check the evolution of CO during these 4 days without assimilation, and one assimilation run where all the data measured by IMG were assimilated (all the measurements performed during one day being assimilated at the same time). The June 19 CO global distribution (mixing ratios, in ppbv) calculated at the surface for these two simulations are plotted respectively in Figure 4 and 5. Figure 6 provides the relative difference (assimilation run minus reference run, divided by reference run) between these two fields. Irregular patterns at specific locations are due to the irregular distribution of data, which do not constrain the model equally for all the grid points. Differences range from -40 to +10% in the northern hemisphere (except for west of California where it reaches +25%), and from -10 to +20% in the southern hemisphere, except for some localized regions where it reaches +30%. Divergences on the CO gradient may come from different factors: in



the northern hemisphere, CO contents may be overestimated by the model due to the underestimation of calculated OH and important transport to high latitudes (see discussion in *Hauglustaine et al.* [1998] and comparison with results provided by other CTMs in *Kanakidou et al.* [1999]). On the contrary, the CO values are generally higher in the southern hemisphere after assimilation, which may result from the retrieval algorithm which tends to overestimate the CO columns where very low values are observed [*Hadji-Lazaro et al.*, 1999].

Local differences also come from the fact that the model uses emission sources provided by climatologies, which does not always correctly represent the particular emission conditions prevailing in 1997, e.g. emissions due to biomass burning. A detailed study of the geographical distribution of the CO emission sources (biogenic, fossil fuel and biomass burning) in the model was undertaken. Figure 7 compares the model CO biomass burning source ( $\text{kg}/\text{m}^2$ ) for June over Africa and the fires detected by the Along Track Scanning Radiometer (ATSR) on ERS2 in June 1997. As it can be seen, the maximum CO emission due to biomass burning is not located at the same place for the model climatology and for the ATSR measurements, which directly impacts on the assimilated CO distribution as can be observed from Figure 6.

#### 4.3. Comparison with the CMDL network measurements

Direct validation of CO total column retrievals from IMG measurements is difficult due to the lack of other CO measurements on the global scale at the same time period. However, data assimilation is a powerful integration tool, allowing to compare the model

surface computed CO (constrained by the assimilation of IMG data) with the surface mixing ratios provided by the NOAA/CMDL network [Novelli *et al.*, 1992; Novelli *et al.*, 1998]. Even if the averaging kernel function shows a lower sensitivity of the instrument at the surface level, the assimilated CO total column modifies the whole model profile and changes the calculated surface mixing ratio.

We used all the daily surface mixing ratios available from CMDL local stations between June 16 and 19 (22 stations) and averaged them when several values were recorded at the same location during the four days period. Table 1. Table 1 details the geographic location of each of the 22 CMDL in-situ measurements, provides the calculated average CO mixing ratios, as well as the co-located results without and with assimilation of IMG CO measured data in the MOZART model. Figure 8 allows to visualize the results, showing mixing ratios classified by CMDL increasing concentration. The assimilation of IMG CO data consistently improved the agreement between the model and the CMDL measured data, as all the data above 55 ppbv (17 stations on 22) were found to be in better agreement after assimilation of IMG CO columns in the model. The persistent influence of the model on the assimilated data can clearly be seen on this picture. For values recorded where low CO mixing ratio occurs (lower than 55 ppbv, all located in the southern hemisphere) divergences are attributed to two different sources: first, the inversion algorithm tends to overestimate the retrieved CO for very low mixing ratios (see discussion before). Second, reversely, a calibration drift (not corrected for this dataset) affects the CMDL data for low mixing ratio values which are then underestimated [Novelli, private communication]. We computed root mean squares

Table 1
---------

differences between the CMDL and the model values, and the agreement was found to be of 29.1% for the reference run and improved to 15.9% for the assimilation run. When removing the five lowest concentration values, the agreement reaches 8.1%.

## 5. Conclusions

In this work, we show how data assimilation of measured CO total columns in a chemistry-transport model allows to:

- generate global fields from sparse and scattered observation data;
- highlight differences between measurements and models;
- compare data provided by a remote sensor with ground-based measurements.

The global distribution of CO during four days in June 1997 was obtained from the analysis of the spectra provided by the IMG nadir-looking instrument. A detailed error budget was calculated for each data, which accounts both for the instrumental and for the retrieval uncertainties. The averaging kernel, that characterize the sensitivity of the CO measurement to the different atmospheric layers, was determined. A sequential data assimilation scheme is used to combine the measured CO total columns, the associated errors, and the averaging kernel, with CO profiles provided by the three-dimensional chemistry-transport model MOZART (version 2). The assimilation of IMG data improves the agreement between the CO surface mixing ratios measured by the CMDL network and those computed by the MOZART model.

In the next five years, several instruments on-board of atmosphere-dedicated platforms will provide a large set of new data in the troposphere. All this information,

along with that provided by in-situ measurements, can be combined through data assimilation techniques in chemistry-transport models, provided averaging kernels and detailed and realistic error budgets are determined. Efforts dedicated towards the development of data assimilation and inversion techniques [Bergamaschi *et al.*, 2000] will help to maximize the scientific return of these new instruments.

Projections indicate that in the future there will be important geographical redistribution of surface emissions of ozone precursors. Remote sensing data will allow to better estimate the global budgets for the main trace gases. If complementary information on emissions is also available (e.g. through instruments flying on the same platform), biomass burning or episodic events may be studied in detail and the impact on other atmospheric species may be investigated. The 1997 Indonesian fire would have provided a very interesting case study to combine global scale measurements and atmospheric models [Hauglustaine *et al.*, 1999; Matsueda *et al.*, 1999]. Unfortunately, IMG measurements were stopped just before due to the failure of the ADEOS solar panels.

Work is in progress to retrieve ozone and methane from the same IMG spectra, which will allow to constrain the model and study how one species influence the concentration of another species, and to investigate on the concentration of other constituents which are not directly measurable from space.

**Acknowledgments.** We are grateful to J. Gille for helpful discussions and financial support in the framework of this study. Claire Granier is acknowledged for useful discussions.

The authors thank IMGDIS/ERSDAC for providing the Level 1 IMG data, Tony Clough for the LBLRTM radiative transfer model, Paul Novelli for providing the NOAA/CMDL CO measurements, and the people from the ATSR team for access to the ATSR World Fire Atlas through the WEB. This work was undertaken in the framework of the ISSWG (IASI Sounding Science Working Group) activities under the auspices of EUMETSAT (European Organization for the Exploitation of Meteorological Satellites) and CNES (Centre National d'Etudes Spatiales). Computer time was provided by the Institut de Développement et des Recherches en Informatique Scientifique (IDRIS). The National Center for Atmospheric Research is sponsored by the National Science Foundation.

## References

- Beer, R., and T. A. Glavich, Remote sensing of the troposphere by infrared emission spectroscopy, *Proc. SPIE, Int. Soc. Opt. Eng.*, 1129, 42-48, 1989.
- Bergamaschi, P., R. Hein, C. A. M. Brenninkmeijer and P. J. Crutzen, Inverse modeling of the CO global cycle. I. Inversion of CO mixing ratio, *J. Geophys. Res.*, 105, D21, 1909-1927, 2000.
- Bovensmann, H., J. P. Burrows, M. Buchwitz, J. Frerick, S. Noël, V. V. Rozanov, K. V. Chance, and A. P. Goede, Sciamachy - Mission objectives and measurement modes, *J. Atmos. Sci.*, 56, 127-150, 1999.
- Brasseur, G. P., D. A. Hauglustaine, S. Walters, P. J. Rasch, J.-F. Müller, C. Granier, and X. Tie, MOZART, a global chemical transport model for ozone and related chemical tracers, I. Model description, *J. Geophys. Res.*, 103, D21, 28,265-28,289, 1998.
- Brasseur G. P., J. J. Orlando and G. S. Tyndall, *Atmospheric Chemistry and Global Change*, Oxford University Press, New York, 1999.
- Cayla, F., and P. Javelle, IASI instrument overview: Advanced and next-generation satellites, *Proc. SPIE, Int. Soc. Opt. Eng.*, 2583, 271-281, 1995.
- Clerbaux, C., P. Chazette and G. Mégie, Tropospheric concentrations of infrared absorbing molecules using a nadir-looking Fourier transform spectrometer: Passive infrared remote sensing of clouds and the atmosphere III, *Proc. SPIE, Int. Soc. Opt. Eng.*, 2578, 148-153, 1995.
- Clerbaux C., P. Chazette, J. Hadji-Lazaro, G. Mégie, J.-F. Müller and S. A. Clough, Remote sensing of CO, CH<sub>4</sub> and O<sub>3</sub> using a space-borne nadir-viewing interferometer, *J. Geophys. Res.*, 103, D15, 18,999- 19,013, 1998a.

- Clerbaux C., J. Hadji-Lazaro, S. Payan, C. Camy Peyret, and J. Wang, Intercomparison of inversion algorithms for the retrieval of CO from IMG/IASI, Proceedings of the 8th International Workshop on Atmospheric Science from Space using Fourier Transform Spectrometry (ASSFTS), MeteoFrance, Toulouse, 1998b.
- Clerbaux C., J. Hadji-Lazaro, S. Payan, C. Camy-Peyret and G. Mégie, Retrieval of CO columns from IMG/ADEOS spectra, *IEEE Transaction on Geoscience and Remote Sensing*, 37, 3, 1657- 1662, 1999.
- Clough, S. A., and M. J. Iacono, Line-by-line calculation of atmospheric fluxes and cooling rates, 2, Application to carbon dioxide, ozone, methane, nitrous oxide, and the halocarbons, *J. Geophys. Res.*, 100, 16,519-16,535, 1995.
- Connors, V. S., B. B. Gormsen, S. Nolf, and H.G. Reichle, Spaceborne observations of the global distribution of carbon monoxide in the middle troposphere during April and October 1994, *J. Geophys. Res.*, 104, D17, 21,455-21,470, 1999.
- Courtier, P., J. Derber, R. Errico, J.-F. Louis et T. Vukicevic, Important literature on the use of adjoint, variational methods and the Kalman filter in meteorology, *Tellus*, 45A, 341-357, 1993.
- Drummond, J. R., and G. S. Mand, The measurement of pollution in the troposphere (MOPITT) instrument: Overall performances and calibration requirements, *J. Atmos. Oceanic. Technol.*, 13, 314-320, 1996.
- Elbern, H. and H. Schmidt, A four-dimensional variational chemistry data assimilation scheme for Eulerian chemistry transport modeling, *J. Geophys. Res.*, 104 (D15), 18,583-18,598, 1999.
- Fisher, M. and D. J. Lary, Lagrangian 4-Dimensional variational data assimilation of

- Chemical-species, *Q. J. R. Meteorol. Soc.*, **121** (527A), 1681-1704, 1995.
- Gupta, M. L., R. J. Cicerone, S. Elliott, Perturbation to global tropospheric oxidizing capacity due to latitudinal redistribution of surface sources of  $\text{NO}_x$ ,  $\text{CH}_4$  and CO, *Geophys. Res. Lett.*, **25** (21), 3931-3934, 1998.
- Hadji-Lazaro, J., C. Clerbaux, and S. Thiria, An inversion algorithm using neural network to retrieve atmospheric CO concentrations from high resolution nadir radiances, *J. Geophys. Res.*, **104** (D19), 23,841-23,854, 1999.
- Hadji-Lazaro, J., C. Clerbaux, P. Couvert, P. Chazette, and C. Boone, Cloud detection in IMG infrared spectra using POLDER data, submitted to *Geophys. Res. Lett.*, 2000.
- Hauglustaine, D. A., G. P. Brasseur, S. Walters, P. J. Rasch, J.-F. Müller, L. K. Emmons, and M. A. Carroll, MOZART: A global chemical transport model for ozone and related chemical tracers, Part 2. Model results and evaluation, *J. Geophys. Res.*, **103**, D21, 28,291-28,335, 1998.
- Hauglustaine, D. A., G. P. Brasseur, J. S. Levine, A sensitivity simulation of tropospheric ozone changes due to the 1997 Indonesian fire emissions, *Geophys. Res. Lett.*, **26**, 21, 3305-3308, 1999.
- Jeuken, A. B., H. J. Eskes, P. F. van Velthoven, H. M. Kelder and E. V. Hölm, Assimilation of total ozone satellite measurements in a three-dimensional tracer transport model, *J. Geophys. Res.*, **104** (D5), 5551-5563, 1999.
- Kanakidou M., F. J. Dentener, G. P. Brasseur, T. K. Berntsen, W. J. Collins, D. A. Hauglustaine, S. Houweling, I. S. A. Isaksen, M. Krol, M. G. Lawrence, J.-F. Müller, N. Poisson, G. J. Roelofs, Y. Wang, W. M. F. Wauben, 3-D global simulations of tropospheric CO distributions - Results of the GIM/IGAC intercomparison 1997



- exercise, *Chemosphere: Global Change Science*, 1, 263-282, 1999.
- Khattatov, B. V., J. C. Gille, L. V. Lyjak, G. P. Brasseur, V. L. Dvortsov, A. E. Roche, and J. W. Waters, Assimilation of photochemically active species and a case analysis of UARS data, *J. Geophys. Res.*, 104 (D15), 18,715-18,737, 1999.
- Khattatov, B. V., J.-F. Lamarque, L. V. Lyjak, R. Menard, P. Levelt, X. Tie, G. P. Brasseur, J. C. Gille, Assimilation of satellite observations of chemical species in global chemistry-transport model, submitted to *J. Geophys. Res.*, 2000.
- Kobayashi H., A. Shimota, K. Kondo, E. Okumura Y. Kameda, H. Shimoda, and T. Ogawa, Development and evaluation of the interferometric monitor for greenhouse gases: a high-throughput Fourier-transform infrared radiometer for nadir Earth observations, *Appl. Optics*, 38 (33), 6801-6807, 1999a.
- Kobayashi H., A. Shimota, C. Yoshigahara, I. Yoshida, Y. Uehara, and K. Kondo, Satellite-borne high-resolution FTIR for lower atmosphere sounding and its evaluation, *IEEE Transaction on Geoscience and Remote Sensing*, 37, 3, 1496- 1507, 1999b.
- Lamarque, J.-F., B. V. Khattatov, J. C. Gille, and G. P. Brasseur, Assimilation of Measurement of Air Pollution from Space (MAPS) CO in a three-dimensional model, *J. Geophys. Res.*, 104 (D21), 26,209-26,218, 1999.
- Matsueda, H., H. Y. Inoue, M. Ishii, Y. Tsutsumi, Large injection of carbon monoxide into the upper troposphere due to intense biomass burning in 1997, *J. Geophys. Res.*, 104 (D21), 26,867-26,879, 1999.
- Novelli, P. C., L. P. Steel, and P. P. Tans, Mixing ratios of carbon monoxide in the troposphere, *J. Geophys. Res.*, 97, 20,731-20,750, 1992.
- Novelli, P. C., K. A. Masarie, and P. M. Lang, Distributions and recent changes of carbon

- monoxide in the lower troposphere, *J. Geophys. Res.*, 103(D15), 19,015-19,033, 1998.
- Parol, F., J.-C. Buriez, C. Vanbauce, P. Couvert, G. Sèze, P. Goloub, and S. Cheinet, First results of the polder 'Earth Radiation Budget and Clouds' Operational algorithm, *IEEE Transaction on Geoscience and Remote Sensing*, 37, 3, 1597-1613, 1999.
- Pougatchev, N. S. and C. P. Rinsland, Spectroscopic study of seasonal variation of carbon monoxide vertical distribution above Kitt Peak, *J. Geophys. Res.*, 100, D1, 1409-1416, 1995.
- Reichle, H. G., B. E. Anderson, V. S. Connors, T. C. Denkins, D. A. Forbes, B. B. Gormsen, R. L. Langenfelds, D. O. Neil, S. R. Nolf, P. C. Novelli, N. S. Pougatchev, M. M. Roell and L. P. Steel, Space shuttle based global CO measurements during April and October 1994, MAPS instrument, data reduction and data validation, *J. Geophys. Res.*, 104 (D17), 21,443-21,454, 1999.
- Talagrand, O., Assimilation of observations, an introduction, *J. Meteor. Soc. Japan*, 75 (1B), 191-209, 1997.
- C. Clerbaux, J. Hadji-Lazaro, D. Hauglustaine and G. Mégie, Service d'Aéronomie du CNRS, Université Paris 6, BP 102, 75252 Paris Cedex 05, France. (e-mail: cathy.clerbaux@aero.jussieu.fr)
- B. Khattatov and J.-F. Lamarque, Atmospheric Chemistry Division, National Center for Atmospheric Research, P.O. Box 3000, Boulder, CO 80307.

Received \_\_\_\_\_

Submitted to the *Journal of Geophysical Research*, 2000.

**Figure 1.** Global distribution of CO total column (molecules/cm<sup>2</sup>) for June 16-19, 1997, as retrieved from cloud-filtered IMG spectra

**Figure 2.** Error assessment (relative accuracy, %) on the retrieved CO data

**Figure 3.** Averaging kernel function for CO inversion calculated for the IMG instrument as a function of altitude (km)

**Figure 4.** CO mixing ratios (ppbv) at the surface for June 19, for the reference run

**Figure 5.** CO mixing ratios (ppbv) at the surface for June 19, after assimilation of 4 days of IMG data

**Figure 6.** Relative difference (%) between the two model runs (before and after assimilation of IMG CO data)

**Figure 7.** Model CO emission sources (kg/m<sup>2</sup>) due to biomass burning over Africa and data from the ATSR World Fire Atlas in June 1997

**Figure 8.** Comparison between the CO mixing ratios at the surface, as measured by the CMDL network and as computed by the MOZART model (with and without assimilation of IMG data) at the same location

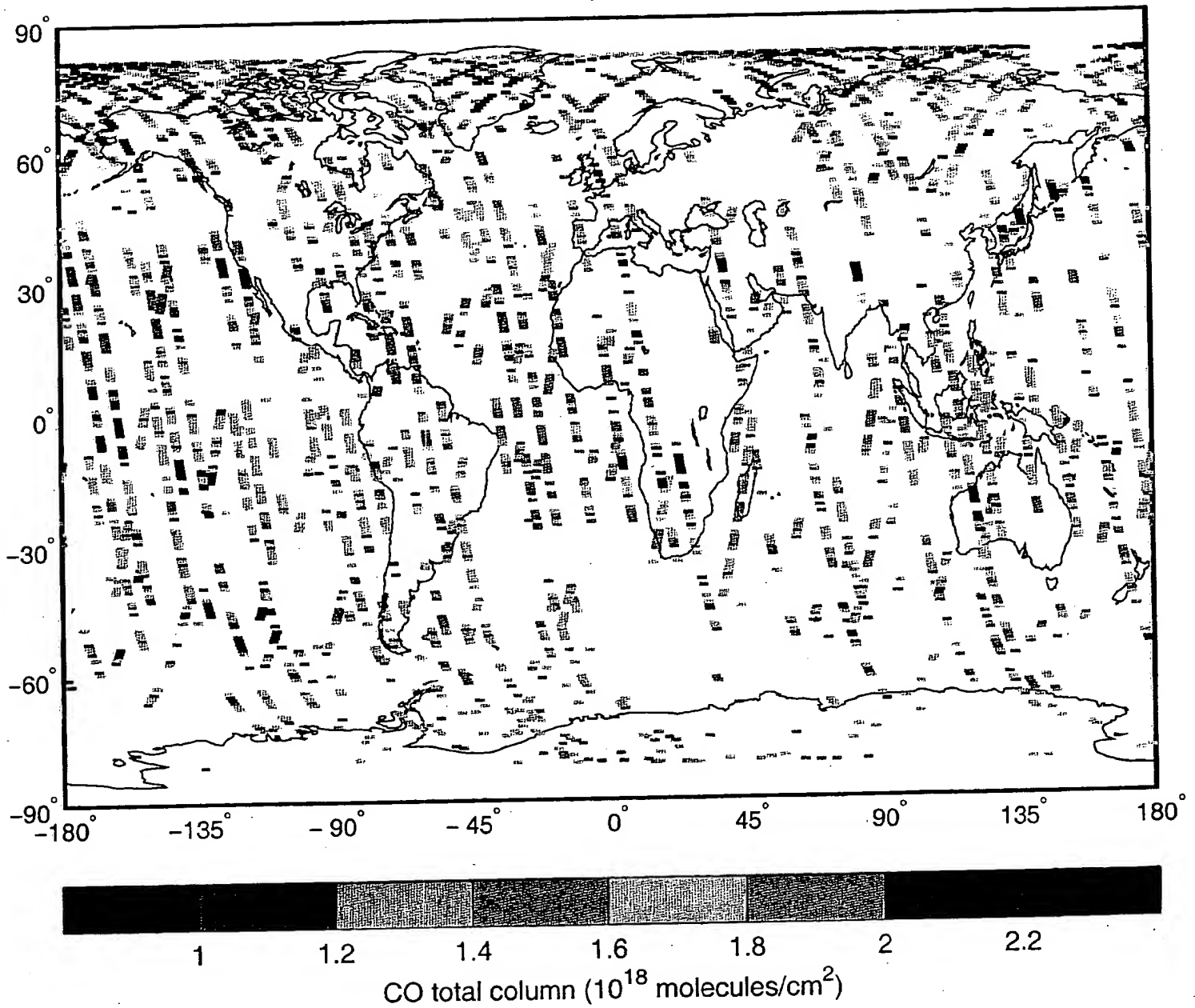
**Table 1.** CO surface mixing ratios (ppbv): measured by the CMDL network, calculated by the MOZART model, and obtained after assimilation of IMG data into the model.

Station	Lat	Lon	CMDL	MOZART	
				Reference run	Assimilation run
ASC	-7.55	-14.25	62.9	71.5	66.0
BRW	71.19	-156.36	95.1	143.9	103.3
BSC	44.10	28.41	146.2	214.0	165.8
CBA	55.12	-162.43	99.7	124.4	94.7
CGO	-40.41	144.41	51.9	60.7	75.5
EIC	-29.09	-109.26	52.6	60.8	62.4
GMI	13.26	144.47	66.5	78.5	66.4
HUN	46.57	16.39	151.9	184.7	149.9
ITN	35.21	-77.23	141.0	221.2	161.6
KUM	19.31	-154.49	82.1	88.2	84.6
LEF	45.56	-90.16	137.8	210.2	148.4
MHD	53.20	-9.54	96.6	126.7	99.5
MID	28.13	-177.22	91.8	104.7	83.1
NWR	40.03	-105.35	100.7	143.8	99.1
OPB	25.00	-153.00	102.6	88.6	91.9
OPC	30.00	-147.00	104.2	93.1	97.7
PSA	-64.55	-64.00	44.5	59.7	67.7

Table 1. (continued)

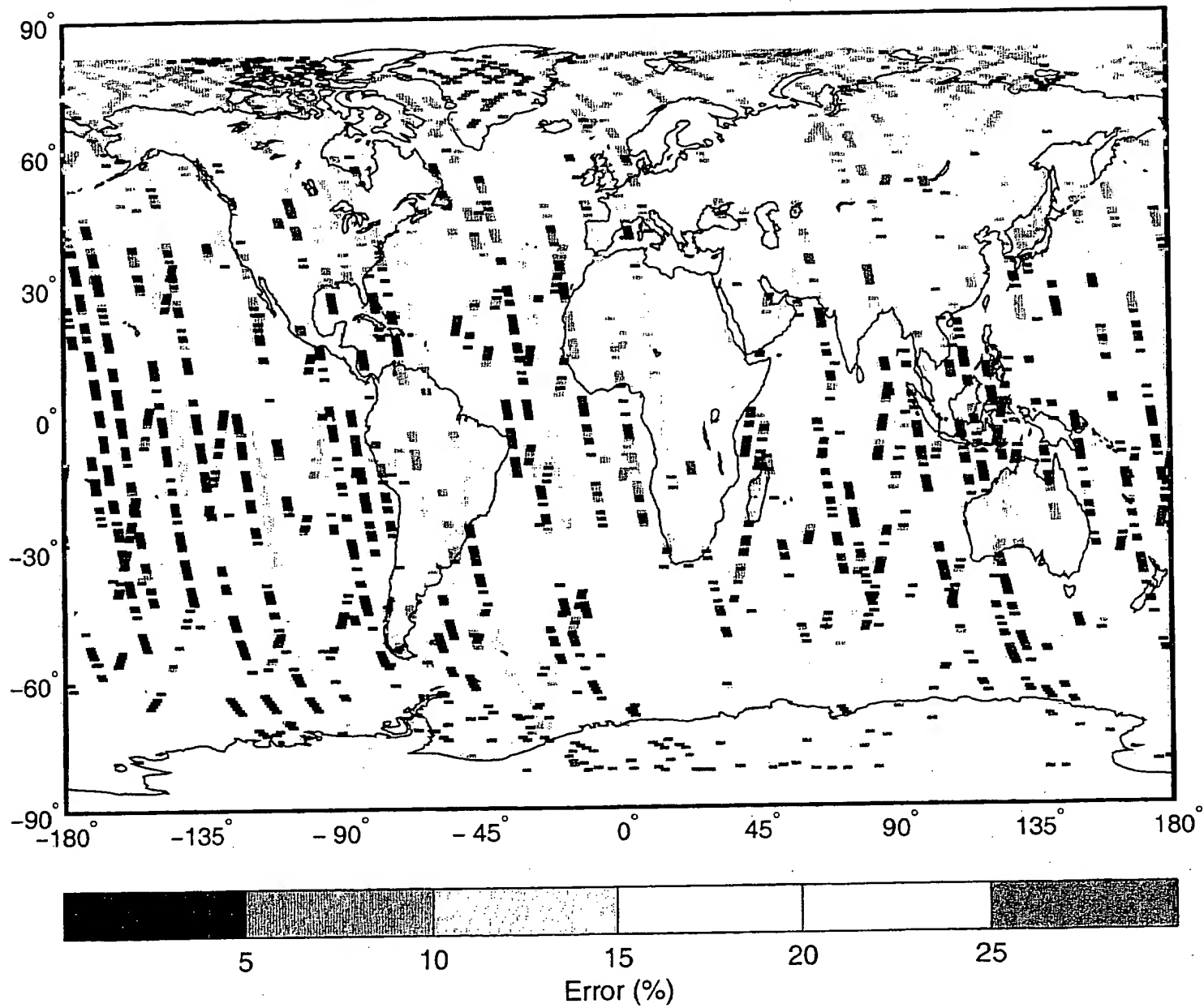
Station	Lat	Lon	CMDL	MOZART	
				Reference run	Assimilation run
RPB	13.10	-59.26	66.3	86.7	75.5
SMO	-14.15	-170.34	49.1	56.8	59.1
SYO	-69.00	39.35	40.8	60.0	71.5
UUM	44.27	111.06	128.6	154.2	113.2
ZEP	78.54	11.53	94.8	147.9	117.2

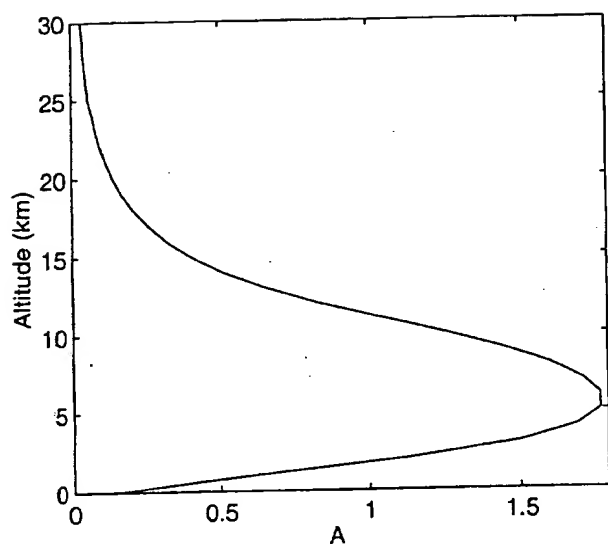
IMG CO retrieval (June 16-19, 1997)



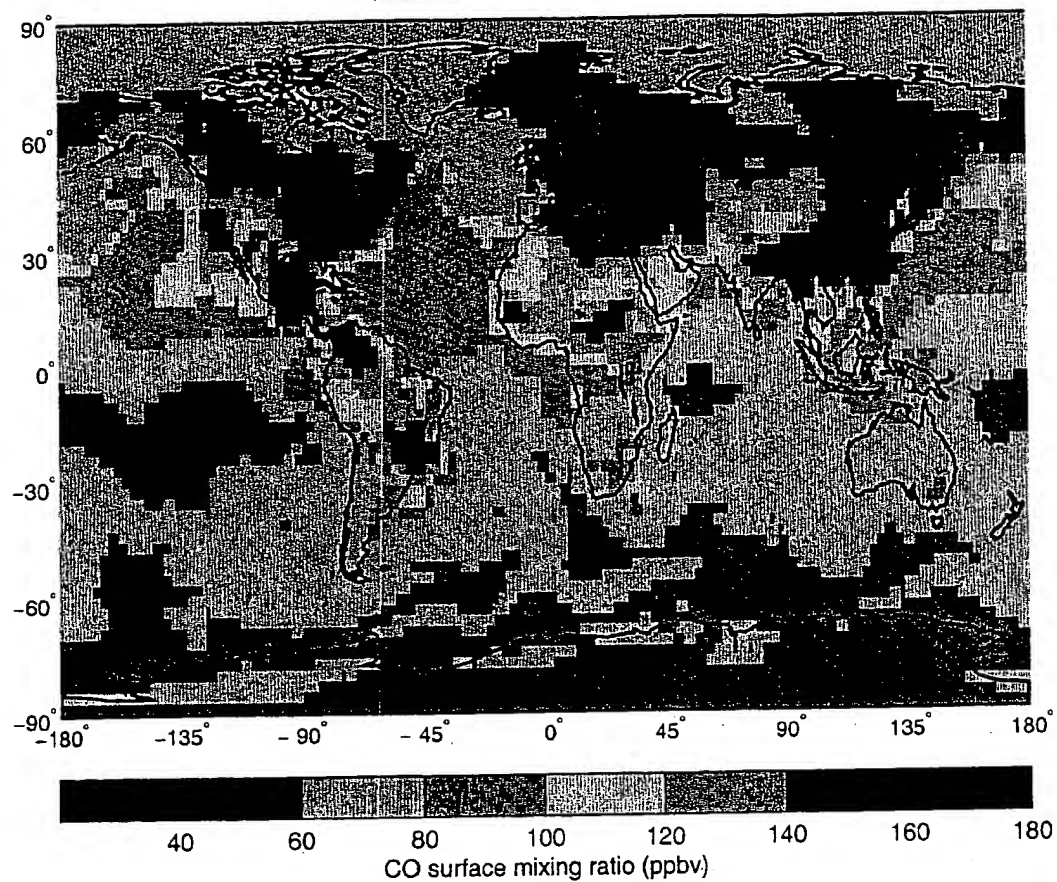


IMG CO accuracy (June 16-19, 1997)

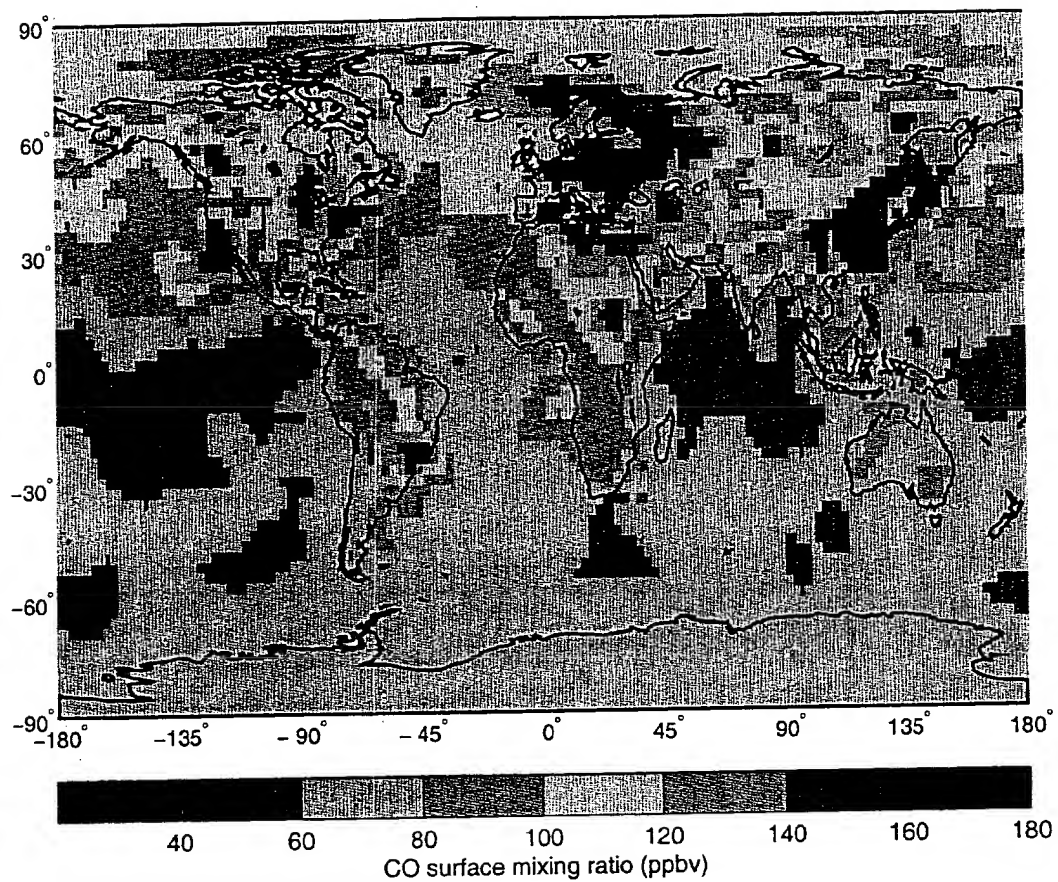




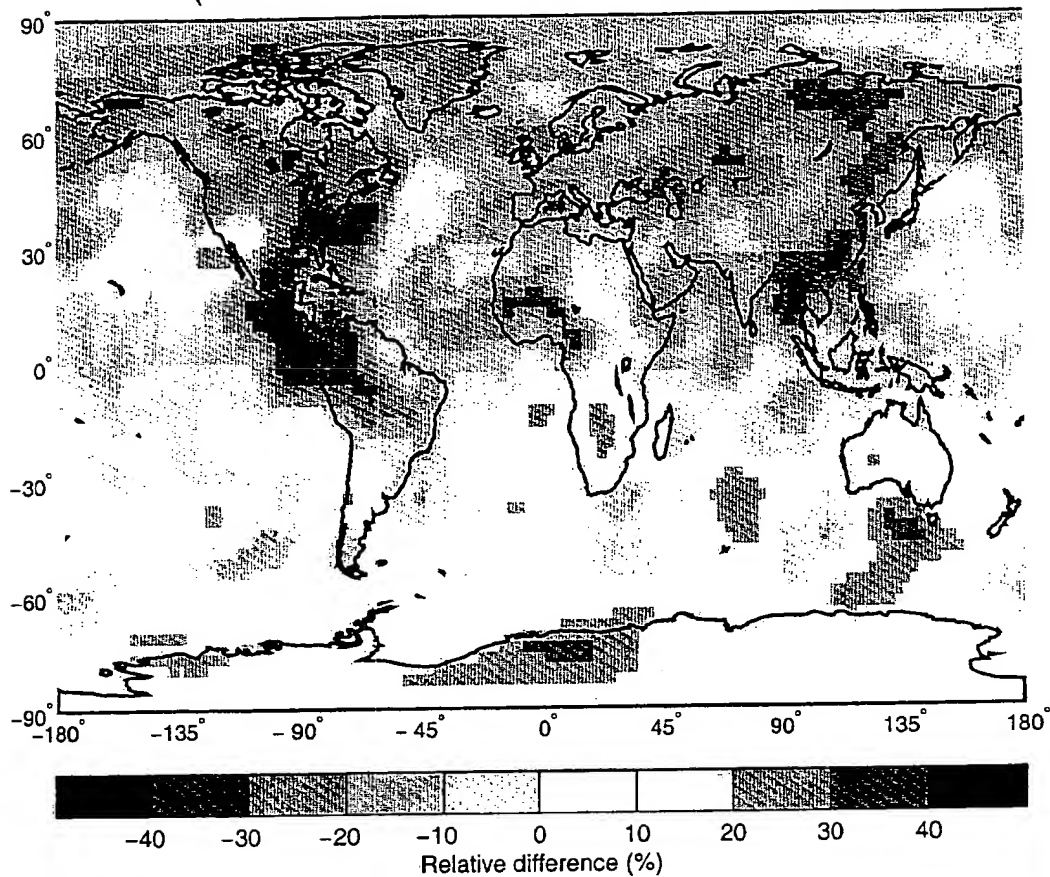
MOZART - Reference run

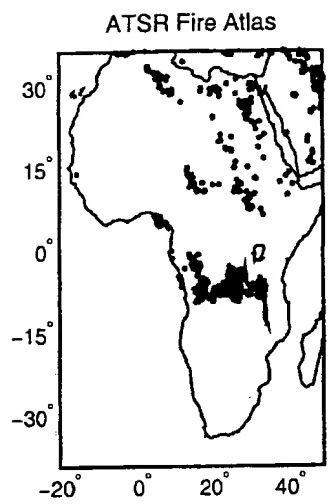
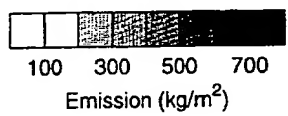
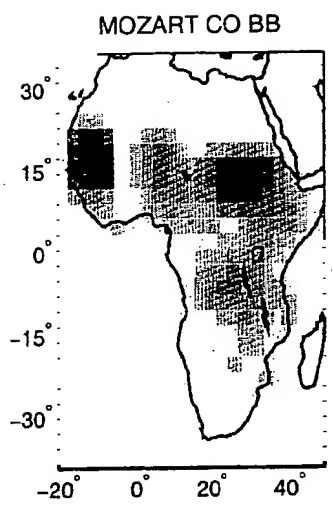


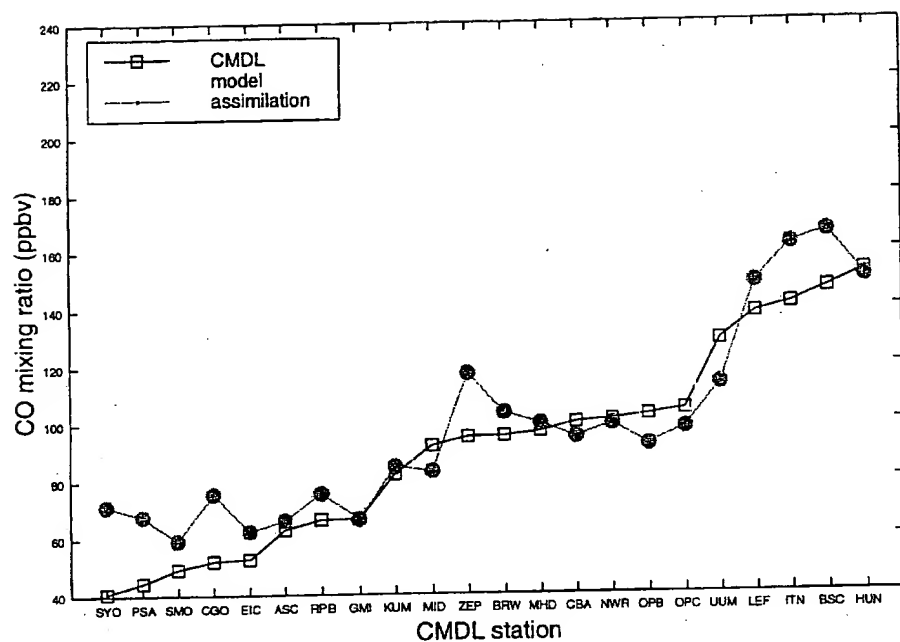
MOZART - Assimilation run



(Assimilation run - Reference run) / Reference run (%)







# On Applications of Photochemical Models to the Design of Measurement Strategies

Boris Khattatov, Lawrence Lyjak, and John Gille

Atmospheric Chemistry Division, National Center for Atmospheric Research

**Abstract.** Several research groups recently demonstrated [e.g., Fisher and Lary, 1995; Elbern et al., 1997; Khattatov et al., 1999] that concentrations of some non-observed chemical species can be constrained to a certain extent by the observed ones through our knowledge of atmospheric photochemistry. By utilizing mathematical relationships between chemically coupled species, observations of a subset of chemicals can be used to determine the future state of the whole system. The goal of this manuscript is to provide a mathematical formalism for assessing uncertainties of such an analysis. Practical applications of this study include designing future instruments and measurement strategies optimized to deliver the maximum amount of information given limited resources. In addition, it opens possibilities for testing our knowledge of atmospheric photochemistry by comparing predicted and measured concentrations and their estimated uncertainties. The proposed framework is used to determine the maximum measurement errors that guarantee specified prediction errors for a typical set of stratospheric chemicals.

## 1. Introduction

Monitoring the chemical composition of the atmosphere is an important but complicated and resource intensive task. It is clearly impossible to measure concentrations of even a limited number of key chemical species at every location and time. In recent years several research groups have demonstrated that specially designed techniques, broadly referred to as chemical data assimilation, can be used, albeit with some limitations, to fill in temporal and spatial gaps between sparse and irregular observations of chemical species [e.g., Fisher and Lary, 1995; Lyster et al., 1997; Elbern et al., 1997; Eskes et al., 1999; Lamarque et al., 1999; Levelt et al., 1998; Menard et al., 2000; Khattatov et al., 1999; Khattatov et al., 2000]. Such techniques have been successfully applied in the stratosphere as well as the troposphere for a variety of atmospheric chemicals.

It was also shown [e.g., Fisher and Lary, 1995; Elbern et al., 1997; Khattatov et al., 1999] that concentrations of some non-observed species can be constrained, at least to some extent, by the observed ones through our knowledge of atmospheric photochemistry. This is done by exploiting mathematical relationships representing photochemical coupling between different species. These relationships are usually given in the form of a computer model. When such relationships exist, it is no longer necessary to have information about concentrations of all chemicals in the system since some of them can, in principal, be derived from others.

The goal of this manuscript is to provide a mathematical formalism for assessing the amount of useful information that can be derived in this fashion. We will characterize "useful information" in terms of errors (or uncertainties or variances) of concentrations of observed and derived chemicals. In particular, we will investigate the following questions: (1) Given concentrations and uncertainties of concentrations of a set of chemicals at time  $t$ , what can be inferred about their concentrations and uncertainties at time  $t + \Delta t$ ? (2) Which chemicals are the most important for determining the complete state of a chemical system and which are the least important? and (3) What are the most relaxed (maximum) measurement errors that guarantee specified prediction errors for a particular set of atmospheric chemicals?

It should be noted that errors resulting from uncertainties in (photo) chemical reactions rates, numerical errors, and errors due to missing photochemical processes in the model are ignored in this study. In principal, these errors can be taken into consideration to some degree by including experimental uncertainties of the reaction rates and/or by parameterizing model error and tuning parameters through systematic comparisons of predicted and observed concentrations. The latter approach is described in detail in Menard et al. [2000a,b]. Incorporation of these additional uncertainties into the mathematical framework proposed here requires elaborate efforts that are beyond the scope of this publication and is a subject of future investigations.

Given these limitations, our results should be considered as the theoretically "best possible" limit. Nevertheless, the proposed mathematical formalism provides quantitative guidance that might be useful in designing future measurement campaigns and instruments. Additionally, this framework provides an opportunity to assess our knowledge of atmospheric photochemistry by comparing predicted and measured concentrations and their estimated uncertainties.

## 2. Mathematical Basis

The mathematical apparatus presented here is largely based on Khattatov et al. [1999]. We will also rely on Gaussian and linear approximations discussed in detail in that paper. Let vector  $x$  represent the state of a time-dependent box



photochemical model, i.e., concentrations of all modeled species in a parcel of air at a given instant. In the case of a box model that includes  $N$  species, the dimension of vector  $\mathbf{x}$  would be  $N$ . The photochemical box model  $\mathbf{M}$  describes the transformation of vector  $\mathbf{x}$  from time  $t$  to time  $t+\Delta t$ . Formally,

$$\mathbf{x}_{t+\Delta t} = \mathbf{M}(t, \mathbf{x}_t) \quad (1)$$

The covariance matrix  $\mathbf{C}$  characterizes uncertainties and cross-correlations between elements of  $\mathbf{x}$ :

$$\mathbf{C} = \langle (\mathbf{x} - \bar{\mathbf{x}})(\mathbf{x} - \bar{\mathbf{x}})^T \rangle \quad (2)$$

where  $\bar{\mathbf{x}}$  represents the true, unknown value of  $\mathbf{x}$ . As described in Khattatov et al. [1999], the time evolution of the covariance matrix is given by

$$\mathbf{C}_{t+\Delta t} = \mathbf{L} \mathbf{C}_t \mathbf{L}^T \quad (3)$$

where the matrix  $\mathbf{L}$  represents the linearization of the model  $\mathbf{M}$ :

$$\mathbf{L} = \frac{d\mathbf{M}}{d\mathbf{x}} \quad (4)$$

The linearized model  $\mathbf{L}$  is an  $N \times N$  matrix that, for small perturbations  $\Delta \mathbf{x}$  to the basic state, allows one to approximate the nonlinear transformation given by the original model as:

$$\Delta \mathbf{x}_{t+\Delta t} = \mathbf{L} \Delta \mathbf{x}_t \quad (5)$$

As discussed in Khattatov et al. [1999], as  $\Delta t$  becomes larger than the lifetime of the shortest-lived chemical constituent in the model, the matrix  $\mathbf{L}$  becomes rank deficient and, hence, non-invertable. In effect, it means that the initial concentration (at time  $t$ ) of this short-lived chemical is not needed anymore for determining the state of the system at time  $t+\Delta t$  since it can be derived from concentrations of other chemicals.

To investigate how initial uncertainties evolve in time we will now concentrate on variances, or diagonal elements of  $\mathbf{C}$  and ignore its off-diagonal elements. Let vector  $\mathbf{v}$  contain the values of all the diagonal elements of  $\mathbf{C}$ . It is easy to see from (3) that

$$\mathbf{v}_{t+\Delta t} = \mathbf{L}^2 \mathbf{v}_t \quad (6)$$

where elements of the matrix  $\mathbf{L}^2$  are simply squared elements of  $\mathbf{L}$ . For large enough  $\Delta t$  both these matrices become rank deficient and non-invertable in the conventional sense. It means that the same uncertainties  $\mathbf{v}_{t+\Delta t}$  of the prediction can be obtained from different initial uncertainties  $\mathbf{v}_t$ . If we assume that initial uncertainties come from measurements, we can pose the following question: what are the maximum measurement uncertainties that lead to prediction errors smaller than a specified upper limit? If vector  $\mathbf{v}_{\max}$  designates the maximum allowed prediction variance, then formally the problem is to maximize each element of  $\mathbf{v}_t$  subject to the following constraints:

$$\begin{aligned} \mathbf{v}_{\max} &\geq \mathbf{L}^2 \mathbf{v}_t \\ \mathbf{v}_t &> 0 \end{aligned} \quad (7)$$

Since  $\mathbf{v}_t$  is a vector, this is a multi-objective optimization problem which, in general, has multiple solutions. Various algorithms have been developed for finding practical solutions to such problems. In the next section we will apply the described mathematical framework to a typical stratospheric chemical system and use the so-called goal attainment algorithm [e.g., Coleman, Branch, and Grace, 1999] to find a solution to (7).

### 3. Application to the Stratosphere

The model used in this study is the same model described in Khattatov et al. [1999]. The model is initialized and run for several days using parameters (temperature, pressure, constituent concentrations) typical for the spring mid-latitude

stratosphere at 10 mb. Concentrations of the following 18 species are predicted: H, OH, HO<sub>2</sub>, H<sub>2</sub>O<sub>2</sub>, NO, NO<sub>2</sub>, NO<sub>3</sub>, N<sub>2</sub>O<sub>5</sub>, HNO<sub>3</sub>, HNO<sub>4</sub>, Cl, ClO, HOCl, HCl, ClONO<sub>2</sub>, O, O(<sup>1</sup>D), and O<sub>3</sub>; and concentrations of several others are held constant: CO, CH<sub>4</sub>, N<sub>2</sub>O, H<sub>2</sub>, H<sub>2</sub>O, and sulfate aerosol. The linearization matrices are automatically computed and stored for each time step of the model integration, which can vary from milliseconds to 15 minutes. The final linearization matrix corresponding to a larger time interval can then be computed by multiplication of the intermediate matrices. Examples of several linearization matrices are shown in Khattatov et al. [1999].

We performed a 24-hour model integration and computed the corresponding 18x18 linearization matrix. We then computed the singular value decomposition (SVD) spectrum of the linearization matrix, shown in blue in Plate 1. The portion of the spectrum corresponding to the nine largest singular values is fairly flat while the tail of the spectrum abruptly drops. This means that projections of the vector of initial concentrations onto the corresponding nine eigenvectors contain most of the information needed to determine concentrations of all 18 constituents after 24 hours.

Plate 1 also presents the SVD spectrum of the matrix  $L^2$  whose elements are the squared elements of matrix  $L$ . According to (6) this matrix determines the evolution of variances. As expected, the tail portion of this SVD spectrum is significantly flatter than that of matrix  $L$  and the "cut-off" value is not obvious. To illustrate the time evolution of relative errors in the model we performed a 10-day model integration, set the values of variances  $v$  at the beginning of the integration to correspond to 10% relative errors, and used (6) to compute variances at each model time step. Results of these calculations are presented in Plate 2.

From Plate 2 one can see that relative errors change in a complicated way in response to the diurnal cycle and photochemical transformations between species. Fairly simple calculations represented by (6) allow one to easily assess how uncertainties associated with a particular set of measurements vary with time. The assumed case when concentrations of all constituents in the model are known with a 10% error is clearly not realistic. However calculations similar to the one performed may still provide some guidance as to how much information is contained in a particular set of measurements. Even if concentrations of some species are not measured at all, various a priori estimates are usually available and can be utilized provided that the corresponding variances are set to reasonably large values.

We will now concentrate on an "inverse" problem and assume that we have a set of requirements, i.e. the maximum allowed errors of prediction at the end of the 24-hour period. What are the maximum possible errors of the measurements (at the beginning of the time interval) that guarantee specified prediction errors? For illustrative purposes we assume that relative prediction errors at the end of the 24-hour interval have to be equal to or less than 10% and attempt to find maximum initial errors that satisfy this criteria. As was mentioned earlier, this problem is, in general, ill-posed and therefore semi-empirical algorithms have to be utilized to address it. A solution obtained with the goal attainment algorithm [Coleman, Branch, and Grace, 1999] is shown in Plate 3.

The bar graph on the right of Plate 3 shows relative errors of constituent concentrations at the end of the 24-hour model integration while the bar graph on the left shows the derived relative errors of initial concentrations. As was required, the final relative errors of concentrations of all species do not exceed 10%, most chemicals showing smaller errors. The initial errors for some species (H, OH, Cl, HOCl, NO<sub>3</sub>, O, O(<sup>1</sup>D)) are so large that they go off the scale of the plot. The actual numerical values correspond to hundreds of percent and indicate that initial concentrations of these chemicals are irrelevant to determining the future state of the system for as long as the initial guess is of the correct order of magnitude. For the rest of the chemicals, initial errors range from about 5 to 20%. Clearly, the smaller the required initial error the more important is the role of the corresponding chemical in determining the future system evolution. For comparison, Plate 4 presents results of the forward error calculations for the case when the initial relative errors for all chemicals are set to 10%. As one can see, this does not guarantee the final errors to be 10%.

#### 4. Discussion

We presented a formal framework for computing time evolution of uncertainties in a chemical system and applied it to a case of typical stratospheric conditions. Uncertainties, or variances, can be considered to be a quantitative measure of the amount of useful information about the chemical system under consideration. The proposed framework allows one to assess how this "information" changes with time. Assuming that the initial estimates of the system state come from measurements, this framework allows one to determine which chemicals should be measured and with what uncertainties in order to be able to make the best possible predictions. The described case of a typical stratospheric system is largely academic and its results confirm quantitatively what is already known, e.g., that concentrations of several key species or linear combinations of species (families) control future evolution of the system. These results are encouraging and we believe that this framework will be practically most useful when applied to complex and poorly studied chemical systems involving a hundred or more chemicals. Tropospheric chemistry in general and boundary layer chemistry in particular are examples of systems where this methodology can provide quantitative guidance and help to establish measurement priorities.

When applying the suggested framework one should keep in mind its limitations. As was mentioned in the introduction, the framework in its present state does not account for several sources of uncertainties in the model and the computed uncertainties are likely to be underestimated. In addition, the method relies on the Gaussian and linear approximation as

discussed in Khattatov *et al.* [1999]. One thus has to establish the applicability of these approximations to a chemical system in question before using the proposed methodology.

Computer codes of the photochemical box model and linearization routines are available from <http://acd.ucar.edu/~boris/Content/0D.htm>.

**Acknowledgments.** The authors are grateful to Steve Massie and Jean-Francois Lamarque for fruitful discussion and valuable comments. We thank two anonymous reviewers for their comments and help in improving the manuscript. This research was supported in part by the NASA UARS guest investigator project under NRA-97-MTPE-04 contract S10109-X and by the NASA's MOPITT project. The National Center for Atmospheric Research is sponsored by the National Science Foundation.

## References

- Coleman, T., M. A. Branch, and A. Grace, Optimization Toolbox User's Guide, for use with Matlab, available from MathWorks, Inc., <http://www.mathworks.com>, 1999.
- Elbern, H., H. Schmidt, and A. Ebel, Variational data assimilation for tropospheric chemistry modeling, *J. Geophys. Res.*, **102**, 15,967-15,985, 1997.
- Eskes, H. J., A. J. M. Pitters, P. F. Levelt, M. A. Allaart, and H. M. Kelder, Variational assimilation of total ozone satellite data in a 2D lat-lon tracer-transport model, *J. Atmos. Sci.*, in press, 1999.
- Fisher, M., and D. J. Lary, Lagrangian four dimensional variational data assimilation of chemical species, *Q. J. R. Meteorol. Soc.*, **121**, 1681-1704, 1995.
- Khattatov, B. V., J. C. Gille, L. V. Lyjak, G. P. Brasseur, V. L. Dvortsov, A. E. Roche, and J. Waters, Assimilation of photochemically active species and a case analysis of UARS data., *J. Geophys. Res.*, **104**, 18,715-18,737, 1999.
- Khattatov, B. V., J.-F. Lamarque, L. V. Lyjak, R. Menard, P. F. Levelt, X. X. Tie, G. P. Brasseur, and J. C. Gille, Assimilation of satellite observations of long-lived chemical species in global chemistry-transport models, *J. Geophys. Res.*, in press, 2000.
- Lamarque, J.-F., B. V. Khattatov, and J. C. Gille, Assimilation of Measurement of Air Pollution from Space (MAPS) CO in a global three-dimensional model, *J. Geophys. Res.*, **104**, 26,209-26,218, 1999.
- Levelt, P. F., B. V. Khattatov, J. C. Gille, G. P. Brasseur, X. X. Tie, and J. Waters, Assimilation of MLS ozone measurements in the global three-dimensional chemistry-transport model ROSE, *Geophys. Res. Lett.*, **25**, 4493-4496, 1998.
- Lyster, P. M., S. E. Cohn, R. Menard, L.-P. Chang, S.-J. Lin, and R. Olsen, An implementation of a two-dimensional filter for atmospheric chemical constituent assimilation on massively parallel computers, *Mon. Weather. Rev.*, **125**, 1674-1686, 1997.
- Menard, R., S.E. Cohn, L.-P. Chang, and P.M. Lyster, Stratospheric assimilation of chemical tracer observations using a Kalman filter. Part I: Formulation, *Mon. Wea. Rev.*, **128**, 2654-2671, 2000a.
- Menard, R., and L.-P. Chang, Stratospheric assimilation of chemical tracer observations using a Kalman filter. Part II: Chi-square validated results and analysis of variance and correlation dynamics, *Mon. Wea. Rev.*, **128**, 2672-2686, 2000b.

B. Khattatov, L. Lyjak, and J. Gille, Atmospheric Chemistry Division, National Center for Atmospheric Research, P. O. Box 3000, Boulder, CO, 80307, USA. (e-mail: [boris@ucar.edu](mailto:boris@ucar.edu), [lvl@ucar.edu](mailto:lvl@ucar.edu), [gille@ucar.edu](mailto:gille@ucar.edu))

(Received September xx, 2000; revised January xx, 2000; accepted March xx, 2000.)

KHATTATOV, LYJAK, AND GILLE: APPLICATION OF MODELS TO MEASUREMENT STRATEGIES DESIGN

KHATTATOV, LYJAK, AND GILLE: APPLICATION OF MODELS TO MEASUREMENT STRATEGIES DESIGN

KHATTATOV, LYJAK, AND GILLE: APPLICATION OF MODELS TO MEASUREMENT STRATEGIES DESIGN

Plate 1. SVD spectrum of matrix  $L$  (in blue, circles) and  $L^2$  (in red, squares).

Plate 2. Time evolution of relative errors.

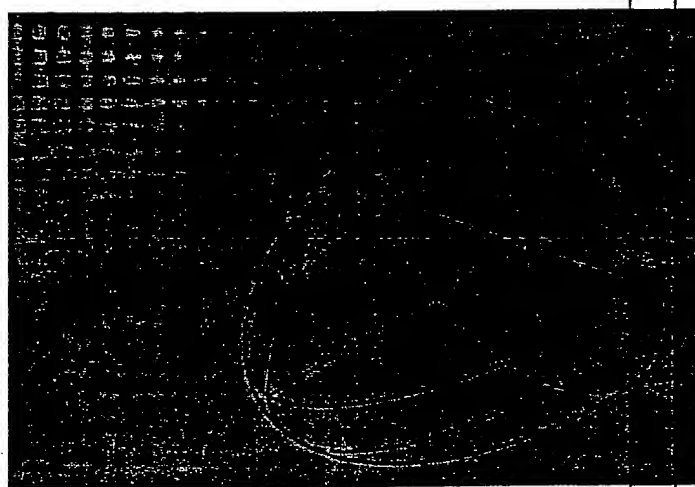
Plate 3. Maximum initial errors that guarantee final errors less than 10 % (left). Actual final errors (right).

Plate 4. Final errors for the case when all initial errors are set to 10%.

Series on Atmospheric, Oceanic and Planetary Physics — Vol. 2

# INVERSE METHODS FOR ATMOSPHERIC SOUNDING

## Theory and Practice



Clive D. Rodgers

Hardcover,  
ISBN: 981022740X  
Publisher: World  
Scientific Publishing  
Company, Incorporated,  
2000

PROPERTY of NCAR  
MOPITT/HIRDLS  
PROGRAM

Scientific

18  
App. No. 60/255,224  
Filing Date: December 12, 2001  
Att. Docket No. 36032.04

INVERSE METHODS FOR ATMOSPHERIC

## Chapter 2

# Information Aspects

As the simple illustration in Chapter 1 shows, there can be more to an inverse problem than meets the eye. The problem may be ill-conditioned, as that example is, or even ill-posed. To make things more complicated, most practical inverse problems are nonlinear too. To gain some understanding of the nature of the problem we will first examine various aspects of the information contained in the measurement. For this purpose we will use only the linear case. Nonlinear problems may be linearised, and the information content and behaviour of the resulting linear equations examined. Further implications of nonlinearity will be dealt with in chapter 5.

### 2.1 Formal Statement of the Problem

The general inverse problem can be regarded as a question of setting up and solving a set of simultaneous linear or non-linear equations, in the presence of experimental error in some of the parameters (the 'measurements'), and quite possibly in the presence of approximations in the formulation of the equations. To examine the information content of the indirect measurement, we will consider the measurements assembled into a vector  $y$ , the *measurement vector*, and the unknowns into a *state vector*  $x$ , describing the state of the atmosphere. Some aspects of the state of the atmosphere, for example the temperature distribution, are properly described by continuous functions rather discrete values, but ways can always be found of approximating continuous functions by discrete values to any desired accuracy. The process of measurement will be described by a *forward model*, which describes the physics of the measurement process.

#### 2.1.1 State and measurement vectors

The quantities to be retrieved can be represented by a state vector,  $x$ , with  $n$  elements,  $x_1, x_2, \dots, x_n$ . Often it will represent a profile of some quantity given at a finite number of levels, enough to adequately represent the possible atmospheric



relevant variables, such as temperature profile, such as a Fourier series, e.g. the air density with the altitude of one

can be represented by a vector  $\mathbf{x}$ . This vector should be the state vector. It is both the measurement measurements are made to be denoted by the vector

the state vector is called the *data vector*,

measurement vector,  $\mathbf{y}$ , determine the physics formally as

(2.1)

error, but it is often necessary to model  $\mathbf{F}(\mathbf{x})$ . Therefore the error and the state vector

(2.2)

$\mathbf{F}(\mathbf{x})$  is a vector valued function of the physics of the system. We know how the physics are measured, such as the temperature distribution or the radiation, and  $\mathbf{F}$  is described as not fully understood, measurements are necessary. The

3. continuous functions, thus most inverse prob-

lems are formally ill-posed or underconstrained in this trivial sense. This is simply dealt with by replacing the truly continuous state function, corresponding to an infinite number of variables, with a representation in terms of a finite number of parameters. This can be done to whatever spatial resolution or degree of accuracy is required for scientific use of the retrieval, e.g., the temperature profile could be represented on a finite grid of points with a spacing appropriate to the application. After discretisation the problem may or may not be underconstrained, depending on the grid spacing required and the information content of the measurement. Discretising the problem before attempting to solve it allows us to use the algebra of vectors and matrices, rather than the more general algebra of Hilbert space, and in any case numerical solutions must always be represented in some discrete form.

### 2.1.3 Weighting function matrix

For the purpose of examining the information content of a measurement it is most convenient to consider a linear problem. A linearisation of the forward model about some reference state  $\mathbf{x}_0$  will be adequate for this purpose, provided that  $\mathbf{F}(\mathbf{x})$  is linear within the error bounds of the retrieval. Write

$$\mathbf{y} - \mathbf{F}(\mathbf{x}_0) = \frac{\partial \mathbf{F}(\mathbf{x})}{\partial \mathbf{x}} (\mathbf{x} - \mathbf{x}_0) + \epsilon = \mathbf{K}(\mathbf{x} - \mathbf{x}_0) + \epsilon, \quad (2.3)$$

which defines the  $m \times n$  *weighting function matrix*  $\mathbf{K}$ , not necessarily square, in which each element is the partial derivative of a forward model element with respect to a state vector element, i.e.  $K_{ij} = \partial F_i(\mathbf{x}) / \partial x_j$ . Derivatives of this type are known as Fréchet derivatives, see Appendix A.6. If  $m < n$  the equations are described as underconstrained (or ill-posed or under-determined) because there are fewer measurements than unknowns. Similarly if  $m > n$  the equations are often described as overconstrained or over-determined. Unfortunately this description is over-simplified, and can easily be wrong; it is possible for a set of equations to be simultaneously over- and under-determined, as will be shown.

The term *weighting function* is peculiar to the atmospheric remote sounding literature, as mentioned in section 1.3 it arises because in the early application of nadir sounding for temperature the forward model takes the form of a weighted mean of the vertical profile of the Planck function. It may also be called the Jacobian (it is a matrix of derivatives), the kernel (hence  $\mathbf{K}$ ), the sensitivity kernel, the tangent linear model or the adjoint, amongst other terms.

### 2.1.4 Vector spaces

The concept of a *linear vector space* is very useful in considering linear equations. We will give two such spaces special names: The *state space* (or model space) is a vector space of dimension  $n$ , within which each conceivable state is represented by a point, or equivalently by a vector from the origin to the point. (Consider the

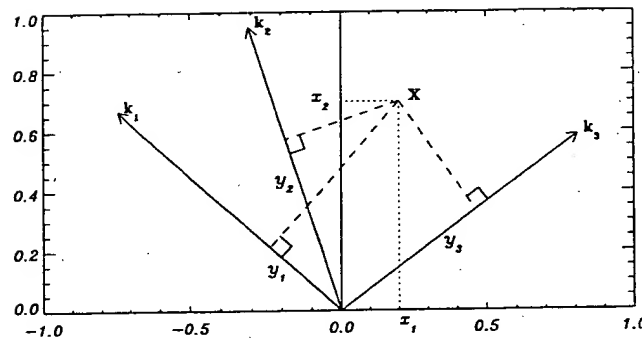


Fig. 2.1 Illustrating a state space in two dimensions, and a measurement space in three dimensions.

origin to be at  $x_0$  for the moment). The *measurement space* (or data space), is a vector space of dimension  $m$ , in which each conceivable measurement is likewise represented by a point or a vector (with the origin at  $F(x_0)$ ). The act of measurement is then equivalent to a mapping from the state space into the measurement space, and the inverse problem is that of finding an appropriate inverse mapping from the measurement space back into the state space. The weighting function matrix  $K$  represents the forward mapping, equivalent to the measurement apart from measurement error  $\epsilon$ . Each row of  $K$ , of dimension  $n$ , can be thought of as a vector  $k_i$  in state space, even though it is not a state. It corresponds to the  $i$ -th measurement  $y_i$  in the sense that the value of the  $i$ -th coordinate of measurement space for a given state vector  $x$  is the vector product of  $x$  and  $k_i$ , plus measurement error. Thus each of the  $m$  rows of  $K$  corresponds to a coordinate in measurement space, providing the mapping from state space to measurement space. The mapping is fuzzy, to an extent determined by the measurement error statistics.

Fig. 2.1 illustrates a state space in two dimensions, in which the state is represented by the point  $x$ , with components  $x_1$  and  $x_2$ . Three measurements are made, with weighting functions corresponding to the three vectors  $k_1$ ,  $k_2$  and  $k_3$ , here chosen to be unit vectors, and therefore of unit length. The measurements  $y_1$ ,  $y_2$  and  $y_3$  correspond to the orthogonal projections of  $x$  onto the  $k$ 's, i.e. the distances from the origin to the intersections of the perpendiculars with the  $k$ -vectors. These three numbers then define a point in 3-dimensional measurement space. This figure also illustrates that such a measurement is overconstrained. Given only the weighting function vectors and the measurements, the state can be found from the intersections of the perpendiculars from the weighting function vectors. However, only two are needed to determine  $x$ , the third is superfluous, and could be inconsistent with the other two if measurement error prevents all three perpendiculars from intersecting in one point. The measurement space is three dimensional, but the state space maps onto a two-dimensional subspace of it because one measurement is always a function of the other two. In the absence of measurement error, points

in measurement space states.

## 2.2 Linear Problem

Consider first a linear of measurement error simultaneous equations

and involves determining a number. More generally, extracted from the measurement solution or no unique

### 2.2.1 Subspaces

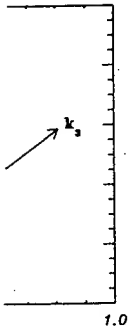
The  $m$  weighting functions will be of dimension  $n$  not linearly independent the matrix  $K$ , denoted rows (or columns). cannot be greater than the vectors forming the may not comprise the  $p$  which is a subspace

We can imagine  $p$  has  $p$  orthogonal basis outside which are orthogonal weighting function space will contribute orthogonal to it, will give This undetermined

The problem will this case the solution are not determined by Their sizes (whether from other arguments

If a retrieval their values:





ment space in three dimen-

space (or data space), is a measurement is likewise  $k_0$ ). The act of measurement into the measurement appropriate inverse mapping

The weighting function  $k_i$  of the measurement apart from  $n$ , can be thought of as  $i$ . It corresponds to the  $i$ -th coordinate of measurement and  $k_i$ , plus measurement coordinate in measurement space. The mapping error statistics.

in which the state is represented by measurements are made, vectors  $k_1$ ,  $k_2$  and  $k_3$ , here

The measurements  $y_1$ ,  $y_2$  of the  $k$ 's, i.e. the distances with the  $k$ -vectors. These measurement space. This figure is strained. Given only the state can be found from the function vectors. However, measurements, and could be inconsistent three perpendiculars from three dimensional, but the because one measurement measurement error, points

in measurement space but not in this subspace of it do not correspond to possible states.

## 2.2 Linear Problems without Measurement Error

Consider first a linear problem with arbitrary numbers of dimensions in the absence of measurement error. In this case the problem reduces to the exact solution of linear simultaneous equations,

$$y = Kx, \quad (2.4)$$

and involves determining whether there are no solutions, one solution, or an infinite number. More generally, it is a matter of investigating what information can be extracted from the measurements  $y$  about the state  $x$  particularly when there is no solution or no unique solution.

### 2.2.1 Subspaces of state space

The  $m$  weighting function vectors  $k_j$  will span some subspace of state space which will be of dimension not greater than  $m$ , and may be less than  $m$  if the vectors are not linearly independent. The dimension of this subspace is known as the *rank* of the matrix  $K$ , denoted by  $p$ , and is equal to the number of linearly independent rows (or columns). If  $m > n$ , more measurements than unknowns, then the rank cannot be greater than  $n$ , and may even be less. This subspace, spanned by the vectors forming the rows of  $K$ , is called the *row space* or *range* of  $K$  and may or may not comprise the whole of state space.  $K$  also has a *column space* of dimension  $p$  which is a subspace of measurement space.

We can imagine an orthogonal coordinate system or *basis* for state space which has  $p$  orthogonal *base vectors* (coordinates) in row space, and  $n - p$  base vectors outside which are orthogonal to row space and therefore orthogonal to all of the weighting function vectors. Only components of the state vector which lie in row space will contribute to the measurement vector, all other components being orthogonal to it, will give a zero contribution to the measurement, i.e. are unmeasurable. This undetermined part of state space is called the *null space* of  $K$ .

The problem will be under-determined if  $p < n$ , i.e. if a null space exists. In this case the solution is non-unique because there are components of the state which are not determined by the measurements, and which could therefore take any value. Their sizes (whether they are taken to be zero or something else) must be determined from other arguments, or they must be explicitly ignored:

*If a retrieved state has components which lie in the null space, their values cannot have been obtained from the measurements.*

Consider just the components of the state vector in the row space. They will be over-determined if  $m > p$  and there are more measurements than the rank of  $K$ , or well-determined if  $m = p$ . Thus it is possible for a problem to be simultaneously over-determined (in row space) and under-determined (if there is a null space), a condition called *mixed-determined*. It is even possible for there to be more measurements than unknowns,  $m > n$ , and for the problem to be under-determined, if  $p < n$ . A problem is well-determined only if  $m = n = p$ .

⇒ **Exercise 2.1:** Construct a simple example of a set of linear equations which is simultaneously over- and under-determined.

If the problem is well determined then a unique solution can be found by solving a set of  $p \times p$  equations. If the problem is overdetermined in the row space and there is no measurement error, then either the measurements must be linearly related in the same way as the  $k_j$ -vectors, or they are inconsistent, and there is no exact solution. The latter is the normal situation when measurement error is present, and will be dealt with in section 2.4.1.

In summary, the measurement represented by  $K$  provides not more than  $p$  independent quantities or pieces of information with which to describe the state.

### 2.2.2 Identifying the null space and the row space

The row space of a given  $K$  can be identified by finding a basis, or coordinate system, for state space of the kind described above, i.e. an orthogonal set of vectors that every  $k_j$  can be expressed in terms of, which therefore must be an orthogonal set of linear combinations of the  $k_j$ . There are many ways of doing this, and there are clearly an infinite number of bases, as any rotation of an orthogonal basis within its own space is also an orthogonal basis for the space. The Gram-Schmidt orthogonalisation is probably the simplest method, but singular vector decomposition\* (Appendix A.4) has some properties which make it rather more useful. We can express  $K$  in the form

$$K = U\Lambda V^T, \quad (2.5)$$

where  $U$  ( $m \times p$ ) and  $V$  ( $n \times p$ ) are matrices of its left and right singular vectors, and  $\Lambda$  is a  $p \times p$  diagonal matrix of non-zero singular values, where  $p$  is the rank of  $K$ . The  $p$  columns of  $V$  form the desired orthogonal basis for the row space, and the columns of  $U$  form a corresponding basis in measurement space for the column space. Inserting Eq. (2.5) in the linearised forward model,  $y = Kx$ , and multiplying

\*Eigenvector and singular vector decompositions are fundamental to understanding the information content of indirect measurements. If you are not familiar with these concepts, you should read Appendix A or relevant textbooks before proceeding.

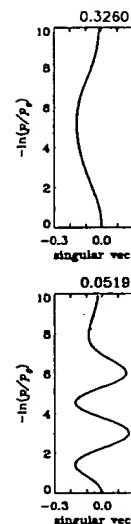


Fig. 2.2 The singular values are given above each

by  $U^T$  gives

so that, putting  $y' =$

indicating that the  $p$  proportional to a component  $V$  matrix forms a natural basis for column space.

Fig. 2.2 shows the corresponding singular values. The corresponding singular functions are orthogonal. Structures in the problem being measured independent of these measurements would be measured with a precision of one.

row space. They will be less than the rank of  $K$ , or may be simultaneously zero (if there is a null space), or there may be more measurements than unknowns, or there may be under-determined, if

the number of linear equations which

can be found by solving the equations in the row space and there must be linearly related in the column space, and there is no exact measurement error is present,

provides not more than  $p$  independent measurements to describe the state.

choice

by finding a basis, or coordinate system, in the row space, and an orthogonal set of vectors in the column space. There must be an orthogonal basis for the row space, and an orthogonal basis for the column space. The Gram-Schmidt method, but singular vector methods make it rather more

(2.5)

left and right singular vectors, where  $p$  is the rank of  $K$ , and  $n$  is the dimension of the row space, and  $m$  is the dimension of the column space.  $y = Kx$ , and multiplying

to understand the information in these concepts, you should

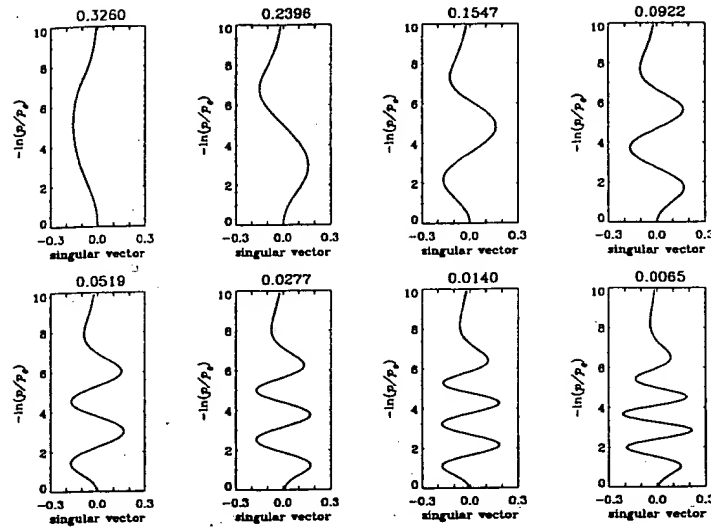


Fig. 2.2 The singular vectors of the weighting functions of Figure 1.1. The corresponding singular values are given above each panel.

by  $U^T$  gives

$$U^T y = \Lambda V^T x, \quad (2.6)$$

so that, putting  $y' = U^T y$  and  $x' = V^T x$  we obtain

$$y' = \Lambda x' \quad (2.7)$$

indicating that the  $p$  transformed measurements  $y'$  in column space, are each proportional to a component of a transformed state  $x'$  in  $p$ -dimensional row space. The  $V$  matrix forms a natural basis for row space, closely related to the  $U$  matrix basis for column space.

Fig. 2.2 shows the eight singular vectors of the weighting functions of Fig. 1.1. The corresponding singular values are given above each frame. This representation can be seen to be qualitatively similar to a Fourier representation, in that the functions are orthogonally, oscillatory, and with an increasing number of oscillations. Structures in the profile corresponding to the singular vectors can be thought of as being measured independently, with a sensitivity given by the singular value. If there were measurement error, then the finer scale structures with smaller singular values would be measured to a lower precision, for example vector number five is measured with a precision about 6.3 times smaller (i.e.  $0.3260/0.0519$ ) than vector number one.

## 2.3 Linear Problems with Measurement Error

### 2.3.1 Describing experimental error

All real measurements are subject to experimental error or 'noise', so that any practical retrieval must allow for this. The proper treatment of experimental error is the dominant consideration in designing retrieval methods. Thus we need a formalism in which to express uncertainty in measurements and the resulting uncertainty in retrievals, and with which to ensure that the latter is as small as possible.

A description of experimental error in terms of probability density functions (*pdf*'s), using a Bayesian approach to probability, gives useful insight. The statement that a scalar measurement has a value  $\bar{y}$  and an error  $\sigma$  is a shorthand way of saying that our knowledge of the true value of the measured parameter is described by a *pdf*  $P(y)$  with a mean  $\bar{y}$  and variance  $\sigma^2$ :

$$\begin{aligned}\bar{y} &= \int y P(y) dy \\ \sigma^2 &= \int (y - \bar{y})^2 P(y) dy\end{aligned}\quad (2.8)$$

and that the probability that  $y$  lies in  $(y, y + dy)$  is  $P(y) dy$ . Probability interpreted this way is a measure of knowledge about  $y$ , rather than a distribution function for repeated trials of a measurement of  $y$ , though repeated trials are a useful way of estimating probability when appropriate. The form of  $P(y)$  is almost always taken to be Gaussian or 'normal':

$$P(y) = N(y - \bar{y}, \sigma) = \frac{1}{(2\pi)^{1/2} \sigma} \exp \left\{ -\frac{(y - \bar{y})^2}{2\sigma^2} \right\}. \quad (2.9)$$

This is usually a good approximation for experimental error, and is very convenient for algebraic manipulations. As we shall see in section 2.7, if the only information available about a *pdf* is its mean and variance, then the Gaussian distribution is the one which contains the least information about the measured quantity, in the sense used in information theory, to be discussed in section 2.5.

When the measured quantity is a vector, a probability density can still be defined over measurement space,  $P(\mathbf{y})$ , with the interpretation that  $P(\mathbf{y}) d\mathbf{y}$  (where  $d\mathbf{y}$  is shorthand for  $dy_1 \dots dy_m$ ) is the probability that the true value of the measurement lies in a multidimensional interval  $(\mathbf{y}, \mathbf{y} + d\mathbf{y})$  in measurement space. Different elements of a vector may be correlated, in the sense that

$$S_{ij} = \mathcal{E}\{(y_i - \bar{y}_i)(y_j - \bar{y}_j)\} \neq 0, \quad (2.10)$$

where  $S_{ij}$  is called the *covariance* of  $y_i$  and  $y_j$ , and  $\mathcal{E}$  is the expected value operator. These covariances can be assembled into a matrix, which we will denote by  $S_y$  for the covariance matrix of  $\mathbf{y}$ . Its diagonal elements are clearly the variances of the individual elements of  $\mathbf{y}$ . A covariance matrix is symmetric and non-negative

definite, and is also covariance in preference to  $\sigma^2$  for variance, because the Gaussian distribution

$$P(\mathbf{y}) = \frac{1}{(2\pi)^{m/2} |S_y|^{1/2}} \exp \left\{ -\frac{1}{2} (\mathbf{y} - \bar{\mathbf{y}})^T S_y^{-1} (\mathbf{y} - \bar{\mathbf{y}}) \right\}$$

where  $S_y$  must be invertible if the  $y_i$  are known exactly,  $S_y$  must be related to the  $S_y$  is diagonal, using

$$P(\mathbf{y}) = \frac{1}{(2\pi)^{m/2} |S_y|^{1/2}} \exp \left\{ -\frac{1}{2} (\mathbf{y} - \bar{\mathbf{y}})^T S_y^{-1} (\mathbf{y} - \bar{\mathbf{y}}) \right\}$$

where  $\mathbf{z} = L^T(\mathbf{y} - \bar{\mathbf{y}})$  are the eigenvalues.) Thus each element of  $\mathbf{z}$ :

where the eigenvectors of  $S_y$  provide a basis for  $\mathbf{y}$ . Statistically independent components with zero eigenvalues,  $c_i$ . Such components  $p_i$  and can be eliminated. Notice that sum

and are ellipsoids in  $\mathbf{y}$  space. The eigenvectors of  $S_y$ . These ellipsoids are

### 2.3.2 The Bayesian

We now turn to the problem of the state. The state  $\mathbf{y}$  according to the formalism, so that the state is statistically independent of measurement error

or 'noise', so that any practical experimental error is the noise. Thus we need a formalism to describe the resulting uncertainty in the measurement as small as possible. Probability density functions provide useful insight. The state  $\sigma$  is a shorthand way of saying that the parameter is described

(2.8)

ly. Probability interpreted as a distribution function for trials are a useful way of saying that  $y$  is almost always taken

$$\frac{(y - \bar{y})^2}{2\sigma^2} \} \quad (2.9)$$

ror, and is very convenient. If, if the only information is the Gaussian distribution is measured quantity, in the section 2.5.

density can still be defined that  $P(y) dy$  (where  $dy$  is the value of the measurement in the measurement space. Different

$$), \quad (2.10)$$

re expected value operator. which we will denote by  $S_y$  are clearly the variances of symmetric and non-negative

definite, and is almost always positive definite. I use the notation  $S_y$  is used for covariance in preference to  $\Sigma_y$ , which might be thought more logical by analogy to  $\sigma^2$  for variance, because of the possible confusion with summation.

The Gaussian distribution for a vector is of the form:

$$P(y) = \frac{1}{(2\pi)^{n/2} |S_y|^{1/2}} \exp \left\{ -\frac{1}{2} (y - \bar{y})^T S_y^{-1} (y - \bar{y}) \right\} \quad (2.11)$$

where  $S_y$  must be nonsingular. If it is singular then there are components of  $y$  that are known exactly, equivalent to  $\sigma = 0$  in the scalar case. Eq. (2.11) can be seen to be related to the scalar Gaussian distribution by transforming to a basis in which  $S_y$  is diagonal, using the eigenvector decomposition  $S_y = L \Lambda L^T$ :

$$P(y) = \frac{1}{(2\pi)^{n/2} |L \Lambda L^T|^{1/2}} \exp \left\{ -\frac{1}{2} (y - \bar{y})^T L \Lambda^{-1} L^T (y - \bar{y}) \right\} \quad (2.12)$$

$$= \frac{1}{(2\pi)^{n/2} |\Lambda|^{1/2}} \exp \left\{ -\frac{1}{2} z^T \Lambda^{-1} z \right\}, \quad (2.13)$$

where  $z = L^T (y - \bar{y})$ . (See Appendix A.2 for the algebra of eigenvectors and eigenvalues.) Thus the pdf can be written as a product of the independent pdf's of each element of  $z$ :

$$P(z) = \prod_i \frac{1}{(2\pi \lambda_i)^{1/2}} \exp \left\{ -\frac{z_i^2}{2\lambda_i} \right\}, \quad (2.14)$$

where the eigenvalue  $\lambda_i$  is the variance of  $z_i$ . The eigenvector transformation provides a basis for measurement space in which the transformed measurements are statistically independent. A singular covariance matrix would have one or more zero eigenvalues, corresponding to elements of  $z$  that are known without error. Such components presumably would not correspond to real physical measurements, and can be eliminated or ignored as appropriate.

Notice that surfaces of constant probability of the pdf are of the form

$$(y - \bar{y})^T S^{-1} (y - \bar{y}) = \sum_i z_i^2 / \lambda_i = \text{constant} \quad (2.15)$$

and are ellipsoids in measurement space, with principal axes corresponding to the eigenvectors of  $S_y$ , and the lengths of these principal axes proportional to  $\lambda_i^{1/2}$ . These ellipsoids can be thought of as the multivariate equivalent of error bars.

### 2.3.2 The Bayesian approach to inverse problems

We now turn to the question of relating the pdf of the measurement to the pdf of the state. The act of measurement maps the state into the measurement space according to the forward model, Eq. (2.2). The measurement error  $\epsilon$  is known only statistically, so that even though  $F(x)$  is a deterministic mapping, in the presence of measurement error a point in state space maps into a region in measurement

space determined by the probability density function of  $\epsilon$ . Conversely, if  $y$  is a given measurement, it could be the result of a mapping from anywhere in a region of state space described by some *pdf*, rather than from a single point, even in the absence of a null space. Furthermore, we may have some prior information about the state, for example a climatology, which can also be conveniently described by a *pdf*, and which can be used to constrain the solution. Such prior knowledge can be thought of as a *virtual measurement*, as, like a real measurement, it provides us with an estimate of some function (often the identity) of the state, together with a measure of the accuracy of the estimate, albeit usually rather a poor one.

We saw in Chapter 1 that the simple-minded approach of solving equations can lead to disaster, so we need to find a more subtle approach. The Bayesian approach is a very helpful way of looking at the noisy inverse problem, in which we have some prior understanding or expectation about some quantity, and want to update the understanding in the light of new information. Imperfect prior knowledge can be quantified as a probability density function over the state space. A measurement, also imperfect because of experimental error, can be quantified as a *pdf* over measurement space. We would like to know how the measurement *pdf* maps into state space, and combines with prior knowledge. Bayes' theorem tells us how.

### 2.3.2.1 Bayes' theorem

Probability density is a scalar-valued function, in our case a function of the state vector or the measurement vector. Let us define:

$P(x)$  as the prior *pdf* the state  $x$ . This means that the quantity  $P(x) dx$  is the probability before the measurement that  $x$  lies in the multidimensional volume  $(x, x + dx)$ , expressing quantitatively our knowledge of  $x$  before the measurement is made. It is normalised so that  $\int P(x) dx = 1$ .

$P(y)$  as the prior *pdf* of the measurement, with a similar meaning. This is the *pdf* of the measurement before it is made.

$P(x, y)$  as the joint prior *pdf* of  $x$  and  $y$ , meaning that  $P(x, y) dx dy$  is the probability that  $x$  lies in  $(x, x + dx)$  and  $y$  lies in  $(y, y + dy)$ .

$P(y|x)$  as the conditional *pdf* of  $y$  given  $x$ , meaning that  $P(y|x) dy$  is the probability that  $y$  lies in  $(y, y + dy)$  when  $x$  has a given value.

$P(x|y)$  as the conditional *pdf* of  $x$  given  $y$ , meaning that  $P(x|y) dx$  is the probability that  $x$  lies in  $(x, x + dx)$  when  $y$  has a given value. This is the quantity that is of interest for solving the inverse problem.

It may seem slightly odd to use the same symbol  $P$  for all of these different functions, but in each case the argument makes it clear which *pdf* is referred to, and the convention eliminates a forest of subscripts.

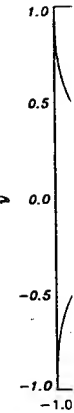


Fig. 2.3

Fig. 2.3 illustrates of  $P(x, y)$ , and  $P(x)$ .

and likewise  $P(y)$  is  $P(y|x)$  is proportional of  $x$ , e.g., along the  $x$  is such that  $\int P(y|x)$  line:

Inserting Eq. (2.16) f

We can use equivalence eliminating  $P(x, y)$  relationship between vector case it states

The left hand side of the measurement is  $P(x)$  of the state which would be obtained if

if  $\epsilon$ . Conversely, if  $y$  is a point anywhere in a region, a single point, even in the absence of prior information about the state, it provides us with a measurement, it provides us with the state, together with a rather poor one.

h of solving equations can be. The Bayesian approach is, in which we have some prior knowledge, and want to update the prior knowledge can be in a space. A measurement, identified as a *pdf* over measurement *pdf* maps into state space tells us how.

use a function of the state

the quantity  $P(x) dx$  is the probability in the multidimensional space of knowledge of  $x$  before a measurement at  $\int P(x) dx = 1$ .

or meaning. This is the *pdf*

$P(x, y) dx dy$  is the probability of  $x$  and  $y$  together.

at  $P(y|x) dy$  is the probability of  $y$  given the value of  $x$ .

that  $P(x|y) dx$  is the probability of  $x$  given the value of  $y$ . This is the problem.

of these different functions, the *pdf* is referred to, and the

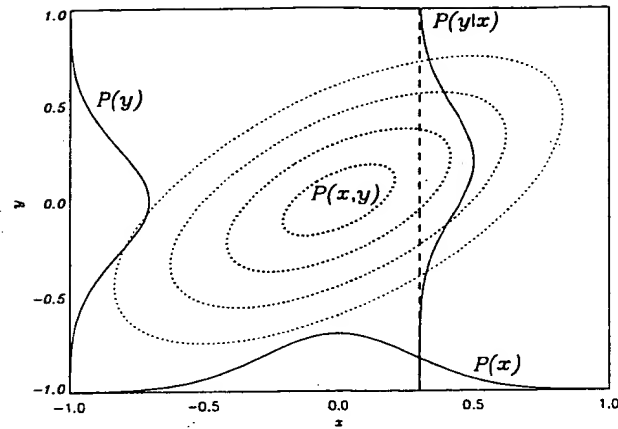


Fig. 2.3 Illustrating Bayes' theorem for a two-dimensional case.

Fig. 2.3 illustrates these concepts when  $x$  and  $y$  are scalars. The contours are of  $P(x, y)$ , and  $P(x)$  is given by the integral over all values of  $y$ :

$$P(x) = \int_{-\infty}^{\infty} P(x, y) dy, \quad (2.16)$$

and likewise  $P(y)$  is found by integrating over all values of  $x$ . The conditional *pdf*  $P(y|x)$  is proportional to the values of  $P(y, x)$  as a function of  $y$  for a given value of  $x$ , e.g., along the cut marked by a dotted line. The constant of proportionality is such that  $\int P(y|x) dy = 1$ , so  $P(y, x)$  should be divided by the integral along the line:

$$P(y|x) = \frac{P(x, y)}{\int P(x, y) dy}. \quad (2.17)$$

Inserting Eq. (2.16) for the integral we obtain

$$P(y|x) = P(x, y)/P(x). \quad (2.18)$$

We can use equivalent arguments to show that  $P(x|y) = P(x, y)/P(y)$ , and by eliminating  $P(x, y)$  between the two equations we obtain Bayes' theorem as the relationship between the two different conditional *pdf*'s. When generalised for the vector case it states that

$$P(x|y) = \frac{P(y|x)P(x)}{P(y)}. \quad (2.19)$$

The left hand side of Eq. (2.19),  $P(x|y)$ , is the posterior *pdf* of the state when the measurement is given. This is what we want to update the prior knowledge  $P(x)$  of the state with the measurement.  $P(y|x)$  describes the knowledge of  $y$  that would be obtained if the state were  $x$ . To write it down explicitly requires only



the forward model and the statistical description of the measurement error. The only remaining quantity required is the denominator,  $P(y)$ . Formally this can be obtained by integrating the expression for  $P(x, y)$ , namely  $P(y|x)P(x)$ , over all  $x$ , but in practice it is only a normalising factor, and is often not needed.

We now have a conceptual approach to the inverse problem:

- Before we make a measurement we have prior knowledge expressed as a prior *pdf*;
- The measurement process is expressed as a forward model which maps the state space into measurement space;
- Bayes' theorem provides a formalism to invert this mapping and calculate a posterior *pdf* by updating the prior *pdf* with a measurement *pdf*.

Note that the Bayesian view is general. It is not just an inverse method which produces a solution which may be compared with those produced by other methods, rather it encompasses all inverse methods by providing a way of characterising the class of possible solutions, considering all possible states, and assigning a probability density to each.

The forward model is never explicitly inverted in this approach, but then an explicit state is not produced as an 'answer'. It provides us with some intuition about how the measurement improves knowledge of the state, but to obtain an explicit retrieval we must choose one state from the ensemble described by the posterior *pdf*, perhaps the expected value or most probable value of the state, together with some measure of the width of the *pdf* to give the accuracy of the retrieval. Thus further work is needed, resulting in expressions mathematically equivalent to inverting the forward model.

### 2.3.2.2 Example: The Linear problem with Gaussian statistics

As a simple illustration of the Bayesian approach consider a linear problem in which all of the *pdf*'s are Gaussian. The Gaussian distribution is commonly used to model probability density functions because many processes are well described by it and because it is algebraically convenient. We use it here for just those reasons.

The multivariate Gaussian distribution for a random vector  $x$  is obtained from Eq. (2.11). The maximum probability value for  $x$  is clearly equal to the expected value  $\bar{x}$ , because the *pdf* is symmetric about  $x = \bar{x}$ , but the reader may like to try:

⇒ *Exercise 2.2:* Solve  $\partial P/\partial x = 0$  for the maximum probability value, and integrate  $\int xP(x) dx$  to confirm that both are equal to  $\bar{x}$

A linear problem is one for which the forward model is linear:

$$y = F(x) + \epsilon = Kx + \epsilon. \quad (2.20)$$

Gaussian statistics are usually a good approximation for the errors in real measure-

ments, so express  $P(y$

-2

where  $c_1$  is a constant but convenient, is to

where  $x_a$  is the *a priori*

Substituting Eqs. (2.

$$-2 \ln P(x|y) = (y$$

where  $c_3$  is a constant it as

i.e. the posterior *pdf* variance  $\hat{S}$ . We can re-terms that are quadr

gives

Likewise equating th

(-)

I have used  $x^T$  is used gives the transpose of for any value of  $x$ , a

and hence

$$\hat{x} =$$

We could equate the Eq. (2.11)  $c_1$ ,  $c_2$  and normalise the *pdf*'s.

5



e measurement error. The  
 $P(y)$ . Formally this can be  
 ely  $P(y|x)P(x)$ , over all  $x$ ,  
 en not needed.  
 problem:

knowledge expressed as a

ard model which maps the

this mapping and calculate  
 a measurement *pdf*.

; an inverse method which  
 roduced by other methods,  
 a way of characterising the  
 and assigning a probability

s approach, but then an ex-  
 s with some intuition about  
 , but to obtain an explicit  
 scribed by the posterior *pdf*,  
 e state, together with some  
 the retrieval. Thus further  
 equivalent to inverting the

statistics

er a linear problem in which  
 is commonly used to model  
 re well described by it and  
 r just those reasons.

a vector  $x$  is obtained from  
 early equal to the expected  
 the reader may like to try:

num probability value, and  
 equal to  $\bar{x}$

linear:

(2.20)

r the errors in real measure-

ments, so express  $P(y|x)$  as

$$-2 \ln P(y|x) = (y - Kx)^T S_e^{-1} (y - Kx) + c_1, \quad (2.21)$$

where  $c_1$  is a constant and  $S_e$  is the measurement error covariance. Less realistic,  
 but convenient, is to describe prior knowledge of  $x$  by a Gaussian *pdf*:

$$-2 \ln P(x) = (x - x_a)^T S_a^{-1} (x - x_a) + c_2, \quad (2.22)$$

where  $x_a$  is the *a priori* value of  $x$ , and  $S_a$  is the associated covariance matrix

$$S_a = E\{(x - x_a)(x - x_a)^T\}. \quad (2.23)$$

Substituting Eqs. (2.21) and (2.22) in Eq. (2.19) we obtain for the posterior *pdf*:

$$-2 \ln P(x|y) = (y - Kx)^T S_e^{-1} (y - Kx) + (x - x_a)^T S_a^{-1} (x - x_a) + c_3, \quad (2.24)$$

where  $c_3$  is a constant. This is a quadratic form in  $x$ , so it must be possible to write  
 it as

$$-2 \ln P(x|y) = (x - \hat{x})^T \hat{S}^{-1} (x - \hat{x}) + c_4, \quad (2.25)$$

ie the posterior *pdf* is also a Gaussian distribution with expected value  $\hat{x}$  and co-  
 variance  $\hat{S}$ . We can relate Eq. (2.25) to Eq. (2.24) by equating like terms. Equating  
 terms that are quadratic in  $x$ :

$$x^T K^T S_e^{-1} K x + x^T S_a^{-1} x = x^T \hat{S}^{-1} x \quad (2.26)$$

gives

$$\hat{S}^{-1} = K^T S_e^{-1} K + S_a^{-1}. \quad (2.27)$$

Likewise equating the terms linear in  $x^T$  gives:

$$(-Kx)^T S_e^{-1} (y) + (x)^T S_a^{-1} (-x_a) = x^T \hat{S}^{-1} (-\hat{x}). \quad (2.28)$$

I have used  $x^T$  is used for convenience only, as equating terms linear in  $x$  simply  
 gives the transpose of this equation. Cancelling the  $x^T$ 's, because this must be valid  
 for any value of  $x$ , and substituting for  $\hat{S}^{-1}$  from Eq. (2.27) gives

$$K^T S_e^{-1} y + S_a^{-1} x_a = (K^T S_e^{-1} K + S_a^{-1}) \hat{x} \quad (2.29)$$

and hence

$$\begin{aligned} \hat{x} &= (K^T S_e^{-1} K + S_a^{-1})^{-1} (K^T S_e^{-1} y + S_a^{-1} x_a) \\ &= x_a + (K^T S_e^{-1} K + S_a^{-1})^{-1} K^T S_e^{-1} (y - Kx_a). \end{aligned} \quad (2.30)$$

We could equate the constant terms, but they add no further information. From  
 Eq. (2.11)  $c_1$ ,  $c_2$  and  $c_4$  must all be of the form  $-\ln[(2\pi)^n |S|]$  in order to correctly  
 normalise the *pdf*'s. An alternate form for  $\hat{x}$  can be obtained from Eq. (2.30):

$$\hat{x} = x_a + S_a K^T (K S_a K^T + S_e)^{-1} (y - Kx_a). \quad (2.31)$$

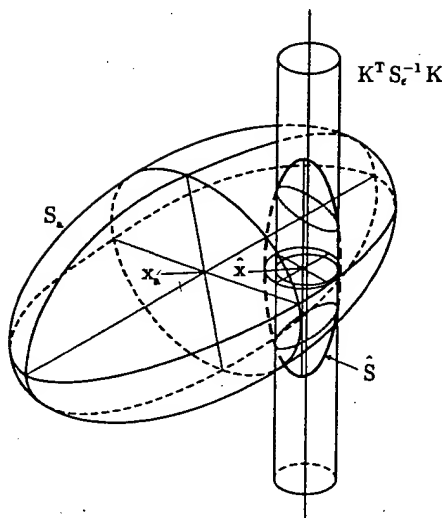


Fig. 2.4 Illustrating the relationship between the prior state estimate, the measurement mapped into state space, and the posterior estimate, for a three-dimensional state space and a two-dimensional measurement space. The large ellipsoid is a contour of the prior *pdf*, the cylinder is a contour of the *pdf* of the state given only the measurement, and the small ellipsoid is a contour of the posterior *pdf*.

A derivation of this will be given in section 4.1. I will describe Eq. (2.30) as the '*n*-form', and Eq. (2.31) as the '*m*-form' from the order of the matrix to be inverted.

Remember the Bayesian solution to the inverse problem is not  $\hat{x}$ , but is the Gaussian *pdf*  $P(x|y)$ , of which  $\hat{x}$  is the expected value and  $\hat{S}$  is the covariance. Note  $\hat{x}$  is a linear function of the prior expected value and the measurement, as might be expected for a linear problem, and that the *inverse* covariance matrix  $\hat{S}^{-1}$  is a linear function of the inverse prior covariance matrix and the inverse measurement error covariance. The terms in Eq. (2.27) are known as Fisher information matrices, and will be discussed in more detail in section 2.5.1.

Fig. 2.4 provides a geometric illustration of the relationship between the prior covariance, the measurement and the posterior covariance when state space has three dimensions and measurement space has two. The large ellipsoid centred on  $x_a$  represents a contour of the prior covariance, outlining the region of state space within which the state is likely to lie. The cylinder represents the region in which states consistent with the measurement might lie, where the axis of the ellipsoid is the set of states corresponding exactly to the measurement, and the cylinder encloses experimental error. The direction of the axis represents the null space. The weighting functions for the two measurement elements are orthogonal to the axis. The small ellipsoid outlines the region which is consistent with both the prior information and the measurement. Note that its centre,  $\hat{x}$ , does not lie on the axis of the cylinder, i.e. the expected value does not fit the measurement exactly.

## 2.4 Degrees of

### 2.4.1 How many

When experimental that can in principle values will now be u of the values is large useful independent the exact problem th useless, a phenomen pieces of information subspace in which ti

As a contrived e an instrument which forward model:

where the errors  $\epsilon_i$  ing the orthogonal

where the errors are be a much smaller c may be no useful in

To identify the ance with the natur covariance. Any co ment error is in eff Unfortunately, cov indicating correlati is not immediately the basis so that th is to transform from

so that the transfor

## 2.4 Degrees of Freedom

### 2.4.1 How many independent quantities can be measured?

When experimental error is not present there are  $p$  independent pieces of information that can in principle be determined from the measurement, but with error, these  $p$  values will now be uncertain to some extent. It is conceivable that the error in some of the values is large enough that the component is worthless, so that the number of useful independent pieces of information may be less than  $p$ . It is possible even in the exact problem that numerical rounding error causes some components to become useless, a phenomenon called 'ill-conditioning'. The number of useful independent pieces of information can be regarded as the 'effective' rank of the problem, and the subspace in which they lie as the 'effective row space'.

As a contrived example, consider a state vector with two elements,  $(x_1, x_2)$ , and an instrument which can measure two rather similar quantities,  $y_1$  and  $y_2$  with the forward model:

$$\begin{pmatrix} y_1 \\ y_2 \end{pmatrix} = \begin{pmatrix} 1.01 & 0.99 \\ 0.99 & 1.01 \end{pmatrix} \begin{pmatrix} x_1 \\ x_2 \end{pmatrix} + \begin{pmatrix} \epsilon_1 \\ \epsilon_2 \end{pmatrix} \quad (2.32)$$

where the errors  $\epsilon_i$  are independent with variance  $\sigma^2$ . This is equivalent to measuring the orthogonal combinations  $z_1$  and  $z_2$ :

$$\begin{aligned} z_1 &= y_1 + y_2 = 2(x_1 + x_2) + \epsilon_1 + \epsilon_2 \\ z_2 &= y_1 - y_2 = 0.02(x_1 - x_2) + \epsilon_1 - \epsilon_2 \end{aligned} \quad (2.33)$$

where the errors are still independent, with variances  $2\sigma^2$ . However  $z_2$  is likely to be a much smaller quantity than  $z_1$  for arbitrary values of  $x_1$  and  $x_2$ , so that there may be no useful information about the difference between  $x_1$  and  $x_2$ .

To identify the effective row space, we compare the measurement error covariance with the natural variability of the measurement vector as expressed by its prior covariance. Any component whose natural variability is smaller than the measurement error is in effect not measurable, and is not part of the effective row space. Unfortunately, covariance matrices generally have non-zero off-diagonal elements indicating correlations between variability of different elements of the vectors, so it is not immediately obvious how to do this. To compare them properly we transform the basis so that the off-diagonal elements disappear. The simplest way to do this is to transform from  $\mathbf{K}$  to  $\bar{\mathbf{K}}$  by

$$\bar{\mathbf{x}} = \mathbf{S}_a^{-\frac{1}{2}}(\mathbf{x} - \mathbf{x}_a) \quad \text{and} \quad \bar{\mathbf{y}} = \mathbf{S}_\epsilon^{-\frac{1}{2}}\mathbf{y} \quad (2.34)$$

so that the transformed forward model is

$$\bar{\mathbf{y}} = \mathbf{S}_\epsilon^{-\frac{1}{2}}\mathbf{K}\mathbf{S}_a^{\frac{1}{2}}\bar{\mathbf{x}} + \mathbf{S}_\epsilon^{-\frac{1}{2}}\boldsymbol{\epsilon} = \bar{\mathbf{K}}\bar{\mathbf{x}} + \bar{\boldsymbol{\epsilon}}. \quad (2.35)$$

$\mathbf{S}_\epsilon^{-1}\mathbf{K}$

mate, the measurement mapped  
nsional state space and a two-  
ur of the prior pdf, the cylinder  
nt, and the small ellipsoid is a

describe Eq. (2.30) as the  
of the matrix to be inverted.  
blem is not  $\hat{\mathbf{x}}$ , but is the  
id  $\hat{\mathbf{S}}$  is the covariance. Note  
the measurement, as might  
covariance matrix  $\hat{\mathbf{S}}^{-1}$  is a  
id the inverse measurement  
isher information matrices,

ationship between the prior  
ance when state space has  
e large ellipsoid centred on  
g the region of state space  
resents the region in which  
re the axis of the ellipsoid  
urement, and the cylinder  
represents the null space.  
ents are orthogonal to the  
sistent with both the prior  
,  $\hat{\mathbf{x}}$ , does not lie on the axis  
measurement exactly.

where  $\bar{K} = S_e^{-\frac{1}{2}} K S_a^{\frac{1}{2}}$ . The covariances of  $\bar{x}$  and  $\bar{\epsilon}$  are both unit matrices in this transformed system, for example

$$S_{\bar{\epsilon}} = \mathcal{E}\{\bar{\epsilon}\bar{\epsilon}^T\} = S_e^{-\frac{1}{2}} \mathcal{E}\{\epsilon\epsilon^T\} S_e^{-\frac{1}{2}} = S_e^{-\frac{1}{2}} S_e S_e^{-\frac{1}{2}} = I_m. \quad (2.36)$$

A covariance matrix, or its inverse, has an infinite number of square roots, see Appendix A.2. Two are particularly useful, namely the positive definite symmetric square root constructed from its eigenvector decomposition,

$$S = L\Lambda L^T \Rightarrow S^{\frac{1}{2}} = L\Lambda^{\frac{1}{2}}L^T \text{ and } S^{-\frac{1}{2}} = L\Lambda^{-\frac{1}{2}}L^T. \quad (2.37)$$

and the upper triangular Cholesky decomposition, of the form  $S = T^T T$ , see section 5.8.1.1 and exercise 5.3. Algebraic derivations are clearer when written in terms of  $S^{\frac{1}{2}}$ , but numerically the Cholesky decomposition is considerably more efficient, and should be used in preference. With this square root we can write

$$\bar{x} = T_a^{-T}(x - x_a), \quad \bar{y} = T_e^{-T}y \text{ and } \bar{K} = T_e^{-T} K T_a^T, \quad (2.38)$$

where the superscript  $-T$  means the transpose of the inverse. This transformation of  $y$  using  $S_e^{-\frac{1}{2}}$  or  $T^{-T}$  is called *prewhitening* as it transforms the noise into white noise.

$\Rightarrow$  **Exercise 2.3:** Why does it not matter which square root we use for prewhitening?

The measurement error covariance and the prior state covariance cannot be compared directly, as they are in different spaces. Rather we should compare the measurement error covariance with the prior covariance of  $\bar{y}$ :

$$S_{\bar{y}} = \mathcal{E}\{\bar{y}\bar{y}^T\} = \mathcal{E}\{(\bar{K}\bar{x} + \bar{\epsilon})(\bar{K}\bar{x} + \bar{\epsilon})^T\} = \bar{K}\bar{K}^T + I_m. \quad (2.39)$$

The component of this covariance due to the variability of the state is  $\bar{K}\bar{K}^T$ , and that due to measurement noise is  $I_m$ .  $\bar{K}\bar{K}^T$  is not normally diagonal, and we still cannot easily compare, so we carry out one more transformation of the forward model, the singular value decomposition  $\bar{K} = U\Lambda V^T$ , as in section 2.2.2 but now with prewhitening, giving

$$y' = U^T \bar{y} = U^T \bar{K} \bar{x} + U^T \bar{\epsilon} = \Lambda V^T \bar{x} + \epsilon' = \Lambda x' + \epsilon'. \quad (2.40)$$

The covariance matrices of  $\epsilon' = U^T \bar{\epsilon}$  and  $x' = V^T \bar{x}$  are both still unity, because  $U^T U$  and  $V^T V$  are both unit matrices. The covariance of the variability of  $y'$  is therefore  $\Lambda^2 + I_m$ , a diagonal matrix, and the elements of  $y'$  which vary more than the noise are those for which  $\lambda_i^2 \gtrsim 1$ . Element corresponding to zero singular values carry no information, only noise. Thus

the number of  
measurement error,  
values of  $S_e^{-\frac{1}{2}}$

$\bar{K}$  will depend on values will not. They comprise the effect by  $S_a^{-\frac{1}{2}}$ ; to return with  $S_a^{\frac{1}{2}}$ .

To use the standard define a state vector is clearly a set of eigenvalues of  $\sigma_e^2 = 0.25 K^2$ , as at levels spaced at assumption, take  $S$  the singular vector values are a factor signal-to-noise ratio of radiance  $y_i$  is 3.16 for a single radiance between radiance is expressed by the measured with a standard the last three with about four.

#### 2.4.2 Degrees

The above discussion pieces of information are greater than all or of  $\bar{K}^T \bar{K}$  greater

We can formalize concept of 'degree' of a measurement the simplest case measurement of a

where  $x$  has prior

both unit matrices in this

$$S_\epsilon^{-\frac{1}{2}} = I_m. \quad (2.36)$$

number of square roots, see positive definite symmetric ion,

$$= LA^{-\frac{1}{2}}L^T. \quad (2.37)$$

form  $S = T^T T$ , see sec- arer when written in terms onsiderably more efficient, we can write

$$T_\epsilon^{-T} K T_a^T, \quad (2.38)$$

verse. This transformation forms the noise into white

square root we use for pre-

tate covariance cannot be er we should compare the of  $\tilde{y}$ :

$$\tilde{K}\tilde{K}^T + I_m. \quad (2.39)$$

of the state is  $\tilde{K}\tilde{K}^T$ , and ally diagonal, and we still sformation of the forward s in section 2.2.2 but now

$$= \Lambda x' + \epsilon'. \quad (2.40)$$

e both still unity, because e of the variability of  $y'$  is f  $y'$  which vary more than ling to zero singular values

the number of independent measurements made to better than measurement error, the effective rank of the problem, is the number of singular values of  $S_\epsilon^{-\frac{1}{2}} K S_a^{\frac{1}{2}}$  which are greater than about unity.

$\tilde{K}$  will depend on which square roots have been used for scaling, but its singular values will not. The corresponding singular vectors in row space, the columns of  $V$ , comprise the effective row space. These are vectors in the state space transformed by  $S_a^{-\frac{1}{2}}$ ; to return them to the original untransformed state space, transform back with  $S_a^{\frac{1}{2}}$ .

To use the standard example from Chapter 1 to illustrate this point, we must first define a state vector and choose some covariance matrices. The measurement vector is clearly a set of eight radiances, and we can take  $S_\epsilon$  to be diagonal with a variance of  $\sigma_\epsilon^2 = 0.25 K^2$ , as in chapter 1. Let us choose the state vector to be the temperature at levels spaced at intervals of 0.1 in  $z = \ln p$ , and, to make a fairly noncommittal assumption, take  $S_a$  to be diagonal with a variance of say  $\sigma_a^2 = 100 K^2$ . In this case the singular vectors of  $\tilde{K}$  are the same as those of  $K$ , Fig. 2.2, and the singular values are a factor of  $\sigma_a/\sigma_\epsilon = 20$  larger. The measurements might appear to have a signal-to-noise ratio of 20, but that would be an overestimate, because the variance of radiance  $y_i$  is not  $\sigma_a^2$ , but  $\sigma_a^2 \sum_j K_{ij}^2 \approx 2.5 K^2$ , giving a signal-to-noise ratio of 3.16 for a single radiance. Even that is an overestimate because of the correlations between radiance variability expressed by  $K S_a K^T$ . The real signal-to-noise ratio is expressed by the singular values of  $\tilde{K}$ . The first five singular vectors would be measured with a signal-to-noise ratios of 6.5, 4.8, 3.1, 1.8 and 1.0 respectively, and the last three with signal to noise of less than unity, so the effective rank of  $K$  is about four.

#### 2.4.2 Degrees of freedom for signal

The above discussion gives a qualitative description of the number of independent pieces of information in a measurement as the number of singular values of  $\tilde{K}$  which are greater than about unity, which is the same as the number of eigenvalues of  $\tilde{K}\tilde{K}^T$  or of  $K^T \tilde{K}$  greater than about unity.

We can formalise this concept and make it more precise by relating it to the concept of 'degrees of freedom', and enquiring how many of the degrees of freedom of a measurement are related to signal, and how many are related to noise. In the simplest case with one degree of freedom let us consider making a single direct measurement of a scalar, with noise:

$$y = x + \epsilon, \quad (2.41)$$

where  $x$  has prior variance  $\sigma_a^2$  and  $\epsilon$  has  $\sigma_\epsilon^2$ . The prior variance of  $y$  will be  $\sigma_y^2 =$

$\sigma_a^2 + \sigma_\epsilon^2$ . The best estimate of  $x$  will be, from Eq. (2.30),

$$\hat{x} = \frac{\sigma_\epsilon^{-2}x + \sigma_a^{-2}x_a}{\sigma_\epsilon^{-2} + \sigma_a^{-2}} = \frac{\sigma_a^2x + \sigma_\epsilon^2x_a}{\sigma_a^2 + \sigma_\epsilon^2}. \quad (2.42)$$

If  $\sigma_a^2 \gg \sigma_\epsilon^2$  then  $y$  will be providing information about  $x$ , but if  $\sigma_a^2 \ll \sigma_\epsilon^2$  then it will be providing information about  $\epsilon$ . In the first case we can say that the measurement provides a 'degree of freedom for signal', and in the second case a 'degree of freedom for noise'.

Now consider the general case of measuring a vector  $y$  with  $m$  degrees of freedom. The most probable state in the Gaussian linear case is the one which minimises

$$\chi^2 = (x - x_a)^T S_a^{-1} (x - x_a) + \epsilon^T S_\epsilon^{-1} \epsilon, \quad (2.43)$$

where  $\epsilon = y - Kx$ . As we have seen, Eq. (2.30), the minimum is at

$$\hat{x} - x_a = G(y - Kx_a) = G[K(x - x_a) + \epsilon], \quad (2.44)$$

where the equivalent of the contribution function of Eq. (1.5) is now a matrix  $G$ , given by

$$G = (K^T S_\epsilon^{-1} K + S_a^{-1})^{-1} K^T S_\epsilon^{-1} = S_a K^T (K S_a K^T + S_\epsilon)^{-1}. \quad (2.45)$$

This matrix has various names in different fields, for example it may be described as a generalised inverse of  $K$ , or as a *gain matrix*, the term I will normally use in this book in preference to contribution function matrix. At the minimum the expected value of  $\chi^2$  is equal to the number of degrees of freedom, or the number of measurements,  $m$ . This can be divided into two parts, corresponding to the two terms in Eq. (2.43):

$$d_s = \mathcal{E}\{(\hat{x} - x_a)^T S_a^{-1} (\hat{x} - x_a)\} \quad (2.46)$$

$$d_n = \mathcal{E}\{\hat{\epsilon}^T S_\epsilon^{-1} \hat{\epsilon}\}. \quad (2.47)$$

The first term measures the part of  $\chi^2$  attributable to the state vector, and the second term that attributable to noise. They may therefore be described as the number of 'degrees of freedom for signal' and 'degrees of freedom for noise', respectively. Thus  $d_s$  describes the number of useful independent quantities there are in a measurement, and hence is a measure of information. It is not necessarily an integer—for example a component with signal-to-noise ratio of unity would provide 0.5 to each of  $d_s$  and  $d_n$ .

We can find explicit expressions for  $d_s$  and  $d_n$  as follows. In the derivation we use the relation for the trace of a product of two matrices  $\text{tr}(\mathbf{CD}) = \text{tr}(\mathbf{DC})$  where  $\mathbf{D}$  and  $\mathbf{C}^T$  are the same shape. It is clear that

$$d_s = \mathcal{E}\{(\hat{x} - x_a)^T S_a^{-1} (\hat{x} - x_a)\} \quad (2.48)$$

$$= \mathcal{E}\{\text{tr}[(\hat{x} - x_a)(\hat{x} - x_a)^T S_a^{-1}]\} \quad (2.49)$$

$$= \text{tr}(S_{\hat{x}} S_a^{-1}) \quad (2.50)$$

where, from Eqs. (2.4

Therefore

and using Eq. (2.45)

By following a simila

$$d_n = \text{tr}(S_\epsilon^{-1} S_{\hat{\epsilon}})$$

$\Rightarrow$  Exercise 2.

and hence  $d_s + d_n = \text{tr}(\mathbf{GK})$ . The matrix detail in Chapter 3. to the true state thr

$$\hat{x} - x_a$$

It is known as the *resolution matrix* (M amongst other terms) information content, as must lie.

Degrees of freedom can also consider  $d_s$  show

and in the latter

where, from Eqs. (2.44) and (2.45),

$$S_{\hat{x}} = \mathcal{E}\{(\hat{x} - x_a)(\hat{x} - x_a)^T\} \quad (2.51)$$

$$= G(KS_a K^T + S_\epsilon)G^T \quad (2.52)$$

$$= S_a K^T (KS_a K^T + S_\epsilon)^{-1} K S_a. \quad (2.53)$$

Therefore

$$d_s = \text{tr}(S_a K^T [KS_a K^T + S_\epsilon]^{-1} K) \quad (2.54)$$

$$= \text{tr}(KS_a K^T [KS_a K^T + S_\epsilon]^{-1}) \quad (2.55)$$

and using Eq. (2.45) in the first of these two forms we also obtain

$$d_s = \text{tr}([K^T S_\epsilon^{-1} K + S_a^{-1}]^{-1} K^T S_\epsilon^{-1} K). \quad (2.56)$$

By following a similar derivation we can show that

$$d_n = \text{tr}(S_\epsilon [KS_a K^T + S_\epsilon]^{-1}) = \text{tr}([K^T S_\epsilon^{-1} K + S_a^{-1}]^{-1} S_a^{-1}) \quad (2.57)$$

$\Rightarrow$  **Exercise 2.4:** Derive these expressions.

and hence  $d_s + d_n = \text{tr}(I_m) = m$  as expected. Note that one of the forms for  $d_s$  is  $\text{tr}(GK)$ . The matrix  $A = GK$  is a very useful quantity, as will be seen in more detail in Chapter 3. For the moment simply note that it relates the expected state to the true state through

$$\hat{x} - x_a = Gy = G[K(x - x_a) + \epsilon] = A(x - x_a) + G\epsilon. \quad (2.58)$$

It is known as the *averaging kernel matrix* (Backus and Gilbert, 1970), the *model resolution matrix* (Menke, 1989), the *state resolution matrix*, or the *resolving kernel*, amongst other terms. It plays a significant rôle in various descriptions of the information content, as it describes the subspace of state space in which the retrieval must lie.

Degrees of freedom will be unchanged through linear transformations. Hence we can also consider  $d_s$  in the  $\tilde{x}, \tilde{y}$  and  $x', y'$  transformations. In the former, we can show

$$d_s = \text{tr}(\tilde{K}^T [\tilde{K} \tilde{K}^T + I_m]^{-1} \tilde{K}) \quad (2.59)$$

$$= \text{tr}(\tilde{K} \tilde{K}^T [\tilde{K} \tilde{K}^T + I_m]^{-1}) \quad (2.60)$$

$$= \text{tr}([\tilde{K}^T \tilde{K} + I_n]^{-1} \tilde{K}^T \tilde{K}) \quad (2.61)$$

and in the latter

$$d_s = \text{tr}(\Lambda^2 (\Lambda^2 + I_m)^{-1}) = \sum_{i=1}^m \lambda_i^2 / (1 + \lambda_i^2). \quad (2.62)$$



The corresponding number of degrees of freedom for noise is given by

$$d_n = \text{tr}((\Lambda^2 + \mathbf{I}_m)^{-1}) = \sum_{i=1}^m 1/(1 + \lambda_i^2). \quad (2.63)$$

To evaluate  $d_n$  it is necessary to regard  $\Lambda$  as an order  $m$  matrix, keeping any zero singular values it might have.

⇒ **Exercise 2.5:** Relate the eigenvectors and values of  $\mathbf{A}$  to the singular vectors and values of  $\tilde{\mathbf{K}}$ . Remember  $\mathbf{A}$  may be asymmetric.

## 2.5 Information Content of a Measurement

'Information' is a very general term that has been used in many different ways by different authors. Degrees of freedom for signal, for example, may be considered to be a measure of information. However in this section I want to discuss two widely used measures that carry the name 'information', namely the Fisher information matrix and the Shannon information content.

### 2.5.1 The Fisher information matrix

The Fisher information matrix arises in the theory of maximum likelihood estimation (e.g. see Stuart, Ord and Arnold (1999) chapters 17 and 18 for a detailed development). Likelihood, as defined by Fisher (1921) is the conditional *pdf*  $P(\mathbf{y}|\mathbf{x})$ , considered as a function of  $\mathbf{x}$  for a given value of  $\mathbf{y}$ . In the context of the Bayesian approach used here, it is the same as the posterior *pdf*  $P(\mathbf{x}|\mathbf{y})$  when there is no prior information, or equivalently when any prior information is considered as being of the same nature as a measurement—a virtual measurement. A maximum likelihood estimator finds the value of  $\mathbf{x}$  which maximises  $L(\mathbf{x}) = P(\mathbf{y}|\mathbf{x})$ . It can be shown (the Cramer–Rao inequality) that the variance of the estimate of  $x$  satisfies, in the scalar case,

$$\text{var}(x) \geq 1/\mathcal{E} \left\{ \left( \frac{\partial \ln L}{\partial x} \right)^2 \right\} \quad (2.64)$$

with the equality holding under certain conditions, which include the linear Gaussian case. The denominator is known as the Fisher information, and generalises to a matrix

$$\mathcal{F} = \mathcal{E} \left\{ \left( \frac{\partial \ln L}{\partial \mathbf{x}} \right) \left( \frac{\partial \ln L}{\partial \mathbf{x}} \right)^T \right\} = \int L(\mathbf{x}) \left( \frac{\partial \ln L(\mathbf{x})}{\partial \mathbf{x}} \right) \left( \frac{\partial \ln L(\mathbf{x})}{\partial \mathbf{x}} \right)^T d\mathbf{x} \quad (2.65)$$

in the multidimensional case. It can be shown that the information matrix of a product of two independent likelihoods, i.e.  $P(\mathbf{y}_1|\mathbf{x})P(\mathbf{y}_2|\mathbf{x})$ , is the sum of the individual matrices, so that information of two independent measurements is additive.

In the Gaussian linear matrix, so we may int

as information matrix of that of the prior an

### 2.5.2 Shannon in

The Shannon definiti which he developed in was to describe the in its applications are mu of probability density entropy. Information ( observing systems, as entropy and informati the concepts carry ov

The concept of sig tion of information co ment of a scalar  $x$ , wi is commonly taken to which have fixed valu like most interesting a than the absolute val where  $\sigma_x$  is the stan surement of a temper signal-to-noise ratio ( variation through the ratio is only 4.

The information c by which knowledge practice the logarithm on the application an it is often convenient example, knowledge bits of information a manipulations, howe

#### 2.5.2.1 Entropy of

Entropy in the ther internal states of a tl



ise is given by

$$\frac{1}{\lambda_i^2}. \quad (2.63)$$

n matrix, keeping any zero

dues of  $\mathbf{A}$  to the singular  
asymmetric.

in many different ways by  
mple, may be considered to  
want to discuss two widely  
ely the Fisher information

maximum likelihood esti-  
rs 17 and 18 for a detailed  
the conditional pdf  $P(y|x)$ ,  
the context of the Bayesian  
( $x|y$ ) when there is no prior  
n is considered as being of  
ent. A maximum likelihood  
=  $P(y|x)$ . It can be shown  
estimate of  $x$  satisfies, in the

(2.64)

ch include the linear Gaus-  
rmation, and generalises to

$$\int \left( \frac{\partial \ln L(\mathbf{x})}{\partial \mathbf{x}} \right)^T d\mathbf{x} \quad (2.65)$$

re information matrix of a  
2|x), is the sum of the indi-  
t measurements is additive.

In the Gaussian linear case, the information matrix is equal to the inverse covariance matrix, so we may interpret the terms in the equation

$$\hat{\mathbf{S}}^{-1} = \mathbf{K}^T \mathbf{S}_e^{-1} \mathbf{K} + \mathbf{S}_a^{-1} \quad (2.66)$$

as information matrices, indicating that the posterior information matrix is the sum of that of the prior and that of the measurement.

## 2.5.2 Shannon information content

The Shannon definition of information content arises from Information Theory, which he developed in the 1940's (Shannon and Weaver, 1949). Its original purpose was to describe the information carrying capacity of communication channels, but its applications are much wider. Information as he defined it depends on the *entropy* of probability density functions, which is very closely related to thermodynamic entropy. Information content is a scalar quantity, and as such is useful for optimising observing systems, as well as characterising and comparing them. We will discuss entropy and information first in terms of direct measurements, and then show how the concepts carry over to indirect measurements and to retrieval theory.

The concept of signal-to-noise ratio gives a hint about how a useful definition of information content might be constructed. Consider a simple direct measurement of a scalar  $x$ , with accuracy  $\sigma$ . The signal-to-noise ratio for the measurement is commonly taken to be  $x/\sigma$ . This is appropriate for measurements of quantities which have fixed values such as physical constants, but for quantities which vary, like most interesting atmospheric parameters, and for which it is the variation rather than the absolute value that is usually of interest, a more useful definition is  $\sigma_x/\sigma$ , where  $\sigma_x$  is the standard deviation of the variability of  $x$ . For example a measurement of a temperature of 300 K to an accuracy of 1 K might have an apparent signal-to-noise ratio of 300, but if it is of a tropical sea surface temperature whose variation through the year is known to be, say, 4 K then the useful signal-to-noise ratio is only 4.

The information content of a measurement can be defined qualitatively as the factor by which knowledge of a quantity is improved by making the measurement. In practice the logarithm of the factor is used, with the base of the logarithm depending on the application and determining the dimensionless 'units'. In information theory it is often convenient to use base two, when the units are 'bits'. In the above example, knowledge is improved by a factor of four, so the measurement provides 2 bits of information about the sea surface temperature. For simplicity of algebraic manipulations, however, natural logarithms are more convenient.

### 2.5.2.1 Entropy of a probability density function

Entropy in the thermodynamic sense is the logarithm of the number of distinct internal states of a thermodynamic system consistent with a measured macro-state

(pressure, temperature, etc). Information is the change in the logarithm of the number of distinct possible internal states of the system being measured, consistent with the change in knowledge of the system resulting from a measurement.

To construct a formal definition of information, as distinct from the informal signal-to-noise ratio, we use the *pdf* as a measure of knowledge of a system. The Gibbs definition of thermodynamic entropy and the Shannon definition for discrete information systems are the same, apart from a numerical factor:

$$S(P) = -k \sum_i p_i \ln p_i, \quad (2.67)$$

where  $p_i$  is the probability of the system being in state  $i$ . In thermodynamics,  $k$  is the Boltzmann constant, and in information theory  $k = 1$  and the logarithm is usually taken to base two. For the detailed reason why this form is chosen, the reader is referred to Shannon and Weaver (1949), but as a simple example consider a discrete system with  $2^n$  states. If all states are equally likely, and nothing is known about the state, then  $p_i = 2^{-n}$ , so that the prior entropy  $S(P) = n$  using the logarithm to base two. If the system is examined and found to be in some definite state  $s$ , then  $p_s = 1$  and  $p_i = 0$  for  $i \neq s$ . In this case the posterior entropy is zero, and the information content is the difference  $n$ , in units of bits. This corresponds to the number of digits of a binary number required to identify the state.

For a continuous *pdf*,  $p_i$  corresponds to  $P(x) dx$  so the  $\ln p_i$  factor needs some attention. Entropy of a continuous *pdf* is defined as

$$S(P) = - \int P(x) \log_2 [P(x)/M(x)] dx, \quad (2.68)$$

where the place of  $dx$  is taken by a measure function,  $M$ , chosen so that  $P/M$  is dimensionless, and so that  $P = M$  corresponds to a state of no knowledge of  $x$ . Choice of  $M$  is analogous to the third law of thermodynamics, in that  $P = M$  determines the zero of entropy. It is often constant, when it may be safely omitted, but it may also be interpreted as a prior *pdf*, in which case Eq. (2.68) is a relative entropy.

If  $P_1(x)$  describes knowledge before a measurement, and  $P_2(x)$  describes it afterwards, then the information content of the measurement is the reduction in entropy:

$$H = S(P_1) - S(P_2). \quad (2.69)$$

### 2.5.2.2 Entropy of a Gaussian distribution

To illustrate that the definition of Eq. (2.68) has the desired properties for continuous *pdf*'s, we will apply it to a scalar Gaussian case, and show that the information content of the measurement is the logarithm of the signal-to-noise ratio. Using the natural logarithm for algebraic convenience, the entropy of the Gaussian *pdf*

Eq. (2.9) is:

$$S = \frac{1}{(2\pi)^{\frac{1}{2}} \sigma} \int$$

$\Rightarrow$  Exercise 2.6:

The information content with variance  $\sigma_1^2$ , and therefore  $\ln(\sigma_1/\sigma_2)$ , i.e.

In the case of a multivariate *pdf* is equivalent to the eigenvalues of  $S$  *pdf*s to be the sum of

$\Rightarrow$  Exercise 2.7: independent

Hence the entropy of elements is, using Eq.

because the determinant of the product is the surface of constant probability, the principal axis of the *pdf* is the logarithm of the constant which depends on the state space occupied.

When we make a measurement, the information content of the measurement is a generalisation of the

Zero eigenvalues, which are known exactly, and the zero length principal axis of the information content, as knowledge before. Hence the information content is first by not increasing. If a component has a non-zero value, then, afterwards, however, the measurement is prob

ge in the logarithm of the being measured, consistent on a measurement.

distinct from the informal knowledge of a system. The non definition for discrete al factor:

(2.67)

3 i. In thermodynamics,  $k$   $k = 1$  and the logarithm by this form is chosen, the a simple example consider a ikely, and nothing is known ropy  $S(P) = n$  using the und to be in some definite e posterior entropy is zero, s of bits. This corresponds identify the state. the  $\ln p_i$  factor needs some

)]  $dx$ , (2.68)

$M$ , chosen so that  $P/M$  is tate of no knowledge of  $x$ . dynamics, in that  $P = M$  n it may be safely omitted, case Eq. (2.68) is a relative

and  $P_2(x)$  describes it after- is the reduction in entropy:

(2.69)

ired properties for continu- l show that the information ginal-to-noise ratio. Using atropy of the Gaussian pdf

Eq. (2.9) is:

$$S = \frac{1}{(2\pi)^{\frac{1}{2}}\sigma} \int \exp \left\{ -\frac{(x-\bar{x})^2}{2\sigma^2} \right\} \left( \ln[(2\pi)^{\frac{1}{2}}\sigma] + \frac{(x-\bar{x})^2}{2\sigma^2} \right) dx. \quad (2.70)$$

$\Rightarrow$  **Exercise 2.6:** Integrate Eq. (2.70) to obtain  $S = \ln \sigma(2\pi e)^{1/2}$ .

The information content of a measurement where the prior knowledge is Gaussian with variance  $\sigma_1^2$ , and the posterior knowledge is Gaussian with variance  $\sigma_2^2$  is therefore  $\ln(\sigma_1/\sigma_2)$ , i.e. the logarithm of the signal-to-noise ratio, as anticipated.

In the case of a multivariate Gaussian distribution, we have already shown that the pdf is equivalent to a product of independent distributions with variances equal to the eigenvalues of  $S_y$ . We would expect the entropy of a product of independent pdfs to be the sum of the entropies of individual pdfs.

$\Rightarrow$  **Exercise 2.7:** Prove that  $S[P(x)P(y)] = S[P(x)] + S[P(y)]$  if  $x$  and  $y$  are independent

Hence the entropy of the multivariate Gaussian distribution for a vector with  $m$  elements is, using Eq. (2.14)

$$\begin{aligned} S[P(y)] &= \sum_{i=1}^m \ln(2\pi e \lambda_i)^{\frac{1}{2}} \\ &= m \ln(2\pi e)^{\frac{1}{2}} + \frac{1}{2} \ln(\prod_i \lambda_i) \\ &= m \ln(2\pi e)^{\frac{1}{2}} + \frac{1}{2} \ln |S_y| \end{aligned} \quad (2.71)$$

because the determinant is equal to the product of the eigenvalues. The square root of the product is also proportional to the volume of an ellipsoid describing a surface of constant probability, as each eigenvalue is proportional to the square of the principal axis of the ellipsoid (Appendix A.3). Therefore the entropy of the pdf is the logarithm of the volume inside a surface of constant probability, plus a constant which depends on the surface chosen. It is a measure of the volume of state space occupied by the pdf which describes knowledge of the state.

When we make a measurement, this 'volume of uncertainty' decreases; the information content of the measurement is a measure of the factor by which it decreases, a generalisation of the scalar concept of signal-to-noise ratio.

Zero eigenvalues, corresponding to a singular covariance matrix, or to quantities known exactly, will lead to negative infinite contributions to the entropy, and zero length principal axes. Such terms should cancel exactly when calculating information content, as knowledge afterwards of these quantities will be the same as knowledge before. However to avoid mathematical difficulties it is best to eliminate them first by not including those basis vectors in the measurement or state space. If a component has finite variance before a measurement and zero variance afterwards, however, then the measurement has provided infinite information! Such a measurement is probably non-physical.

The information content of a measurement when the prior covariance is  $S_1$  and the posterior covariance is  $S_2$  can be written as

$$H = \frac{1}{2} \ln |S_1| - \frac{1}{2} \ln |S_2| = \frac{1}{2} \ln |S_1 S_2^{-1}| = -\frac{1}{2} \ln |S_2 S_1^{-1}|. \quad (2.72)$$

### 2.5.2.3 Information content in the linear Gaussian case

The information content of a measurement can be evaluated either in state space ( $H_s$ ) or in measurement space ( $H_m$ ), and we would expect to obtain the same value in either case. In state space it depends on the entropies of the *pdf* of the state before and after the measurement:

$$\begin{aligned} H_s &= S[P(\mathbf{x})] - S[P(\mathbf{x}|\mathbf{y})] \\ &= \frac{1}{2} \ln |S_a| - \frac{1}{2} \ln |\hat{S}| \\ &= \frac{1}{2} \ln |\hat{S}^{-1} S_a|. \end{aligned} \quad (2.73)$$

Putting Eq. (2.27) for  $\hat{S}$  in the linear Gaussian case into the third expression in Eq. (2.73) gives the following, using the properties of determinants given in Appendix A.5:

$$\begin{aligned} H_s &= \frac{1}{2} \ln |(K^T S_e^{-1} K + S_a^{-1}) S_a| \\ &= \frac{1}{2} \ln |S_a^{\frac{1}{2}} K^T S_e^{-1} K S_a^{\frac{1}{2}} + I_n| \\ &= \frac{1}{2} \ln |\tilde{K}^T \tilde{K} + I_n|. \end{aligned} \quad (2.74)$$

In measurement space, the information content is the difference between the entropy of the prior estimate of  $\mathbf{y}$  and the posterior estimate:

$$H_m = S[P(\mathbf{y})] - S[P(\mathbf{y}|\mathbf{x})]. \quad (2.75)$$

The covariance for  $P(\mathbf{y})$  before the measurement is

$$\begin{aligned} S_{y_a} &= \mathcal{E}\{(\mathbf{y} - \mathbf{y}_a)(\mathbf{y} - \mathbf{y}_a)^T\} \\ &= \mathcal{E}\{K(\mathbf{x} - \mathbf{x}_a)(\mathbf{x} - \mathbf{x}_a)^T K^T + \epsilon \epsilon^T\} \\ &= K S_a K^T + S_e \end{aligned} \quad (2.76)$$

and the posterior covariance is  $S_e$ , so the information content is, in various forms:

$$\begin{aligned} H_m &= \frac{1}{2} \ln |S_e^{-1} (K S_a K^T + S_e)| \\ &= \frac{1}{2} \ln |S_e^{-\frac{1}{2}} K S_a K^T S_e^{-\frac{1}{2}} + I_m| \\ &= \frac{1}{2} \ln |\tilde{K} \tilde{K}^T + I_m|. \end{aligned} \quad (2.77)$$

Note that  $\tilde{K} \tilde{K}^T$  and  $\tilde{K}^T \tilde{K}$  have the same non-zero eigenvalues, therefore both  $H_m$  and  $H_s$  are equal to  $\sum_i \frac{1}{2} \ln(1 + \lambda_i^2)$  where  $\lambda_i$  is a singular value of  $\tilde{K}$ .

⇒ **Exercise 2.8**  
the information  
space or in s

The averaging k  
briefly in section 2.4  
be related to the inf  
as

and hence

which we may relat  
with Eq. (2.54) or (  
degrees of freedom  
matrix:

$$\begin{aligned} H &= \\ d_s &= \end{aligned}$$

## 2.6 The Standard Freedom

In order to illustra  
with the standard c  
cases, firstly and r  
 $\sigma_a^2 = 100 K^2$ , and s  
non-zero off-diagor  
corresponding to k  
measurement, but  
adjacent levels (in  
is unrealistically la

A more reason  
for the second cas  
based on a first or  
of a random walk.  
 $T_{i+1} - \bar{T}_{i+1}$  at lev

where the regress  
Gaussian random

covariance is  $S_1$  and

$$3_2 S_1^{-1} |. \quad (2.72)$$

either in state space  
tain the same value  
the pdf of the state

(2.73)

third expression in  
inants given in Ap-

(2.74)

between the entropy

(2.75)

(2.76)

is, in various forms:

(2.77)

, therefore both  $H_m$   
ie of  $\tilde{K}$ .

⇒ **Exercise 2.8:** With the aid of Bayes' theorem, show that for general pdf's the information content is the same whether computed in measurement space or in state space.

The averaging kernel matrix for the linear Gaussian problem was introduced briefly in section 2.4.2 in connexion with degrees of freedom for signal. It can also be related to the information content as follows. From Eq. (2.45), we can write it as

$$A = GK = (K^T S_e^{-1} K + S_a^{-1})^{-1} K^T S_e^{-1} K \quad (2.78)$$

and hence

$$I - A = (K^T S_e^{-1} K + S_a^{-1})^{-1} S_a^{-1} = \hat{S} S_a^{-1} \quad (2.79)$$

which we may relate to information content through Eq. (2.73). This, together with Eq. (2.54) or (2.56) gives the following relations between information content, degrees of freedom for signal, the singular values of  $\tilde{K}$  and the averaging kernel matrix:

$$\begin{aligned} H &= \frac{1}{2} \sum_i \ln(1 + \lambda_i^2) = -\frac{1}{2} \ln |\mathbf{I}_n - \mathbf{A}| \\ d_s &= \sum_i \lambda_i^2 / (1 + \lambda_i^2) = \text{tr}(\mathbf{A}). \end{aligned} \quad (2.80)$$

## 2.6 The Standard Example: Information Content and Degrees of Freedom

In order to illustrate the concepts of information content and degrees of freedom with the standard example, an *a priori* covariance matrix is needed. I will use two cases, firstly and most simply a diagonal matrix with a variance at each level of  $\sigma_a^2 = 100 \text{ K}^2$ , and secondly a matrix with the same values on the diagonal but with non-zero off-diagonal elements. The first case has reasonable values at each level, corresponding to knowledge of the temperature to about  $\pm 10 \text{ K}$  before we make the measurement, but it implicitly assumes that the temperature difference between adjacent levels (in this case about 700 m apart) is known to only about  $\pm 14 \text{ K}$ . This is unrealistically large.

A more reasonable *a priori* would have adjacent levels correlated. Therefore for the second case I have therefore constructed a simple covariance matrix model based on a first order auto-regressive model, or Markov process. This is a variant of a random walk. Take the departure of the temperature from the mean,  $\delta T_{i+1} = T_{i+1} - \bar{T}_{i+1}$  at level  $i + 1$  to be related to that at level  $i$  by:

$$\delta T_{i+1} = \beta \delta T_i + \xi_i \quad (2.81)$$

where the regression coefficient  $\beta$  is a constant between zero and unity and  $\xi_i$  is Gaussian random variable, uncorrelated with  $\delta T_i$ , and with constant variance  $\sigma_\xi^2$ .

$$S_{ij} = \sigma_a^2 \beta^{2|i-j|} \quad (2.82)$$
$$S_{ij} = \sigma_a^2 \exp \left( -|i-j| \frac{\delta z}{h} \right) \quad (2.83)$$

*The Standard*

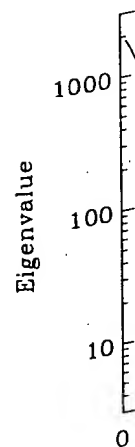


Table 2.1 Singular values of  $\tilde{\mathbf{K}}$ , together with contributions of each vector to the degrees of freedom  $d_s$  and information content  $H$  for both covariance matrices. Measurement noise variance is  $0.25 \mathbf{K}^2$ .

Diagonal covariance				Full covariance		
$i$	$\lambda_i$	$d_{si}$	$H_i$ (bits)	$\lambda_i$	$d_{si}$	$H_i$ (bits)
1	6.51929	0.97701	2.72149	27.81364	0.99871	4.79865
2	4.79231	0.95827	2.29147	18.07567	0.99695	4.17818
3	3.09445	0.90544	1.70134	9.94379	0.98999	3.32105
4	1.84370	0.77269	1.06862	5.00738	0.96165	2.35227
5	1.03787	0.51858	0.52731	2.39204	0.85123	1.37443
6	0.55497	0.23547	0.19368	1.09086	0.54337	0.56546
7	0.27941	0.07242	0.05423	0.46770	0.17948	0.14270
8	0.13011	0.01665	0.01211	0.17989	0.03135	0.02297
<b>totals</b>		4.45653	8.57024		5.55272	16.75571

the last two giving lit  
singular vectors.

For the non-diagonal elements, which are tightly constrained,  $d_{ij}$  can be smaller. However, the contributions to  $d_s$  and the covariance is 332.2 bit/s. The nondiagonal elements in the space, by a factor of 2.

The reason for this structure. The non-d smaller variance at s variance at all scales ted as the solid line the dotted line. The 1 The corresponding ve sponding to the large spacing of the weight while it is more const

It is clear that the  
can constrain the solution  
Chapter 10.

For the diagonal matrix, we obtain a total  $d_s = 4.46$  and  $H = 8.6$  bits, indicating that about four and a half quantities are measured, and about  $2^{8.6} = 380$  different atmospheric states can be distinguished. This corresponds to the first four of five singular values being greater than about unity, the first three giving close to one degree of freedom, next two or three giving a fraction of a degree of freedom, and

of  $\delta T$  tends to  $\sigma_\xi^2/(1-\beta^2)$ , we get a covariance matrix

(2.82)

ial elements. We can also

(2.83)

e length scale at which the which gives a length scale  $\simeq 3$  K. This provides some ly exist in the atmosphere, e atmosphere is represented  $\ln p$ .

f each vector to the degrees of es. Measurement noise variance

#### Full covariance

	$d_{si}$	$H_i$ (bits)
4	0.99871	4.79865
7	0.99695	4.17818
9	0.98999	3.32105
3	0.96165	2.35227
4	0.85123	1.37443
6	0.54337	0.56546
0	0.17948	0.14270
9	0.03135	0.02297
	5.55272	16.75571

ontributions of each singu- n content  $H$  for both prior he singular vectors for the e non-diagonal case are

and  $H = 8.6$  bits, indicating d about  $2^{8.6} = 380$  different nds to the first four of five t three giving close to one of a degree of freedom, and

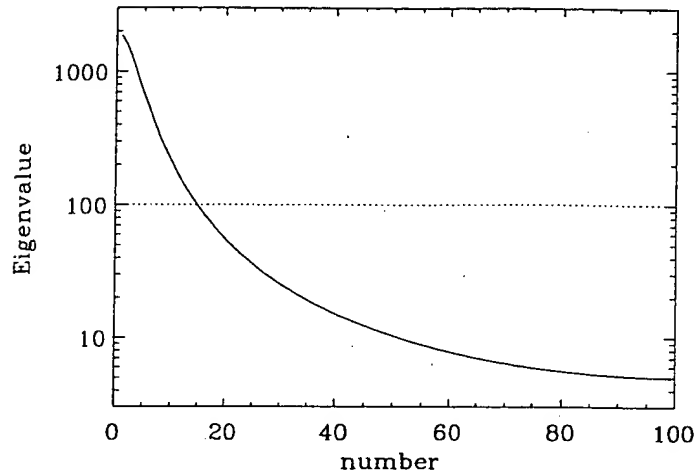


Fig. 2.5 Solid: eigenvalues of a non-diagonal model covariance matrix; dotted: variance of a diagonal covariance matrix with the same total variance.

the last two giving little. This is echoed in the information content of each of the singular vectors.

For the non-diagonal matrix, we would expect that as the *a priori* is more tightly constrained, both the information content and the degrees of freedom would be smaller. However this does not seem to be the case, the singular values and contributions to  $d_s$  and  $H$  all being larger. The entropy of the diagonal prior covariance is 332.2 bits (i.e.  $100\log_2 10$ ), while that of the non-diagonal one is 210.2 bits. The nondiagonal covariance is restricted to a much smaller volume of state space, by a factor of  $2^{122} \simeq 5 \times 10^{37}$ .

The reason for this paradox is that the weighting functions see only large scale structure. The non-diagonal covariance has a larger variance at these scales, and smaller variance at small scales, in contrast to the diagonal covariance which has variance at all scales equally. The eigenvalues of the non-diagonal matrix are plotted as the solid line in Fig. 2.5, and those of the diagonal matrix are plotted as the dotted line. The first 14 values of the non-diagonal matrix are larger than 100. The corresponding vectors are quasi-sinusoidal, with the largest wavelength corresponding to the largest eigenvalue, see Fig. 3.2. Thus at the scale of the width and spacing of the weighting functions, the non-diagonal *a priori* is less constrained, while it is more constrained at scales which cannot be measured.

It is clear that the *a priori* covariance is important, and that an incorrect one can constrain the solution inappropriately. This will be discussed in more detail in Chapter 10.



## 2.7 Probability Density Functions and the Maximum Entropy Principle

It is necessary to be able to estimate probability density functions, and often on the basis of very little information. They are not quantities that are measured directly, and have to be related somehow to the various different kinds of information we have about a system. It is common to assume that if we make a measurement of some quantity, and make an error estimate, that the corresponding *pdf* is Gaussian, but why? The central limit theorem is on reason often cited, but there is another, more subtle, reason.

In the Bayesian view, probability density is a measure of knowledge. It is reasonable to take as a guiding principle in quantifying a *pdf* the 'maximum entropy principle' that the region of state space that we believe the state to lie in should be as large as possible consistent with what is known about the variability of the state. Entropy is an appropriate measure of the size of the region, so a set of parameters describing the system can be interpreted in terms of a *pdf* by finding the function for which the entropy is maximum, or equivalently, the information is minimum, consistent with the available parameters.

I will illustrate the ideas using three examples of *pdfs* of a single random variable  $x$ . Assume in the first example that we know nothing at all about its variability, except that  $x$  lies in some known range  $(a, b)$ . What is an appropriate prior *pdf* with which to describe  $x$ ? Intuition tells us that all values in  $(a, b)$  are equally likely, so that  $P(x) = 1/(b - a)$  within the range, and zero outside. The principle of maximum entropy tells us that  $P(x)$  must maximise:

$$S(P) = - \int_a^b P(x) \ln P(x) dx \quad (2.84)$$

subject to the condition that  $\int_a^b P(x) dx = 1$ . Maximising  $S(P)$  with respect to  $P$  gives:

$$-\ln P(x) - 1 + \mu = 0 \quad (2.85)$$

where  $\mu$  is the Lagrangian multiplier for the condition.  $P(x)$  is clearly a constant, and its value is found from the unit area condition to be  $1/(b - a)$ , as expected. If we know nothing at all about  $x$ , i.e.  $b - a \rightarrow \infty$ , and  $P(x) \rightarrow 0$  everywhere, a reasonable conclusion.

Now consider the case where we also know that the expected value of  $x$  is  $\bar{x}$ , but we know nothing about its variability. Now we have the extra condition:

$$\int_a^b xP(x) dx = \bar{x} \quad (2.86)$$

and the maximisation gives:

$$-\ln P(x) - 1 + \mu + \nu x = 0 \quad (2.87)$$

where  $\nu$  is the Lagrangian multiplier. If  $a$  and  $b$  are general, this leads to a more general distribution. If  $a$  and  $b$  are both positive, i.e.  $a = 0$  and  $b = \infty$ , the distribution is exponential. If  $a$  and  $b$  are both negative, it is straightforward to show that the distribution is Gaussian.

$P(x)$

This is an example of a probability density function with mean  $\bar{x}$ , and is in fact the maximum entropy distribution consistent with the constraint the *pdf* would have a mean of  $\bar{x}$ .

The third example is the case where we know the mean and the variance, and there is no finite range for  $x$ .

In this case it is possible to find a probability distribution with mean  $\bar{x}$  and variance  $\sigma^2$ .

$\Rightarrow$  Exercise 2.9: Show that the Gaussian distribution is the maximum entropy distribution consistent with the constraints of fixed mean and variance.

This is the primary reason for the use of the maximum entropy principle when only the mean and variance are known. It allows us to compare possible distributions with the same mean and variance, and choose the one with maximum entropy, or minimum information.

The measure function for the above examples, and the above could be restated in terms of the probability density function  $y = x^2$ , where all that is required is that  $y$  is both positive and finite. The above to determine that the distribution from  $x$  being uniformly distributed, making the maximum entropy distribution. It will transform with the same constraints as  $x$  being equivalent to selecting a probability density function to be uniform.

Construction of a probability density function in Chapter 10.



## Minimum Entropy

functions, and often on the that are measured directly, nt kinds of information we we make a measurement of responding *pdf* is Gaussian, cited, but there is another,

re of knowledge. It is rea- *pdf* the 'maximum entropy the state to lie in should be the variability of the state. gion, so a set of parameters *pdf* by finding the function e information is minimum,

of a single random variable at all about its variability, is an appropriate prior *pdf* values in  $(a, b)$  are equally zero outside. The principle

(2.84)

ing  $S(P)$  with respect to  $P$

(2.85)

$P(x)$  is clearly a constant, be  $1/(b-a)$ , as expected. and  $P(x) \rightarrow 0$  everywhere, a

expected value of  $x$  is  $\bar{x}$ , but e extra condition:

(2.86)

(2.87)

where  $\nu$  is the Lagrangian multiplier for the extra condition. For the case where  $a$  and  $b$  are general, this leads to complicated but straightforward algebra which the reader may explore at leisure. Consider only the case where it is known that  $x$  is positive, i.e.  $a = 0$  and  $b = \infty$ . On substituting  $P(x) = \exp(-1 + \mu + \nu x)$  into the constraints, it is straightforward to show that  $\nu = -1/\bar{x}$ , and hence that:

$$P(x) = \begin{cases} (1/\bar{x}) \exp(-x/\bar{x}) & \text{for } x \geq 0 \\ 0 & \text{for } x < 0. \end{cases} \quad (2.88)$$

This is an example of a *pdf* where the most likely value, at  $x = 0$ , is not near the mean,  $\bar{x}$ , and is in fact at an extreme of the range of  $x$ . Without the positivity constraint the *pdf* would be zero everywhere, as in the case of no information at all.

The third example is when an expected value and a variance are both known, and there is no finite range limitation. Now we have three constraints on  $P(x)$ :

$$\begin{aligned} \int P(x) dx &= 1 \\ \int xP(x) dx &= \bar{x} \\ \int (x - \bar{x})^2 P(x) dx &= \sigma^2. \end{aligned} \quad (2.89)$$

In this case it is possible to show that the maximum entropy *pdf* is the normal distribution with mean  $\bar{x}$  and variance  $\sigma^2$ .

$\Rightarrow$  **Exercise 2.9:** Show this

This is the primary reason why the Gaussian distribution is an appropriate default when only the mean and variance (or covariance, in general) are known. Of all possible distributions with a given mean and variance, the Gaussian has maximum entropy, or minimum information.

The measure function  $M(x)$ , Eq. (2.68), has been ignored (or set to a constant) in the above examples, and a few words of explanation are in order. The first example above could be restated by describing the system in terms of a single variable  $y = x^2$ , where all that is known is that  $y$  lies in the range  $(a^2, b^2)$  where  $a$  and  $b$  are both positive for the purpose of this discussion. We could then follow the arguments above to determine that  $y$  must be uniformly distributed in  $(a^2, b^2)$ , a different result from  $x$  being uniformly distributed in  $(a, b)$ . The measure function is a means of making the maximum entropy *pdf* independent of the coordinate system, because it will transform with the coordinate system. The choice of measure function is equivalent to selecting a coordinate system in which a non-informative *pdf* would be uniform.

Construction of a *a priori* for practical retrievals will be discussed in more detail in Chapter 10.

# Remote sensing of atmospheric carbon monoxide with the MOPITT Airborne Test Radiometer (MATR)

Mark W. Smith\*, Stephen R. Shertz, and Nuri Delen

Atmospheric Chemistry Division

National Center for Atmospheric Research

PO Box 3000, Boulder, CO 80307-3000

## ABSTRACT

The MOPITT Airborne Test Radiometer (MATR) uses gas filter correlation radiometry to measure tropospheric carbon monoxide (CO) with three optical channels or methane (CH<sub>4</sub>) with one channel. MATR uses the same gas correlation techniques as does the MOPITT satellite instrument, namely length modulation and pressure modulation. MATR data serves to test retrieval techniques for converting infrared radiometric data into atmospheric CO, or CH<sub>4</sub>, amounts. MATR will also be applied to MOPITT data validation. This paper gives an overview of the MATR instrument design; it discusses the results of laboratory testing and calibration; and it presents results from recent flights.

**Keywords:** MATR, MOPITT, carbon monoxide, remote sensing, gas correlation, radiometry, infrared

## 1. INTRODUCTION

The MOPITT Airborne Test Radiometer (MATR) is a 3-channel gas filter correlation radiometer that supports the Measurements Of Pollutants In The Troposphere (MOPITT) satellite program. MOPITT will be launched on the EOS Terra platform and will measure tropospheric carbon monoxide (CO) profiles and methane (CH<sub>4</sub>) columns.<sup>1,2</sup> MATR uses the same physical techniques as MOPITT (i.e., gas filter correlation radiometry with pressure modulation and length modulation) to remotely sense atmospheric CO, or CH<sub>4</sub>, from an aircraft. MATR has two functions. The first function is to collect data to test our ability to retrieve correct atmospheric CO, or CH<sub>4</sub>, gas amounts from MOPITT-like gas filter radiometer data. The second function is to help validate MOPITT data as described in the MOPITT data validation plan.<sup>3</sup> The MOPITT CO and CH<sub>4</sub> retrieval techniques have been described elsewhere.<sup>4-6</sup> CO and CH<sub>4</sub> are of scientific interest because of their roles as abundant fuels in the photochemical oxidation, or low temperature combustion, process that occurs in the troposphere.<sup>7</sup>

The basic measurement technique that is used by both MOPITT and MATR is remote sensing by means of infrared radiometry. The instruments measure infrared radiation (IR); gas concentrations in the atmosphere are inferred from the IR measurements. Fig. 1 depicts two fundamentally different types of atmospheric radiative transfer processes. In the first type of process, shown at left in Fig. 1, infrared radiation is emitted by the surface of the earth and then absorbed and partially re-emitted by the atmosphere. Because the atmosphere is in general colder than the surface of the earth, less radiation is re-emitted than is absorbed, resulting in net absorption. In the second type of process, shown at right in Fig. 1, infrared radiation is emitted by the sun and then partially absorbed by the atmosphere. Both processes can occur simultaneously. However, the first process is dominant for the CO fundamental absorption band near 4.6 micrometers, while the second process is dominant for the CO first overtone band near 2.3 micrometers, as well as for the methane bands near 2.2 micrometers.

## 2. INSTRUMENT DESIGN

MATR has been developed in stages, starting with a laboratory breadboard instrument that had only a 2.2/2.3 micrometer LMC channel. A flight prototype, again with only a 2.3/2.3 micrometer LMC channel, was then built. A few test flights were made with this instrument in 1996.<sup>8</sup> The second generation flight instrument, with 3 optical channels, is described in this paper.

\* Correspondence: Email: [mwsmith@ncar.ucar.edu](mailto:mwsmith@ncar.ucar.edu); Telephone: 303 497 1856; Fax: 303 497 1492



## 2.1 Optical Design

Fig. 2 shows the layout of the MATR optical table. As stated earlier, MATR has 3 optical channels. Channels 1 and 2 use a length modulated gas correlation cell (LMC) filled with CO. Channel 1 has a spectral pass band centered near 2.33 micrometers with a full width at half maximum (FWHM) of about 0.022 micrometers. It provides information about CO throughout an entire atmospheric column. Channel 2 has a spectral pass band centered near 4.61 micrometers with a FWHM of about 0.110 micrometers. It provides information about CO weighted in the mid-troposphere. Channel 3 has nominally the same spectral pass band as channel 2, but it uses a pressure modulated gas correlation cell (PMC) to provide information about CO weighted in the upper troposphere. By changing a band pass filter and the gas in the LMC, MATR can alternatively operate with a single channel centered near 2.27 micrometers to measure CH<sub>4</sub> column amounts.

A rotating input mirror selects one of four sources of input radiation: scene, cold blackbody, hot blackbody, or tungsten lamp. The last three sources are used for in-flight radiometric calibration. MATR collects scene data with a nominally nadir view, except when the aircraft is pitched up or down or is banking. The instrument full angle field of view (FOV) is approximately 5.7°, or 0.1 radians, producing a ground instantaneous FOV of about 1.2 km from the standard 12 km flight altitude.

The chopper produces an approximately square chopped waveform with a chopping frequency of about 400 Hz in normal operation. The data processing scheme uses only data acquired with the chopper fully open or fully closed, which comprises about 70% of the data.

Beam splitter 1 transmits most of the 2.2 to 2.3 micrometer radiation and about half of the 4.6 micrometer radiation to the LMC. It reflects about half of the 4.6 micrometer radiation towards the PMC. Beam splitter 2 transmits the 2.2 to 2.3 micrometer radiation to the channel 1 detector and reflects 4.6 micrometer radiation to the channel 2 detector.

The LMC is very similar to the version described in detail by Tolton and Drummond<sup>9</sup> and its operation will only be summarized here. The absorption path length for the correlation gas in the LMC is made to alternate between 2 mm and 10 mm by means of an internally rotating glass displacer. The displacer is a bow tie shaped piece of CaF<sub>2</sub> that is nearly transparent at the MATR operational wavelengths. The correlation gas in the LMC may be either CO or CH<sub>4</sub>. The standard operating pressure is 80 kPa and the standard modulation frequency is 1/32 of the chopping frequency.

The PMC was built by the University of Oxford and is similar to the MOPITT flight PMCs. Again, the operation of a PMC has been described in detail elsewhere<sup>10,11</sup> and will only be summarized here. A pair of pistons changes the volume of a gas reservoir and this causes the pressure of the correlation gas in the PMC optical cell to oscillate from about 5 to 11 kPa at 1/8 of the chopping frequency.

The LMC and the PMC provide extremely high resolution spectral filtering. This resolution is on the order of the widths of the gas lines in the cells, or roughly 0.1 to 1 nm, depending on cell conditions. Additional low resolution filters are required to set the overall optical pass band for each channel. These filters limit detector response to spectral regions in which the correlation gas has strong absorption features. A pair of filters set the spectral pass band of each optical channel in MATR. The actual spectral pass band for each channel is set by a narrow filter that is located external to each detector Dewar. These filters are located where the optical beam is nearly collimated, so as to minimize angle of incidence effects on the filter. A second filter, with a moderately broad pass band, is located in each Dewar. This filter is cooled to liquid nitrogen temperature and blocks most of the thermal background radiation. Radiation is converging rapidly on to the detector element in each Dewar, and this produces an inevitable shift in the pass band of the filters in the Dewars. However, this shift has no real impact on the ability of the cooled filter to block thermal background radiation.

The MATR infrared detectors each use a single 4 mm diameter InSb element that is cooled by liquid nitrogen in a Dewar. The detector elements operate in photo-voltaic mode with a matched transimpedance pre-amplifier. The input FET's and first stage feedback resistors for each pre-amplifier are mounted on a cold finger inside each Dewar to minimize Johnson noise from the feedback resistors. DC-coupled outputs from the detectors are used to check for saturation. AC-coupled outputs are amplified and filtered and then used as the primary radiometric signals.

## 2.2 In-flight Radiometric Calibration Assembly

In-flight radiometric calibration is accomplished with the use of three calibration sources. A pair of blackbodies, one heated to about 40 °C and one cooled to about 2 °C, is used to derive radiometric gain and offset coefficients for the 4.6 micrometer channels. A thin sheet of Spectralon diffusing material that is illuminated by a quartz tungsten halogen (QTH) lamp is used as a source for the 2.3 micrometer channel. The blackbody temperatures as well as the supply voltage and current for the QTH lamp are monitored and recorded in normal operation. The in-flight blackbodies are calibrated in the laboratory against a

reference blackbody that has been calibrated directly by NIST. The in-flight QTH source is calibrated against a set of QTH lamps that were purchased from a vendor; the vendor supplied reports that trace lamp calibration to NIST reference standards.

### 2.3 Thermal Control

The optical table is completely enclosed in a foam insulated box. The interior of the box is stabilized at about 32 °C by a combination of convective and conductive heating. A heat pump removes the power that is generated from the chopper motor, which is the only appreciable heat source on the optical table. Temperatures are monitored and recorded for 16 points throughout the instrument, in addition to the blackbodies.

### 2.4 Auxiliary Instrumentation

Post-flight data analysis requires auxiliary information in addition to the detector outputs and instrument temperatures. A global positioning system (GPS) provides latitude, longitude and geometrical altitude. Ambient pressure at flight altitude, as determined by an aircraft altimeter, is also recorded. A position and orientation system provides aircraft attitude data. When interpreting the radiometric data, it is useful to know if the scene was clear or cloudy, water or land, vegetated or bare, simple or complex, etc. This information is provided by a nadir-viewing video camera that has a full-angle FOV of 14.4°, which is about 2.5 times greater than MATR's FOV.

### 2.5 Instrument Control and Data Acquisition

Instrument control and data acquisition are performed by an industrial grade rack mounted computer that contains five data acquisition boards: two general purpose A/D and digital I/O boards, one counter/timer board, and a pair of dual-port RS-232 boards. The computer has a 133 MHz 586 CPU and a 6 GByte hard drive. A backup copy of data is written in real time onto a 1 Gbyte removable media Jaz disk, which can hold about 8 hours worth of data. These large capacity removable disks provide a convenient means of transferring data to other platforms for post-flight processing.

All data acquisition software has been developed using National Instrument's LabWindows/CVI and NiDAQ software. The main source code is written in ANSI C, with frequent calls to National Instruments' library functions. All user interaction is handled through graphical user interface (GUI) display panels. The code is compiled into a standalone executable file. The software features numerous real time displays that allow all of the instrument outputs to be viewed either as low level (i.e., unprocessed) values or as numerically processed values. This has been useful to monitor the instrument for correct operation in-flight, as well as to diagnose problems when they occur.

### 2.6 Size, Weight and Power

The overall size of the MATR optical table is 41 cm wide by 67 cm long by 39 cm high, including thermal and electrical controls, but not including the in-flight radiometric calibration assembly. Additional electronics and the video recorder occupy about 24" in height in a standard 19" wide electronics rack. The position and orientation system uses another 7" of rack height. The power supply electronics use as input 28 V DC and 110 V AC electrical power that is supplied by the aircraft. Total power consumption is somewhat less than 1400 W (50 A) at 28 V DC and less than 330 W (3 A) at 110 V AC. Power for the detectors' pre-amplifiers is provided by a pair of nominally 12 V re-chargeable lead acid storage batteries, for minimum electrical noise. An un-interruptible power supply (UPS) with 110 V AC output ensures power integrity to the computer.

### 2.7 Aircraft

MATR has been flown in a Cessna Citation II aircraft that is owned by the Department of Energy and operated out of the Remote Sensing Laboratory in Las Vegas, Nevada. The service ceiling for the aircraft is 13 km, but in practice a cruise altitude of 12 km has been used for MATR deployments. The standard cruise speed at 12 km altitude is about 660 km/hr. The flight range (until 30 minute reserve) is about 2,400 km.

## 3. LAB TESTING AND CALIBRATION

A variety of tests and calibrations have been carried out for MATR. These include the following: calibration of temperature, pressure, and other engineering transducers; tests to establish the timing of the gas modulations and chopping with respect to the data acquisition timing; linearity tests; gain setting tests; scan mirror repeatability tests; checks for total out-of-field (stray

light) response; characterization of the effect of chopper blade temperature on radiometric response; radiometric calibration; tests of signal-to-noise ratio with a stable radiance source; tests of the LMC behavior as a function of fill pressure; tests of the PMC pressure cycle. This paper will present in detail the results of only a few of the most significant tests and calibrations.

### 3.1 Detector Output Waveforms and Instrument Timing

In order to process the gas correlation data from MATR, it is necessary first to establish the timing of the gas modulations and chopping with respect to the data acquisition. The LMC, PMC and chopper are all phase locked to reference frequencies that are derived from a single master clock, which is also tied to the data acquisition timing. The data acquisition trigger is derived from the actual phases of the modulators as determined from optical encoders. The first chopper transition that follows an LMC short-to-long path transition triggers a data acquisition sequence. Data is then acquired for a period of time that corresponds to 5 LMC states, which equals 5 PMC cycles.

Fig. 3 shows the AC-coupled output of the channel 2 detector (4.6 micrometer LMC channel). The chopper produces the high speed, nearly square wave chopping. The amplitude of this square wave is proportional to the difference between the chopper blade radiance and the input source radiance, as observed through the LMC. The overall modulation envelope is produced by the LMC. The low, flat portions of the envelope correspond to strong absorption by the 10-mm gas path ( $\text{CaF}_2$  displacer is out of the beam). The high, flat portions correspond to weaker absorption by the 2-mm gas path ( $\text{CaF}_2$  displacer is in the beam). The sloping portions occur when the edge of the  $\text{CaF}_2$  displacer is moving through the beam. As mentioned before, the only data retained for processing is that acquired with the chopper fully open or fully closed, and with the displacer completely in the beam or completely out. The data shown in Fig. 3 is used to determine when these conditions are true.

Fig. 4 shows how the high resolution spectral filtering of a gas correlation device is derived. In this idealized case, 3 gas absorption lines are present within the pass band of the channel filter. The thin dashed line at top shows transmittance through the gas and band pass filter with a small amount of gas in the correlation cell. This state corresponds to the intervals from 0.02 to 0.03 s and from 0.06 to 0.07 s in Fig. 3. The other thin dashed line shows transmittance with a large amount of gas in the correlation cell. This corresponds to the intervals from 0.0 to 0.01 s, from 0.04 to 0.05 s, and from 0.08 to 0.09 s in Fig. 3. One can numerically convert the chopped signal amplitudes for these two states into average and difference signal amplitudes. These average and difference signal amplitudes then correspond to two distinct spectral response functions. The average spectral response function, shown as a heavy solid line in Fig. 4, is very close to the transmittance of the band pass filter, with slight dips at the gas absorption wavelengths. The difference spectral response function, shown as a thin solid line in Fig. 4, peaks only at wavelengths where the gas in the correlation cell absorbs.

Fig. 5 shows the AC-coupled output of the channel 3 detector (4.6 micrometer PMC channel). The high frequency modulation of the chopper is still evident. However, the modulation envelope produced by the PMC has a sinusoidal character due to the more or less sinusoidal variation of pressure in the PMC. For the PMC, data is again considered valid only when the high frequency chopper is fully opened or fully closed. However, a two term Fourier expansion is used to describe the PMC modulation envelope.

### 3.2 Spectral characterization

Knowledge of the instrument's spectral response functions, illustrated in idealized form in Fig. 4, is important for analysis of many of the tests and calibrations, and is especially important for carrying out retrievals of atmospheric  $\text{CO}$ , or  $\text{CH}_4$ . The spectral response functions can be separated into two components: the first is the transmittance of the gas in the correlation cell for each channel; the second is the transmittance of the band pass filter in each channel. As the spectral parameters of  $\text{CO}$  (i.e., line positions, line strengths, and pressure broadening coefficients) have been measured with very good precision and accuracy,<sup>12</sup> it is possible to calculate with sufficient precision and accuracy the transmittance of the gas in the correlation cells, provided we determine with sufficient precision and accuracy the path length, temperature, and pressure for each state of each correlation cell.

For the transmittance of the band pass filters, we originally used the transmittance curves that were supplied by the filter manufacturers. We also had the transmittance of one of the 4.6 micrometer filters measured by colleagues at the University of Toronto, using a Fourier transform spectrometer. The results of the two different characterizations are shown in Fig. 6. There is a shift of approximately 0.006 nm between the two results. This shift has not been very significant when interpreting laboratory tests, and the manufacturer's filter profile was used to analyze the results presented in sections 3.3 and 3.4. However, the filter shift has been very significant for retrievals of atmospheric  $\text{CO}$ , and this will be discussed in sections 4.1 and 5.

### 3.3 LMC Modulation Tests

For this paper, LMC modulation is defined as the ratio of the LMC difference signal radiance to the LMC average signal radiance, or  $R(D/A)$ . Fig. 7 shows measured and calculated values of  $R(D/A)$  for the 2.3 micrometer LMC channel for CO fill pressures from 0 to 90 kPa (measurements) or 100 kPa (calculations only). Best fit lines are also shown. The best fit slopes for the measurements and calculations agree to within about 0.3%. Ideally the intercept values should be zero. The intercept for the calculations is non-zero and slightly negative (i.e.,  $-5.2 \times 10^{-6}$ ) because  $R(D/A)$  is not a strictly linear function of LMC fill pressure. The intercept for the measurements is non-zero and slightly positive (i.e.,  $4.2 \times 10^{-6}$ ). The intercept for the measurements is influenced by the slight non-linearity in  $R(D/A)$  as well as by the slight modulation that is produced by the  $\text{CaF}_2$  displacer. This spurious modulation has also been called the LMC imbalance.<sup>9</sup>

Fig. 8 shows measured and calculated values of  $R(D/A)$  for the 4.6 micrometer LMC channel for CO fill pressures from 0 to 80 kPa. Values for views of the hot blackbody (HBB) at 40 °C and of the cold blackbody (CBB) at 2 °C are plotted. Measured values are shown as discreet markers (filled circles for the HBB and open circles for the CBB). Calculated values are plotted as lines (solid for the HBB and dashed for the CBB). Because the absorption by the fundamental band at 4.6 micrometers is so much stronger than absorption by the first harmonic band at 2.3 micrometers,  $R(D/A)$  at 4.6 micrometers is not an especially linear function of CO fill pressure, and so best fit lines are not shown. The calculated values for the HBB and CBB are in fact identical. The measured values for viewing the HBB agree with the calculated values to within 0.7% at 80 kPa, while for the CBB the agreement is about 2.7%. For the HBB, the agreement between the measured and calculated values is about the same for all fill pressures. However, the measured and calculated values for the CBB converge at the midpoint, or 40 kPa, and then diverge at lower and higher fill pressures. This indicates that some unknown source of instrument error is present when viewing the CBB. Inspection of the average and difference radiance signals shows that almost all of the error is associated with the difference signal. However, the source of the error has not yet been identified.

### 3.4 PMC pressure cycle tests

Fig. 9 shows measured and calculated values of the PMC pressure cycle. The calculations were performed using a model that was originally developed to describe PMCs that were carried aboard the ISAMS satellite.<sup>13</sup> After adjustments were made to various model parameters, the model was able to do a good job of predicting the maximum and minimum pressures in the PMC. However, the measured pressure has a more rapid decrease from the maximum and a less rapid increase from the minimum than does the calculated pressure. Alternatively one could say that the measured pressure has a slight phase lead when the expansion portion of the cycle begins, and a slight phase lag when the compression portion of the cycle begins. Although only pressure is plotted, the model calculates both the pressure and the temperature of the gas in the PMC. Both pressure and temperature are required to calculate the transmittance of the correlation gas in the PMC.

## 4. FLIGHT RESULTS

MATR was put through a set of flights in February and March, 1998. The instrument functioned with no outright failures, but several problems were noted. In particular, some thermal control problems were discovered and addressed. In addition, a leak in the LMC was noted and fixed. Another set of flights were made in January and February, 1999. CO retrievals from two of these flights are shown in Figs. 10 and 11. The retrievals used only the 4.6 micrometer LMC (channel 2) data. The retrieval process used is relatively straightforward. A forward model is used to calculate atmospheric radiance values, starting with an assumed surface emissivity of 0.98, with water vapor and temperature profiles obtained from nearby radio sondes, with CO values set initially to 100 ppbv mixing ratio at all altitudes, and with fixed profiles for other absorbing species. Surface temperature is then adjusted until the calculated average signal radiance agrees with the measured average signal radiance. The CO mixing ratio is then adjusted until the calculated difference signal radiance agrees with the measured difference signal radiance. A final iteration is then made to the surface temperature.

### 4.1 Flight results over Carr, Colorado

Fig. 10 shows CO values that were retrieved from MATR measurements made over Carr, Colorado on 4 Feb. 1999. On this day in situ measurements, made by a group from the NOAA Climate and Monitoring Diagnostics Laboratory, were also available. A CO mixing ratio of 80 ppbv was retrieved when the manufacturer's filter profile was used. A CO mixing ratio of 155 ppbv was retrieved when the University of Toronto filter profile was used. Compared to the in situ results, the value retrieved using the manufacturer's filter profile is too low, while the value retrieved using the manufacturer's filter profile is too high.

#### 4.2 Flight results over Los Angeles and Pacific Ocean

Fig. 11 shows CO values that were retrieved from MATR measurements made over Los Angeles and the nearby Pacific Ocean on 22 Jan. 1999. Only results obtained using the manufacturer's filter profile are shown. On this day fairly strong winds were blowing from the west to the east, and so the air over the Pacific could be considered "unpolluted". The average value over the ocean is 56 ppbv, and the concentrations over Los Angeles peak near 200 ppb. Based on the results obtained over Carr, Colorado, these values are probably too low. However, Fig. 11 clearly shows a strong instrumental response when going from a region where low and constant CO values are expected (i.e., the Pacific Ocean) to a region where high and variable CO values are expected (i.e., the Los Angeles basin). The standard deviation of the measurements over the Pacific is 3.8 ppbv, with a time period for signal averaging that corresponds to about 2.5 km of distance traveled by the Citation aircraft. Even if this standard deviation were doubled (based on the different results over Carr for the different filter profiles), the precision is well within the target of 10 ppbv. Furthermore, this is with spatial resolution of 1.2 km (across the flight track) by 2.5 km (along the flight track), which is quite small compared to the MOPITT pixel size of about 22 km by 22 km.

#### 5. Summary and Discussion

MATR was conceived for two functions: first to collect data to test our ability to retrieve correct atmospheric CO, or CH<sub>4</sub>, gas amounts from MOPITT-like gas filter radiometer data; and second to help validate MOPITT data. The instrument has been designed, built, and flown to collect data. The retrieval results from recent flights strongly suggest the need to calibrate carefully the spectral response of the band pass filters in each channel. Although two different measurements were made of the band pass filters for the 4.6 micrometer channels, the results differ, and there is no clear criteria for deciding which, if either, result is correct. Furthermore, these measurements were made on the band pass filters alone. Although the transmittance of the rest of the optics is not expected to vary strongly with wavelength, a true end-to-end calibration of the entire MATR instrument should be performed. A monochromator system has been assembled for this purpose and these measurements are planned for the near future. There is also a need to understand the anomalous behavior of the LMC thermal channel when looking at the cold blackbody source. There is also a need to obtain additional data to compare MATR retrieval results to in situ measurements, as a single day is really insufficient to demonstrate valid instrument performance. Additional flights to obtain this data are scheduled for August, 1999. Finally, additional work needs to be done to make use of the channel 1 (2.3 micrometer LMC) and channel 3 (4.6 micrometer PMC) data. This work is under way.

#### ACKNOWLEDGMENTS

The MATR project is funded by NASA under contract NAS5-30888 administered through Dr. Michael King's office and this funding is gratefully acknowledged. John Gille supervises the MATR project. Kate Paulin made the calculations of PMC pressure cycle that are shown in Fig. 9.

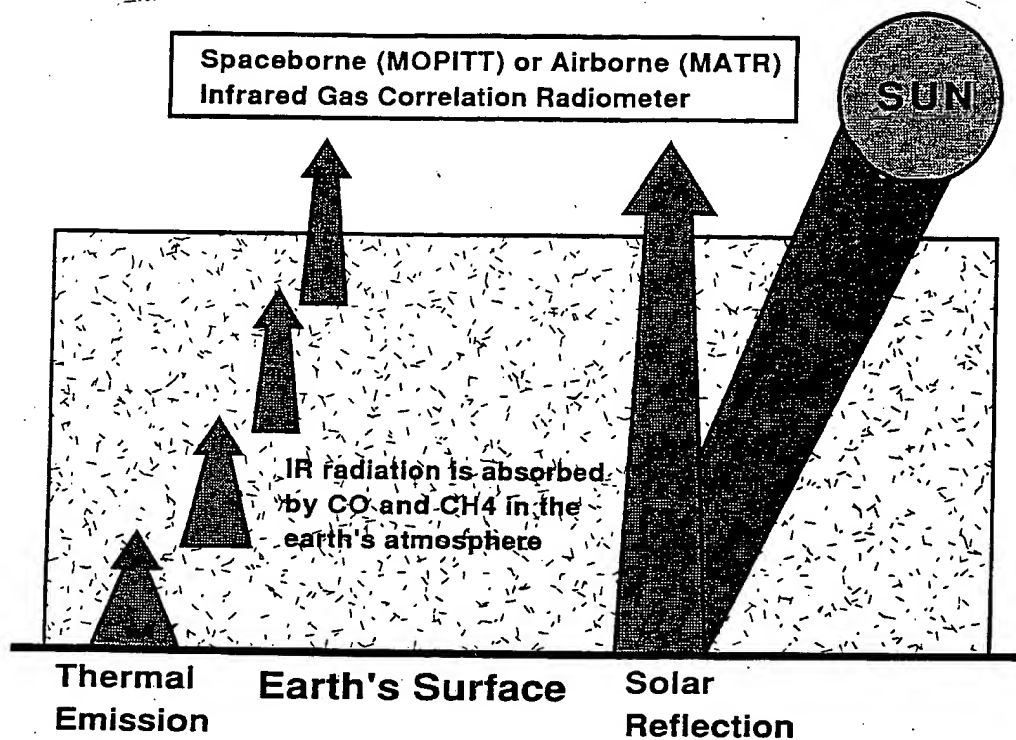


Figure 1. Schematic illustration of atmospheric radiative transfer and remote sensing processes.

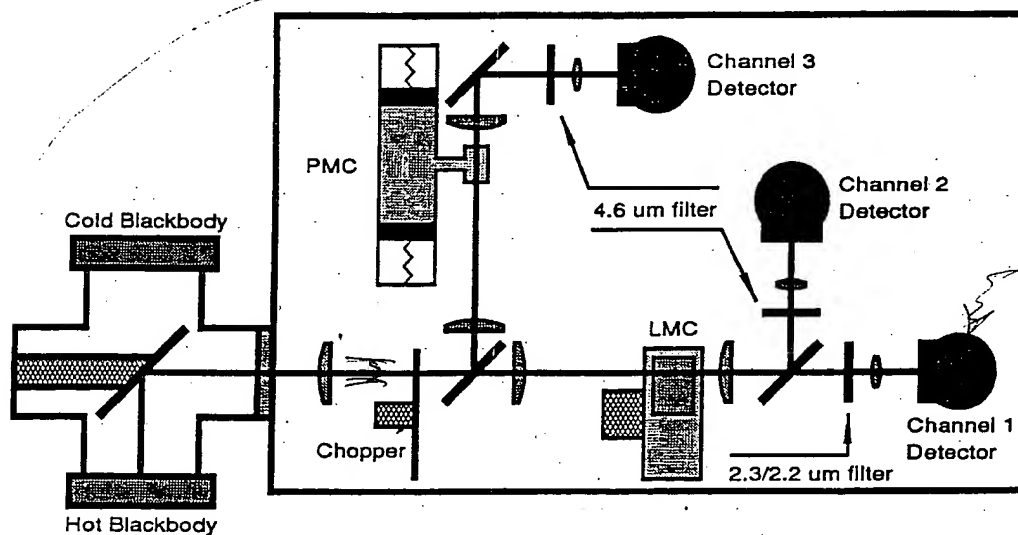


Figure 2. MATR optical table.



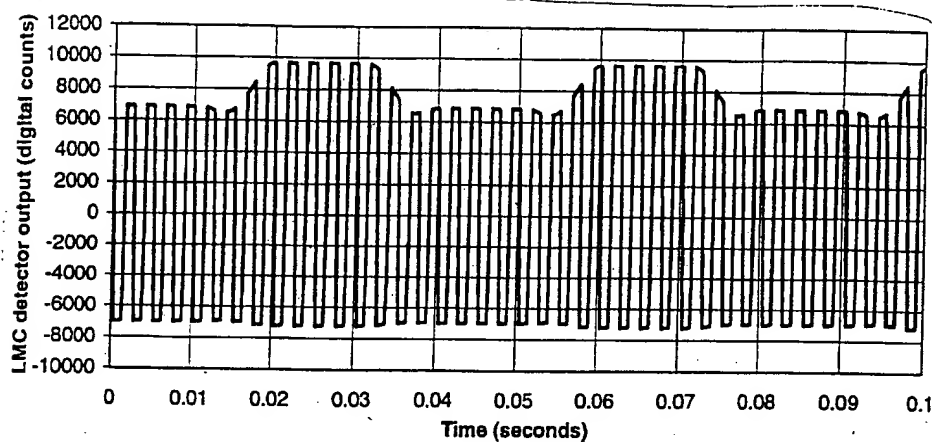


Figure 3. AC-coupled detector signal for MATR 4.6 micrometer LMC channel.

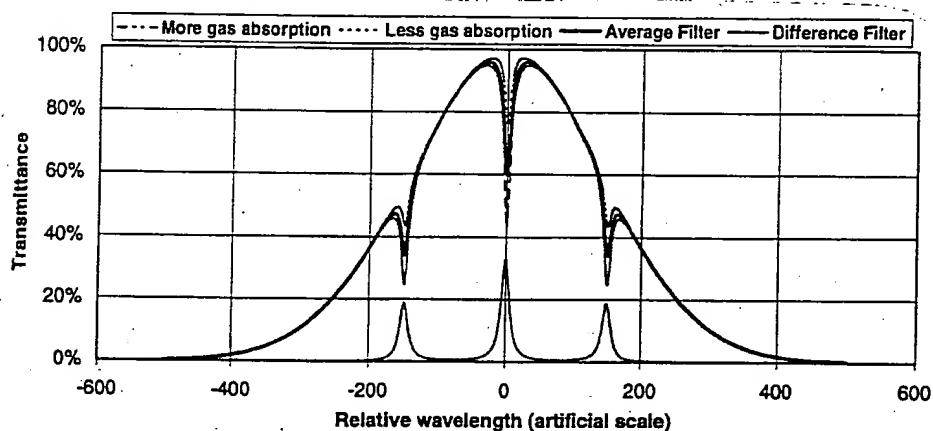


Figure 4. Idealized spectral response functions for a gas correlation filter radiometer.

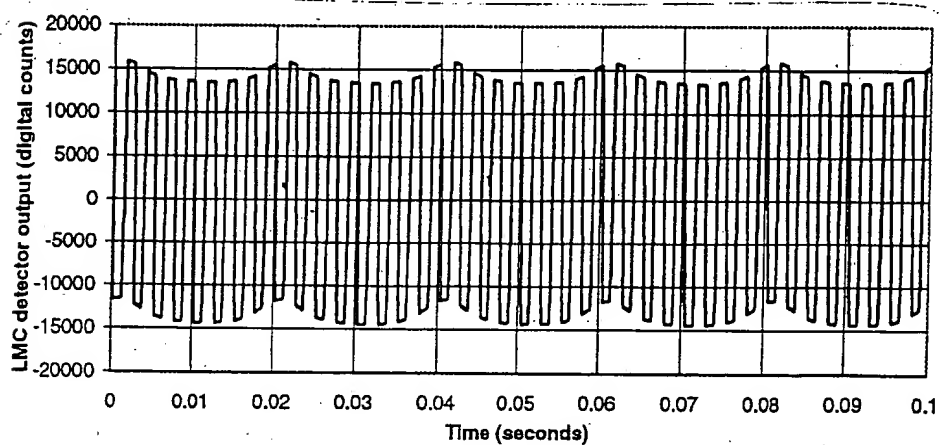


Figure 5. AC-coupled detector signal for MATR 4.6 micrometer PMC channel.

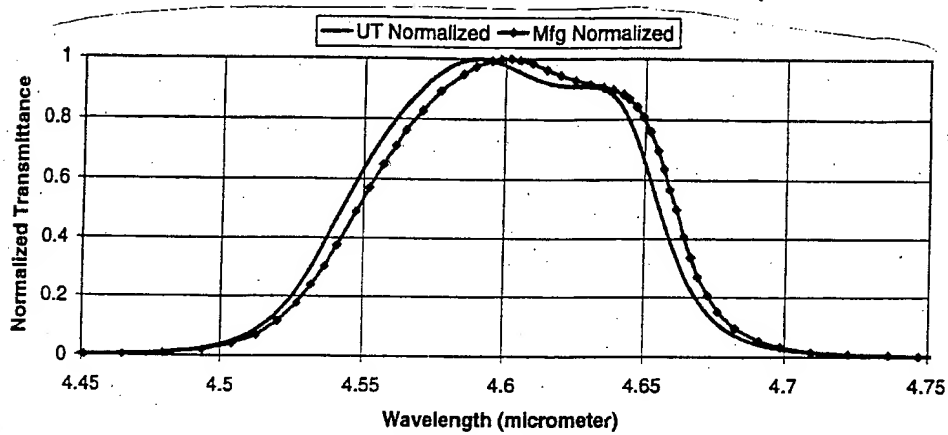


Figure 6. Spectral pass band for 4.6 micrometer channels as determined by filter manufacturer and University of Toronto.

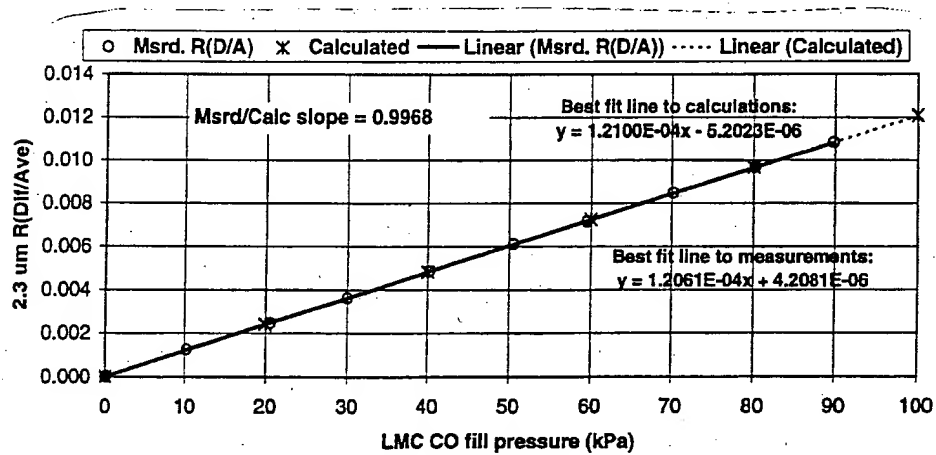


Figure 7. Ratio(Dif/Ave) as a function of LMC fill pressure for 2.3 micrometer channel.

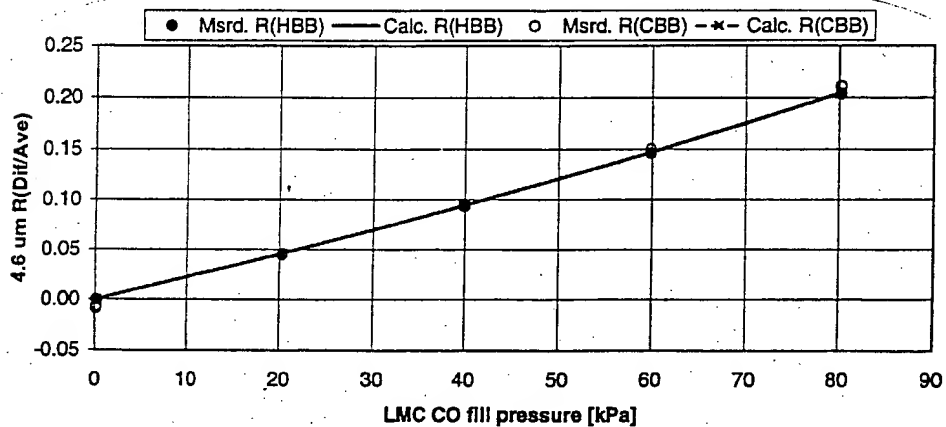


Figure 8. Ratio(Dif/Ave) as a function of LMC fill pressure for 4.6 micrometer channel.

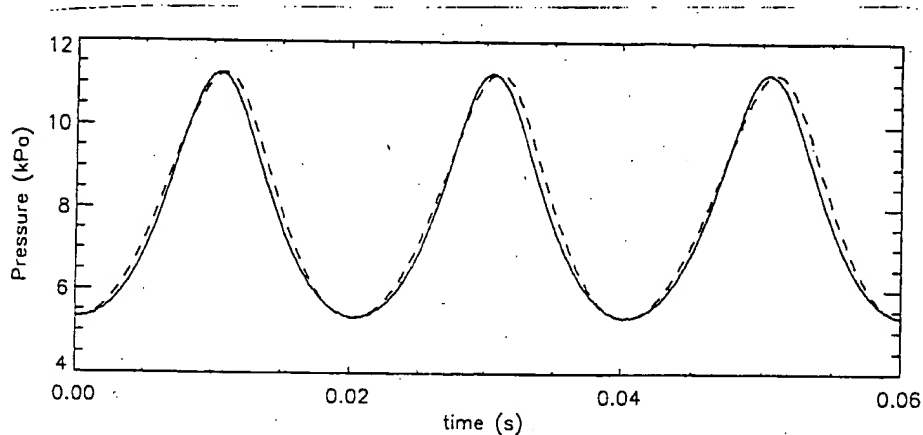


Figure 9 Calculated (dashed line) and measured (solid line) PMC pressure cycles.

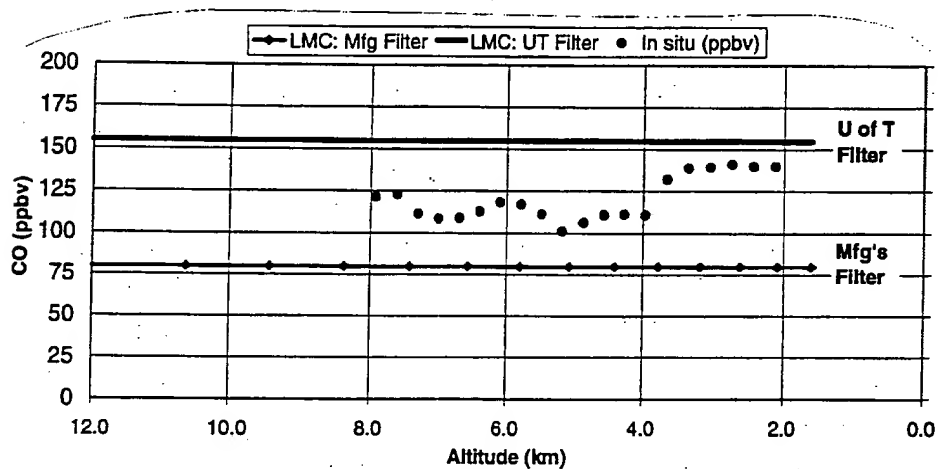


Figure 10. CO values from in-situ measurements and MATR retrievals over Carr, CO on 4 Feb. 1999 for both filter profiles

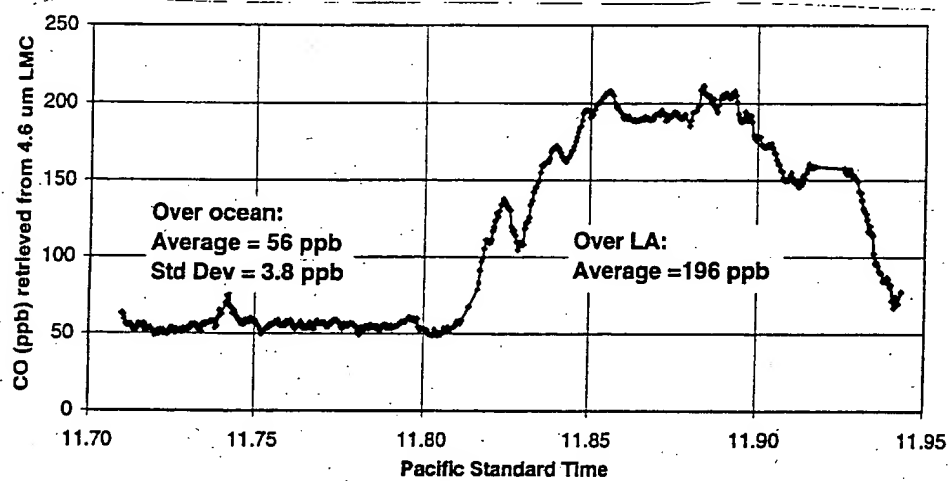


Figure 11. CO retrieved from MATR data over Los Angeles and Pacific on 22 Jan. 1999 using manufacturer's filter profile.

## REFERENCES

1. J.R. Drummond, "Measurements of Pollution in the Troposphere (MOPITT)," in *The Use of EOS for Studies of Atmospheric Physics*, J.C. Gille and G. Visconti, Eds., pp. 77-101, North-Holland, Amsterdam (1992).
2. J.R. Drummond, G.P. Brasseur, G.R. Davis, J.C. Gille, J.C. McConnell, G.D. Peskett, H.G. Reichle, Jr., and N. Roulet, "MOPITT Mission Description Document," Department of Physics, University of Toronto, Toronto, Canada (Oct. 1996). Available HTTP: <http://www.atmosp.physics.utoronto.ca> Directory: /Research Groups/MOPITT
3. J. Wang, J. Gille, P. Bailey, M. Smith, L. Pan, D. Edwards, L. Rokke, J. Drummond, G. Davis, H. Reichle, "MOPITT Data Validation Plan," National Center for Atmospheric Research, Boulder, Colo. (Sept. 1996). Available HTTP: <http://eos.acd.ucar.edu> Directory: /mopitt/val\_plans.html File: Version 3 validation plan (in various formats).
4. L. Pan, J.C. Gille, D.P. Edwards, P.L. Bailey, "Retrieval of tropospheric carbon monoxide for the MOPITT experiment," *J. Geophys. Res.*, **103** (D24), pp. 32,277-32,290 (Dec. 1998).
5. L. Pan, J.C. Gille, C.D. Rodgers, D.P. Edwards, P.L. Bailey, L.A. Rokke, J. Wang, "Analysis and characterization of the retrieval algorithm for measuring tropospheric CO using the MOPITT instrument," *Proc. of SPIE*, **2830**, pp. 159-168 (Aug. 1996).
6. NCAR MOPITT Team, "MOPITT: Algorithm Theoretical Basis Document," National Center for Atmospheric Research, Boulder, Colo. (July 1995). Available HTTP: <http://eos.acd.ucar.edu> Directory: /mopitt/atbds.html File: Level-2 ATBD (in various formats).
7. J.H. Seinfeld, S.N. Pandis, *Atmospheric Chemistry and Physics*, Chapter 5, John Wiley & Sons, New York (1998).
8. M.W. Smith and S. R. Shertz, "Current plans and status of MOPITT Algorithm Test Radiometer (MATR)," *Proc. of SPIE*, **2820**, pp. 78-86 (Aug. 1996).
9. B.T. Tolton and J.R. Drummond, "Characterization of the length-modulated radiometer," *Appl. Opt.*, **36** (22), pp. 5409-5420 (Aug. 1997).
10. J.T. Houghton, F.W. Taylor, and C.D. Rodgers, *Remote Sounding of Atmospheres*, pp. 93-107, Cambridge University Press, Cambridge (1984).
11. F.W. Taylor, "Pressure Modulator Radiometry," in *Spectrometric Techniques, Vol. III*, G. A. Vanasse, Ed., pp. 137-196, Academic Press, New York (1983).
12. L.S. Rothman, R.R. Gamache, R.H. Tipping, C.P. Rinsland, M.A.H. Smith, D. Chris Benner, V. Malathy Devi, J.-M. Flaud, C. Camy-Peyret, A. Perrin, A. Goldman, S.T. Massie, L.R. Brown, and R.A. Toth, "The HITRAN molecular database: editions of 1991 and 1992," *J. Quant. Spectrosc. Radiat. Transfer*, **48**, 5/6, pp. 469-507 (1992).
13. P. Venters, "The ISAMS PMC model," ISAMS document SW304, Oxford University (1991).

NING ELECTRONICS

n," *Aspen Int. Conf.*  
ir Force Cambridge

nglewood Cliffs, NJ,

ation, *Transmission,*

*Infra-red Radiation,*

ation, *Transmission,*

Microwave Frequen-

*Infra-red Radiation,*

## chapter 8

# The Radiometric Performance Equation

### 8.1 INTRODUCTION

The radiometric performance equation is central to the approach to system design given in this text. Its development in this chapter follows the development of the "measurement equation" given in the National Bureau of Standards "Self-Study Manual."<sup>1,2</sup> A general expression of the equation is written first; and then by appropriate assumptions and simplifications the general equation is rewritten for two illustrative systems. The examples given here deal only with the spatial, spectral, and temporal domains. Polarization is neglected. The two measurement configurations are (1) the extended-area source and (2) the distant small-area source. In each case, the detector is characterized in terms of the detectivity.

This chapter also includes (1) a general discussion that summarizes the important features of the radiometric performance equation; (2) a set of orderly steps for writing the equation; and finally, (3) a summary of the limitations of the radiometric performance equation.

### 8.2 THE RADIOMETRIC PERFORMANCE EQUATION

The radiometric performance equation provides a criterion for the optimum design of electro-optical systems that is based on the premise that an overriding requirement for all systems designed for information processing is adequate signal-to-noise ratio (SNR). In the radiometric analysis of the feasibility study (Sec. 2.5.1), top priority is given to the signal-to-noise ratio.

Then, depending upon the specific application, spatial or spectral resolution, speed of response, etc., might be important in trade-off studies.

A general form of the equation was given in Sec. 2.6 as the ratio of the effective flux  $\Phi_{\text{eff}}$  to the noise equivalent flux (NEF).

$$\text{SNR} = \frac{\Phi_{\text{eff}}}{\text{NEF}} \quad (8.1)$$

where  $\Phi_{\text{eff}}$  is the effective flux, defined as the magnitude of flux incident upon the sensor detector that is effective in evoking a response in the sensor output as given in Sec. 5.10. The NEF is defined as the change in flux that produces an average change in the output signal equal to the root-mean-square (rms) noise in the output signal.<sup>3</sup>

Table 8.1 lists the system and subsystem figures of merit with the corresponding symbols and units. From the list of alternative subsystem figures of merit, those must be selected for inclusion in the equation that provide for optimization of system performance goals while simultaneously maximizing the signal-to-noise ratio.

It is important to remember that polarization is being ignored in the development given here. In addition, the effects of nonlinearity and hysteresis are being set aside although they are often a consideration in the design of real systems.

Other assumptions about the system must be made before the performance equation can be written. For example, the appropriate figure of merit for the detector depends upon the limiting noise mechanism and the detector responsivity. For purposes of illustration, it is assumed that the detector can be characterized in terms of the detectivity.

Equation (8.1) can now be expanded in terms of subsystem figures of merit for a measurement configuration as illustrated in Fig. 2.3, using Eqs. (5.28) for the effective flux upon a detector and (6.6) for the detector NEF in terms of  $D^*$  and correcting for dc restoration as follows:

$$\text{SNR} = \frac{D^*(\lambda) \tau_p \tau_e}{\beta (2A_d f_2)^{1/2}} \int_{\theta} \int_{\phi} \int_{\lambda} \Phi_s(\lambda, \theta, \Phi) \mathcal{R}(\lambda) d\theta d\phi d\lambda \quad (8.2)$$

where  $D^*(\lambda)$  is the detectivity, in  $\text{cm Hz}^{1/2}/\text{W}$

$\tau_e$  is the optical efficiency (unitless)

$\beta$  is the chopping factor (unitless)

$\sqrt{2}$  is the phase detection noise factor (unitless)

$A_d$  is the detector area, in  $\text{cm}^2$

$f_2$  is the electrical (low-pass) noise filter cutoff frequency, in  $\text{s}^{-1}$

$\Phi_s(\lambda)$  is the source spectral flux, in  $\phi/\mu\text{m}$

$\mathcal{R}(\lambda)$  is the sensor relative spectral response function

$\Phi$  is the polar angle

$\phi$  is the azimuthal angle

$\lambda$  is the wavelength, in  $\mu\text{m}$

Table 8.1 SYST

	T <sub>r</sub>
<b>Source</b>	
Stance [radiance]	
Areance [exitance]	
Pointance [intensity]	
<b>Path</b>	
Path transmittance	
<b>Receiver</b>	
Areance [irradiance]	
Aperture area	
<b>Spatial</b>	
Throughput (genera)	
Relative aperture	
Field of view (linear)	
Field of view (solid)	
<b>Spectral</b>	
Free spectral range	
Bandwidth	
Resolving power	
<b>Polarization</b>	
Stokes parameters	
<b>Optical</b>	
Optical efficiency	
Chopping factor	
<b>Detectors</b>	
Noise equivalent pc	
Responsivity	
Detectivity	
<b>Electronics</b>	
Noise bandwidth	
Time constant	
Rise time	
Noise voltage	
<b>System</b>	
Noise equivalent pc	
Noise equivalent st	
[Noise equivalent r	
Noise equivalent sp	
[Noise equivalent s]	
Noise equivalent fl	
Noise equivalent sp	

or spectral resolution studies.  
as the ratio of the

(8.1)

of flux incident on the sensor  
change in flux that to the root-mean-

of merit with the native subsystem  
the equation that it simultaneously

ing ignored in the clarity and hysteresis  
in the design

before the performance  
appropriate figure of merit  
mechanism and the assumed that the

system figures of merit  
Fig. 2.3, using Eqs. the detector NEP  
is:

$$\theta d\phi d\lambda \quad (8.2)$$

s)

off frequency, in

ction

Table 8.1 SYSTEM AND SUBSYSTEM FIGURES OF MERIT

Term	Symbol	Unit
<b>Source</b>		
Sterance [radiance]	$L$	$\text{W cm}^{-2} \text{ sr}^{-1}$
Areance [exitance]	$M$	$\text{W/cm}^2$
Pointance [intensity]	$I$	$\text{W/sr}$
<b>Path</b>		
Path transmittance	$\tau_p$	—
<b>Receiver</b>		
Areance [irradiance]	$E$	$\phi/\text{cm}^2$
Aperture area	$A_c$	$\text{cm}^2$
<b>Spatial</b>		
Throughput (general)	$A\Omega$	$\text{cm}^2 \text{ sr}$
Relative aperture	$F$	—
Field of view (linear)	$\theta$	$\text{deg } (^\circ), \text{ rad}$
Field of view (solid)	$\Omega$	$\text{sr}$
<b>Spectral</b>		
Free spectral range	$\lambda_1 - \lambda_2$	$\mu\text{m}$
Bandwidth	$\Delta\lambda$	$\mu\text{m}$
Resolving power	$\delta\lambda$	$\mu\text{m}$
<b>Polarization</b>		
Stokes parameters		
<b>Optical</b>		
Optical efficiency	$\tau_e$	—
Chopping factor	$\beta$	—
<b>Detectors</b>		
Noise equivalent power	NEP	W
Responsivity	$\mathcal{R}$	$\text{V/W}$
Detectivity	$D^*$	$\text{cm Hz}^{1/2}/\text{W}$
<b>Electronics</b>		
Noise bandwidth	$\Delta f$	$\text{Hz (s}^{-1}\text{)}$
Time constant	$T_c$	s
Rise time	$T_r$	s
Noise voltage	$V_n$	V rms
<b>System</b>		
Noise equivalent power	NEP	W
Noise equivalent sterance	NES	$\phi \text{ cm}^{-2} \text{ sr}^{-1}$
[Noise equivalent radiance]	[NER]	$\text{W cm}^{-2} \text{ sr}^{-1}$
Noise equivalent spectral sterance	NES	$\phi \text{ cm}^{-2} \text{ sr}^{-1} \mu\text{m}^{-1}$
[Noise equivalent spectral radiance]	[NESR]	$\text{W cm}^{-2} \text{ sr}^{-1}$
Noise equivalent flux density	NEFD	$\text{W/cm}^2$
Noise equivalent spectral flux density	NESFD	$\text{W cm}^{-2} \mu\text{m}^{-1}$

### 8.2.1 The Extended-Area Source

The radiometric performance equation must be written in a form containing the desired radiometric quantity to characterize the source. It is written most appropriately for the extended-area source in terms of the sterance [radiance] as follows:

$$\text{SNR} = \frac{D^*(\lambda) \tau_p \tau_e}{\beta (2A_d f_2)^{1/2}} \int_{A_s} \int_{\omega_s} \int_{\lambda} L_s(\lambda) \mathcal{R}(\lambda) \cos \theta dA_s d\lambda d\omega_s \quad (8.3)$$

where  $L_s(\lambda)$  is the source sterance [radiance] in  $\text{W cm}^{-2} \text{sr}^{-1} \mu\text{m}^{-1}$  and  $A_s$  is the source area in  $\text{cm}^2$ .

Equation (8.3) can be integrated based upon a number of simplifying assumptions:<sup>4</sup>

1. The source sterance [radiance] is uniform over the source area  $A_s$ .
2. The source sterance [radiance] is uniform over the system spectral response function.
3. The solid angle is independent of the source area.
4. The path is contained in a homogeneous medium where the index of refraction exhibits unity value.

Then Eq. (8.3) can be written as

$$\text{SNR} = \frac{L_s(\lambda) \Delta\lambda D^*(\lambda) \tau_e \tau_p A_{fs} \pi}{\beta (2A_d f_2)^{1/2} 4F^2} \quad (8.4)$$

where, by the invariance theorem,

$$\Omega_s A_s = \Omega_c A_c = A_{fs} \pi / 4F^2 \quad (8.5)$$

and where  $\int dA_s = A_s$ , the source area, in  $\text{cm}^2$

$\int \cos \theta d\omega_s = \Omega_s$ , source solid angle, in sr

$\int L_s(\lambda) \mathcal{R}(\lambda) d\lambda = L_s(\lambda) \Delta\lambda$ , the effective flux, in  $\text{W cm}^{-2} \text{sr}^{-1}$

For the case where the detector serves as the field stop,  $A_{fs} = A_d$ , as illustrated in Fig 5.3, Eq. (8.4) can be written as

$$\text{SNR} = \frac{L_s(\lambda) \Delta\lambda D^*(\lambda) \tau_e \tau_p \pi (A_d / 2f_2)^{1/2}}{4F^2 \beta} \quad (8.6)$$

Equation (8.6) provides for system optimization and sensitivity analysis.<sup>5</sup> In consideration of the most obvious parameters, the SNR is maximized by maximizing the source spectral sterance [radiance]  $L_s(\lambda)$ , the detectivity  $D^*$ , the optical efficiency  $\tau_e$ , and the path transmittance  $\tau_p$ . The effect of the magnitude of the bandwidth  $\Delta\lambda$ , the detector area  $A_d$ , the relative aperture  $F$ , and the electrical noise frequency  $f_2$  warrants more careful consideration.

Equation (8.6) corresponds to "fast" aperture, or  $f$ -number. Eq. (8.6) does not mean that the SNR is true that the SNR is extended-area source traded off for aperture.

The SNR is accomplished by the fact that for noise increases proportional to the square root of the detector area.

The conclusion is that noise-limiting camera temperatures and available noise.<sup>6</sup> In the Eq. (6.5) is a preamplifier noise and to detector area.

The electrical noise bandwidth. The square root of the noise bandwidth over SNR.

The SNR trade-off is necessary serious limiting factors. In the spectral resolution conditions, the time resolution increases SNR.

### 8.2.2 Distant Source

In this case the SNR of a distant source can be characterized by a noise density  $I$  in  $\text{W/sr}$ , as follows:

where  $I_s(\lambda)$  is



Equation (8.6) illustrates that the SNR is more sensitive to the relative aperture, or  $f$ -number, than any other parameter. Lower  $f$ -number corresponds to "faster optics" and to increased throughput and SNR. However, Eq. (8.6) does not contain an explicit term for the sensor field of view. It is true that the SNR is independent of field of view in the case of a uniform extended-area source; this follows from the fact that field of view can be traded off for aperture area.

The SNR is not very sensitive to increases in the throughput that are accomplished by increasing the detector field-stop area. This results from the fact that for detectors most appropriately characterized with  $D^*$ , the noise increases with the square root of detector area; hence, NEP is proportional to the square root of detector area.

The conclusions drawn from Eq. (8.6) may not be valid for different noise-limiting cases. For example, extrinsic detectors operated at cryogenic temperatures and shielded from any background may not produce measurable noise.<sup>6</sup> In this case the limiting noise originates in the preamplifier, and Eq. (6.5) is a more appropriate expression of the detector NEP. The preamplifier noise is often directly proportional to the detector capacitance and to detector area. In this case the SNR is more or less independent of detector area.

The electrical noise bandwidth also determines the system information bandwidth. Equation (8.6) shows that SNR is inversely proportional to the square root of bandwidth. This means that NEP is not very sensitive to noise bandwidth and that information bandwidth can often take precedent over SNR.

The SNR is directly proportional to the bandwidth  $\Delta\lambda$ , and a trade-off is necessary between SNR and spectral resolution. This becomes a serious limiting factor for high-resolution spectrometer sensors. High spectral resolution has implications for noise bandwidth also. In most applications, the time available for a complete scan is fixed, and increasing the resolution increases the bandwidth requirement further, compromising the SNR.

### 8.2.2 Distant Small-Area Source

In this case the radiometric performance equation is to be written in terms of a distant small area or "point source." It is most appropriate to characterize a nonresolvable point source in terms of the pointance [intensity]  $I$  in W/sr, using Eqs. (5.32) and (6.6) and correcting for dc restoration as follows:

$$\text{SNR} = \frac{I_s(\lambda) \Delta\lambda D^*(\lambda) \tau_e \tau_p \pi (A_d/2f_2)^{1/2}}{4F^2 \beta \Omega_c s^2} \quad (8.7)$$

where  $I_s(\lambda)$  is the source spectral pointance [intensity] in units of

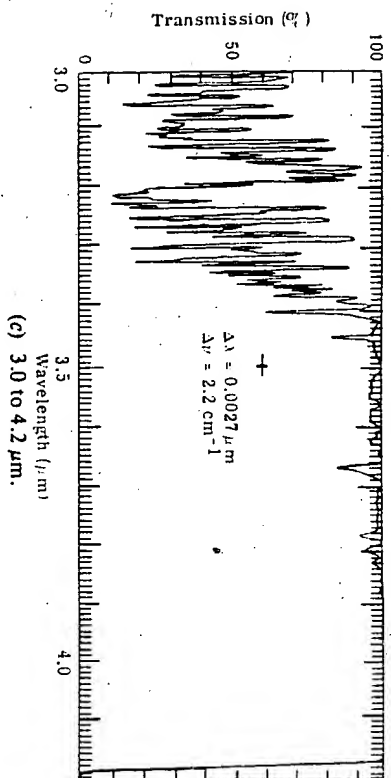
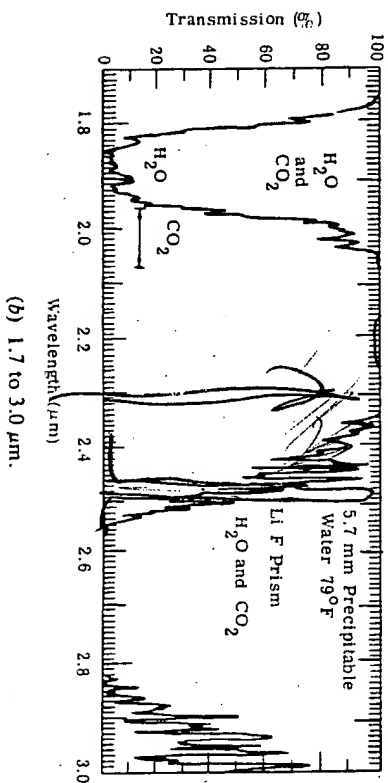
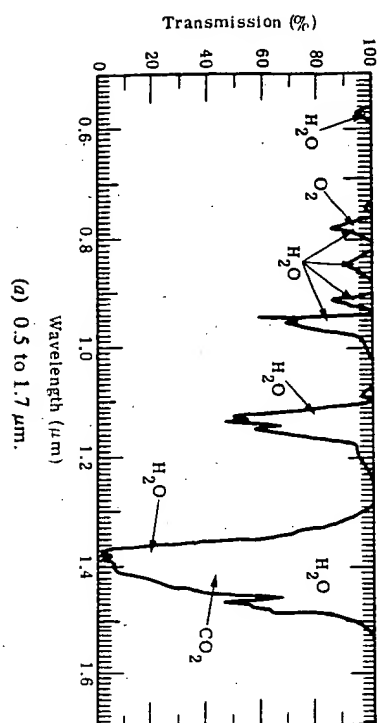


Fig. 5-31. Atmospheric transmission at sea level over a 0.3 km path.

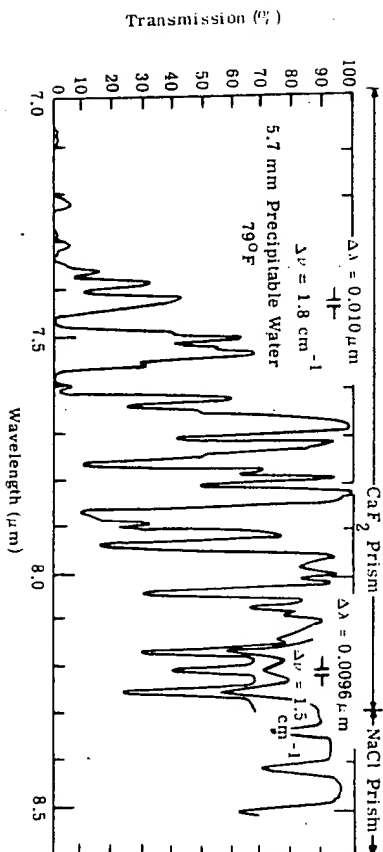
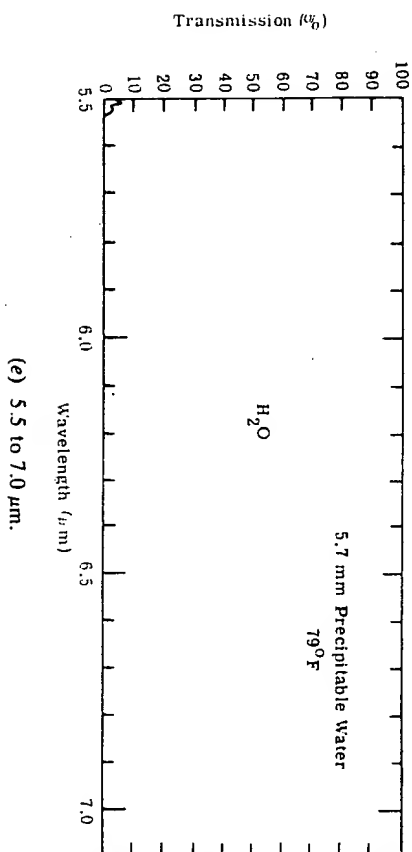
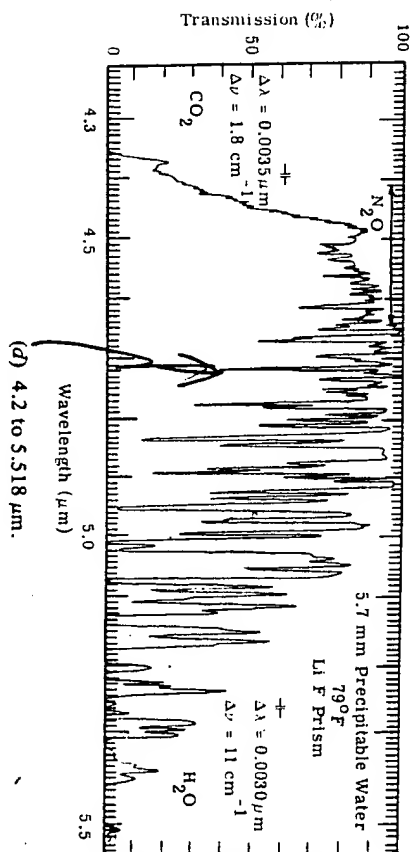


Fig. 5-31 (Continued). Atmospheric transmission at sea level over a 0.3 km path.

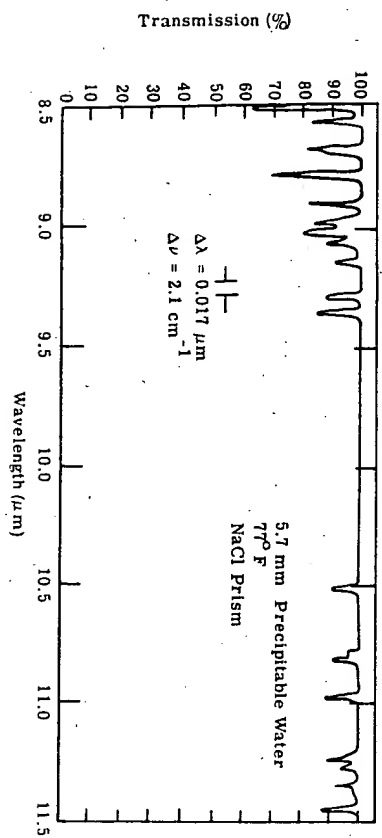
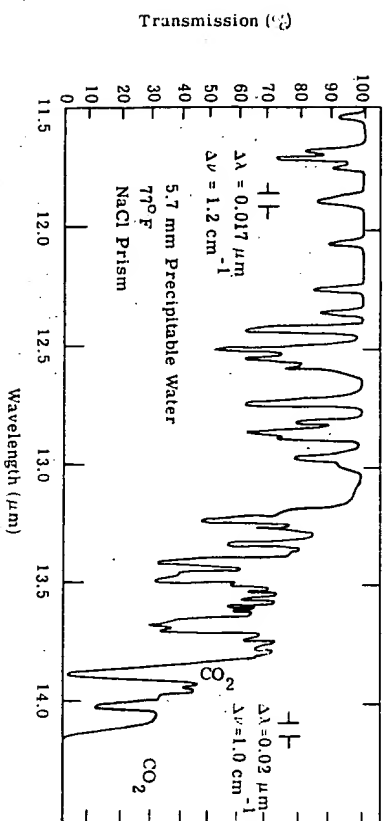
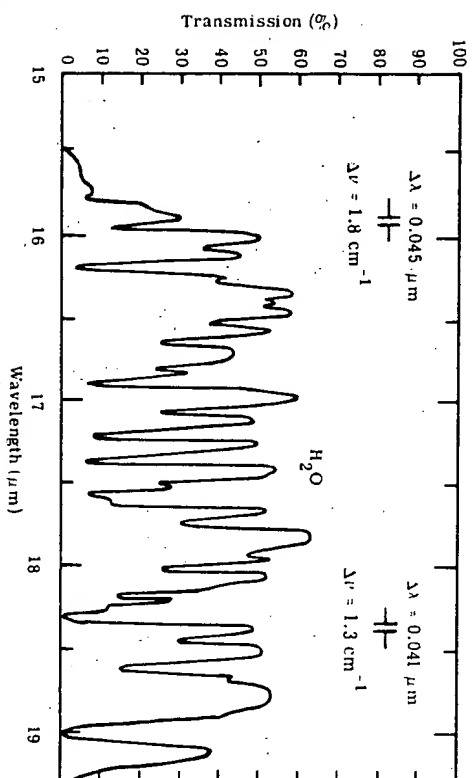
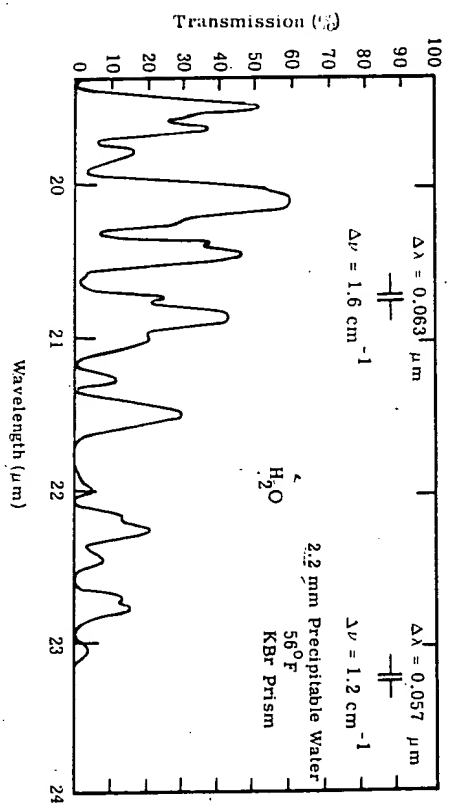
(g) 8.5 to 11.5  $\mu\text{m}$ .(h) 11.5 to 14.0  $\mu\text{m}$ .(i) 15.0 to 19.0  $\mu\text{m}$ .(j) 19.0 to 24.0  $\mu\text{m}$ .

Fig. 5-31 (Continued). Atmospheric transmission at sea level over a 0.3 km path.

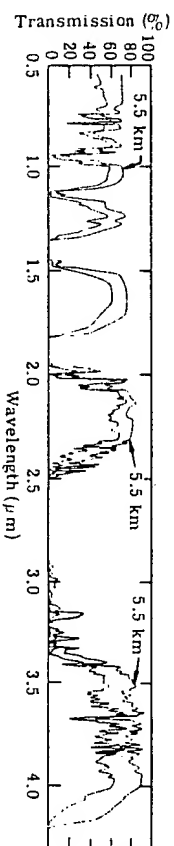
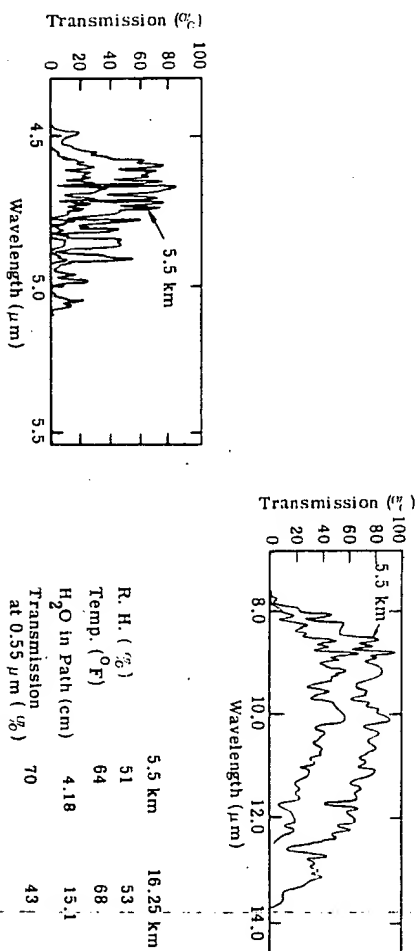
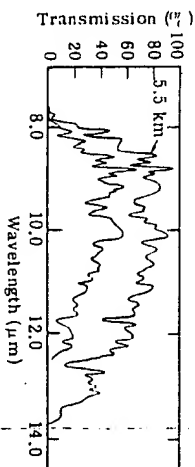
(a) 0.5 to 4.0  $\mu\text{m}$ .(b) 4.5 to 5.5  $\mu\text{m}$ .(c) 8.0 to 14.0  $\mu\text{m}$ .

Fig. 5-32. Atmospheric transmission at sea level over 5.5 and 16.25 km paths.

# ANALYSIS AND CHARACTERIZATION OF THE RETRIEVAL ALGORITHM FOR MEASURING TROPOSPHERIC CO USING THE MOPITT INSTRUMENT

Liwen Pan, John C. Gille, Clive D. Rodgers\*, David P. Edwards,  
Paul L. Bailey, Laurie A. Rokke and Jinxue Wang

National Center for Atmospheric Research,  
P.O. Box 3000, Boulder, CO 80307-3000 USA

\*Atmospheric, Oceanic and Planetary Physics  
Clarendon Laboratory, Parks Road, Oxford OX1 3PU U.K.

## ABSTRACT

We have developed a retrieval algorithm for deriving the tropospheric CO profile and column amount from the radiances measured by the Measurements of Pollution In The Troposphere (MOPITT) instrument. The main components of the algorithm are a fast radiative transfer model, based on the GENLN2 line-by-line model, and a maximum likelihood inversion method. The retrieval *a priori* information is derived from the results of several aircraft *in situ* measurements and a three-dimensional chemical-transport model.

This paper discusses the CO retrieval algorithm with an emphasis on the analysis and characterization of the algorithm. Forward model and retrieval sensitivities, along with the *a priori* information used in the retrieval are discussed in terms of their orthogonal components. Examples of ensemble retrieval experiments are also included.

Key Words: passive remote sensing, retrieval algorithm, tropospheric carbon monoxide

## 1. INTRODUCTION

The scientific objective of the Measurements of Pollution In The Troposphere (MOPITT) experiment is to monitor the spatial and temporal variation of CO and CH<sub>4</sub> in the troposphere. Scheduled for Launch in 1998 on board the EOS/AM satellite, the MOPITT instrument will produce a global tropospheric CO and CH<sub>4</sub> dataset. This dataset should provide a basis for studying the source/sink/ transport of these trace gases and this in turn will provide a better understanding of related tropospheric chemistry.

The MOPITT instrument and its scientific objective have been described in previous publications.<sup>1-2</sup> This paper discusses the CO retrieval algorithm for MOPITT with an emphasis on the analysis and characterization of the algorithm.

MOPITT makes measurements in three spectral bands. A thermal band at 4.7  $\mu\text{m}$  and a solar band at 2.3  $\mu\text{m}$  are used to measure CO. A solar band at 2.2  $\mu\text{m}$  is used to measure CH<sub>4</sub>. The

goal is to measure tropospheric CO column amount and vertical distributions with a 10% accuracy for four tropospheric layers and measure CH<sub>4</sub> column amount with a 1% accuracy.

The MOPITT instrument utilizes gas correlation spectroscopy.<sup>1</sup> The instrument has eight radiometers which utilize two pressure-modulated correlation cells (PMCs) and four length-modulated correlation cells (LMCs), to form six channels for CO measurement and two channels for CH<sub>4</sub> measurement. Table 1 summarizes the basic characteristics of the MOPITT channels. Detailed descriptions of the instrument can be found in references 1 and 2.

Radiometers	1	2	3	4	5	6	7	8
Gas Species	CO	CO	CO	CO	CO	CO	CH <sub>4</sub>	CH <sub>4</sub>
Modulator Type & number	PMC2	PMC1	LMC1	LMC3	LMC1	LMC3	LMC2	LMC4
Nominal Gas Pressure (mb)	38	75	200	800	200	800	800	800
Mid-Wavenumber (cm <sup>-1</sup> )	2166	2166	2166	2166	4285	4285	4430	4430
Wavenumber Range (cm <sup>-1</sup> )	52	52	52	52	40	40	139	139

Table 1. MOPITT channel characteristics.

In section 2, we present the formulation of the retrieval algorithm (for clear sky and cloud cleared pixels). Section 3 describes the retrieval sensitivity and information content. Section 4 provides example results.

## 2. DESCRIPTION OF THE ALGORITHM

The MOPITT CO retrieval algorithm uses a maximum likelihood method that has been described by Rodgers.<sup>3</sup> A fast radiative transfer model was developed to calculate the forward signals.<sup>4</sup> *A priori* statistics were compiled using both a collection of *in situ* measured CO profiles and the output of a three-dimensional chemical-transport model. Further improvements to the *a priori* information database are in progress.

### 2.1. Forward Model

The radiative transfer equations and the forward signal calculations for MOPITT have been described in detail in a previous publication.<sup>5</sup> In this section, we provide a brief summary of the forward model.

For every observed scene, each MOPITT radiometer reports two signals: an average (A) signal and a difference (D) signal. The A signals will provide background atmospheric and surface information. The D signals will provide target gas information. Each D signal response function serves as an effective high resolution filter that selects the CO absorption information at different pressure levels of the atmosphere and allows the instrument to measure the vertical distribution of CO.

Denoting A and D signals by superscripts A and D, respectively, each signal can be represented as:

$$S_i^{A,D} = \int_{\Delta\nu} I(\nu, h) R_i^{A,D}(\nu) d\nu, \quad i = 1, \dots, 8, \quad (1)$$

where  $i$  denotes the radiometer as listed in Table 1,  $I(\nu, h)$  is the spectral radiance at the top of the atmosphere,  $R_i^A(\nu)$  and  $R_i^D(\nu)$  are the A and D response functions, respectively. Later in the paper, we use  $A_i$  and  $D_i$  to represent the  $i$ th A signal and D signal, respectively, for convenience.

For the thermal band, the radiance at the top of the atmosphere is mostly the transmitted surface emission of the earth, although the reflected solar radiation is not negligible, *i.e.*,

$$I(\nu, h) = I(\nu, h_s) \tau(\nu, h_s) + \int_{h_s}^h B(\nu, T(z)) \frac{d\tau(\nu, z, q(z))}{dz} dz, \quad (2)$$

$$I(\nu, h_s) = \epsilon B(\nu, T_s) + (1 - \epsilon) I_b(\nu, h_s), \quad (3)$$

where  $I(\nu, h_s)$  is the monochromatic surface radiance at the height  $h_s$ ;  $\tau(\nu, z)$  is the monochromatic atmospheric transmittance from  $z$  to  $h$ ;  $B(\nu, T(z))$  is the Planck function at the local temperature  $T(z)$ ,  $\epsilon$  is the surface emissivity,  $T_s$  is the surface temperature and  $I_b$  is the downward radiance reaching the surface.

For the solar band, the radiance is dominated by the transmitted solar radiation,

$$I(\nu, h) = \frac{F_0}{\pi} \sec \theta_{sun} \tau(\nu, h_s, \theta_{sun}) (1 - \epsilon) \tau(\nu, h_s, \theta_{sat}), \quad (4)$$

where  $F_0$  is the incident solar flux density at the top of the atmosphere,  $\theta_{sun}$  is the solar zenith angle,  $(1 - \epsilon)$  is the surface reflectivity, and  $\theta_{sat}$  is the satellite zenith angle.

As indicated by Eqs. (1) and (4), the ratio  $S^D/S^A$  is independent of the surface parameters, as long as the spectral variation of  $\epsilon$  over the bandpass is negligible. Our forward model study has shown that the effect of interfering species is also largely canceled when the ratio is taken.<sup>5</sup> For this reason, we defined a radiometer R signal as  $R_i = D_i/A_i$ . In the retrieval, we use the R signals as the solar band signals.

## 2.2. The Inverse Model

The CO profile retrieval problem can be posed as solving the equation:

$$\bar{y} = F(\bar{x}) + \bar{N}_\epsilon, \quad (5)$$

where  $\bar{y}$  is the measurement vector,  $\bar{x}$  is the state vector,  $F(\bar{x})$  is the forward model function,  $\bar{N}_\epsilon$  is the instrument noise.

In our algorithm, the measurement vector,  $\bar{y}$ , is formed by the thermal band A and D signals and the solar band R signals. The state vector,  $\bar{x}$ , is chosen to include all the parameters to be retrieved, *i.e.*, the CO mixing ratios for a set of layers, the lower surface temperature  $T_s$ , and thermal band surface emissivity  $\epsilon$ :

$$\bar{y} = (S_i) = \begin{pmatrix} A_1 \\ \vdots \\ A_4 \\ D_1 \\ \vdots \\ D_4 \\ R_5 \\ R_6 \end{pmatrix}, \quad \bar{x} = (x_j) = \begin{pmatrix} \epsilon \\ T_s \\ q_1 \\ q_2 \\ \vdots \\ q_m \end{pmatrix}. \quad (6)$$

The forward function is linearized around an initial guess state vector  $\bar{x}_0$ :

$$F(\bar{x}) = F(\bar{x}_0) + K\Delta\bar{x}, \quad (7)$$

and the matrix K is the weighting function:

$$K = (k_{ij}) = \begin{pmatrix} \frac{\partial S_i}{\partial x_j} \end{pmatrix}. \quad (8)$$

The maximum likelihood solution to Eq.(5) using a Newtonian iteration is:<sup>3</sup>

$$\bar{x}_{n+1} = \bar{x}_0 + C_a K_n^T (K_n C_a K_n^T + C_\epsilon)^{-1} [\bar{y} - \bar{y}_n - K_n (\bar{x}_0 - \bar{x}_n)], \quad (9)$$

where  $\bar{x}_0$  is the *a priori* state vector and the initial guess for the retrieval,  $n$  is the order of iteration,  $C_a$  is the *a priori* covariance matrix for CO and the surface parameters,

$$C_a = E\{(\bar{x} - \bar{x}_0)(\bar{x} - \bar{x}_0)^T\} \quad (10)$$

and  $C_\epsilon$  is the measurement error covariance matrix,

$$C_\epsilon = E\{\bar{N}_\epsilon \bar{N}_\epsilon^T\}. \quad (11)$$

The covariance for the retrieved state vector is:

$$\hat{C} = C_a - C_a K^T (K C_a K^T + C_\epsilon)^{-1} K C_a. \quad (12)$$

The retrieval algorithm first derives the CO profile. The total column amount is then computed from an integration of the profile.

### 2.3 Retrieval *A Priori* Information

We have used two groups of CO profiles as the retrieval *a priori* information. One is compiled from aircraft *in situ* measurements. The other is compiled from the output of a chemical-transport model developed by Brasseur *et al* at NCAR.<sup>6</sup> The work presented in this paper used an ensemble of 152 *in situ* measured profiles both as the true atmosphere for retrieval simulations and to compute the *a priori* statistics for the retrieval. These profiles are compiled from the work of Seiler and Fishman (1981)<sup>7</sup>, STRAT0Z III and TROPOZ II experiments by Marengo *et al*<sup>8-9</sup>, and the GTE/TRACE-A experiment by Sachse *et al*.<sup>10</sup>

Figure 1 shows a comparison of the mean profiles between the *in situ* measurement ensemble and the model output CO profiles. Also shown in Figure 1 is a U.S. standard CO profile from the AFGL atmospheric model.<sup>11</sup> The large tail, near surface, in the *in situ* measured mean reflects the fact that the aircraft measurements over sampled heavily polluted coastal cities and airports. In the work reported in this paper, we have modified the boundary layer CO values to avoid the large variance produced by this over sampling.

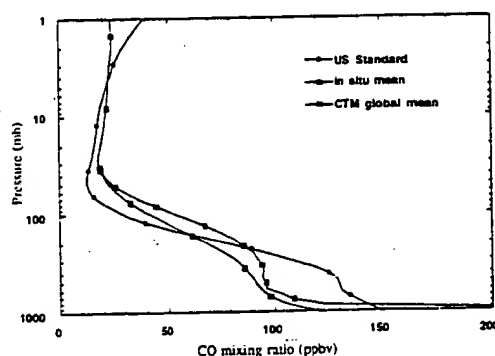


Figure 1. CO profiles from a U.S. Standard model,<sup>11</sup> the *in situ* measurements and a 3D model.<sup>6</sup>

## 3. ANALYSIS AND CHARACTERIZATION OF THE ALGORITHM

### 3.1. Forward Model Sensitivity

The sensitivity of the forward signals to the retrieval parameters is represented by the weighting functions. We present the weighting functions in three groups. The first group, plotted in Figure 2, is the sensitivity to surface parameters. The second group, plotted in Figure 3a, is the CO sensitivity of the A signals. The third group, plotted in Figure 3b, is the CO sensitivity of the D and R signals.

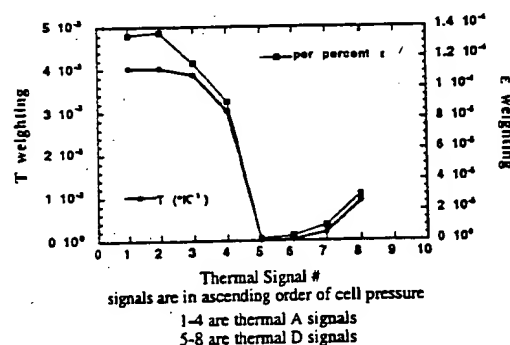


Figure 2. Sensitivities of the thermal band signals to the surface T and  $\epsilon$ .

As indicated by Figure 2, the A signals have a larger sensitivity to the surface parameters and their sensitivities decrease as the modulation cell pressure increases. The D signals are less sensitive to the surface parameters and their sensitivities increase as the modulation cell pressure increases.



Figures 3 shows that the A signals are also very sensitive to the atmospheric CO but the sensitivities are all peaked in the mid-troposphere (~ 500 mb). The D and R signals have a range of sensitivities which provide the vertical resolutions that the profile retrieval requires.

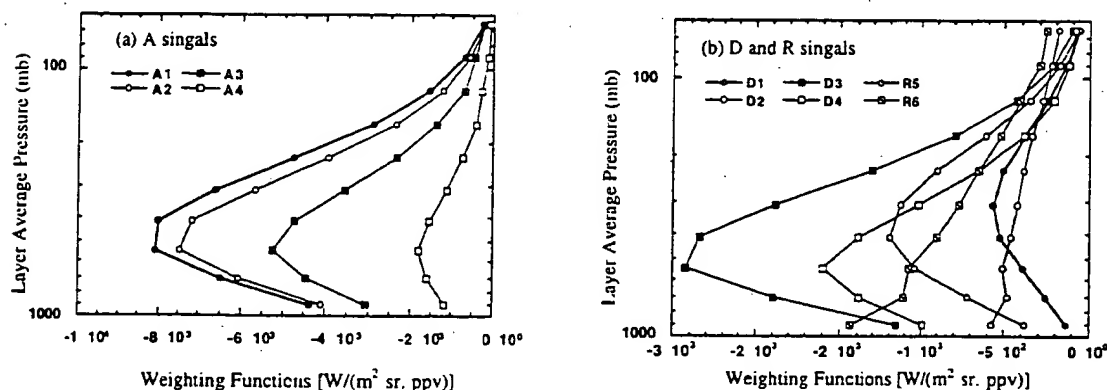


Figure 3. MOPITT weighting functions calculated using the mean profile of the *in situ* measured ensemble.

The orthogonal components of the weighting functions and their corresponding signal-to-noise ratios, for a unit change of CO, are given by the eigenvectors and eigenvalues of an information matrix:

$$H = P^T C^{-1} P \quad (13)$$

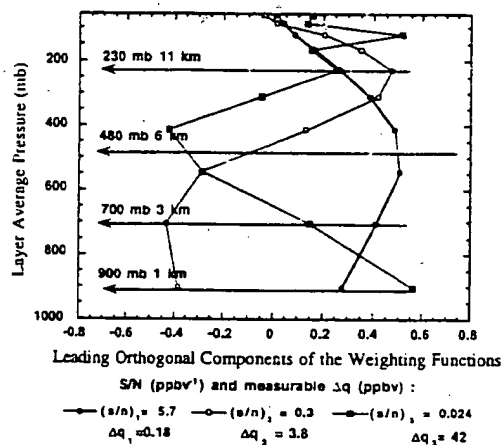


Figure 4. Three leading components of the weighting functions and their corresponding signal-to-noise ratio per ppbv CO change.

the values used for  $C_e$ , *i.e.* the assumed instrument noise, which is subject to change for the actual radiometers.

where  $K$  is the weighting function matrix and  $C_e$  represents the instrument noise as defined in Eq.(11). We have performed this analysis using the predicted instrument noise from the MOPITT Mission Description Document (MDD).<sup>2</sup> The results of this analysis are plotted in Figure 4. As listed in the legend, the three leading components have the signal-to-noise ratio 5.7, 0.3, and 0.024 per ppbv CO change. The inverse of these numbers give the smallest measurable change of CO in the direction defined by each corresponding component. The peak positions of the three components are as indicated in the Figure. Note that these results strongly depend on

### 3.2. Characterization of the A Priori Information

We have examined the characteristics of both measured and model *a priori* statistics using an eigenvalue decomposition. As an example, Figure 5 displays the eigenvectors of the covariance matrix computed from the *in situ* measurement ensemble, scaled by their corresponding eigenvalues. These vectors give the independent components of the *a priori* variance. The effectiveness of the measurement should be evaluated in comparison with these values of the *a priori* variance.

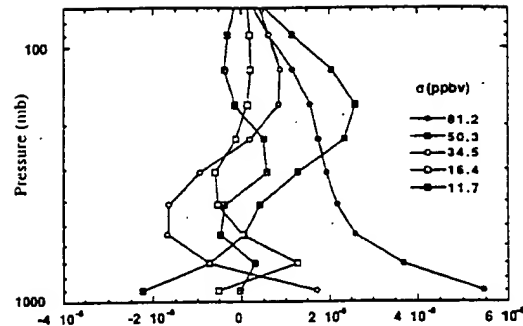


Figure 5. Orthogonal components of the *a priori* constraint from the *in situ* ensemble and their corresponding variance values.

### 3.3. Characterization of the Retrieval

For the purpose of analyzing retrieval characteristics, the retrieved state can be expressed as a transformation of the true state.<sup>12</sup> If we denote the true state as  $\bar{x}$ , the *a priori* state as  $\bar{x}_0$ , and neglect the uncertainties of all model parameters, the forward model equation can be written as:

$$\begin{aligned}\bar{y} &= F(\bar{x}) + \bar{N}_\epsilon \\ &= F(\bar{x}_0) + \frac{\partial F}{\partial \bar{x}}(\bar{x} - \bar{x}_0) + \bar{N}_\epsilon \\ &= \bar{y}_0 + K(\bar{x} - \bar{x}_0) + \bar{N}_\epsilon\end{aligned}\quad (14)$$

Similarly, denoting the retrieved state as  $\hat{\bar{x}}$ , the inverse function as  $I(\bar{y})$ , we can write the inverse model equation as:

$$\begin{aligned}\hat{\bar{x}} &= I(\bar{y}) \\ &= I(\bar{y}_0) + \frac{\partial I}{\partial \bar{y}}(\bar{y} - \bar{y}_0) \\ &= I_0 + D(\bar{y} - \bar{y}_0)\end{aligned}\quad (15)$$

where  $D = \partial I / \partial \bar{y}$  is named the contribution function matrix and represents the sensitivity of the inverse model function to the measurement vector. We have also neglected the inverse parameter uncertainties.

Eqs. (14) and (15) can be combined to express the retrieved state as a weighted mean of the true state and the *a priori* state, plus the contribution of the noise:

$$\begin{aligned}
\hat{\bar{x}} &= T(F(\bar{x}), \bar{N}_\varepsilon) \\
&= T(\bar{x}_0) + DK(\bar{x} - \bar{x}_0) + D\bar{N}_\varepsilon \\
&\equiv \bar{x}_0 + A(\bar{x} - \bar{x}_0) + D\bar{N}_\varepsilon \\
&= A\bar{x} + (I - A)\bar{x}_0 + D\bar{N}_\varepsilon
\end{aligned} \tag{16}$$

where the rows of the matrix  $A=DK$  are named the averaging kernels. In Eq.(16), the step from line 2 to line 3 has assumed that the retrieval model is unbiased. In our case, the explicit form of the averaging kernel matrix can be shown as:

$$A = C_a K^T (K^T C_a K + C_\varepsilon)^{-1} K. \tag{17}$$

Eq.(16) shows the importance of averaging kernels as characteristic functions of the retrieval. The closer the matrix  $A$  is to the unit matrix, the better the retrieved state resembles the true state. The difference  $I-A$  represents the "smoothing error" which in turn reflects the limits of the resolving power of the measurement.

Figure 6 shows an example of a set of averaging kernels for the MOPITT CO profile retrieval, calculated using the weighting functions in Figure 3, the *a priori* covariance described in Figure 5 and the noise values estimated in the MOPITT MDD.<sup>2</sup> The apparent groupings of the averaging kernel peaks around 200 mb and 500 mb reflects the highest sensitivities of the forward model, as shown in Figure 4.

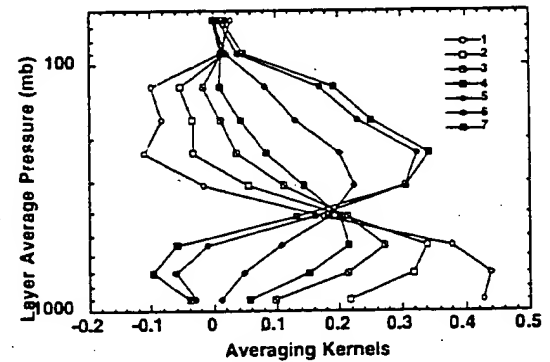


Figure 6. The first seven averaging kernels for a two-kilometer atmosphere layering.

In order to quantify the smoothing error given by the matrix difference  $I-A$ , we have performed an eigenvalue analysis of the  $A$  matrix. Since the  $A$  matrix is asymmetric, it has a set of left and right eigenvectors. Figure 7 shows the three leading right eigenvectors of the  $A$  matrix and their corresponding eigenvalues, for the CO part of the state vector. Using this set of

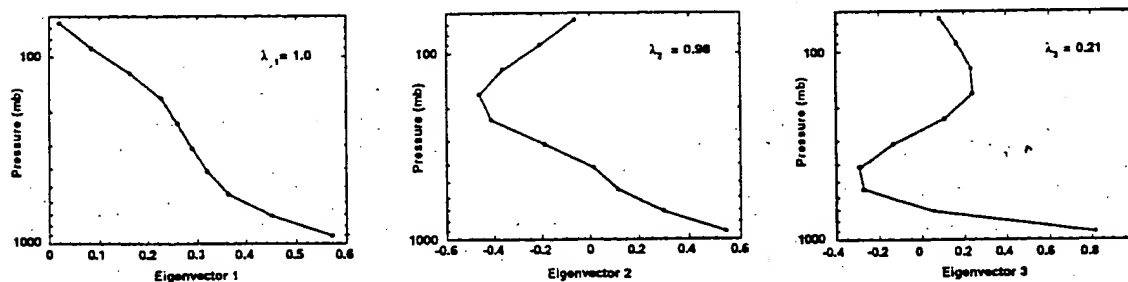


Figure 7. The three leading right eigenvectors of the averaging kernel matrix (for the CO part of the state vector) and their corresponding eigenvalues.

eigenvectors as a basis, Eq.(16) can be transformed. It can then be shown that in the direction defined by the first eigenvector, which corresponds to a unit eigenvalue, the retrieved CO profile best resembles the true CO profile state. In the directions defined by the second and the third eigenvectors, the smoothing error increases with the increased departure of the corresponding eigenvalues from unity.

#### 4. EXAMPLES OF RETRIEVAL EXPERIMENTS

Numerous ensemble retrieval experiments have been conducted, both to evaluate and test the algorithm and to study the sensitivity of the retrievals to various parameters. In this section, we show some sample results. These experiments were conducted using the *in situ* measurement ensemble as the true atmosphere. The ensemble mean and variance were used as the retrieval *a priori* constraints. The noise levels were taken from the MOPITT MDD<sup>2</sup> and the retrieval used a two-kilometer layering. The retrieved profiles are reported as layer average mixing ratios.

Figure 8 shows the CO column retrieval results from four retrieval experiments. These four experiments were designed to estimate the effect of instrument noise, the uncertainties in the ancillary data (*i.e.*, the water vapor profile and the temperature profile information). The length of each horizontal bar indicates the ensemble RMS of the retrieval error.

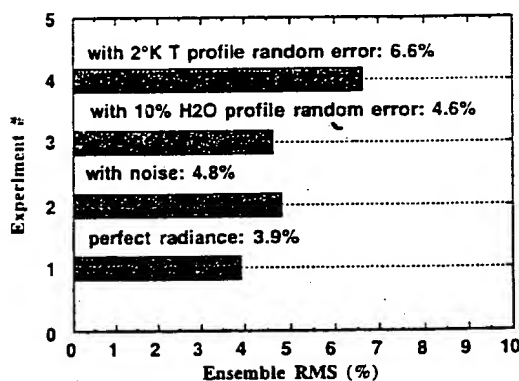


Figure 8. Percentage deviation of retrieved CO column amount from the truth. Shown in the figure are results of four retrieval experiments

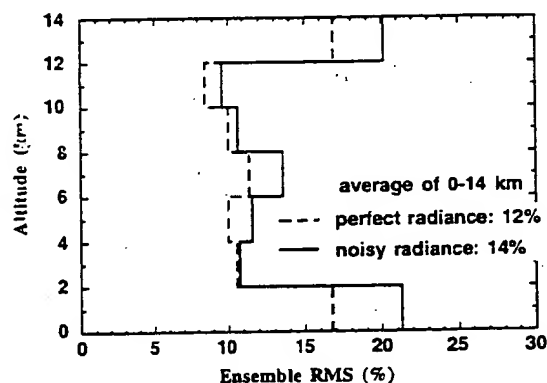


Figure 9. Ensemble rms deviation of retrieved CO profiles using perfect radiance (dashed) and noisy radiance (solid).

Figure 9 shows two sets of CO profile retrieval results given in terms of ensemble RMS error. One set is retrieved from simulated "perfect radiance" and the other from simulated noisy radiance. The smoothing error is responsible for the retrieval errors using perfect radiance. The difference of the two shows the effect of instrument noise. Again, the retrieval error is smaller for the ranges where MOPITT has higher measurement sensitivities, as shown in Figure 4.

#### 5. SUMMARY

We have discussed the MOPITT CO retrieval algorithm for the clear sky and cloud cleared pixels in terms of the forward model sensitivities and vertical resolutions, the *a priori* constraints and the inverse model sensitivities and vertical resolutions. Examples of retrieval experiments are also included. These results depend on the *a priori* constraints and the instrument noise levels used. Compilation of an improved *a priori* ensemble is in progress. Actual instrument noise levels will be measured during prelaunch calibrations.

## 6. ACKNOWLEDGMENT

This work was supported by the National Aeronautics and Space Administration Earth Observing System (EOS) Program under Contract NAS5-30888 and was also supported in part by the National Science Foundation.

## 7. REFERENCES

1. J. R. Drummond, Measurements of Pollution in the Troposphere (MOPITT), in *The use of EOS for Studies of Atmospheric Physics*, edited by J. C. Gille and G. Visconti, pp. 77-101, North Holland, Amsterdam, 1992.
2. J. R. Drummond, G.P. Brasseur, G. R. Davis, J.C. Gille, J.C. McConnell, G.D. Pesket, H.G. Reichle, and N. Roulet, MOPITT Mission Description Document, Department of Physics, University of Toronto, Toronto, Ontario, CANADA, M5S 1A7, 1993.
3. C.D. Rodgers, Retrieval of atmospheric temperature and composition from remote measurements of thermal radiation, *Rev. Geophys. and Space Phys.*, 14, 609-624, 1976.
4. MOPITT Algorithm Theoretical Basis Document (Level 1 to Level 2), Version 2, by NCAR MOPITT Team, July 1995.
5. L. Pan, D. P. Edwards, J. Gille, M. Smith and J. Drummond, Satellite Remote Sensing of Tropospheric CO and CH<sub>4</sub>: Forward Model Studies of the MOPITT Instrument; *Applied Optics*, 34(14), 6976-6988, 1995.
6. The heritage of this model is IMAGES, see J-F Muller, J.-F. and G. P. Brasseur, IMAGES: A three-dimensional chemical transport model of the global troposphere, *J. Geophys. Res.*, 100 pp.16445-16490, 1995.
7. W. Seiler, and J. Fishman, The distribution of carbon monoxide and ozone in the free troposphere; *J. Geophys. Res.*, 86, 7225-7265, 1981.
8. A. M. Marenco. and S. Prieur, Meridional and vertical CO and CH<sub>4</sub> distributions in the background troposphere (70°N-60°S; 0-12 km altitude) from scientific aircraft measurements during the STRAT0Z III experiment (June 1984); *Atmospheric Environment*, 23 185-200, 1989.
9. A. M. Marenco , The airborne programmes Stratoz and Tropoz: a study of atmospheric chemistry on regional and global scale, *International Symposium: Space, Aeronautics and Atmospheric Environment (1994)* (CIC Meteo-France, March 15-17 1994, Toulouse); Cepadues Editions (Toulous France: August 1994)
10. TRACE-A data is archived on NASA Langley DAAC. Data used in this work is from a private communication with G. Sachse and J. Logan.
11. G. P. Anderson, S.A. Clough, F. X. Kneizys, J. H. Chetwynd, and E. P. Shettle, *AFGL Atmospheric Constituent Profiles (0-120km)*, AFGL-TR-86-0110, AFGL (OPI), Hanscom AFB, MA 01736 (1986).
12. C.D. Rodgers, Characterization and error analysis of profiles retrieved from remote sounding measurements, *J. Geophys. Res.*, 95, 5587-5595, 1990.

## Calibration of a length modulated radiometer

Boyd T. Tolton and James R. Drummond

University of Toronto, Department of Physics, 60 St. George Street  
Toronto, Ontario, Canada, M5S 1A7

### 1. ABSTRACT

MOPITT (Measurements Of Pollution In The Troposphere) is a satellite instrument which will be launched in 1998 on the EOS-AMI platform of the Earth Observing System. The primary objective of the MOPITT instrument is to enhance our knowledge of the lower atmosphere by measuring atmospheric profiles of carbon monoxide (CO) and methane (CH<sub>4</sub>). Operationally MOPITT will employ a new form of correlation radiometer known as the Length Modulated Radiometer (LMR). To date, the LMR has been successfully implemented in a ground-based remote sounding instrument measuring CO, and is currently being implemented on two airplane-based instrument known as MATR and MOPITT-A. The operating principle of the LMR is the modulation of a static gas cell path length by means of an optically inert filler material. This paper will describe aspects of the operation of an LMR. Topics that will be covered include an discussion of the sources of optical imbalance in the LMR and the radiometric calibration of the LMR with CO. An analysis of the sources of error in the radiometric calibration of an LMR will also be presented.

**Keywords:** Length Modulated Radiometer, LMR, correlation spectrometry, correlation radiometry, carbon monoxide, MOPITT

### 2. CORRELATION RADIOMETRY

For many years, the temperature and composition of the atmosphere have been remotely measured using a technique known as correlation radiometry<sup>1-7</sup>. The fundamental principles of correlation radiometry are demonstrated in Figure 1. A correlation radiometer operates by modulating the amount of a radiatively active gas in a gas cell, or "correlation cell". This results in a modulation of the transmission through the cell at wavenumbers near the spectral lines of the gas. A narrow band-pass spectral filter limits the radiation field being measured to the spectral region corresponding to the spectral band of the gas. By measuring the modulated radiation that passes through the system as a function of time, two instrument signals can be defined; an average signal ( $S_{avg}$ ), proportional to the average radiation transmitted through the system, and a difference signal ( $S_{diff}$ ), proportional to the difference in the radiation transmitted between the gas amount modulation states. These signals can be expressed in the following manner:

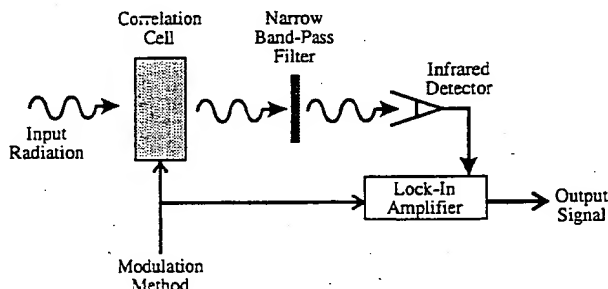


**Figure 1:** A schematic illustrating the principles and major components of a correlation radiometer.

$$S_{diff} = G \int_{\nu_1}^{\nu_2} I_{\nu} \mathfrak{T}_{\nu}(fil) (\mathfrak{T}_{\nu}(s1) - \mathfrak{T}_{\nu}(s2)) d\nu \quad (1)$$

$$S_{avg} = G \int_{\nu_1}^{\nu_2} I_{\nu} \mathfrak{T}_{\nu}(fil) \left[ \frac{(\mathfrak{T}_{\nu}(s1) + \mathfrak{T}_{\nu}(s2))}{2} \right] d\nu \quad (2)$$

where  $G$  represents the instrument gain function,  $I_{\nu}$  is the radiant intensity incident on the correlation cell,  $\mathfrak{T}_{\nu}(fil)$  is the transmission of the narrow band-pass filter with a pass band region extending from  $\nu_1$  to  $\nu_2$ , and  $\mathfrak{T}_{\nu}(s1)$  and  $\mathfrak{T}_{\nu}(s2)$  are the spectral transmittances of the two gas density states of the correlation radiometer.  $S_{diff}$  is mostly sensitive to wavenumbers at or near the spectral lines of the gas in the correlation cell; whereas  $S_{avg}$  is mostly sensitive to the background radiation field. Therefore, since the signals are a product of a whole spectral band of a gas, the energy grasp of the radiometer is improved over a spectrometer of similar spectral selectivity.

Devices which use the technique of correlation radiometry include the selective chopper radiometer<sup>3</sup> (SCR) and the pressure modulator radiometer<sup>3</sup> (PMR). The SCR operates by either switching between two (or more) gas cells with different gas amounts in a static optical path, or by switching between two optical paths. The PMR operates by modulating the pressure inside a static gas cell. Both SCRs and the PMRs have been flown successfully on balloons, aircraft and satellites<sup>13</sup>.

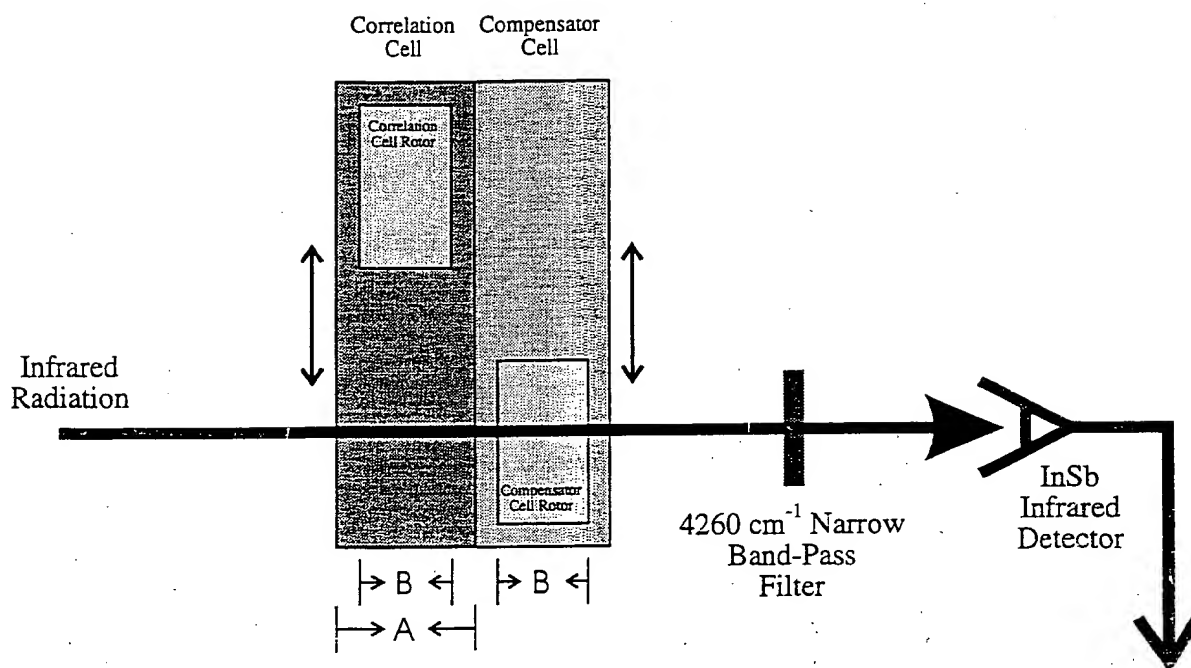
A new form of correlation radiometer known as the Length Modulated Radiometer (LMR) has been proposed<sup>9</sup>. The correlation cell of the LMR performs gas density (molecules per  $\text{cm}^2$ ) modulation by modulating the path length through the correlation cell. Path length modulation is performed by rotating, within the correlation cell, a piece of an optically inert filler material in and out of the optical path through the cell.

The LMR has been operated successfully in a ground-based remote sounding instrument for measuring atmospheric column amounts of carbon monoxide<sup>10</sup>. The LMR is also being implemented in the MOPITT (Measurements Of Pollution In The Troposphere) satellite instrument. MOPITT will be launched on the NASA's Earth Observing System satellite EOS-AM1 in 1998<sup>11</sup>. This research has been motivated by the need to develop and understand the limitations of the technique of length modulation for use in both instruments.

### 3. IMBALANCE

All forms of correlation radiometers suffer to some extent from a systematic error known as "imbalance". Stated simply, imbalance is any signal that is produced by the radiometer at the same frequency as the gas density modulation, but is not a result of the absorption of radiation by the gas in the correlation cell. These spurious signals are instead produced by small modifications in the optics of the radiometer generated directly and/or indirectly by the mechanism that drives the gas density modulation.

The mechanism for gas density modulation in the LMR unfortunately creates a large imbalance condition as the optics between the two states of the correlation cell are grossly different. To combat this problem, the LMR was designed with



### Mk III LMC

Figure 2: A schematic of the LMR demonstrating the principle of gas path length modulation. As the rotors rotate, the gas path length through the correlation cell of the LMC is modulated between A and B. The compensator rotor is driven such that the thickness of rotor that the radiation passes through remains constant.

A second cell known as the compensator cell, containing a second identical rotor (see Figure 2). The compensator rotor is oriented such that the radiation always passes through the same thickness of rotor. Since the path length of rotor that the radiation passes through remains constant, imbalance due to changes in the optics of the two gas amount states are minimized. In operation, the compensator cell is either evacuated or filled with a radiatively inert gas. Together, the unit containing the correlation cell, compensator cell and the mechanisms which drive the rotors in each cell is known as the Length Modulated Cell (LMC).

The LMR can operate at high pressure levels which, in satellite-based applications, makes them ideal for mid- to low-tropospheric remote sounding measurements. It was for this reasons that the LMR was chosen for use in the MOPITT satellite instrument.

To characterise imbalance mathematically, consider  $S_{diff}$  and  $S_{avg}$  if the transmissions of the optics and the gas were separated out for each state:

$$S_{diff} = G \int_{v_1}^{v_2} I_v \mathfrak{T}_v(fil) (\mathfrak{T}_1 \mathfrak{T}_v(s1) - \mathfrak{T}_2 \mathfrak{T}_v(s2)) dv \quad (3)$$



$$S_{avg} = G \int_{\nu_1}^{\nu_2} I_{\nu} \mathfrak{T}_{\nu}(fil) \left[ \frac{(\mathfrak{T}_1 \mathfrak{T}_{\nu}(s1) + \mathfrak{T}_2 \mathfrak{T}_{\nu}(s2))}{2} \right] d\nu \quad (4)$$

where  $\mathfrak{T}_1$  and  $\mathfrak{T}_2$  are the transmission of the two optical paths, and  $\mathfrak{T}_{\nu}(s1)$  and  $\mathfrak{T}_{\nu}(s2)$  are the transmissions of the two gas density states. In principle, the imbalance of the length modulated radiometer can be determined by evacuating the correlation cell of the LMC, thus setting the gaseous transmission ( $\mathfrak{T}_{\nu}(s1)$  and  $\mathfrak{T}_{\nu}(s2)$ ) terms to unity.

Laboratory measurements of the imbalance in the LMR have been made. The optical configuration of the LMR used in these measurements is shown in Figure 3 and is known as the "double-pass" configuration; as the radiation passes twice through the LMC. The purpose of double-passing the LMC is to remove imbalance induced by non-parallelism between the LMC rotors. Included in the laboratory setup was a source of radiation (halogen bulbs), a 600 Hz tuning fork chopper (to separate the radiation of the bulb from the background), a LMC, a narrow band-pass filter (to limit the radiation field to a narrow band around the  $4260 \text{ cm}^{-1}$  absorption band of CO), and a InSb infrared detector. The  $4260 \text{ cm}^{-1}$  band of CO was chosen for this research as this was the absorption band used by the ground-based LMR instrument for measuring the atmospheric CO column<sup>10</sup>. An instrument signal ( $S_{inst}$ ) was defined as the ratio of  $S_{diff}$  to  $S_{avg}$ :

$$S_{inst} = \frac{S_{diff}}{S_{avg}} \quad (5)$$

Defining  $S_{inst}$  in this manner is convenient as, to first order, it is insensitive to the instrument gain function, to drifts in the temperature of the radiation source, and to "grey" absorption (constant absorption independent of wavenumber in the spectral range of interest) in the instrument.

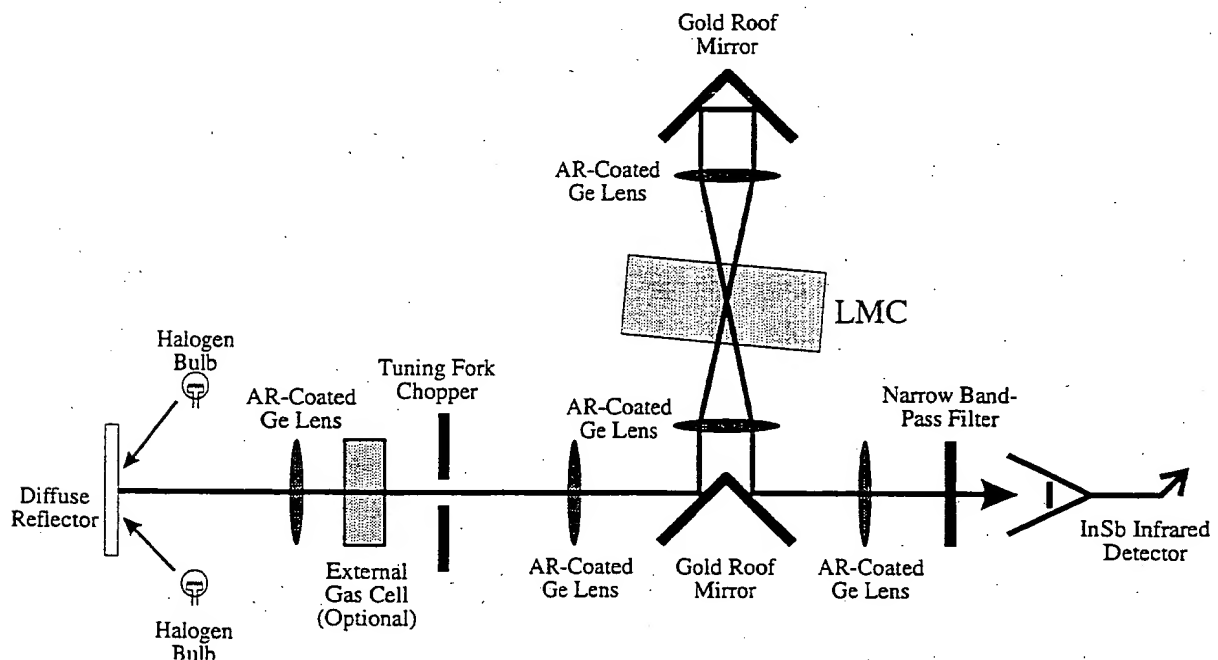


Figure 3: A schematic of the "double-pass" optical configuration of a LMR used in this research.

The imbalance of the LMR can be measured by evacuating the correlation cell ( $\mathfrak{S}_v(s1) = \mathfrak{S}_v(s2) = 1$ ):

$$K = \frac{S_{diff}}{S_{avg}} (P=0) = \frac{2 \int_{v_1}^{v_2} I_v \mathfrak{S}_v(fil) (\mathfrak{S}_1 - \mathfrak{S}_2) dv}{\int_{v_1}^{v_2} I_v \mathfrak{S}_v(fil) (\mathfrak{S}_1 + \mathfrak{S}_2) dv} = \frac{\mathfrak{S}_1 - \mathfrak{S}_2}{\mathfrak{S}} \quad (6)$$

$K$  is known as the *evacuated imbalance*, and represents the fractional difference in the transmission of the two gas path length states of the LMC. In operation, it is desirable for the imbalance to be either less than or known and stable to the resolution of the measurement. Therefore, the required imbalance of the LMR is a function of the measurement being made. For the ground-based instrument, the maximum resolution in the  $S_{max}$  required to make a  $\pm 10\%$  measurement of the atmospheric CO column was  $\pm 2 \times 10^{-5} \cdot 10$ .

#### 4. THE IMPLEMENTATION OF A LMR

A cross-sectional diagram of the LMC used in this work is shown in Figure 4. The LMC is cylindrical in shape with a diameter of 150.4 mm and a thickness of 54.4 mm (minus the motor cup). It consists of two gas cells with an optically inert rotor in each. The body was built entirely from 6061 Aluminum. The two cells are constructed from three cell walls; a correlation cell wall, a compensator cell wall, and a centre wall (which acts as an inner wall to both the correlation cell and compensator cell). The compensator rotor is driven at a rotation rate of approximately 10 Hz by a DC motor located in a cup in the compensator cell wall. Both the compensator rotor and the correlation rotor are mounted onto shafts which are secured to the centre wall on bearing mounts. The correlation cell rotor is driven by a magnetic coupling to the compensator rotor, through the centre wall.

The optical material used for both the rotors and the windows was calcium fluoride ( $\text{CaF}_2$ ). It was chosen for its high

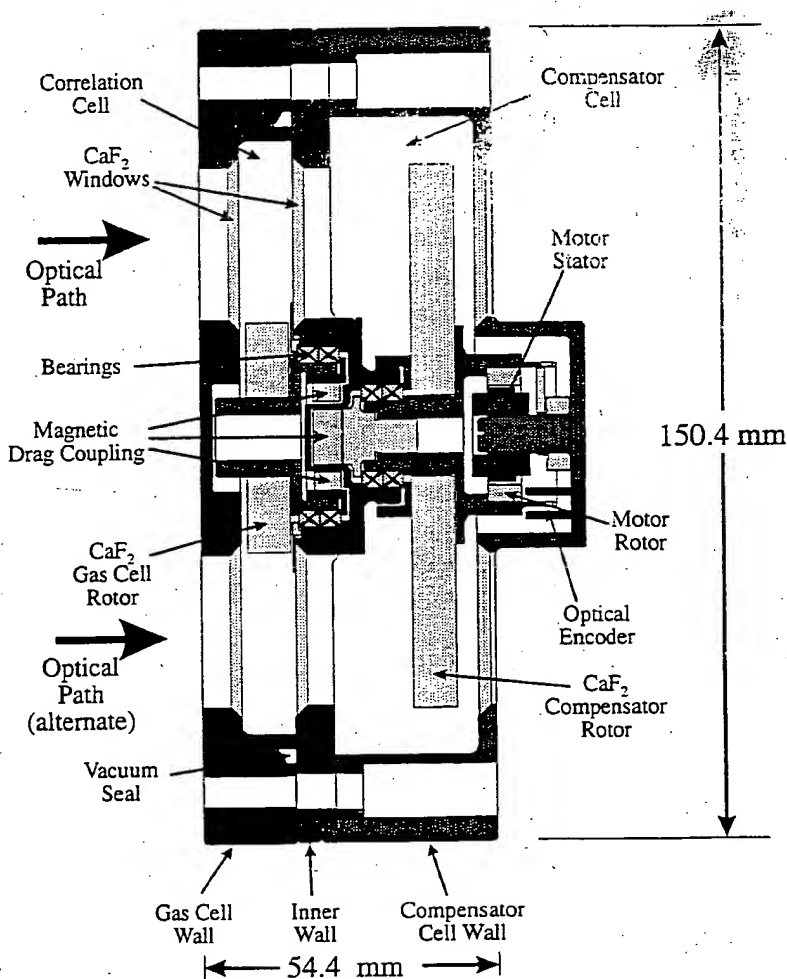


Figure 4: A cross-section of the LMC used in this work.

transmissivity in the near infrared (specifically in the  $2130\text{ cm}^{-1}$  and  $4260\text{ cm}^{-1}$  bands of CO) and low index of refraction ( $n = 1.43$ ), and hence, low reflectivity. The shape of the rotors in the LMC is similar to that of a bow-tie. This shape makes the rotors rotationally balanced about their central axis and allows for path length modulation. As the rotor rotates, the "wings" of the rotor cut in and out of the optical path. This results in four gas path length states or "sectors" per rotation. The magnetic coupling between the rotors holds the two rotors  $90^\circ$  out of phase with each other as they rotate. This ensures that the thickness of  $\text{CaF}_2$  in the optical path remains constant. The thickness of the rotors is 8.0 mm and the (largest) diameter is 100.5 mm. The length of the optical path through the correlation cell of the LMC is 10 mm. Therefore, the ratio of gas path length modulation is 10 mm : 2 mm or 5:1. To reduce possible sources of imbalance, the rotors have been manufactured to strict specifications for parallelism between the faces and uniformity in thickness between rotors. Both rotors were manufactured from the same  $\text{CaF}_2$  blank and the polishing of the blank was performed before the rotors were cut from it.

## 5. IMBALANCE SOURCES IN THE LMR

There are three main categories of imbalance sources in the LMR: imbalance caused by localised modifications in the effective transmission through the rotors, imbalance caused by reflections off the rotor surfaces, and imbalance caused by changes in the gas pressure in the LMC. The following is a summary of the known imbalance sources in the LMR.

### 5.1. Effective Transmission Imbalance Sources

Imbalance in the LMR can be caused by absorption and scattering of radiation off small imperfections on the rotor surfaces, such as dips and scratches, and/or inadequate cleaning. The effects of these imperfections are to partially interrupt the radiation beam passing through the rotors thus producing localised decreases in the detector signal. One means of reducing these effects is to increase the size of the beam passing through the rotors. To this end, in all laboratory measurements, a diffuse radiation source was used. The radiation source used was three halogen bulbs reflecting into the optical chain off a diffusely reflecting surface (as shown in Figure 3). In general, the imbalance due to rotor imperfections was  $<10^{-4}$ .

### 5.2. Reflection Imbalance Sources

Potentially, the largest source of imbalance in the LMR is reflections off of the optical surfaces in the LMC (all optics in the LMC are  $\text{CaF}_2$ ). The reflectivity of a vacuum- $\text{CaF}_2$  interface (at small angles relative to the normal) is approximately 3%. Reflections off the rotors can cause imbalance by two means. The first is due to differences in the reflective losses off the rotor surfaces. If for some reason there is a difference between the reflectances of the rotors, then the intensity of the transmitted radiation will vary depending on which rotor is in the optical path. The second reflection imbalance source occurs if, by some means, a reflected beam off one rotor (or part of the reflected beam) is directed onto the detector but the corresponding reflection from the other rotor is lost.

Imbalance caused by single reflections off of the LMC rotors can be easily seen and identified. Unfortunately it is a product of the double-pass optical configuration. It is caused by a single reflection off the surfaces of one rotor being directed into the returning beam of the double-pass optics. Fortunately, this imbalance source is easy to eliminate. By rotating the LMC (typically  $5^\circ - 10^\circ$ ) towards the source (away from the detector as shown in Figure 3), all single reflections off of the rotors are directed away from the detector, thus removing this imbalance source.

Imbalance produced by double reflections (reflection of a reflection) in the LMC have been observed. A double

reflection results in low intensity beams travelling offset but parallel to the original transmitted beam. Their offset distance is dependent on the angle that the original beam makes with the LMC optics, and the distance between reflecting surfaces. Since the rotors and the windows of the LMC are both made of  $\text{CaF}_2$ , with a reflectivity of approximately 3% per surface, doubly reflected beams will have an intensity of approximately  $10^{-3}$  or 0.1% of the original. At any one time, there are 16  $\text{CaF}_2$  surfaces in the optical path (three windows and one rotor, passed through twice), resulting in a large number of double reflections. Imbalance results if the doubly reflected radiation that hits the detector element varies over the rotation.

In order to investigate (and hopefully reduce) imbalance caused by double reflections, two strategies were explored. The first was to see if symmetry in the optics of the correlation cell and the compensator cell would reduce the imbalance. This would not reduce the intensity of the doubly reflected beams, but should make their offsets as identical as possible. A study of the effects of window placement showed that by placing the LMC windows into a symmetric configuration, a smaller but significant improvement in double reflection imbalance resulted. Unfortunately, the LMC used in this study could not be operated in a symmetric state with vacuum seals. The second strategy was to AR-coat the windows and/or the rotors of the LMC. By reducing the reflectivity of the one or both surfaces, the doubly reflected beams would be reduced. The coatings were a dual-band AR-coating (over the  $2130\text{ cm}^{-1}$  and the  $4260\text{ cm}^{-1}$  CO band) with a net reflectance of approximately 0.3% in those bands (a reduction in reflectivity of approximately one order of magnitude). The net effect of the AR-coatings was to reduce imbalance produced by double reflections by an order of magnitude for each surface that was coated. This agrees well with the reduction in reflectance due to the AR-coatings. However, imbalance levels were found to increase with the use of AR-coated rotors. This was due to non-uniform coatings causing non-uniform transmission through the rotors. From these results, it was decided that the LMC should be operated with AR-coated windows and uncoated rotors.

### 5.3. Gas Pressure Imbalance Effects

When gas is introduced into the correlation cell of the LMC, three effects occur: a bowing of the LMC body due to changes in the pressure, changes in the reflectivity of the optical surfaces in the correlation cell due to changes in the refractive index of the gas, and the correlation effects discussed in section 2. The first effect is the "gas-dependent pressure effect" and the second is the "index of refraction effect".

The gas-independent pressure effect causes imbalance by modifying the double reflections within the LMC. Any motion in the windows would affect the geometry of the double reflections in the LMC, and would therefore affect the imbalance. These changes result in either positive or negative changes in imbalance, depending on how the geometry of the double reflections are changed. These can be mitigated by designing a stiff housing and by using AR-coating the windows. With AR-coated windows in the LMC, this effect induces imbalance levels of approximately  $10^{-5}$ .

The index of refraction effect is caused by changes in the effective transmission of the correlation rotor. As the pressure of the gas in the correlation cell is increased, so does the index of refraction of the gas. This results in a decrease in the reflectivity of the correlation rotor surfaces as the difference in index of refraction between the  $\text{CaF}_2$  and the gas is reduced and an increase in the effective transmission through the rotor. However, the effective transmission of the compensator rotor remains unchanged. Therefore, as the correlation cell gas pressure is varied, so does the imbalance. Operationally, for an LMC filled with 1 atm of CO, this effect produces imbalance of approximately  $2 \times 10^{-4}$ .

### 5.4. Summary of LMR Imbalance Sources

Table 1 contains a list of the known sources of imbalance in a double-passed LMR, and an estimate of their magnitudes. These sources include:

Imbalance Source	Estimated Magnitude Of Imbalance Source	
	Uncoated Windows	AR-Coated Windows
Cleaning	$< 10^{-4}$	$< 10^{-4}$
Optical State of the Rotors	$< 10^{-4}$	$< 10^{-4}$
Single Reflections	$3 \times 10^{-2}$	$3 \times 10^{-2}$
Double Reflections	$< 5 \times 10^{-3}$	$< 5 \times 10^{-4}$
Gas-Independent Pressure Effect	$5 \times 10^{-5}$	$10^{-5}$
Index of Refraction Effect	$2 \times 10^{-4}$	$2 \times 10^{-4}$

**Table 1:** A table listing the known sources of imbalance in the LMC, with estimates of magnitude.

- 1) Cleaning: Imbalance produced by differences between the transmission of the rotors caused by contaminants on the optical surfaces of the rotor.
- 2) Optical State of the Rotors: Imbalance produced by differences between the transmissions of the rotors caused by surface digs and scratches.
- 3) Single Reflections: Imbalance produced by radiation being singly reflected off of a rotor onto the detector.
- 4) Double Reflections: Imbalance produced by radiation being doubly reflected off of a rotor and a window in the LMC, and travelling (offset) with the main beam to the detector.
- 5) Gas-Independent Effect: Changes in imbalance produced by bowing of the correlation cell walls (as the cell pressure changes) slightly modifying the geometry of the double reflections within the LMC.
- 6) Index of Refraction Effect: Changes in imbalance produced by changes in the index of refraction of the gas, resulting in changes in the transmission of the rotors.

## 6. RADIOMETRIC CALIBRATION OF THE LMR WITH CARBON MONOXIDE

In the laboratory, a number of measurements of CO in the LMC have been performed. These measurements were used to calibrate a ground-based LMR for use as a remote sounding instrument for measuring CO<sup>10</sup>. The results we expressed in terms of an *instrument calibration ratio* ( $S_{cal}$ ) which is equal to the ratio of the experimental  $S_{inst}$  to a calculated theoretical  $S_{inst}$ :

$$S_{cal} = \frac{S_{inst}(\text{experimental})}{S_{inst}(\text{theoretical})} \quad (7)$$

The results of a series of  $S_{cal}$  measurements which were made over a three month period in the Fall of 1994 is presented in Figure 5. Each measurement was made with the LMC filled with nominally 1 atm of CO. In total there were 52  $S_{cal}$  measurements. This plot shows that the

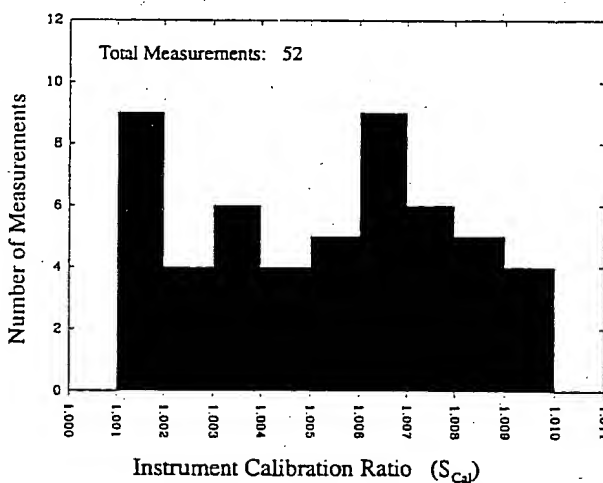


**Figure 5:** A Histogram of  $S_{cal}$  measurements taken over period from August to November 1994. All Measurements were made with a CO fill in the LMC of approximately 1 atm.

measured  $S_{cal}$  ranged between 1.001 and 1.010.

The value of the measured  $S_{cal}$  shows how well the radiometric properties of the experiment were understood. In general, measurements of  $S_{cal}$  showed that experimental  $S_{inst}$  was up to 1% higher than the theoretical  $S_{inst}$ . This difference was due to an inadequate calculation of the theoretical  $S_{inst}$ . Some of the possible errors in the calculation include: errors in the spectral line data, error in gas purity, errors in the radiation source temperature, errors in the narrow band-pass filter transmission profile, and errors in the optical parameters of the LMC including the gas path length through the correlation cell and the angle that the double-passing beam passes through the LMC. The results of an error budget calculation are presented in Table 2. Specifically, it presents the required error in or value of a parameter that would result in a 1.0% increase in the theoretical  $S_{inst}$ . The results of these calculations show that the most important sources of error come from the spectral line data (line strength and line width), and the measurement of the narrow band-pass filter profile. Thus in order to improve the accuracy of the prediction of the radiometric performance of the LMR, these parameters must be known to higher accuracy. It should be noted, however, that different error sources would produce different noise features. For example, any error in the spectral line data would produce non-unity values in  $S_{cal}$ . It would not, however, produce variation in the measured  $S_{cal}$ . Errors which might vary from measurement to measurement (such as the LMC pressure or the filter profile), might not affect the average  $S_{cal}$  but could affect the variations in  $S_{cal}$ .

Source of Error	Error in Knowledge	Assumed Value	Required error to increase the theoretical $S_{inst}$ by 1.0%	Required value to increase the theoretical $S_{inst}$ by 1.0%
Line Strength	$\pm 2\%$ to $\pm 5\%$		+1.1%	
Line Width	$\pm 5\%$ to $\pm 10\%$		+7.2%	
Gas Temperature	$\pm 0.2^\circ \text{C}$		-2.6 $^\circ \text{C}$	
Gas Pressure	$\pm 0.05\%$		+1.0%	
Gas Purity		100%		101.1%
Filament Temperature		2850 K		1250 K
Filter Shift		0 $\text{cm}^{-1}$		Can not be achieved
Filter Width		104.8 $\text{cm}^{-1}$		102.6 $\text{cm}^{-1}$
Correlation Cell Length		10.00 mm		9.60 mm
Double-Pass Beam Angle		3.6 $^\circ$		9.4 $^\circ$

**Table 2:** A table listing 10 sources of error in the calculation of the theoretical  $S_{inst}$ . For each source, either the magnitude of the error in the source or the assumed value of the source is listed, along with the required error or value that would result in a 1.0% increase in the theoretical  $S_{inst}$ .

## 7. SUMMARY

This paper has described the development of a new form of correlation radiometer known as a Length Modulated Radiometer (LMR). The principal component of the LMR is the Length Modulated Cell (LMC), which is a gas cell which is undergoing gas path length modulation by means of an optically inert bow-tie shaped rotor ( $\text{CaF}_2$ ). This paper discussed two main topics in the operation of the LMR: imbalance and radiometric calibration.

Imbalance in a correlation radiometer is any signal that appears to be due absorption of the gas in the correlation cell, but instead, is due to small difference in the optics resulting from the gas density modulation technique. In the LMR, a number of sources of imbalance have been identified and quantified, and whenever possible, ameliorated. They can be classified under three categories: effective transmission imbalance sources, reflection imbalance sources, and gas pressure imbalance effects. Effective transmission imbalance sources refer to imbalance caused by imperfections in the  $\text{CaF}_2$  rotors causing reductions in the amount of radiation transmitted through the rotors. These imperfections include digs, scratches, dust and/or oils on the rotor surface. Reflection imbalance sources refer to imbalance caused single and double reflections off the optical surfaces in the LMC. To reduce this source of imbalance, the LMR is operated with the LMC at a  $5^\circ$  tilt relative to the double-pass optics axis (to remove single reflections) and with AR-coated cell windows (to reduce the magnitude of the double reflections). Gas pressure imbalance effects refer to changes in the imbalance levels caused by changes in the pressure of the gas in the correlation cell of the LMC. An index of refraction pressure effect results from changes in the index of refraction of the gas with changes in pressure. This results in changes in the reflections off and transmission through the correlation cell rotor, resulting in a sensitivity in imbalance to the gas pressure. A gas-independent pressure effect results from modification to the geometry double reflection due to bowing of the LMC cell walls with pressure. This effect was minimised by AR-coating of the LMC windows. In operation, the LMR imbalance levels was typically in the low  $10^{-4}$  range.

This paper also presented the results of a series of radiometric calibrations of the LMR with  $\text{CO}$ . These calibrations show that the radiometric response of the LMR is predictable to  $\pm 0.5\%$ . The major sources of the error are associated with the spectral line data and the narrow-band pass filter transmission profile.

## 8. ACKNOWLEDGEMENTS

The work presented here would not have been possible without the cooperation and support of a large number of people and organisations. We would particularly like to thank the MOPITT team at the University of Toronto; specifically Mr. G. Bailak and Mr. P. Chen. Funding for this research was provided by the Canadian Space Agency (CSA), Natural Sciences and Engineering Research Council (NSERC), and Atmospheric Environment Services of Canada (AES).

## 9. REFERENCES

1. P. G. Abel, P. J. Ellis, J. T. Houghton, G. Peckman, C. D. Rodgers, S. D. Smith, and E. J. Williamson, "Remote Sounding of Atmospheric Temperature from Satellites II. The Selective Chopper Radiometer for Nimbus D," *Proc. Roy. Soc. Lond.* **A320**, 35 - 55 (1970).
2. P. Ellis, G. Holah, J. T. Houghton F.R.S., T. S. Jones, G. Peckham, G. D. Peskett, D. R. Pick, C. D. Rodgers, H. Roscoe, R. Sandwell, S. D. Smith, and E. J. Williamson, "Remote Sensing of Atmospheric Temperature from Satellites IV. The Selective Chopper for Nimbus 5," *Proc. Roy. Soc. Lond.* **A334**, 149 - 170 (1973).
3. F. W. Taylor, J. T. Houghton, G. D. Peskett, C. D. Rodgers, E. J. Williamson, "Radiometer for Remote Sounding of the Upper Atmosphere," *Appl. Opt.* **11**, 135 - 141 (1972).
4. C. P. Chaloner, J. R. Drummond, J. T. Houghton, R. F. Jarnot, and H. K. Roscoe, "Infra-red Measurements of Stratospheric Composition I. The Balloon Instrument and Water Vapour Measurements," *Proc. Roy. Soc. Lond.* **A364**,

145 - 149 (1978).

5. J. R. Drummond et al., "The Stratospheric and Mesospheric Sounder on NIMBUS 7," *Phil. Trans. Roy. Soc. Lond.* **A296**, 219 - 241 (1980).

6. H. G. Reichle Jr., V. S. Connors, J. A. Holland, W. D. Hypes, H. A. Wallio, J. C. Casas, E. P. Condon, B. B. Gormsen, M. S. Saylor, and Hesketh, "Middle and Upper Tropospheric Carbon Monoxide Mixing Ratios as Measured by Satellite-Borne Remote Sensor During November 1981," *J. Geophys. Res.* **91**, d10, 10865 - 10887 (1986).

7. H. G. Reichle Jr., V. S. Connors, J. A. Holland, R. T. Sherrill, H. A. Wallio, J. C. Casas, E. P. Condon, B. B. Gormsen, and W. Seiler, "The Distribution of Middle Tropospheric Carbon Monoxide During Early October 1984," *J. Geophys. Res.* **95**, 9845 - 9856 (1990).

8. J. T. Houghton, and S. D. Smith, "Remote Sounding of Atmospheric Temperature from Satellites, I. Introduction," *Proc. Roy. Soc. Lond.*, **A320**, 23 - 32 (1970).

9. J. R. Drummond, "Novel correlation radiometer: the length-modulated radiometer," *Appl. Opt.* **28**, 2451 - 2452 (1989).

10. B. T. Tolton, "A Length-Modulated Radiometer for Remote Sounding of Carbon Monoxide," Ph.D. Thesis (Department of Physics, University of Toronto, 1996).

11. J. R. Drummond, G. P. Brasseur, G. R. Davis, J. C. Gille, J. C. McConnel, G. D. Pesket, H. G. Reichle, and N. Roulet, *MOPITT Mission Description Document*, (Department of Physics, University of Toronto, Toronto, Ontario, Canada, M5S 1A7, [http://www.atmosp.physics.utoronto.ca/mopitt/mdd\\_93/index.html](http://www.atmosp.physics.utoronto.ca/mopitt/mdd_93/index.html)) 1993.

12. L. S. Rothman, R. R. Gamache, R. H. Tipping, C. P. Rinsland, M. A. H. Smith, D. C. Benner, V. M. Devi, J. -M. Flaud, C. Camy-Peyret, A. Perrin, A. Goldman, S. T. Massie, L. R. Brown, and R. A. Toth, "The Hitran Molecular Database: Editions of 1991 and 1992," *J. Quant. Spectrosc. Radiant. Transfer* **48**, 469 - 507 (1992).